Fatigue and extreme wave loads on bottom fixed offshore wind turbines. Effects from fully nonlinear wave forcing on the structural dynamics.

Schløer, Signe

Publication date:
2013

Document Version
Publisher's PDF, also known as Version of record

DTU Wind Energy

Fatigue and extreme wave loads on bottom fixed offshore wind turbines

Effects from fully nonlinear wave forcing on the structural dynamics

Department of Wind Energy Report 2014

Signe Schløer

DTU Wind Energy PhD-0017
ISBN: 978-87-92896-47-6

July 2013

DTU Vindenergi
Institut for Vindenergi

Author (s): Signe Schløer

Title: Fatigue and extreme wave loads on bottom fixed offshore wind turbines
Effects from fully nonlinear wave forcing on the structural dynamics

Department: Department of Wind Energy

DTU Wind Energy PhD-0017

ISBN: 978-87-92896-47-6

ISBN: 978-87-92896-47-6

July 2013

Predace
This thesis is submitted in partial fulfillment of the Ph.D. degree from the Technical University of Denmark.
The work was performed at the Fluid Mechanics Section of Department of Wind Energy at the Technical University of Denmark, in the period Mai 2010 to July 2013. The study has been performed under the supervision of Associate Professor Henrik Bredmose as main supervisor and Senior Researcher Robert F. Mikkelsen as cosupervisor.
This research was carried out as part of the Statkraft Ocean Energy Research Program (SOERP), sponsored by Statkraft.

Technical University of Denmark
Department of Wind Energy
Frederiksborgvej 399
Building 118
4000 Roskilde
Denmark
www.vindenergi.dtu.dk

Acknowledgement

First and foremost I would like to thank my supervisor, Henrik Bredmose. I am very grateful for all his help the last three years. I appreciate his support and guidance throughout the project. Without his patience, knowledge and ability to explain I had never manage to finish the project.
I would also like to give my thanks to my co-supervisor Robert Mikkelsen. During the project he always took time to help me understand the dynamics of a wind turbine and explain me technical details concerning Flex5.

Stig Øye has provided me asses to Flex5 and further helped me setting up the code with the NREL-5MW wind turbine. Further, he made Flex5 ready to include the soil model in the Flex5 calculations. Stig Øye offered me a lot of friendly help in understanding Flex5 and discussing the results from Flex5.
Associate Professor Allan Engsig-Karup is thanked for providing access to the fully nonlinear wave model, OceanWave3D. Harry Bingham has been very helpful when I had problems with the calculations in OceanWave3D and open for discussions and understandings of the results. He is further thanked for helping implementing the wave breaking filter in OceanWave3D.
It has also been possible to implement a soil model in Flex5 as Ole Hededal and Rasmus Tofte Klinkvort provided me their soil model. I appreciate that they had time to introduce and explain me the model and helping me during the implementation, when I had questions to the model.

Jørgen Junker Jensen is thanked for providing input to the probability analysis and DONG Energy and Niels Jacob Tarp Johansen for providing the met-ocean-data used in the analysis.
Bo Terp Paulsen provided me with calculation for the CFD and 3D analysis. This is also appreciated.
I also appreciate the many discussion, inputs and interest in my project, which I have received from Jørgen Krokstad.
Torben J. Larsen and Taeseong Kim are thanked for fruitful discussions and inputs. The PhD-project is part of the ForskEL-project, “Wave loads on offshore wind turbines”. The partners of this project are also thanked for useful discussions.
As part of my project I visit Ole Gunnar Dahlhaug and the Department of Energy and Process Engineering at Norwegian University of Science and Technology, NTNU in the spring 2012. I am very grateful for the welcome and help I received during the stay. I also visit Marintek and Statkraft during the stay and would like to thanks the colleague here for introducing me to their work.

Finally, the research was carried out as part of the Statkraft Ocean Energy Research Program, sponsored by Statkraft (www.statkraft.no). This support is gratefully acknowledged. The program has been very rewarding, and allowed for contact people at NTNU and Upsalla University and provided knowledge about many areas in the research of Ocean Energy.

Abstract

Since the world's first offshore wind farm was built in the early 1990s in Denmark, the offshore wind industry has increased tremendously in Europe, and will increase even more the next years. Both the water depth and the size of the wind turbines have increased continually since the first offshore wind farms.
As wind farms are being moved further offshore the wave loads become larger compared to the wind loads and therefore more important in the design of offshore wind turbines. Yet, the water depth is still only shallow or intermediate where the waves should be described by nonlinear irregular wave models. In today's design, however, often only linear or second-order irregular wave theory is used to describe the stochastic process of the waves. The extreme waves are often described by the fully nonlinear stream function theory, which only is valid for regular waves on a flat bed. For this reason it is important to investigate the significance of nonlinearity for irregular waves both in the determination of the extreme loads where the irregular nonlinear waves can become more steep than waves from nonlinear regular wave theory and in the determination of fatigue loads where nonlinear waves will transfer energy to higher frequencies which can be close to the wind turbines eigenfrequency.
In the present thesis the response of an offshore wind turbine placed on a monopile foundation is investigated when exposed to linear and fully nonlinear irregular waves. The focus of the investigations is the consequence of incorporation of full nonlinearity in the wave kinematics. In the main part of the thesis six wind and sea states with increasing wind speed and significant wave height are considered. The wave realizations are considered at four different water depths to investigate the effect of water depth on the wave nonlinearity.
A fully nonlinear potential-flow model, Engsig-Karup *et al.* (2009), is used to calculated both the linear and fully nonlinear wave kinematics. The wave forces are calculated by Morison's equation. The aeroelastic calculations are carried out in Flex5, Øye (1996), to study the dynamic effects of the wave nonlinearity.
In first part of the thesis, the linear and nonlinear wave realizations are compared and the static wave forcing based on the two wave theories analysed. This analysis is followed by dynamic calculations where the effects of wave nonlinearity on the structural dynamics are investigated. Focus is on the sectional moments in the tower and monopile. The equivalent loads and accumulated equivalent load due to the six wind and sea states are further calculated and compared.
The wind forcing and the aerodynamic damping are often dominating over the effects from the waves. The misalignment between the wind and wave directions is therefore also included in the analysis. In this way it is possible to investigate how the nonlinearity of the waves affects the structural dynamics and fatigue damage in situations where the effects of the wind are insignificant.
Damping of the structural response is an important parameter, when the nonlinearity of the waves is investigated. Besides aerodynamic damping other damping effects also exist which affect the structural dynamics. The magnitude of the hydrodynamic damping is therefore also investigated in the thesis.
To investigate the effects of the soil in the dynamic analyses, a soil model, Hededal & Klinkvort (2010) and Klinkvort (2012), is implemented in Flex5. With this model it is possible both to investigate the structural response and damping due to the soil and compared it against classical p-y curves combined with a constant damping factor.
The potential flow solver is further compared with a CFD-solver, where the detailed flow around the monopile when exposed to waves and the corresponding pressure acting on the cylinder are calculated. The structural response due to the forces from the CFD-solver is compared against the

structural response due to the forces based on the potential-flow solver and Morison's equation. Finally a small study of the effect of including wave directionality in the dynamic analysis is performed.
All the analyses in this thesis contribute to the understanding of how important the wave nonlinearity is in the design of offshore wind turbines.

Resumé

Siden verdens første havvindmøllepark blev bygget i Danmark i begyndelsen af 1990'erne er havvindmølleindustrien vokset enormt i Europa og vil stige endnu mere i de næste år. Både vanddybden og størrelsen på vindmøllerne er steget kontinuerligt siden de første havvindmølleparker. Som vindmølleparkerne flyttes mere og mere offshore, bliver bølgelasterne større i forhold til vindlasterne og derfor vigtigere i projekteringen af havvindmøller. Vanddyden er dog stadig kun lavvande eller mellemdybt, hvor bølgerne skal beskrives med ikkelineær irregulær bølgeteori. I projekteringen i dag bruges der dog ofte kun lineær- eller andenordens irregulær bølgeteori til at beskrive de stokastiske bølger. De ekstreme bølger er ofte beskrevet med den fuldt ikkelineære strøm funktions teori, som kun er gyldig for regulære bølger på en flad havbund. Det er derfor vigtigt at undersøge vigtigheden af irregulære bølgers ikkelinearitet. Både når de ekstreme laster findes, hvor de ikkelineære irregulære bølger kan være mere stejle end bølger baseret på regulær ikkelineær bølgeteori og i bestemmelsen af udmattelseslaster, hvor de ikkelineære bølger flytter energi til højere frekvenser, som kan være tæt på vindmøllens egenfrekvens.
I denne afhandling betragtes responset af en havvindmølle placeret på en monopæl, når den er udsat for lineære og fuldt ikkelineære irregulære bølger. Fokus er at undersøge konsekvenserne af inkorporering af fuldt ikkelinearitet i bølgekinematikken. Seks vind og sø-tilstande med stigende vindhastighed og signifikant bølgehøjde betragtes i hovedparten af afhandlingen. Bølgerealisationerne betragtes på fire vanddybder for at undersøge effekten af vanddybden på ikkelineariteten.
En fuldt ikkelineær potential-strømningsmodel, Engsig-Karup *et al.* (2009), anvendes for at beregne den lineære og ikkelineære bølgekinematik. Bølgelasterne beregnes af Morisons ligning. De aeroelastiske beregninger udføres i Flex5, Øye (1996).
I første del af afhandlingen sammenlignes de lineære og ikkelineære bølgerealisationer samt de statiske bølgelaster baseret på de to bølgeteorier. Denne analyse er efterfulgt af dynamiske beregninger, hvor effekterne af bølge ikkelineariteten på den strukturelle dynamik undersøges. Fokus er på snitmomenterne i vindmølletårnet og i monopælen. Derudover beregnes og sammenlignes de seks vind og søtilstandes tilsvarende udmattelseslaster. Både vindlasten og den aerodynamiske dæmpning dominerer ofte over effekten fra bølgerne. Forskellen mellem vind- og bølgeretningen er derfor også medtaget i analysen. På denne måde er det muligt at undersøge, hvordan bølgernes ikkelinearitet påvirker den strukturelle dynamik og udmattelseslasterne i situationer, hvor vindens påvirkning er ubetydelig. Dæmpningen af det strukturelle respons er en vigtig parameter, når bølgernes ikkelinearitet undersøges. Udover aerodynamiske dæmpning påvirker andre typer dæmpning også den strukturelle dynamik. Størrelsesordenen af den hydrodynamiske dæmpning undersøges derfor også i afhandlingen.
For at undersøge hvordan jorden påvirker den strukturelle dynamik, er en jordmodel, Hededal & Klinkvort (2010) and Klinkvort (2012), implementeret i Flex5. Med denne model er det muligt både at undersøge det strukturelle respons og dæmpning forårsaget af jorden og sammenligne dette med klassiske *p-y* kurver kombineret med en konstant dæmpningsfaktor.
Potential-strømningsmodelen sammenlignes yderligere med en CFD-løser, hvor den detaljerede strømning omkring monopælen og det tilsvarende tryk på pælen beregnes, når pælen er udsat for bølgepåvirkning. Det strukturelle respons forårsaget af kræfterne fra CFD-løseren sammenlignes med det strukturelle respons forårsaget af kræfterne baseret på potential-strømningsmodelen kombineret med Morisons ligning. Til sidst udføres en mindre undersøgelse af effekten af retningsbestemte bølger i den dynamiske analyse.
Alle analyserne i denne afhandling bidrager til forståelsen af, hvor vigtigt bølgernes ikkelinearitet er i projekteringen af havvindmøller.

Contents

List of symbols

A	Added mass
$\tilde{\mathsf{A}}$	Modal added mass
$\hat{A}$	Amplitude
A_s	Strength reduction parameter
$\mathscr{A}$	Area
a and a_v	Horizontal particle acceleration
$\hat{a}$	Amplitude
B	Directional spreading function
B	Hydrodynamic damping
$\tilde{\mathsf{B}}$	Modal hydrodynamic damping
b	Scale parameter
$\hat{b}$	Amplitude
C_R	Restoring force
C_m	Added mass coefficient
C_M	Inertia coefficient
C_D	Drag coefficient
C_{12}	Coupling coefficient
c	Frequency parameter
c	Damping factor
D	Diameter
D_{fat}	Fatigue damage
D_s	Spreading function
dx	Grid distance
E	Modulus of elasticity
E_{kin}	Kinetic energy
F	Force
f	Force per meter
f_{drag}	Drag force in the soil
f_{face}	Face force in the soil
f_s	Force in the soil
f_u	Ultimate bearing capacity
$f_{u,virgin}$	Virgin curve in soil
f_d	Drag force in Morison's equation
f_{dc}	Axial divergence correction term ín Morison's equation
f_{cfd}	Force based on CFD-calculations
$\hat{f}$	Frequency
$\hat{f}_p$	Peak frequency
$\mathbf{GA}$	Generalized added mass
$\mathbf{GB}$	Generalized hydrodynamic damping
$\mathbf{GM}$	Generalized mass
$\mathbf{GK}$	Generalized stiffness
$\mathbf{GC}$	Generalized damping
$\mathbf{GF}$	Generalized force
g	Acceleration of gravity
$g_{\tau b}$	Morlet wavelet
H	Wave height
H_b	Wave height at wave breaking
H_{max}	Maximum wave height
H_0	Wave height at deep water
H_s	Significant wave height
H	Dynamic amplication factor

Continues on Next Page...

List of symbols (continued)

h	Water depth
h_0	Deep water depth
I	Moment of inertia
I_{ref}	Turbulence intensity reference
I_t	Turbulent intensity
KC	Keulegan-Carpenter number
$\tilde{\mathsf{K}}$	Modal stiffness
k	Wave number
k_x and k_y	Wave number components
k_b	Wave number at wave breaking
k_m	Soil modulus parameter
kh	Nondimensinal wave number
k	Stiffness factor
k_s	Soil stiffness factor
L	Wave length
L_b	Wave length at wave breaking
L_{eq}	Equivalent load
$L_{eq,acc}$	Accumulated equivalent load
L	Length of beam
L_P	Length of monopile
L_T	Length of tower
M	Moment
M_{top}	Mass of wind turbine subtracted the tower
$\tilde{\mathsf{M}}$	Modal mass
m	Mass
m	Slope of S-N curve
N	Number
N_{eq}	Number of cycles in equivalent load
N_x	Number of grid points in horizontal direction in wave model
N_z	Number of grid points in vertical direction in wave model
N_s	Number of cycles in $\hat{S} - N_s$-curve
N_{eq}	Number of cycles in equivalent loads
$\underline{\mathsf{n}}_1$, $\underline{\mathsf{n}}_2$ and $\underline{\mathsf{n}}_3$	Vector
P	Probability of exceedance
$\hat{P}$	Probability of occurrence
$\hat{P}_{rel}$	Relative probability of occurrence
P	Point
p	Pressure
S	Wave spectrum
$\hat{S}$	Rainflow vector containing amplitudes
S_t	Step function
Sk	Skewness
s	Sea bed slope
T	Period, total time
T_p	Peak wave period
t	Time
t	Thickness
u and v	Horizontal particle velocity
u and v	Displacement in fore-aft and side-to-side direction
u_P	Displacement of monopile
u_T	Displacement of tower
V	Wind velocity

Continues on Next Page...

List of symbols (continued)

W	Work
V_{hub}	Wind velocity at hub
w	Vertical particle velocity
Z_{max}	Surface elevation on cylinder
x_0	Eigenvector
x, y and z	Cartesian coordinates
α	Generalized coordinate
α_0	Scalar
$\hat{\alpha}$	Hardening parameter in soil section
$\tilde{\alpha}$	Local volume ratio of water
β	Parameter in the step function used in the soil model
δ	Logarithmic decrement
ϵ	Random number between zero and unity which represent the phase-angle
ζ	Damping ratio
η	Surface elevation
θ	Angular deflection
$\tilde{\theta}$	Angle
κ	Curvature
$\tilde{\kappa}$	Relation between H_s and T_p
$\tilde{\lambda}$	Froude scale factor
ξ	Horizontal coordinate
ρ	Density of water
σ	Vertical coordinate
$\hat{\sigma}$	Standard deviation
ϕ	Velocity potential
φ	Shape function
$\hat{\varphi}$	Wave directions in multi-directional sea
$\hat{\varphi}_m$	Mean wave directions in multi-directional sea
ψ	Random number between zero and unity
ω	Angular frequency
ω_0	Angular eigenfrequency

Chapter 1

Introduction

The first offshore wind farm in the world, *Vindeby*, was build in Denmark in 1991. Eleven 450 kW wind turbines were erected i water depths of 2-4 m. Since then the offshore wind industry has increased tremendously, in particular in Europe. 90 % of all offshore wind energy capacity in the world is installed in Europe, with a total of 1662 wind turbines distributed on 55 offshore wind farms in 10 countries. Since 2008 UK has been the leader in offshore wind[1]. 59 % of the capacity in Europe is installed in UK. The two first offshore wind turbines in UK were build in 2001 near Blyth Harbour and the first commercial offshore wind farm in UK was build in 2003. Since then the capacity has increased every year. Today UK has 20 operational wind farms installed with the total capacity of 3.3 GW. Denmark follows after UK in having most capacity in Europe with 18 %. Today 870 MW wind power on the sea is installed in Denmark divided between 11 wind farms. The size of the wind turbines has increased continuously since the first offshore wind farm in 1991. The average size of offshore wind turbines installed in 2012 was 4 MW. The European Wind Energy Association (EWEA) does not expect that the size will increase significantly the next years due to the dominance of the Siemens 3.6 MW wind turbine, Wilkes & Moccia (2013). However, wind farms with 5 MW wind turbines exist, e.g *Alpha Ventus* in Germany, *Ormonde* in UK and *Thornton Bank 1* in Belgium.

The size of the wind farms still increases and was in 2012 in average 271 MW but is expected to increase during the next years. In recent years a new offshore wind farm in Denmark *Anholt* has been build. It is the largest offshore wind farm in Denmark with a capacity of 400 MW. The wind farm is expected to be fully operating in the autumn 2013. According to the energy-agreement established by the Danish parliament in 2012 two large scale offshore wind parks are further planned. *Horns Rev III* will have a capacity of 400 MW and *Kriegers Flak* will have a capacity of 600 MW. The wind parks are expected to be ready for operating in the period 2017-2020. UK has two wind farms larger than 400 MW in capacity *London Array 1* with 630 MW and *Greater Gabbard* with 504 MW,

While the first offshore wind farms were placed at shallow and intermediate depths, the sites available for newer wind farms have larger depths. In Denmark the wind farm *Middelgrunden* was built in year 2000 in water depths of 2-6 m and in year 2002 *Horns Rev* was built in 6-13 m of water depth. Today the average water depth of offshore wind farms is $\sim$ 22 m in Europe, Wilkes & Moccia (2013). The largest water depths for offshore non-floating wind farms are around 40 m. *Alpha Ventus* in Germany is built in depths of 30-45 m. Further three offshore wind farms in Germany with depths around 40 m are under installation. At these large depths jackets, tripods and tripiles are used as substructures. The general expectation is also, according to Van Der Tempel (2006), that with larger, heavier turbines in deeper water, the jackets and similar types of substructures will be good candidates for future offshore wind turbines. However, in general monopiles are still the most popular substructure. 73 % percent of the wind turbines installed in 2012 had monopile substructures followed by jackets with 13 %.

The advantage of offshore wind turbines compared to on land wind turbines is the stronger stable wind which is found offshore. The wind resources offshore are up to 50 % larger than on land[2].

[1] http://www.renewableuk.com/en/renewable-energy/wind-energy/offshore-wind/

[2] http://www.windpower.org/da/planlaegning/offshore.html, accessed: 2013-06-27

Further, in land it is difficult to place the turbines such that they are not interfering with human activities, which is not a problem offshore. The largest disadvantage of offshore wind turbines is the cost of energy which is not competitive to on-land wind turbines, primarily due to cabling, maintenance costs and the offshore foundations. There is today therefore a focus on making the design of the offshore wind turbines and foundations as cost effective as possible.
One thing that can bring the foundation costs significantly down is to reduce the number of uncertainties in the design. The design depends both on aerodynamic loads, hydrodynamic loads and soil loads which interact through the structural response and produces dynamic loads. There are uncertainties in determining all three types of loads and combining the loads in the structural analysis, Frandsen *et al.* (2006). As the water depths of the offshore wind farms increases the hydrodynamic loads become more and more important relative to the aerodynamic loads, and the uncertainty in the wave loads more and more significant. In this thesis focus is on the hydrodynamic loads. Some of todays design methods to determine the hydrodynamic loads are compared against more advanced and time consuming methods.
Henderson *et al.* (2003) outlines the procedures necessary to calculate the critical wave loading, for either the fatigue or extreme cases as

1. Determining the design wave or wave climate
2. Selecting appropriate wave and load calculation models
3. Determining the effect on the structure

The three steps are in the following gone through and some of the uncertainties in the methods outlined and discussed.

1.1 Design basis

In the first step metocean data are considered. Metocean stands for meteorological (wind) and oceanographic (waves and currents). Jacobsen & Rugbjerg (2005) explain in detail how the metocean data for offshore wind farms are established. In the preliminary design global data from measurements as close to the site as possible are considered. In the detailed design data from measurements at the site is preferred. To base the design only on measurements 10 years of data should according to Jacobsen & Rugbjerg (2005) be obtained. Such a long data record very rarely exists for a site. Instead the available measurements, which do often not span more than 2 years, are supplemented with hindcast data from numerical modelling with spectral wave models. In the hindcast modelling, measured data are used to predict how waves, currents and water levels will be in the future. It is therefore assumed that the past represent the future. The hindcast modelling is driven by atmospheric pressure and wind from meteorological data. To do proper hindcast modelling, informations about the bathymetry and tidal level are also necessary. The models are calibrated and validated against measured data. Since the models cover a large area the long-term calibration can be made for areas with available long measurement data. The hindcast study are used to establish a data base of environmental data of wind speeds, V, significant wave height, H_s, wave peak periods, T_p, maximum wave heights and periods, current velocities and water depths.
To find the extreme design data, methods such as peak over threshold are most often used. The extreme events are fitted to an extreme value distribution (often Weibull distributions are used), and extrapolated to the probability of occurrence level, which is used in the design. It is important to be careful in the choice of distribution and the data fitting, because the results may be sensitive to for example a change of the treshold value.
In the design basis for the fatigue analysis the wave climate for each wind speed is gathered in a H_s-T_p matrix, where the probability of occurrence for each combination of the significant wave height and peak wave period is stated. The wind and wave data are gathered in bins, the bins of the wind speed cover often 2 m/s, the bins of the significant wave height cover 0.5 m and the bins of the peak wave periods 1 s, Fischer *et al.* (2010). In case of misalignment between wind and wave directions a fourth dimension is included in the scatter diagrams. All these combinations of wind speed, wave height and wave period can not be included in the design. A lumping of the wave and wind parameters is therefore carried out to reduce the number of load cases.

1.1.1 Lumping of wave parameters conditional to the wind speed

In Kühn (2001) a method to reduce the number of load cases are explained in detail.
In a first step the damage calculations of each load case are calculated in a simple and fast way. The aerodynamic fatigue damage, $L_{eq,a}$, for each wind load case is calculated by considering the wind turbine without the foundation in the time domain. The hydrodynamic fatigue damage, $L_{eq,h}$, is calculated for each wave load case by considering the foundation only. The calculations are done in the frequency domain and the aerodynamic damping is added to the structural damping as a factor. In Van Der Tempel (2006) it is concluded that the linearized frequency domain approach to calculate the equivalent loads due to the waves can be applied without loss of accuracy compared to time domain calculations as long as the structure is inertia dominated, which often is the case for monopile substructures. The fatigue damage for each combined load case is calculated by direct quadratic superposition of the aerodynamic and hydrodynamic contributions, $L_{eq} = \sqrt{L_{eq,a}^2 + L_{eq,h}^2}$. The total fatigue damage is next calculated by including the probability of occurrence of each load case. Kühn (2001) gives an example where the design basis consists of 235 load cases for operational conditions, and if the load cases where the wind turbine is parked also is taken into account the design basis consist of 440 load cases. For these load cases, the error in the fatigue damage due to the simplified calculation method compared to the case where the wind turbine and foundation are considered as one system affected both by the aerodynamic and hydrodynamic loads is 5 %. In Van Der Tempel (2006) it was also found that the uncoupling of wind turbine and the support structure in the fatigue analyses can give accurate results as long as the aerodynamic damping is taken into account as an additional damping in the support structure model.
In a next step the load cases are lumped, which is an iterative process. The fatigue damage of the lumped load cases are calculated as explained above where the aerodynamic and hydrodynamic fatigue damage are calculated separately and afterwards superposed. The lumping of the load cases is refined until the total fatigue damage of the lumped load cases match the total fatigue damage due to all the load cases. The process is relatively fast. Kühn (2001) mentions a computational effort of about 1 hour. In the example of Kühn (2001) the 440 load cases are reduced to 37 load cases, and the difference in the fatigue damage is 0.6 %.
Besides these load cases which are associated with normal energy production or when the wind turbine is parked, fatigue damage is also caused by start-up, shut-down and installation. Also, if directionality exist between the wind and waves the above lumping is done for each direction.
Norton (2003) made a simple analysis of how the fatigue damage changes if the number of load cases are reduced. Three fatigue calculations where considered where the bins of the design bases were of different size resulting in 205, 39 and 14 load cases, respectively. The fatigue damage in the bottom of the monopile did not change more than 1-2 % when the number of load cases were reduced. This analysis confirms the findings of Kühn (2001), that the number of load cases can be reduced with out changing the fatigue damage significantly.

1.2 Models for hydrodynamic loads

During the process of determining the design load cases, the wave theories used to calculate the wave forcing should be found. Both the extreme and the fatigue response depend on the dynamic behavior of the structure. Therefore, to accurately model the loads from waves an irregular wave theory should be used. At the same time offshore wind farms are often placed in intermediate or shallow water where wave nonlinearity is important. This however is usually ignored for the irregular waves, such that linear wave theory is applied for the irregular waves and fully nonlinear stream function wave theory is used to describe the extreme waves although this theory is restricted to regular waves on a flat bed. Large waves in the linear irregular time series are sometimes replaced with nonlinear stream functions waves, to include the effects from the wave nonlinearity in the calculations of the fatigue damage. Also to extend the linear wave theory from still water level and up to the surface elevation Wheeler stretching or delta stretching, both recommended by IEC61400-3 (2009), or other stretching methods are used.
Nonlinear waves can be more steep than linear waves resulting in an impulsive response of the

structure, which was seen in Schløer *et al.* (2012). Further, as nonlinear waves develop, energy is moved from the peak of the wave spectrum to smaller and larger frequencies. There is therefore a larger risk, that nonlinear waves contain energy at the first structural frequency, which can lead to excitation of the natural modes. Analysis of measured data from the Kvitebjørn field indicated that two storm events contributed with respectively 30% and 60% of the predicted accumulated damage in two different braces on the jacket structure, Økland (2010). Thus, the large waves associated with the storm wave climate induced large damage on a very short time scale which indicates the importance of structural response to strongly nonlinear waves.

Several authors have in the last years emphasized the significance of using a nonlinear irregular wave theory in the design of offshore wind turbines. Camp *et al.* (2003) writes that the nonlinear wave loading is important for the extreme design but at shallow water, which is the case for offshore wind turbines, the nonlinearity is also important in the fatigue analysis and that the nonlinearity results in a substantial increase in the hydrodynamic loads. Agarwal & Manuel (2011) used an integrated wind-wave response simulation analysis method to compare the loads from linear and second-order nonlinear irregular waves. They concluded that it is important to consider nonlinear wave loads in the design. Gravesen *et al.* (2003) stated that in the extreme design, the wave loads are not estimated accurately by linear wave theory combined with Wheeler stretching and that at that time only regular nonlinear theories as higher-order Stokes theory or stream function waves had been available to calculate the extreme waves. Gravesen *et al.* (2003) used a higher-order Boussinesq model to describe the nonlinear irregular waves. However, the effects of the nonlinearity were not compared to linear wave theory in the paper. Frandsen *et al.* (2006) found that it is necessary to investigate when the engineering models for the wave kinematics and loads are sufficiently accurate and when more advanced models are necessary.

Even though the standards require that the wave theory used is chosen with due consideration of the water depth and range of validity of the theory, DNV-OS-J101 (2010), it is still not known whether the nonlinearity of the waves in combination with irregularity of the waves are important in the design of offshore wind turbines. Besides a closed study in the framework of Carbon Trust, where the nonlinear dynamic loads of offshore wind turbines were investigated, no such studies has to the authors knowledge been performed previously.

In standard design of offshore wind turbines the wave loads are calculated by Morison's equation, which in its most simple form consist of a drag term based on the waves particle velocity and an inertia term based on the waves particle acceleration. In the two terms two empirical coefficients also appear, a drag and an inertia coefficient. They are found by experiments and depends on the Keulegan–Carpenter number, the Reynolds number and the surface roughness of the structure. The waves interaction with the structure is not taken into account in the Morison's equation, which therefore only is valid for slender structures, where diffraction effects are negligible. For non-slender structures a diffraction correction of the added mass can be applied following the method of MacCamy & Fuchs (1954). However, the method is only valid for linear wave theory.

The loads due to wave breaking are also important to include in the design. Camp *et al.* (2003) found that the measured wave loads at Blyth offshore wind farm were higher than any of the applied theories predicted. This difference was partly explained with the breaking waves. Marino *et al.* (2011) enhanced linear wave load calculations with intermittent application of the breaking wave load model of Wienke & Oumeraci (2005). They found that the impact due to the impulsive forces from the breaking waves can be up to three times larger than the impact due to the linear loads. In the standards wave breaking is included by a slamming force which is applied on top of the Morison's force. This force is also based on an empirical slamming coefficient. For a more detailed computation of the wave-structure interaction, a CFD-model, which resolves the flow around the structure can be used. From such a model the pressure around the structure can be extracted and the wave forcing calculated. As such models however are CPU-intensive, their role is rather to benchmark simpler models than for direct application in design.

1.3 Structural response

When the design load cases and methods to calculate the hydrodynamic loads are determined, the fatigue damage (FLS) loads and ultimate loads (ULS) are calculated, and it is investigated how the loads affect the structure. In the fatigue analysis the lumped load cases are considered and adequate structural capacity must be ensured. In ULS the most extreme single event (often 50 year load case) is considered, and it is ensured that the damage is below failure. There is a variety of design situations which has to be considered in the design of offshore wind turbines such as; power production, start up, shut down, parked transport, maintenance and fault conditions, DNV-OS-J101 (2010). For each design situation there is a number of load cases which have to be considered. In DNV-OS-J101 (2010) 31 load cases are mentioned. For each load case six 10 min stochastic realizations or a continuous 60 min period are required. These load cases consist in practice often of many sub-load cases because the whole range of wind speeds is considered. In practice up to perhaps 2000 load cases are therefore considered. In these analyses integrated simulation codes are used. Such codes calculate the coupled response of both the wind turbine and foundation in the time domain. The codes include the hydrodynamic and aerodynamic loads, the control system and the structural dynamics. Of such codes can be named Bladed, FAST, ADAMS, HAWC2 and Flex5. These codes and other codes are compared in detail in Molenaar (2003). All the codes use the blade element momentum theory to calculate the aerodynamic forces on the blades. Bladed, Flex5 and FAST are modal based programmes where the structural dynamics are described by mode shapes with modal masses, damping and stiffness. HAWC2 and ADAMS are based on multi-body formulations, where the system consists of a finite number of rigid bodies coupled by inelastic joints and therefore can be described with a finite number of ordinary differential equations. As part of the Statkraft Ocean Energy Research Program Thomassen *et al.* (2012) have developed the ASHES software, which performs integrated aeroelastic calculations with a main focus on visualization of the wind and wave loads and the resulting response in a live, real-time graphical controlled manner. To verify and compare the aeroelastic codes used in the offshore wind industry the Offshore Code Comparison Collaboration, (OC3) for IEA Task 23 Offshore Wind Technology and Deployment, Jonkman & Musial (2010) has been conducted from 2007-2010. The purpose of the project was to discuss the modelling strategies, develop benchmark models and to compare and discuss the simulation from the different codes. The project provides a systematic comparison of the codes with focus on the support structure and offshore loads, Passon & Kühn (2005) and is an important step in the development and verification of the codes used in the offshore wind industry. In the analysis, the NREL 5MW baseline wind turbine was considered, Jonkman *et al.* (2009). This wind turbine is a theoretical wind turbine developed in order to have a wind turbine which can be used in research as reference. Four different substructures was considered in OC3; a rigid monopile, a flexible monopile where the soil-pile interactions also were considered, a tripod and a floating spar-buoy. In 2010 a new task began Offshore Code Comparison Collaboration Continuation, (OC4) where a jacket and semi-submersible platform are considered as support structures.

The effects from the waves on the structure depend strongly on the properties of the structure. The tower is wind dominated due to the wind loads on the rotor and is only affected by the waves through the motion of the pile. As the monopile itself is relatively stiff compared to the frequencies of the wave forcing, it reacts mainly quasi-statically to the wave loads. The tower, however, is less stiff and gives rise to a first natural frequency of typically 0.23-0.30 Hz for the full structure. High frequency wave loads can thereby excite the tower through quasi-static motion of the monopile. Next the monopile will take part in the structural vibration associated with the first global natural frequency. The properties of the tower and monopile are indicated in figure 1.1. Other factors which are important when the influence of the wave forcing on the structural dynamics are investigated is discussed below.

Aerodynamic forcing and damping

The aerodynamic forcing and damping in the fore-aft direction is the dominating load effect for the structural response when the wind turbine is in operation. The relative importance of the effect from the waves on the structural response therefore depends very much on how strong the effects

from the wind at the same time are. The aerodynamic damping of the wind turbine depends on the work done by the thrust force on the blades during a cycle of fore-aft vibration compared to the kinetic energy associated with the vibrations. The thrust force is largest at rated wind speed and decreases for smaller and larger wind speeds. In the side-to-side direction the aerodynamic loads and therefore also the aerodynamic damping are small when the wind turbine operates. In cases with misaligned wind and waves, the effects from the waves in the side-to-side direction can therefore be important. Kim & Natarajan (2013) considered a wind turbine with a monopile foundation in water depths of 20 and 35 m. They found that the extreme overturning moment in the bottom of the foundation increased by 26.8 % and 56.9 %, respectively, in the side-to-side direction when the angle between the wind and wave direction went from being 0° to 15°. When the wind turbine is parked the blades are pitched to a large angle. In such situations the thrust force in the fore-aft direction is small and the wave forcing can be important in the fore-aft direction in the structural response. In figure 1.1 the fore-aft direction and side-to-side direction of a wind turbine are indicated.

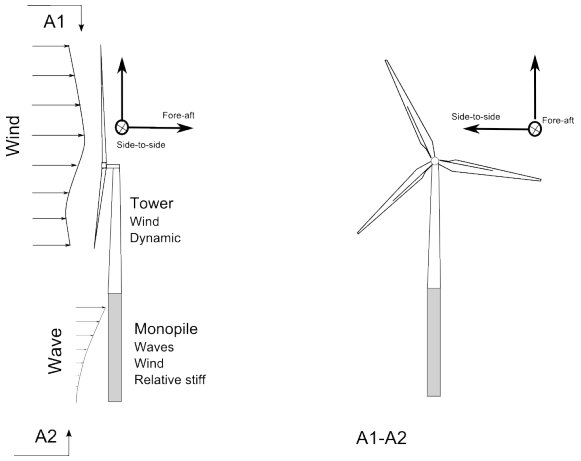

Figure 1.1: *The fore-aft and side-to-side direction of a wind turbine.*

Broad band forcing, springing, ringing and impulsive excitation

The structural first eigenfrequency of offshore wind turbines on monopile foundations is typically in the range 0.23-0.30 Hz. The peak frequencies of the most common sea states are therefore smaller than the structural eigenfrequency. The high-frequency part of the spectrum can however still contain energy at frequencies around the structural first eigenfrequency. The broad band forcing which can occur if the waves contain energy at the same frequency as the structure is thus very important in the structural design. This effect is linear and can therefore both occur for linear and nonlinear waves.

As already mentioned when the wave theories was discussed, energy is moved from the peak frequency to lower and higher frequencies as nonlinear waves develop. For very nonlinear sea states it is also possible to identify smaller peaks at the higher harmonics, i.e. at multiplies of the peak frequency. When the higher harmonics are close to the structural frequency there exist a larger risk of dynamic excitation of the structure. This type of excitation is a steady state response defined as springing. In figure 1.2 a springing response is illustrated.

Another nonlinear phenomena which there has been an increasing focus on the last years in the offshore wind industry is ringing. The ringing phenomenon is related to intermittent resonant forcing of the natural frequency from nonlinear individual steep large nonlinear waves. An example of such a response are also shown in figure 1.2. The response increases over some periods, before the maximum value is reached. The phenomenon was discussed intensively in the 1990s for deep water TLPs. The detailed hydrodynamic forcing that leads to ringing-response in intermediate and shallow water is expected to be stronger than at deep water. This was confirmed by the investigations of Bredmose *et al.* (2012) and Paulsen *et al.* (2013*c*). Ringing is therefore also likely

to be important in the design of offshore wind turbines both in ULS and perhaps also in FLS. In the standard DNV-OS-J101 (2010), it is said that ringing effects only are important when they are combined with extreme first order events, ie. when a extreme wave occur and is therefore related to the ultimate design. Others on the other hand argue that ringing itself is a very important effect that can cause significant fatigue damage on structure. In the research magazine Apollon (Vogt (2013)), John Grue, a professor at Oslo University, claimed that it is very important that ringing is taken into consideration.

There are many definitions of ringing, but all have in common that ringing is a nonlinear effect. According to Malenica & Molin (1995) ringing is a strongly nonlinear phenomena which occur in the loading process. Chaplin *et al.* (1997) say that ringing only occur during passage of very steep waves and is a non-Gaussian process. Ringing, though is not an effect due to breaking waves or slamming, Faltinsen *et al.* (1995). Ringing is according to Grue & Huseby (2002) and Krokstad *et al.* (1998) associated with a secondary load cycle which occur about one quarter wave period later than the main peak of the force. If the structural frequency is about 4 times the wave frequency this secondary load cycle causes a resonance response. de Ridder *et al.* (2011) found that waves with higher harmonics close to the structural eigenfrequency of the wind turbines resulted in excitation of the tower at it first mode. This strong transient ringing responses will according to Waisman *et al.* (2002) decay to a steady state which depends on the system damping.

Another type of response are impulsive excitation, which occur due to large steep waves and results in a sudden impulsive response of the structure which afterwards dampens. An example is shown in figure 1.2, where it is seen that the response experience a very abrupt excitation. This type of response are due to slamming and the response do not depend on what frequencies the energy in the wave has.

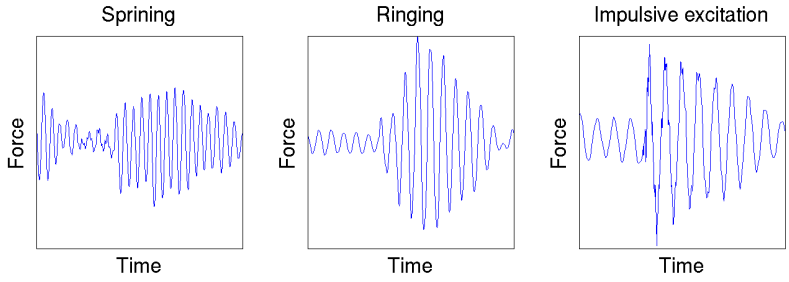

Figure 1.2: *Example of springing, ringing and impulsive excitation.*

Water depth

The water depth is also an important factor for the effects of the wave forcing on the structural response. As the water depth increases the wave forcing becomes larger relative to the aerodynamic forcing and therefore more important in the design. This is primarily due to the larger water column where the wave forces works and the larger moment arm relatively to the mudline. Opposite to this effect, the wave steepness increases as the water depth decreases, which can lead to larger extreme load. This effect is a nonlinear effect and is therefore much stronger for nonlinear waves. This emphasises that it can be important to use nonlinear wave theories. The large steep waves can cause impulsive responses.

1.4 Scope of work in the present thesis

The above discussion clearly shows that there is a need for a fully nonlinear irregular wave model to investigate the importance of the nonlinear wave effects in the design of offshore wind turbines. The present thesis contributes to the interpretation of the effects from wave nonlinearity in the structural dynamics of offshore wind turbines.

In the thesis the NREL offshore 5MW baseline wind turbine, Jonkman & Musial (2010), placed on a monopile is considered. The monopile is chosen as substructure, since it is still the most popular substructure. In the main part of the thesis the foundation of the wind turbine is not considered. Instead a rigid foundation is assumed, where the monopile is fixed at the sea bed.
To calculate the dynamic loads a fully nonlinear wave model OceanWave3D, Engsig-Karup *et al.* (2009), and the aeroelastic code Flex5, Øye (1996), are used. The hydrodynamic loads are calculated by Morison's equation. The nonlinear wave model is a potential flow model. One limitation of the model is that it can not handle wave breaking. To include such effects a more advanced CFD-model can be used. However, these models are better suited for benchmark or detailed analysis of short time series due to their CPU-demands. The potential flow model was therefore chosen due to its robustness and efficiency. The model still describes the wave kinematics more accurately than the more simple models which are used in design today. The potential flow model is computationally demanding relative to existing models, but it is a good model to investigate the effects from the wave nonlinearity. In first part of the thesis the two models, OceanWave3D and Flex5 are described in more detail. In the remaining part of the thesis a number of load and response effects are treated. This is outlined in the following.

Effects of wave nonlinearity on fatigue and extreme loads
With the potential flow model it is possible both to calculate linear and fully nonlinear irregular waves. It is therefore possible to compare these two wave theories. In the first part of chapter 4 linear and nonlinear irregular wave realizations are compared and the static wave forcing based on the two wave theories analysed.
Hereafter dynamic calculations are done in Flex5 and the structural response due to the hydrodynamic forcing from linear and nonlinear irregular wave realizations is compared. The combined contribution from hydrodynamic and aerodynamic loads to the fatigue damage of the turbine and foundation is also considered and it is investigated for which situations the nonlinearity of the waves is important. Six wind and sea states, representative for the North Sea, are considered, which cover the wind speeds from below cut-in wind speed to above cut-out wind speed. In this way the cases with a parked wind turbine are also included in the analysis. While a real fatigue design would involve a much larger set of wave climates, the chosen sea states provide a simplified basis for a study of the influence on fatigue from wave nonlinearity.
To include the effect of the water depth in the analysis the offshore wind turbine is considered at four different water depths. Focus in the present analysis is on the monopile and the wind turbine tower.

Wind-wave misalignment
In the design of offshore wind turbines the aerodynamic loads are typically dominating over the hydrodynamic loads. Therefore, in situation where the wind and wave direction are misaligned, the effects from the hydrodynamic loads can become more important due to the lack of aerodynamic loads and damping in the direction of the waves. In chapter 5 it is therefore investigated whether the nonlinearity affects the fatigue in misaligned conditions.

Hydrodynamic damping
Besides aerodynamic damping there exist other types of damping in an offshore wind turbine; soil damping, hydrodynamic damping, structural damping and tower dampers. During stand still or when there is a misalignment between the wind and wave direction the aerodynamic damping becomes insignificant and other types of damping therefore become important. In chapter 6 the magnitude of the hydrodynamic radiation damping from the waves is therefore investigated by use of the radiation/diffraction program WAMIT, Newman (1994).

Soil damping by a new soil model
Next to aerodynamic damping, soil damping gives the largest contribution to the overall damping. In today's design, the foundation interaction with the soil is often described by p-y urves. These curves describe the nonlinear elastic relations between the lateral displacement of the monopile, y, and the soil pressure, p. The curves are based on monotonic loading of small-diameter piles, but are still used for offshore wind turbines where the diameter of the piles are large and subjected to cyclic

loading of wind and waves. The curves therefore contain no information about hysteresis effects and how the pressure changes when the soil previously has been subject to large deformations. Such effects can however impose to structural damping, Larsen *et al.* (2005).
In the present analysis the soil model of Hededal & Klinkvort (2010) is implemented in Flex5. In this model, the soil is described by uncoupled nonlinear cycling springs and includes effects like hysteresis and creation of gaps between pile and soil at reversed loading. When the pile is moving in the gap the friction between the soil and pile are also included.
The soil model and the implementation in Flex5 is described in chapter 7. Next the response of the monopile and wind turbine tower using this soil model are compared against the response obtained with classical p-y curves and combined with a constant damping factor.

Aeroelastic response to CFD wave loads
The potential flow model, OceanWave3D, can as discussed earlier not handle wave breaking. Further, the loads are very often, and also in this thesis, determined from Morison's equation where the undisturbed wave kinematics are considered. Effects as wave run up on the cylinder and detailed wave-structure interaction are therefore also ignored. With the CFD-solver, OpenFOAM, however it is possible to calculate the detailed flow around a cylinder exposed to waves and the corresponding pressure acting on the cylinder.
In chapter 8 the wave forces based on OceanWave3D and Morison's equation are compared against wave forces from OpenFOAM. The analysis is both based on static calculation and dynamic analysis in Flex5. The dynamic effects due to the more detailed wave loads are analysed. Further, it is investigated how well OceanWave3D in combination with Morison's equation describes the hydrodynamic loads.

3D load effects
Besides wave breaking the effect of 3D-wave spreading is also often ignored in the hydrodynamic calculations. Many analysis are based on 2-dimensional waves, even though ocean waves are generally 3-dimensional directionally spread. The last analysis in the thesis is a small study of the influence of directional spreading on the response in the wind turbine tower and monopile. The wave kinematics are calculated in OceanWave3D and the analysis is therefore based on fully nonlinear irregular waves.

A summary and the conclusions are provided as the last chaper of the thesis.

Chapter 2

The hydrodynamic model, OceanWave3D

The wave kinematics are calculated by the fully nonlinear potential wave model of Engsig-Karup *et al.* (2009). The model solves the 3D Laplace equation (2.1) for the velocity potential, Φ, and the free surface elevation, η, with nonlinear boundary conditions at the free surface, (2.2)-(2.3) and the impermeability condition at the sea bed, (2.4),

$$\frac{\partial^2 \Phi}{\partial x^2} + \frac{\partial^2 \Phi}{\partial y^2} + \frac{\partial^2 \Phi}{\partial z^2} = 0 \quad \text{for} \quad -h \leq z < \eta. \tag{2.1}$$

The model is based on a flexible–order finite difference approximation of the potential flow of non-overturning waves.
At each time step the surface elevation, η, and velocity potential, Φ, at the free surface is calculated by the kinematic and dynamic boundary condition at the free surface

$$\frac{\partial \eta}{\partial t} = \frac{\partial \Phi}{\partial z} - \frac{\partial \Phi}{\partial x}\frac{\partial \eta}{\partial x} - \frac{\partial \Phi}{\partial y}\frac{\partial \eta}{\partial y} \quad \text{for} \quad z = \eta, \tag{2.2}$$

$$\frac{\partial \Phi}{\partial z} = -\frac{\nabla \Phi \cdot \nabla \Phi}{2} - g\eta = 0 \quad \text{for} \quad z = \eta. \tag{2.3}$$

In order to solve these equations forward in time, $t + \Delta t$, the vertical Euler velocity $w = \frac{\partial \Phi}{\partial z}$ at the free surface has to be known at time t. This quantity is found by solving the Laplace equation, (2.1), in the fluid volume together with the impermeability condition at the sea bed together with the known velocity potential at the free surface and the surface elevation at time t.

$$\frac{\partial \Phi}{\partial z} = -\frac{\partial h}{\partial x}\frac{\partial \Phi}{\partial x} - \frac{\partial h}{\partial y}\frac{\partial \Phi}{\partial y} \quad \text{for} \quad z = -h. \tag{2.4}$$

Due to the change in surface elevation the physical z-coordinate of the grid points changes with time. To avoid recalculation of the finite difference coefficients at each time step the physical coordinate system, (x,z), is mapped to a fixed computational domain (ξ,σ) where the grid points do not change with time. For the horizontal grid points, $\xi = x$, while the vertical coordinate σ, is defined by

$$\sigma_i = \sin\left(\frac{\pi(i-1)}{2(N_z-1)}\right), \quad \text{where} \tag{2.5}$$

$$z_i(t) = \sigma_i\left(\eta(t) + h\right) - h, \quad i = 1, 2, ..N_z.$$

The number of grid points in the vertical direction is N_z.

The model is validated against two-directional linear regular waves and two-directional stream function waves in Engsig-Karup *et al.* (2009). Recently the model has also been validated against irregular wave model tests, c.f. Bredmose *et al.* (2013) and Paulsen *et al.* (2013*a*). The wave model is found to make a good reproduction of the wave fields in both papers.
The model is in the present analysis used to calculate unidirectional linear and fully nonlinear irregular waves moving up along a sloping sea bed. The waves are generated at the left boundary of the domain. The waves are described by a linear JONSWAP-spectrum at the generation zone, as described in DNV-OS-J101 (2010). In this formulation the peak enhancement factor increases as the ratio $T_p/\sqrt{H_s}$ decreases. The larger the peak wave period, T_p, is compared with the significant wave height, H_s, the more energy is contained around the peak frequency in the spectrum.
It is, through the nondimensional wave number kh, ensured that the generation zone is in deep water where linear wave theory is valid. Here k is the wave number based on T_p and h the water depth. Deep water exist for $kh > \pi$ and shallow water for $kh < \pi/10$.
Inside the domain the nonlinearity of the waves is generated by the nonlinear boundary conditions. When linear waves are calculated the nonlinear terms are turned off in the equations.
At the end of the domain another relaxation zone is defined, where the waves are absorbed numerically. The length of the relaxation zone is adjusted such that reflection of the waves is avoided.

2.1 Wave breaking model

A consequence of using a fully nonlinear wave model is the possibility of wave steepening to the point of physical wave breaking. The wave model is only valid up to wave breaking, and very steep waves can cause a numerical breakdown. To handle the wave breaking a strong local filter is applied in the wave model. This is not an attempt to formulate a model for physical breaking but rather a way to solve the problem with high unphysical accelerations which the model can not handle.
As a first attempt the free Eulerian vertical surface acceleration $\frac{\partial^2\eta}{\partial t^2}$ was used as the criterion for wave breaking. This assumption is purely geometrical and is a linear estimate of the vertical point acceleration. The breaking wave filter is applied every time $\frac{\partial^2\eta}{\partial t^2}$ reaches a defined value. The filter smooths a 10-point region centered at the point which exceeds the defined value with a 3-point filter.

To investigate for which value of $\frac{\partial^2\eta}{\partial t^2}$ a wave starts to break, six stream function waves close to wave breaking were considered and analysed. Stream function wave theory, Fenton (1988), provides a fully nonlinear 2-dimensional regular wave on a flat bed. The waves considered are shown in figure 2.1. All six waves are close to the "Williams' points", Williams (1981), which indicate wave breaking. Fenton (1990) approximated the Williams' points by the equation

$$\frac{H_{max}}{h} = \frac{0.141063\frac{L}{h} + 0.0095721\left(\frac{L}{h}\right)^2 + 0.0077829\left(\frac{L}{h}\right)^3}{1 + 0.0788340\frac{L}{h} + 0.0317567\left(\frac{L}{h}\right)^2 + 0.0093407\left(\frac{L}{h}\right)^3}. \tag{2.6}$$

In table 2.1 the ratio H_{max}/H of the six waves are stated. The waves are 4-6% smaller than H_{max} in equation (2.6).
The Mitche breaking wave criteria, Mitche (1944), states that waves starts to break when the limiting wave steepness is exceeded

$$\frac{H_b}{L_b} = 0.14\tanh(k_b h_b), \tag{2.7}$$

where b indicates breaking conditions. Also in table 2.1 the ratio $\frac{H_b/L_b}{L/H}$ of the six waves are stated. All the waves are below the Mitche wave breaking criteria. It is further seen that the six waves are closer to their limits when the Williams points are considered compared to when the Miche criteria is considered.
It was difficult to find solutions for steeper waves closer to the breaking wave criteria. The derivatives of the wave kinematics often had some small oscillations, which occurred both if the derivatives

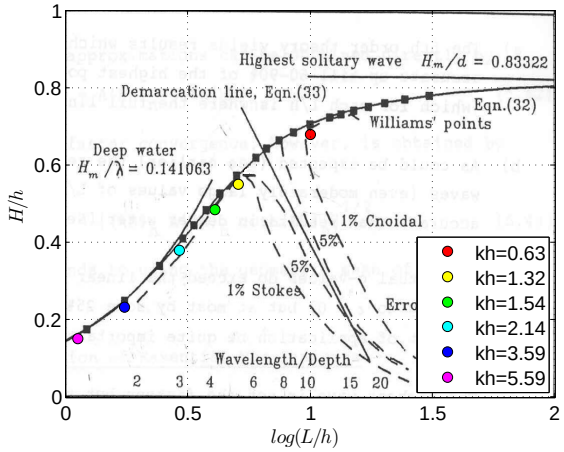

Figure 2.1: *The 6 waves and their relation between h, H and L. The figure is from Fenton (1990).*

were calculated from the analytical solution of the stream function wave or if they were calculated numerical using the midpoint rule on a 5 point stencil which is accurate to fourth order.

kh	0.63	1.32	1.54	2.14	3.59	5.59
H_{max}/H	1.04	1.05	1.05	1.05	1.06	1.06
$\frac{H_b/L_b}{L/H}$	1.13	1.09	1.08	1.08	1.08	1.08

Table 2.1: *The table indicate how close the six waves in figure 2.1 are to H_{max} in equation (2.6) and the breaking limit in equation (2.7).*

In figure 2.2a the largest absolute values of $\frac{\partial^2\eta}{\partial t^2}$ are shown as function of the largest slope of the surface elevation $\frac{d\eta}{dx}$. It is seen that values between $-4.5g$ and $-5g$, where g is the acceleration of gravity, corresponds to the maximum wave height for the stream function waves. A value of $-4.8g$ is therefore used in the computations done in Schløer *et al.* (2011) as the criterion for wave breaking.
A more physical wave breaking criteria is the free downward vertical particle acceleration, $\frac{dw}{dt}$,

$$\frac{dw}{dt} = \frac{\partial w}{\partial t} + \frac{\partial w}{\partial z}\frac{dz}{dt} + \frac{\partial w}{\partial x}\frac{dx}{dt}. \tag{2.8}$$

This criteria indicates how fast a water particle on the surface elevation accelerates vertically.
It is therefore investigated whether there is a relation between $\frac{\partial^2\eta}{\partial t^2}$ and $\frac{dw}{dt}$ and what the criteria for $\frac{dw}{dt}$ is. The stream function waves in figure 2.1 are again considered.
Figure 2.2b shows the relationship between $\frac{dw}{dt}$ and $\frac{d\eta}{dx}$. The vertical particle acceleration $\frac{dw}{dt}$ is close to $-0.37g$ for all six waves.
The relation between $\frac{\partial^2\eta}{\partial t^2}$ and $\frac{dw}{dt}$ is similar for all six waves as shown in figure 2.2c. The comparison indicates that there exist a relationship between the two parameters and that using $\frac{\partial^2\eta}{\partial t^2}$ and $\frac{dw}{dt}$ as a breaking wave criteria both are acceptable assumptions.
Babanin (2009) discusses the different breaking wave criteria presented in the literature and summarizes that for regular waves the criteria is often found to be $\frac{dw}{dt} = -0.5g$. The reason that a value of $-0.37g$ is found in the present analysis must be because the waves still are below the limiting wave steepness as shown in table 2.1.
In real seas Babanin (2009) refer to the work of Longuet-Higgins (1985) who suggest that the criteria for real seas should be $\frac{dw}{dt} = -1g$. The increase in the criteria is explained with the fact that in real seas the waves are a superposition of an unlimited number of wave components. The particle acceleration is therefore a sum of individual accelerations. So even though a wave in the real sea has the same or smaller steepness as a regular wave, the particle acceleration can be larger.

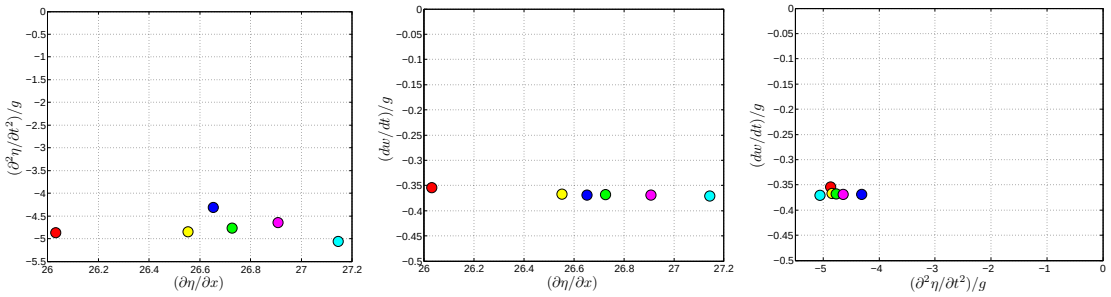

(a) **(b)** **(c)**

Figure 2.2: *The relationship between* $\frac{\partial^2\eta}{\partial t^2}$, $\frac{dw}{dt}$ *and* $\frac{\partial\eta}{\partial x}$ *of stream functions waves of limiting steepness.*

A value of $\frac{dw}{dt} = -1g$ has therefore been chosen as the new criterion for wave breaking and is used in for the analysis in the present thesis.
Physically it makes good sense to assume that the wave is breaking when $\frac{dw}{dt} = -1g$ i.e. when the particle experiences a "free fall".

2.2 Interpolation of the wave kinematics in the z-direction

Engsig-Karup *et al.* (2009) checked the energy conservation of a stream function wave in the wave model and found that a resolution of 32 grid points per wave length and 9 points in the vertical z-direction using sixth-order operators and a Courant number of 0.5 leads to highly accurate solutions and energy losses of less than 10^{-4} per wave period for $kh = 2\pi$. A number of $N_z = 9$ points in the vertical direction is applied for the calculations in this thesis.
In a water depth of $h = 20 - 40\,\text{m}$ this can give a large distance between the points, especially close to the sea bed where the distance between the points is largest, cf. equation (2.5). In Flex5 a fixed distance between the points are assumed and the wave kinematics at the points are found by linear interpolation. It is therefore desired to evaluate the wave kinematics in more points through the depth as postprocessing, before the wave kinematics are used in Flex5. More points could of course also be defined in the wave model but that would increase the calculation time which is unwanted.
The Matlab-function `interp1.m` is used to interpolate between the 9 points. The interpolation method is the cubic-spline interpolation. To investigate how accurate this method is a stream function wave with $H = 2.8\,\text{m}$ and $T = 6.8\,\text{s}$ in a water depth of 20 m and 40 m is calculated both with nine points through the depth, $N_z = 9$, and with 19 points through the depth, $N_z = 19$. The surface elevation of the two waves are shown in figure 2.3 for one wave period. The horizontal velocity and acceleration of the stream function wave with $N_z = 9$ are interpolated in order to find the values in the same 19 points as is used for the stream function wave with $N_z = 19$.
The horizontal velocity, u, and acceleration, a, as function of z at different times indicated with black stars in figure 2.3 are shown in figure 2.4. The velocity and acceleration are both shown for the stream function wave with $N_z = 9$, $N_z = 19$ and for the interpolated values. The relative errors between the solution with $N_z = 19$ and the interpolated values are seen in figure 2.5 and calculated as

$$Error_u = \frac{u_{N_z=19} - u_{interp}}{\max(u_{N_z=19})}, \quad Error_a = \frac{a_{N_z=19} - a_{interp}}{\max(a_{N_z=19})}. \tag{2.9}$$

In general the largest errors occur close to the sea bed and at times where the velocities and accelerations are close to zero. The error is therefore not significant because the solution itself is close to zero. The largest error occurs for the acceleration and is $\sim 1.5\%$ for both depths.

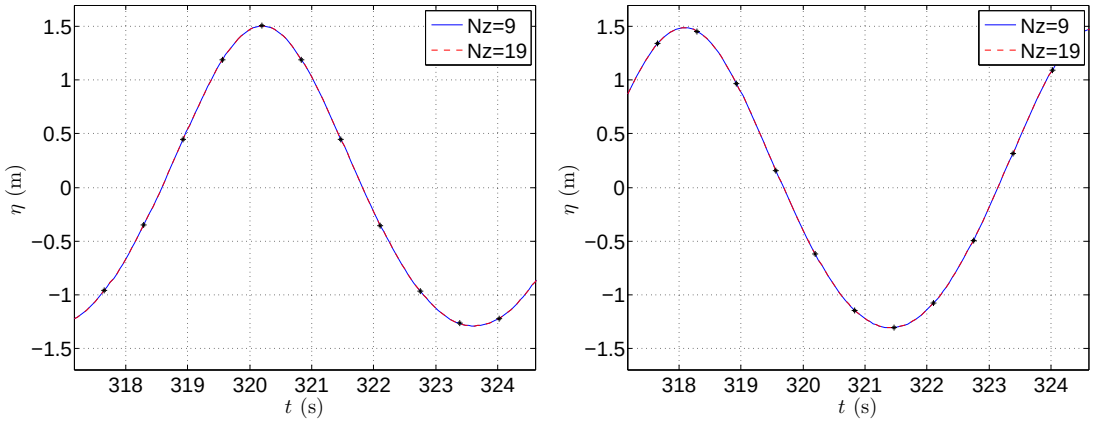

(a) $h = 20\,\mathrm{m}$. **(b)** $h = 40\,\mathrm{m}$.

Figure 2.3: *The surface elevation for the stream function wave with $N_z = 9$ and $N_z = 19$.*

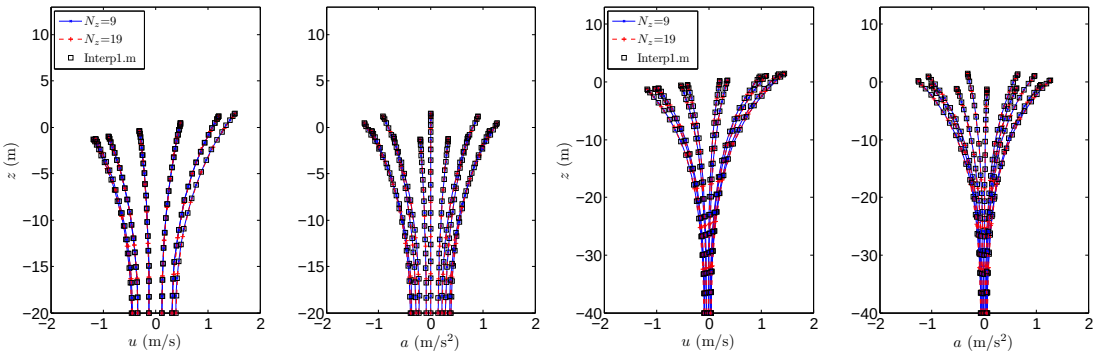

(a) $h = 20\,\mathrm{m}$. **(b)** $h = 40\,\mathrm{m}$.

Figure 2.4: *The horizontal velocity, u, and acceleration, a, as function of z for different times, indicated in figure 2.3.*

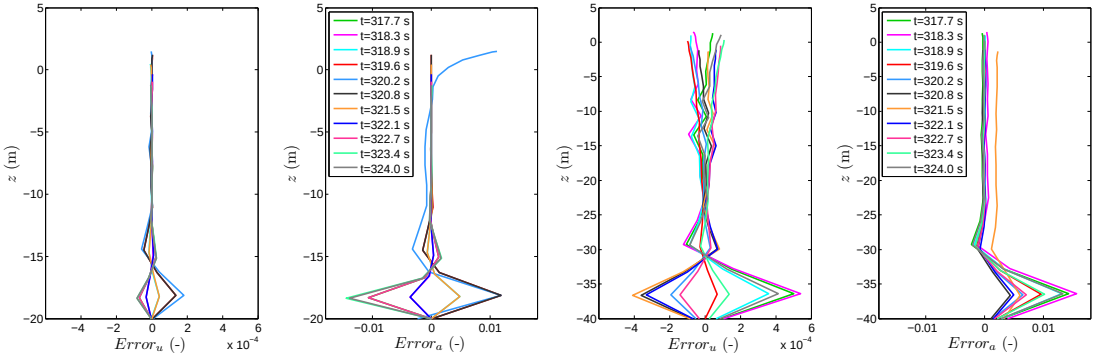

(a) $h = 20\,\mathrm{m}$. **(b)** $h = 40\,\mathrm{m}$.

Figure 2.5: *The relative error between the horizontal velocity, u, and acceleration, a, for the stream function wave with $N_x = 19$ and the interpolated values.*

A linear interpolation would for comparison give an error of approximately 4%. The error is therefore reduced significantly by evaluating the wave kinematics in more points by cubic-spline interpolation. This method is therefore applied in the analysis in the present thesis.

Chapter 3

The aeroelastic code, Flex5

The aeroelastic code Flex5, Øye (1996), is widely used in the industry to model the dynamic behavior of the wind turbine and monopile foundation. The aerodynamic loads on the blades are calculated by the unsteady blade-element-momentum (BEM) method while the wave forcing is calculated by Morison's equation. The program uses in general 28 degrees of freedom to calculate the deflection of the structure. The deflection of the monopile, tower and blades are found by shape functions. The tower and monopile are modeled as a beam with a diameter and wall thickness. The monopile is clamped at the bottom which either can be at the seabed or at a specified distance below the sea bed. The induced mass of the surrounding water and potential water inside the pile is included as distributed mass in the dynamic calculations. The wave kinematics and wind turbulence are specified in separate files and are calculated in advance.

3.1 The equation of motion

In order to calculate the displacements and sectional forces of the wind turbine and substructure the equation of motion is solved.

$$\rho\mathscr{A}\ddot{\mathsf{u}} + (EI\mathsf{u}_{xx})_{xx} + \mathsf{c}\dot{\mathsf{u}} = F. \tag{3.1}$$

The force F represents the external loads acting on the beam, and subscribt x means that the term is differentiated with respect to x, which is the coordinate along the beam. "Dot" over the variables indicates that the term is differentiated with respect to time. First term in equation (3.1) is the massterm, where $\mathscr{A}$ is the cross sectional area of the beam and ρ the density. The stiffness factor is given by the modulus of elasticity, E, and moment of inertia, I. The damping is given by c.
The displacement of the beam, $\mathsf{u} = \mathsf{u}(x,t)$, can be expressed in terms of the shape functions, φ_j, and the scalar, α_j

$$\mathsf{u}(x,t) = \sum_{j=1}^{N} \alpha_j(t)\varphi_j(x), \tag{3.2}$$

where N is the number of shape functions and α_j is the generalized coordinate specifying the contribution to the total deflection from each shape function.
Shape functions, φ, are often introduced, when the equation of motion of a system is solved, in order to decrease the number of degrees of freedom in the system and thereby the computational time. The deflection of the structure is described by the linear combination of the shape functions. Shape functions can either be static, where they are found from the deflection caused by a static force acting on the structure or they can be model shape functions. Modal shape functions are based on the eigenmodes of the structure. An eigenmode is a free vibration without the presence of an external load. The only load is therefore the inertia force due to the mass and acceleration of

the structure. An eigenmode describes the properties of a structure through a natural frequency (eigenvalue), modal damping and mode shape. The mode depends on the mass, stiffness and boundary conditions of the structure. The equation of motion can be expressed in terms of the shape functions by combining equation (3.1) and (3.2)

$$\rho\mathscr{A}\sum_{j=1}^{N}\ddot{\alpha_j}\varphi_j+\sum_{j=1}^{N}\alpha_j(EI\varphi_{j,xx})_{xx}+\mathsf{c}\sum_{j=1}^{N}\dot{\alpha_j}\varphi_j(x)=F. \tag{3.3}$$

Each term in equation (3.3) is multiplied with φ_i and integrated along the length of the beam L

$$\int_0^{\mathsf{L}}\rho\mathscr{A}\sum_{j=1}^{N}\ddot{\alpha_j}\varphi_j\varphi_i+\sum_{j=1}^{N}\alpha_j(EI\varphi_{j,xx})_{xx}\varphi_i+\mathsf{c}\sum_{j=1}^{N}\dot{\alpha_j}\varphi_j\varphi_i\,dx=\int_0^{\mathsf{L}}F\varphi_i dx. \tag{3.4}$$

The second term on the left hand side is rewritten.

$$\begin{aligned}\sum_{j=1}^{N}\left(\int_0^{\mathsf{L}}\alpha_j(EI\varphi_{j,xx})_{xx}\varphi_i dx\right)&=\sum_{j=1}^{N}\alpha_j\left([(EI\varphi_{j,xx})_x\varphi_i]_0^{\mathsf{L}}-\int_0^{\mathsf{L}}(EI\varphi_{j,xx})_x\varphi_{i,x}dx\right)\\&=\sum_{j=1}^{N}\alpha_j\left([(EI\varphi_{j,xx})_x\varphi_i-(EI\varphi_{j,xx})\varphi_{i,x}]_0^{\mathsf{L}}+\int_0^{\mathsf{L}}(EI\varphi_{j,xx})\varphi_{i,xx}dx\right)\\&=\sum_{j=1}^{N}\alpha_j\int_0^{\mathsf{L}}(EI\varphi_{j,xx})\varphi_{i,xx}dx.\end{aligned} \tag{3.5}$$

The last reduction of equation (3.5) is due to the boundary conditions which say that $\varphi=0$ and $\varphi_x=0$ at $x=0$ and $\varphi_{xx}=0$ at $x=\mathsf{L}$.
Equation (3.4) now reads

$$\mathbf{GM}\underline{\ddot{\alpha}}+\mathbf{GK}\underline{\alpha}+\mathbf{GC}\underline{\dot{\alpha}}=\mathbf{GF}, \tag{3.6}$$

where **GM**, **KM**, **CM** are the generalized mass matrix, stiffness matrix and damping matrix and **GF** are the generalized force vector given as

$$\begin{aligned}GM_{ij}&=\int_0^{\mathsf{L}}\rho\mathscr{A}\varphi_i\varphi_j dx,\\GK_{ij}&=\int_0^{\mathsf{L}}EI\varphi_{i,xx}\varphi_{j,xx}dx,\\GC_{ij}&=\int_0^{\mathsf{L}}\mathsf{c}\varphi_j\varphi_i dx,\\GF_i&=\int_0^{\mathsf{L}}F\varphi_i dx.\end{aligned} \tag{3.7}$$

How the terms in equation (3.7) are derived in Flex5 are explained in more details in section 3.1.2. Due to aerodynamic loads, equation (3.6) is coupled. The force on the right hand side of the equation does not only depend on the time but also on the displacement and velocities of the system. The equation can therefore only be solved numerically. If the values $\underline{\alpha}$ and $\underline{\dot{\alpha}}$ are known at time t^n the loads can be calculated by the unsteady BEM method. The acceleration $\underline{\ddot{\alpha}}$ is then found from

$$\underline{\ddot{\alpha}}=\mathbf{GM}^{-1}(\mathbf{GF}-\mathbf{GC}\underline{\dot{\alpha}}-\mathbf{GK}\underline{\alpha})=\mathbf{GM}^{-1}\mathbf{F}(\underline{\alpha},\underline{\dot{\alpha}},t^n). \tag{3.8}$$

When $\underline{\alpha}$, $\underline{\dot{\alpha}}$ and $\underline{\ddot{\alpha}}$ are known at time t^n a Runga-Kutta-Nyström scheme is used in Flex5 to calculated $\underline{\alpha}$ and $\underline{\dot{\alpha}}$ at time t^{n+1}. Through this routine, the displacement and sectional forces in the wind turbine and substructure are calculated and the dynamics of the structure can be analysed.

3.1.1 The shape functions for the monopile and tower

In the present thesis the focus is on the dynamics of the wind turbine tower and the monopile. Only the shape functions of the tower and monopile are therefore described in more details.
The monopile has in Flex5 six degrees of freedom (DOF). Two of them (displacement in- and rotation around the vertical axis) are by the program forced to be stiff which reduces the total number of DOFs in Flex5 from 28 to 26. The last four DOFs work in pairs and describe the displacement and rotation of the monopile in the two horizontal directions and are the same in both directions.
The shape functions in the monopile are static and found by prescribing a desired deflection, which are found by adding a force and moment, resulting in the desired deflection. The shape functions of the DOFs are shown in figure 3.1. The first shape function describes a unit displacement at the top of the monopile while the rotational angle is zero. The second shape function describes a unit rotation at the top of the monopile while the displacement is zero. At the bottom of the pile both the displacement and rotation are zero for both DOFs.

The tower has four degrees of freedom, two in each horizontal direction. The shape functions are shown in figure 3.2. The first shape function is static and found by applying a unit force a distance above the tower top. This results in a unit displacement and a rotation at the top of the tower, while both are zero at the bottombottom. The second shape function is a modal shape function and describes a unit rotation at the top of the tower while the displacement is zero.
If all four DOFs are free in both the monopile and the tower four different natural modes are produced in both directions. For the stiffest modes the eigenfrequencies can become quite high. This can be a problem due to the Runge-Kutta time stepping algorithm, used in Flex5, because it requires a minimum of 3 steps per period of the mode with the highest frequency to remain stable. To handle this problem the second DOF in each direction in the monopile is slaved to the first DOF. The slaving is done by assuming proportionality by specified coupling coefficients. The coupling coefficients are calculated corresponding to the static deflection of the monopile with a horizontal load at the nacelle. The total number of DOFs in the present Flex5 setup are therefore only 24. The above assumption should not change the accuracy of the results significantly. The total deflection of the monopile and tower are still very close to be accurate. The only change is that the high-frequency mode is eliminated. Since this frequency is larger than 4 Hz, and therefore much larger than the frequencies in the wave- and wind spectra, the elimination should not have any significance in the dynamic analysis.

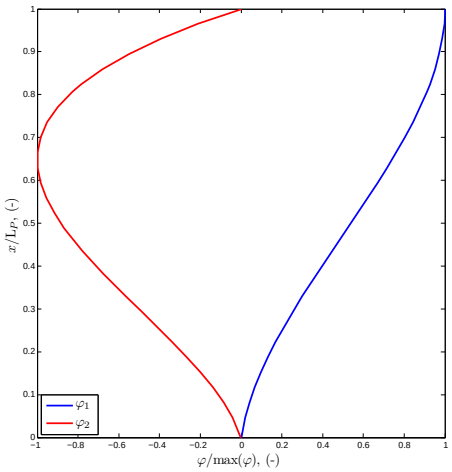

Figure 3.1: *The shape functions in the monopile.*

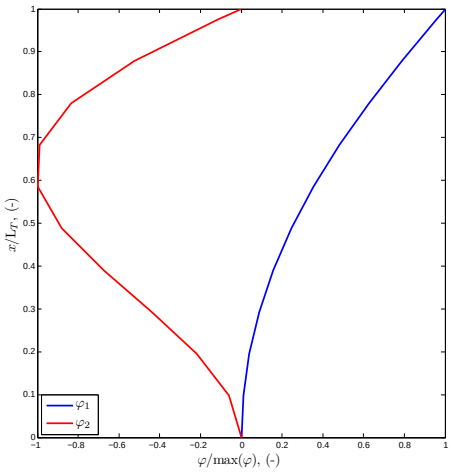

Figure 3.2: *The shape functions in the tower.*

In the following it is explained how the shape functions in the monopile and tower are calculated. The monopile and tower are treated as beams with the length L_P and L_T, respectively. The

coordinate, x, along the monopile and tower are zero in the bottom of the monopile and in the bottom of the tower.

The pile

To find the forces that gives the desired deflections of the shape functions, the curvature, κ, angular deflection, θ, and lateral deflection, φ, are first found from a unit force, $F = 1$, and a unit moment, $M = 1$ acting at the top of the pile separately

$$\kappa_F(x) = \Delta x \frac{F}{EI}, \quad \frac{d\theta_F}{dx} = \kappa_F(x), \quad \frac{d\varphi_F}{dx} = \theta_F(x), \tag{3.9}$$

$$\kappa_M(x) = \frac{M}{EI}, \quad \frac{d\theta_M}{dx} = \kappa_M(x), \quad \frac{d\varphi_M}{dx} = \theta_M(x), \tag{3.10}$$

where $\Delta x = \mathsf{L}_P - x$. The force and moment and the corresponding deflections are illustrated in figure 3.3. In the following, the angular deflection and deflection found from equations (3.9) and (3.10) at the top of the pile are named θ_{FP}, θ_{MP}, φ_{FP} and φ_{MP}.

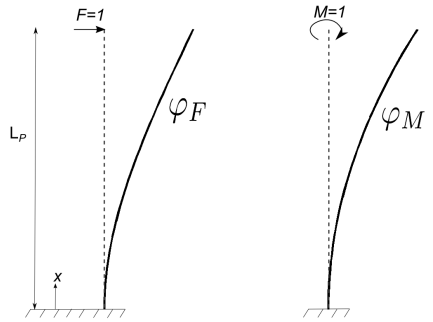

Figure 3.3: *The unit force and moment and the corresponfing deflections in the monopile.*

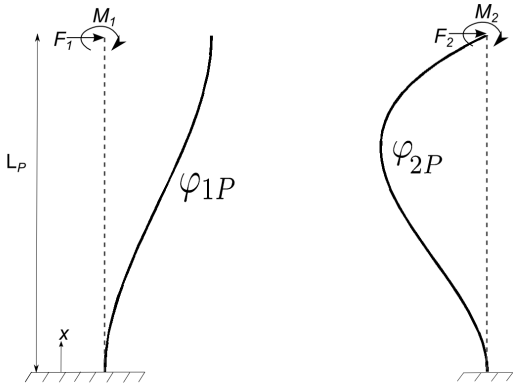

Figure 3.4: *The force and moment which is acting in the top of the pile to find the first and second mode shape function.*

To find the first shape function, φ_{1p}, a force and moment are defined at the top of the pile such that it is ensured that the angular deflection is zero at the top of the pile. The force and moment are illustrated in figure 3.4. The moment is based on the angular deflections, θ_{FP} and θ_{MP}

$$F_1 = 1 \quad \text{and} \quad M_1 = -\frac{\theta_{FP}}{\theta_{MP}}. \tag{3.11}$$

The curvature, κ_{1P}, angular deflection, θ_{1P}, and deflection, φ_{1P}, is then found

$$\kappa_{1P}(x) = \frac{F_1 \Delta x - M_1}{EI}, \quad \frac{d\theta_{1\mathsf{P}}}{dx} = \kappa_{1P}(x), \quad \frac{d\varphi_{1\mathsf{P}}}{dx} = \theta_{1P}(x). \tag{3.12}$$

The shape function is normalised with the deflection at the top of the pile, which are

$$\varphi_{1P}(\mathsf{L}_P) = \varphi_{FP} - \varphi_{MP}\frac{\theta_{FP}}{\theta_{MP}}, \tag{3.13}$$

and is shown in figure 3.4. The second shape function, φ_{2P}, is based on a force and moment at the top of the pile that ensures that the deflection is zero at the top of the pile, which are

$$F_2 = -\frac{\varphi_{MP}}{\varphi_{FP}} \quad \text{and} \quad M_2 = 1. \tag{3.14}$$

The force and moment are illustrated in figure 3.4. The shape function is found as in equation (3.12) but where F_1 and M_1 are replaced with F_2 and M_2. The shape function is normalised with the angular deflection at the top of pile

$$\theta_{2P}(\mathsf{L}_P) = \theta_{MP} - \theta_{FP}\frac{\varphi_{MP}}{\varphi_{FP}}, \tag{3.15}$$

and is shown in figure 3.4.
The slaving of the second DOF to the first DOF is made by considering a force at the nacelle which gives a unit deflection at the top of the monopile for the first shape function. The force also results in a angular deflection at the top of the monopile for the second shape function. The coupling coefficient is the ratio between the angular deflection and the deflection $C_{12} = \theta_{2P}(\mathsf{L}_P)/\varphi_{1P}(\mathsf{L}_P)$.

The tower

The tower's first shape function is found from a unit force, F_1, acting in the point, P_K, the distance X above the tower top, as illustrated in figure 3.5. The distance represents the distance from the yaw ring and up to the rotating axis in the wind turbine. The resulting bending moment in the tower is $M(x) = (X + \Delta x)F$ with $\Delta x = \mathsf{L}_T - x$.

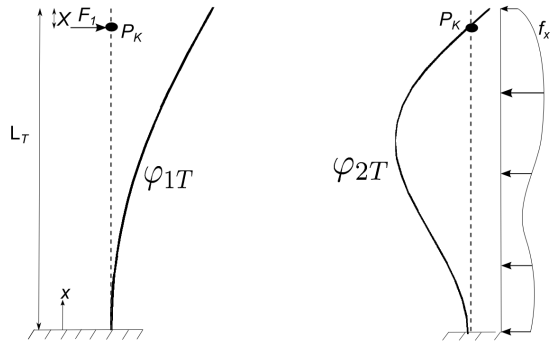

Figure 3.5: *The forces to find the first and second shape function in the tower.*

From the bending moment κ_{1T}, θ_{1T} and φ_{1T} are calculated in the same way as in the pile. The shape function is normalised with the deflection of the tower in the point where the unit force is acting, which are

$$\varphi_{1T}(\mathsf{L}_T + X) = \varphi_{1T}(\mathsf{L}_T) + \theta_{1T}(\mathsf{L}_T)X, \tag{3.16}$$

and is shown in figure 3.5. The angular deflection of the tower is related to the deflection by a factor $C_{kob} = \theta_{1T}(\mathsf{L}_T)/\varphi_{1T}(\mathsf{L}_T + X)$.
Since the first shape function is a static shape it does not have a eigenfrequency. This is however estimated in Flex5 in order to calculate a damping factor of the first shape function

$$\omega_{1T}^2 = \frac{GK_{i,i}}{\mathsf{M}_{top} + GM_{i,i}}, \tag{3.17}$$

where $GK_{i,i}$ and $GM_{i,i}$ is the generalised mass and stiffness for this shape function, and explained in more details in section 3.1.2. The top mass M_{top} is the mass of wind turbine subtracted the mass of the tower.
The second shape function is based on the eigenmode of the tower where the point, P_K, is fixed against translation but where the rotation is free. As explained previous an eigenmode is a free vibration without the presence of external loads. The only force acting on the tower is therefore the inertia force, $f(x) = m(x)\varphi_{2T}(x)\ddot{\alpha}$.
The shape function is found by iteration. In the first iteration step the shape function in the tower is assumed to be one, $\varphi_{2T}(x) = 1$ and a unit acceleration is assumed, $\ddot{\alpha} = 1$. Based on $f(x)$ the bending moment, the curvature, the angular deflection and the deflection is found.

$$\kappa_{2T}(x) = \frac{f(x)\Delta x}{EI}, \quad \frac{d\theta_{2T}}{dx} = \kappa_{2T}(x), \quad \frac{d\varphi_{2T}}{dx} = \theta_{2T}(x), \quad \Delta x = \mathsf{L}_T + X - x. \tag{3.18}$$

With the definition of the force, the shape function, φ_{2T}, is non-zero in the point P_K. To get a zero deflection in point P_K the value of φ_{2T} in this point is multiplied with the first shape function in the tower and afterwards subtracted from the second shape function. The same is done with the angular deflection and the curvature

$$\kappa_{2T} = \kappa_{2T} - \kappa_{1T}\varphi_{2T}(\mathsf{L}_T + X), \quad \theta_{2T} = \theta_{2T} - \theta_{1T}\varphi_{2T}(\mathsf{L}_T + X), \quad \varphi_{2T} = \varphi_{2T} - \varphi_{1T}\varphi_{2T}(\mathsf{L}_T + X). \tag{3.19}$$

Finally, κ_{2T}, θ_{2T} and φ_{2T} are normalised such that the angular deflection in top of the tower is one, $\theta_{2T}(\mathsf{L}_T) = 1$. The shape function is also shown in figure 3.5
In next iteration step the force is $f(x) = \mathsf{m}(x)\varphi_{2T}(x)$ where the acceleration again is a unit acceleration. The acceleration could also have been represented by ω_{2T}, which is the eigenfrequency of the second shape function based on the last iteration step. But it does not change the result, since the shape function are normalised.
The iteration stops when φ_{2T} is converged. Afterwards the eigenfrequency is found from the applied force, f(x), which is a force which gives an angular deflection of 1 in the point P_K

$$f(x) = \mathsf{m}(x)\varphi_{2T}(x)\frac{1}{\theta_{2T}(\mathsf{L}_T + X)}. \tag{3.20}$$

Since it is an eigenmode the force can also be written as

$$f(x) = \mathsf{m}(x)\varphi_{2T}(x)\omega_{2T}^2. \tag{3.21}$$

Combining equation (3.20) and (3.21) gives the eigenfrequency

$$\omega_{2T} = \sqrt{\frac{1}{\theta_{2T}(\mathsf{L}_T + X)}}. \tag{3.22}$$

3.1.2 The generalised matrices in Flex5

In Flex5 the generalised matrices and vectors are found by the principle of virtual work. For purely eigenmodes the stiffness and damping matrix are diagonal matrices, but since the shape functions in the monopile are static the stiffness and damping matrix are not fully diagonal, but all three

matrices are symmetric. To illustrate how the generalised matrices are calculated in Flex5 a simple example is in the following considered.
A pile with length L_P and a tower with length L_T on top of the pile is considered. The displacement of the pile, u_{1P}, and tower, u_{1T}, are described by the generalised coordinate, α_i, and a shape function, φ_i

$$\mathsf{u}_{1P}(x) = \alpha_{1P}\varphi_{1P}(x) \quad \text{and} \quad \mathsf{u}_{1T}(x) = \alpha_{1T}\varphi_{1T}(x) + \mathsf{u}_{1P}(x = L_P), \tag{3.23}$$

with x being the coordinate along the pile and tower. The system consists therefore of two degrees of freedom (DOF). The shape functions are equal to the monopile and tower's first shape function in Flex5. The shape functions are normalized so $\varphi_{1P} = 1$ and $\varphi_{1T} = 1$ in the top of the pile and tower.
Both the pile and tower have a distributed mass, $m(x)$, stiffness, $\mathsf{k}(x)$, and damping, $\mathsf{c}(x)$
The damping of a beam with a modal shape function is found from the damping ratio which is the ratio between the damping and critical damping, c_r

$$\zeta = \frac{\delta}{2\pi} = \frac{\mathsf{c}}{\mathsf{c}_r} = \frac{\mathsf{c}}{2\sqrt{m\mathsf{k}}} = \frac{\mathsf{c}}{2\sqrt{\frac{\mathsf{k}}{\omega_0^2}\mathsf{k}}} \Leftrightarrow \mathsf{c} = \frac{\delta}{2\pi}\frac{2\mathsf{k}}{\omega_0} = \frac{\delta\mathsf{k}}{\pi\omega_0}. \tag{3.24}$$

The relation between the damping ratio, ζ and logarithmic decrement is found by assuming $\zeta << 1$

$$\delta = \frac{2\pi\zeta}{\sqrt{1-\zeta^2}} \sim 2\pi\zeta. \tag{3.25}$$

The critical damping, $\mathsf{c}_r = 2\sqrt{m\mathsf{k}}$, is found if the equation of motion is solved for a free vibration (the external force is zero) with viscous damping.
With the chosen degrees of freedom in the monopile, it is not possible to calculate an eigenfrequency for the degrees of freedom in the pile. The logarithmic decrement, δ, and a corresponding eigenfrequency, $\hat{f}_p$, in the monopile is therefore given as input values and the damping factor calculated as

$$\mathsf{c} = \frac{\delta\mathsf{k}}{2\pi^2\hat{f}_p}. \tag{3.26}$$

Both the damping in equation (3.24) and (3.26) is proportional to the stiffness, k, which is found by solving the equation of motion for a free vibration without the viscous damping and gives

$$\mathsf{k}(x) = \omega_0^2 m(x), \tag{3.27}$$

with ω_0 being the corresponding angular eigenfrequency.
In the principle of virtual work the external virtual work should be equal to the internal virtual work. The generalised force **GF** is doing the external virtual work and the generalised matrices **GM**, **GK** and **GC** are doing the internal virtual work.
If point forces are considered the virtual work is the work done by the forces to move the generalised coordinates α_i a unit displacement. In the example here, if the force is acting in top of the pile or tower the virtual work corresponds to the displacement of the top of the pile or tower, $\alpha_i\varphi_i(\mathsf{L}_i)$. If a distributed force is considered it is the work done by the force to move the whole pile or tower, $\alpha_i\varphi_i(x)$.

The generalized force

The generalised force vector **GF** is found by the principle of virtual work as the work done by the external forces to move the generalised coordinates a unit displacement with the other coordinate zero. The external forces are first added up and integrated such that a point force in the top of the pile, F_P, and in the top of the tower, F_T, are considered.

If the generalised coordinate $\alpha_{1P} = 1$ then the displacement of the pile and the tower are $\mathsf{u}_{1P}(\mathsf{L}_P) = 1\varphi_{1P}(\mathsf{L}_P)$ and $\mathsf{u}_{1T}(\mathsf{L}_T) = \mathsf{u}_{1P}(\mathsf{L}_P)$. Both forces contribute therefore to the work. For $\alpha_{1T} = 1$ the displacement of the tower is $\mathsf{u}_{T1}(\mathsf{L}_T) = 1 \cdot \varphi_{1T}(\mathsf{L}_T)$, while the displacement of the pile is zero. This means that only the force in the tower F_T is contributing to the work.
The generalised force vector therefore reads

$$\mathbf{GF} = \begin{bmatrix} F_P \cdot 1\varphi_{1P}(\mathsf{L}_P) + F_T \cdot 1\varphi_{1P}(\mathsf{L}_P) \\ \\ F_T \cdot 1\varphi_{1T}(\mathsf{L}_T) \end{bmatrix} = \begin{bmatrix} F_P + F_T \\ \\ F_T \end{bmatrix}. \tag{3.28}$$

The generalized mass matrix

The first column in the generalised mass matrix is found by considering which forces are necessary to accelerate the first generalised coordinate by one unit. The forces are therefore inertia forces, which are distributed forces, because the masses of the pile and tower vary with x. If $\ddot{\alpha}_{1P} = 1$ the pile is accelerated with $\ddot{\mathsf{u}}_{1P}(x) = 1 \cdot \varphi_{1P}(x)$ and the tower is accelerated with $\ddot{\mathsf{u}}_{1T}(x) = 1\varphi_{1P}(\mathsf{L}_P)$, so $f_P(x) = 1 \cdot \varphi_{1P}(x) m_P(x)$ and $f_T(x) = 1\varphi_{1P}(\mathsf{L}_P) \cdot m_T(x)$. The first row in the generalized matrix describes the work done by the forces to move the first generalised coordinate a unit displacement. For $\alpha_{1P} = 1$ the displacement of the pile and tower is $\mathsf{u}_{1P}(x) = 1 \cdot \varphi_{1P}(x)$ and $\mathsf{u}_{1T}(x) = 1\varphi_{1P}(\mathsf{L}_P)$. Therefore both inertia forces contribute to the total work

$$GM_{1,1} = \int_0^{\mathsf{L}_P} 1\varphi_{1P}(x) m_P(x) \cdot 1\varphi_{1P}(x) dx + \int_0^{\mathsf{L}_T} 1 m_T(x) \varphi_{1P}(\mathsf{L}_P) \cdot 1\varphi_{1P}(\mathsf{L}_P) dx. \tag{3.29}$$

The second row in the generalized matrix describes the work done by the forces to move the second generalised coordinate a unit displacement. For $\alpha_{1T} = 1$ the displacement of the pile is zero and the displacement of the tower is $\mathsf{u}_{1T}(x) = 1 \cdot \varphi_{1T}(x)$. Therefore only the second inertia force contributes to the total work

$$GM_{2,1} = \int_0^{\mathsf{L}_T} 1\varphi_{1P}(\mathsf{L}_P) . m_T(x) \cdot 1\varphi_{1T}(x) dx \tag{3.30}$$

The second column in the generalised mass matrix is found in same manner, but this time it is the second generalised coordinate which is accelerated a unit. The pile is not accelerated so the first inertia force is zero while the acceleration of the tower is due to the force, $f_T(x) = 1 \cdot \varphi_{1T}(x) m_T(x)$. If the first generalised coordinate is moved a unit displacement, both inertia forces are contributing to the work, however since $f_P(x) = 0$ the work is

$$GM_{1,2} = \int_0^{\mathsf{L}_T} 1 \cdot \varphi_{1T}(x) m_T(x) \cdot 1\varphi_{1P}(\mathsf{L}_P) dx. \tag{3.31}$$

When the second generalised coordinate is moved a unit displacement only the second force contribute to the work

$$GM_{2,2} = \int_0^{\mathsf{L}_T} 1\varphi_{1T}(x) \cdot m_T(x) \cdot 1\varphi_{1T}(x) dx. \tag{3.32}$$

The generalised mass matrix therefore reads

$$\mathbf{GM} = \begin{bmatrix} \int_0^{\mathsf{L}_P} m_P(x) \varphi_{1T}(x)^2 dx + \int_0^{\mathsf{L}_T} m_T(x) dx & \int_0^{\mathsf{L}_T} m_T(x) \varphi_{1T}(x) dx \\ \\ \int_0^{\mathsf{L}_T} m_T(x) \varphi_{1T}(x) dx & \int_0^{\mathsf{L}_T} m_T(x) \varphi_{1T}(x)^2 dx \end{bmatrix}. \tag{3.33}$$

It is important to remember that the mass $m_P(x)$ represents both the mass of the monopile and the added mass term from Morison's equation $\rho C_m \mathscr{A}(x)$, where $C_m = 1$ is the hydrodynamic mass coefficient and $\hat{A}$ is the cross sectional area of the pile. The added mass is a function of time due to the change in the surface elevation. The generalised mass in the monopile is therefore also a function of time.

The generalized stiffness and damping matrix

For the stiffness matrix the generalised forces required to move the generalised coordinates a unit static displacement with the other zero are considered.
As explained in section 3.1.1 both a force and a moment in the top of the pile is necessary to give a displacement of the pile and still respect the shape function. If a unit force, $F = 1$, and a moment $M = -\theta_{FP}/\theta_{MP}$ are considered the displacement in the top of the pile, $\varphi_{1P}(\mathsf{L}_P)$, is given in equation (3.13). Since the generalised force shall give an unit displacement, the force and moment are normalised with this displacement, $F_P = 1/\varphi_{1P}(\mathsf{L}_P)$ and $M_P = (\theta_{FP}/\theta_{MP}))/\varphi_{1P}(\mathsf{L}_P)$. No force in the tower is required to move the pile a unit displacement so $F_T = 0$.
To move the first generalised coordinate a unit displacement both F_P and M_P are doing a work. The tower is also moved a unit displacement but since the force in the tower is zero no work is done in the tower. The work therefore is

$$GK_{1,1} = 1(F_P + M_P) = \frac{\left(1 - \frac{\theta_{FP}}{\theta_{MP}}\right)}{\varphi_{FP} - \varphi_{MP}\frac{\theta_{FP}}{\theta_{FP}}}. \tag{3.34}$$

To move the second coordinate a unit displacement only the force in the tower is doing a work, but since this is zero,

$$GK_{1,2} = 0. \tag{3.35}$$

To give the second generalised coordinate a static unit displacement the force in the tower, F_T, is required. To avoid that the first generalised coordinate is moved together with the second coordinate, F_P is working in the other direction of F_T with the same magnitude, $F_P = -F_T$. If a unit force is applied in top of the tower the deflection in the top of the tower, $\varphi_{1T}(\mathsf{L}_T)$, is given in equation (3.16), where $X = 0$ in this example. To ensure that the generalised coordinate is moved by only a unit displacement the force necessary is $F_T = 1/\varphi_{1T}(\mathsf{L}_T)$.
If the first coordinate is moved a unit displacement both the pile and the tower is moved, so both forces are contributing to the work

$$GK_{2,1} = -F_P + F_T = 0. \tag{3.36}$$

If the second coordinate is moved, only the tower is moved so only the second force contribute to the work,

$$GK_{2,2} = 1/\varphi_{1T}(\mathsf{L}_T). \tag{3.37}$$

This term is equal to ω_{2T}^2, where ω_{2T} is the eigenfrequency of the second shape function in the tower. The stiffness is therefore proportional to the eigenfrequency as stated in equation (3.27).
The generalised stiffness matrix thereby reads

$$\mathbf{GK} = \begin{bmatrix} \frac{\left(1-\frac{\theta_{FP}}{\theta_{MP}}\right)}{\varphi_{FP}-\varphi_{MP}\frac{\theta_{FP}}{\theta_{FP}}} & 0 \\ 0 & \frac{1}{\varphi_{2T}(\mathsf{L}_T)} \end{bmatrix}. \tag{3.38}$$

For the damping matrix the generalised forces considered are forces necessary to obtain a unit velocity of the generalised coordinate with the other zero. The damping factor in the pile and tower are given by equation (3.24) and (3.26). The generalised damping matrix is found in similar manner as the stiffness matrix and gives

$$\mathbf{GD} = \begin{bmatrix} \mathsf{c}_1\frac{\left(1-\frac{\theta_{FP}}{\theta_{MP}}\right)}{\varphi_{FP}-\varphi_{MP}\frac{\theta_{FP}}{\theta_{FP}}} & 0 \\ 0 & \mathsf{c}_2\frac{1}{\varphi_{2T}(\mathsf{L}_T)} \end{bmatrix} = \begin{bmatrix} \frac{\delta_1}{\pi\omega_1}GK_{1,1} & 0 \\ 0 & \frac{\delta_2}{\pi\omega_2}GK_{2,2} \end{bmatrix}. \tag{3.39}$$

As stated in equation (3.24) and (3.26) the damping is proportional to the stiffness.

3.2 The external forces in Flex5

The external forces in Flex5 are the aerodynamic forces from the wind and the hydrodynamic forces from the waves. The aerodynamic loads are calculated by the unsteady BEM method. The idea of the BEM-method is to determine the relative velocity felt by the blades. When this is known it is fairly easy to determine the lift and drag forces on the blades and from this the trust and power. With the unsteady method the dynamics of the wind turbine structure is taken into account when the aerodynamic loads are calculated. The unsteady BEM method will not be explained in this thesis but for a detailed explanation of the method see for instance Hansen *et al.* (2005).
The distributed hydrodynamic load on the structure is calculated by Morison's equation, which is extended following the work of Rainey (1989) and Rainey (1995). In Flex5 the wave realization can have an arbitrary angle to the wind direction. The unidirectional wave kinematics are therefore projected to the fore-aft (fa) and side-to-side (ss) direction in Flex5 and the Morison forces are both calculated in the fore-aft direction, f_{fa} and in the side-to-side direction, f_{ss}

$$\begin{aligned} f_{fa}(z,t) =& \rho\mathscr{A}(z)C_m a_{fa}(z,t) + \rho\mathscr{A}(z)a_{fa}(z,t) + \rho\mathscr{A}(z)C_m w_z(z,t)\left(u_{fa}(z,t) - \dot{\mathsf{u}}(z,t)\right) + \\ & \frac{1}{2}\rho C_D D\left(u_{fa}(z,t) - \dot{\mathsf{u}}(z,t)\right)\sqrt{\left(u_{fa}(z,t) - \dot{\mathsf{u}}(z,t)\right)^2 + \left(u_{ss}(z,t) - \dot{\mathsf{v}}(z,t)\right)^2} \\ f_{ss}(z,t) =& \rho\mathscr{A}(z)C_m a_{ss}(z,t) + \rho\mathscr{A}(z)a_{ss}(z,t) + \rho\mathscr{A}(z)C_m w_z(z,t)\left(u_{ss}(z,t) - \dot{\mathsf{v}}(z,t)\right) + \\ & \frac{1}{2}\rho C_D D\left(u_{ss}(z,t) - \dot{\mathsf{v}}(z,t)\right)\sqrt{\left(u_{fa}(z,t) - \dot{\mathsf{u}}(z,t)\right)^2 + \left(v_{ss}(z,t) - \dot{\mathsf{v}}(z,t)\right)^2}. \end{aligned} \tag{3.40}$$

Here $\rho = 1025$ m^2/s is the density of water; $\mathscr{A}(z)$ is the cross sectional area of the pile; C_D and C_m are the drag- and added mass coefficient respectively. If nothing else is stated they both have a value of 1 through the thesis. The horizontal and vertical particle velocities are named $u(z,t)$ and $w(z,t)$ respectively, and $a(z,t)$ are the horizontal particle acceleration. The structural velocity and acceleration in the fore-aft direction, $\dot{\mathsf{u}}(z,t)$ and $\ddot{\mathsf{u}}(z,t)$, and in the side-to-side direction, $\dot{\mathsf{v}}(z,t)$ and $\ddot{\mathsf{v}}(z,t)$, are zero in the first part of the thesis which concerns the forcing on a fixed monopile, but are included in the calculations in Flex5. The third term in equation (3.40) is the axial divergence correction, which according to Manners & Rainey (1992) corrects for the assumption that the cylinder is slender in the vertical direction, which it is not. The structural acceleration, $\ddot{\mathsf{u}}$ and $\ddot{\mathsf{v}}$, is not subtracted from the particle acceleration in the added mass term. Instead the subtraction is included in the mass matrix in the aeroelastic code, Flex5, cf. equation (3.8).
Following Rainey (1995) a final point force is added to the Morison's equation to represent the change of kinetic energy associated with the change of welted area. The force is calculated in both the fore-aft and side-to-side direction in Flex5

$$\begin{aligned} F_{s,fa} &= -\frac{1}{2}\rho\mathscr{A}C_m\eta_x\left(u_{fa}(z,t) - \dot{\mathsf{u}}(z,t)\right)^2, \\ F_s, ss &= -\frac{1}{2}\rho\mathscr{A}C_m\eta_x\left(u_{ss}(z,t) - \dot{\mathsf{v}}(z,t)\right)^2. \end{aligned} \tag{3.41}$$

Here η_x is the slope of the surface elevation and represents the change of the surface elevation along the pile-diameter. Rainey (1995) explains that the pressure in the free surface region decays over a distance proportional to the cylinder radius. In case of a slender body as the monopile the pressure field constitutes a point load. The point load corresponds to the effect when a cylinder is dragged obliquely out of the water. The water loses kinetic energy as the wetted part of the cylinder becomes smaller. The energy loss requires a force at the surface intersection. The axial divergence correction term in equation (3.40) term and the point force, equation (3.41) are in the following named the "Rainey terms". The Rainey-terms are both included when the linear and nonlinear wave forcing is calculated. In this way it is only the wave kinematics that causes the differences in the linear and nonlinear wave forcing.
The surface elevation, the horizontal and vertical particle velocity and the slope of the surface elevation is provided by the numerical wave model.
Since the vertical position of the grid points in the wave model, z, varies with time, the horizontal particle acceleration in a single point must be evaluated from the partial derivative

$$a(z,t) = \frac{du}{dt} = \frac{\partial u}{\partial t} + \frac{\partial u}{\partial z}\frac{dz}{dt} + \frac{\partial u}{\partial x}\frac{dx}{dt} = \frac{\partial u}{\partial t} + \frac{\partial u}{\partial z}w(z,t) + \frac{\partial u}{\partial x}u(z,t). \tag{3.42}$$

The term $\frac{\partial u}{\partial z}$ is also provided by the hydrodynamic model. The term $\frac{\partial u}{\partial x}$ is from conservation of continuity equal to $-\frac{\partial w}{\partial z}$ which together with $\frac{\partial u}{\partial t}$ is calculated as post-processing using the mid-point rule on a 5 point stencil which is accurate to fourth order.

The diffraction effects starts to become significant for $D/L > 0.2$, where D is the pile diameter and L the wave length. For the irregular waves in the wave-realizations which have frequencies larger than $\hat{f} \sim 0.22\,\text{Hz}$ ($T < 4.5$ s) the ratio D/L is larger than 0.2 for pile diameters between 6 m and 6.5 m. Diffraction effects are therefore present for the wave realizations considered in the present thesis and imply that the inertia force decreases for these waves. It is therefore desirable to introduce a diffraction correction of the added mass coefficient, C_m. MacCamy-Fuchs theory, MacCamy & Fuchs (1954) provides such a correction for linear waves. However, the diffraction theory is only valid for linear waves and in the wave spectra for nonlinear wave realizations it is not possible to see which waves are free or bound waves. It is therefore difficult to apply the correction of the inertia coefficients to the nonlinear wave realizations. Since we want a clean approach where the linear and nonlinear wave realizations are treated identically the inertia coefficient are not corrected for the diffraction of the waves in the present thesis.

3.3 The NREL 5MW wind turbine

The NREL 5MW wind turbine is a reference wind turbine developed by the National Renewable Energy Laboratory, Jonkman *et al.* (2009). The wind turbine is a conventional three-bladed upwind variable-speed variable blade-pitch-to-feather-controlled turbine. The wind turbine is used as reference wind turbine in many research projects.
In Jonkman *et al.* (2009), the steady state response of the system as function of the wind speed is shown for different outputs. To validate the implementation of the NREL 5MW wind turbine in Flex5, the steady state response of the same outputs are calculated and compared with the outputs of Jonkman *et al.* (2009) in figure 3.6. The figures are taken from Jonkman *et al.* (2009) and the results from the current implementation are plotted on top as stars,"*". The output parameters are named the same as in Jonkman *et al.* (2009) and is explained in the following:

GenSpeed Rotational speed of the generator.
RotPwr The mechanical power.
GenPwr The generator power.
RotThrust Rotor thrust.
RotTorq Rotor torque.
RotSpeed Rotational speed of the rotor.
BlPitch1 Pitch angle of blade 1.
GenTq Torque of the generator.
TSR Tip speed ratio.
OoPDefl1 Out-of-plane tip deflections of blade 1.
IPDefl1 In-plane tip deflections of blade 1.
TTDspFA Fore-aft deflection of the tower top.
TTDspSS Side-to-side deflection of the tower top.

The responses compare well for all wind speeds. The wind turbine therefore generates the expected electrical power. The out-of-plane tip deflection (OoPDefl1) is the parameter where the deviation is largest, but it has not been possible to find an explanation for this. In the analysis in this thesis the focus is on the dynamics of the structure. It is therefore also important that the structure has the correct response. To investigate this, the implementation is validated against the comparison of different aeroelastic codes done in the "Offshore Code Comparison Collaboration (OC3) for IEA Task 23 Offshore Wind Technology and Deployment", Jonkman & Musial (2010). In the present thesis the foundation is rigid and the comparison is therefore done with phase 1 of OC3; Monopile with Rigid Foundation. The wind turbine is placed in a water depth of 20 m and the height of the wind turbine tower is reduced by 10 m, which also is done in the present thesis. The cases from OC3 which are used in the validation are stated in table 3.1
According to Jonkman & Musial (2010) the results from the different codes compare in general very well. This was however achieved after five iterations, where the controller interface was adjusted and misinterpreted turbine data specifications corrected.

Case	Enabled DOF's	Wind	Wave
2.1a	None: constant rotor speed and fixed blade pitch	Steady, uniform, no shear, $V_{hub} = 8\,\mathrm{m/s}$	None
3.1	Tower, drive train, blades	Steady, uniform, no shear, $V_{hub} = 8\,\mathrm{m/s}$	None
4.1	Substructure, tower	None	Regular linear, $H = 6\,\mathrm{m}$, $T = 10\,\mathrm{s}$
5.1	Substructure, tower, drive train, blades	Steady, uniform, no shear, $V_{hub} = 8\,\mathrm{m/s}$	Regular linear, $H = 6\,\mathrm{m}$, $T = 10\,\mathrm{s}$

Table 3.1: *The load cases from OC3, which are used in the validation.*

The current implementation is compared against other Flex5 codes provided by the Endowed Chair of Wind Energy at the University of Stuttgart, (SWE) and Natural Gas Energy, (DONG). The implementation is also compared against HAWC2 provided by Risøe Natinal Laboratoty, now DTU

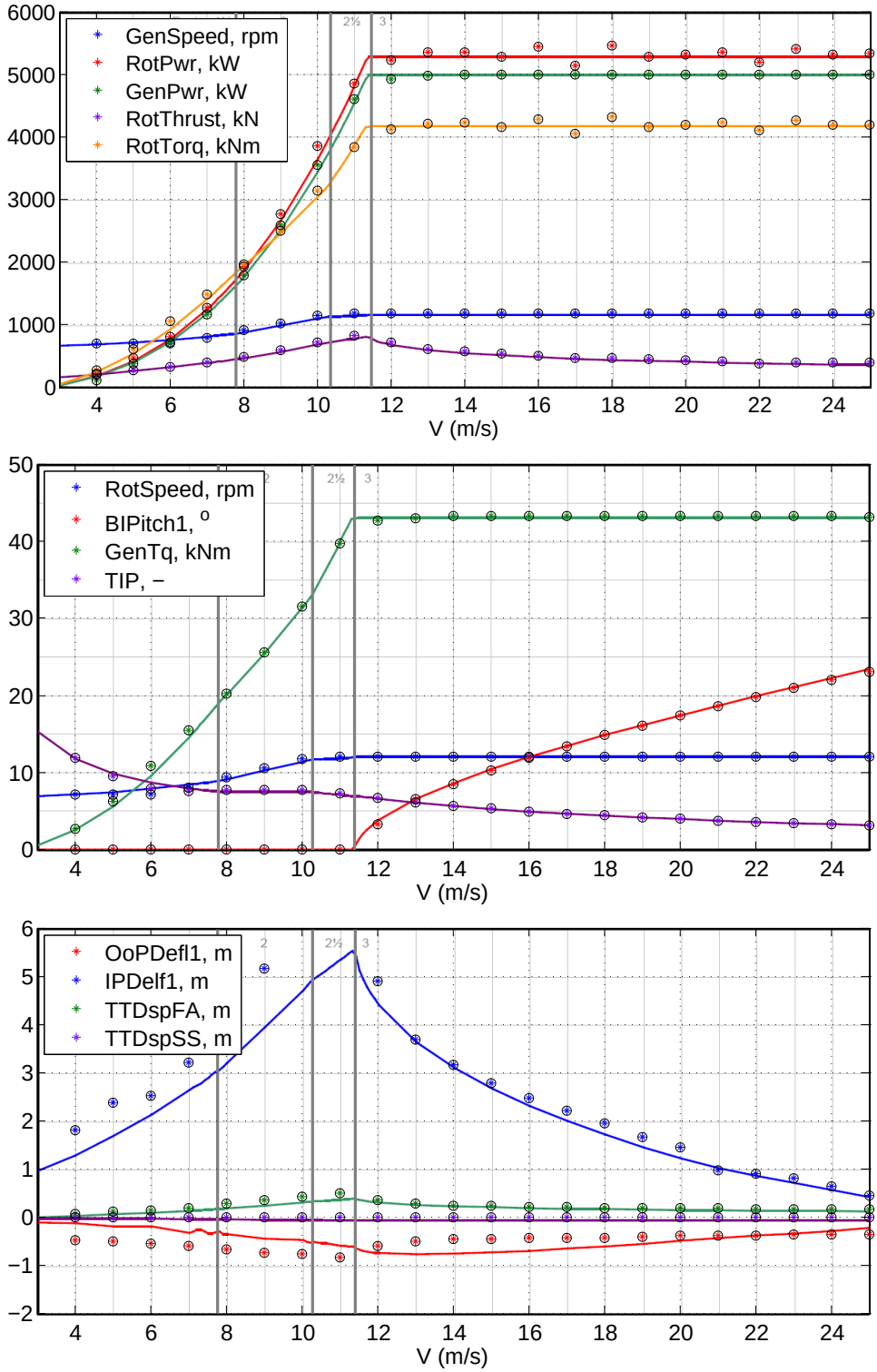

Figure 3.6: *Steady-state responses as a function of wind speed. The figures are from Jonkman* et al. *(2009).*

Wind Energy.

The eigenfreqiencies of the first 8 degrees of freedom are stated in table 3.2. The eigenfrequencies for the present implementation is named "DTU". The eigenfrequencies are very similar to the other codes except for the blades asymmetric flapwise modes, where the eigenfrequencies are smaller

than the other codes. Why these two eigenfrequencies are smaller is not understood; it would be expected that they at least would be close to the frequencies from SWE and DONG, which also are FLex5 codes. In Jonkman *et al.* (2009), the eigenfrequencies are also calculated. With the code ADAMS, the eigenfrequency of the first flapwise yaw mode is 0.6296 Hz, which is close to what is calculated with the current Flex5 code. It does not explain the difference between the current code and SWE and DONG, but it shows that there is a deviation in the eigenfrequencies.
The reason that the eigenfrequency of the blade collective flap mode is different from the eigenfrequencies from SWE and DONG, can be that these eigenfrequencies are switched with the asymmetric flapwise pitch mode.

	DTU	SWE	DONG	Risøe
1st Tower Fore-Aft	0.278	0.278	0.279	0.274
1st Tower Side-to-Side	0.282	0.282	0.283	0.276
1st Drivetrain Torsion	0.618	0.621	0.6200	0.602
1st Blade Collective Flap	0.695	0.666	0.667	0.696
1st Blade Asymmetric Flapwise Pitch	0.632	0.692	0.692	0.660
1st Blade Asymmetric Flapwise Yaw	0.629	0.674	0.664	0.625
1st Blade Asymmetric Edgewise Pitch	1.089	1.085	1.084	1.072
1st Blade Asymmetric Edgewise Yaw	1.103	1.000	1.099	1.087

Table 3.2: *The first eigenfrequencies in Hertz of the wind turbine and foundation from the different codes.*

As a start, the current implementation is compared with the other codes for load case 2.1a, in which all degrees of freedom are turned off and the wind speed is constant at 8 m/s. No waves are present. The shear force and bending moment on blade 1 at the root and the rotor torque are compared in figure 3.7. The results from the current implementation is the black line with the legend "DTU".
The purpose of this load case was to compare the aerodynamic loads on the blades. Jonkman & Musial (2010) found that there was a obvious difference between the load calculations of the different codes and explained the differences among the aerodynamic models and corrections which have been implemented into the codes.
The rotor torque and shear force are similar to SWE but a little smaller, but still larger than that the code from Risøe. The bending moment is significant smaller than the other codes. In Jonkman & Musial (2010) it is not stated particular at what point on the blades the forces and moments are considered just that it is at the root. When the blades are described in Jonkman *et al.* (2009) the first point on the blades is 1.5 m from the root. The bending moment and shear force of "DTU" are therefore found at this point. However, if they instead are found 1.0 m from the root, the bending moment becomes similar to that from SWE, as shown in figure 3.8.

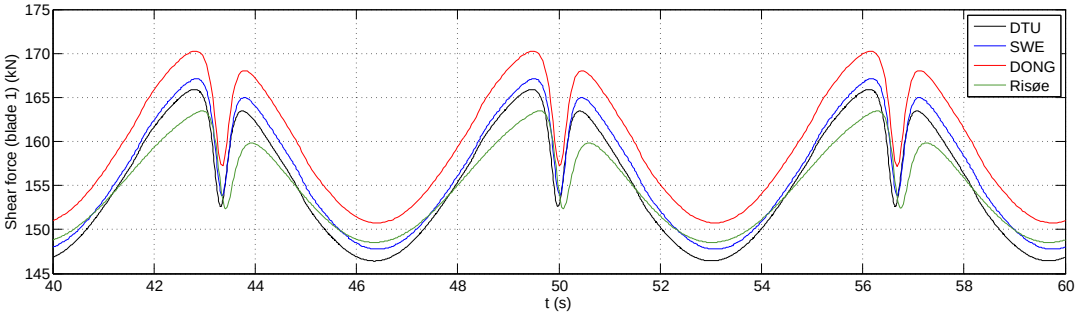

(a) Shear force at blade root.

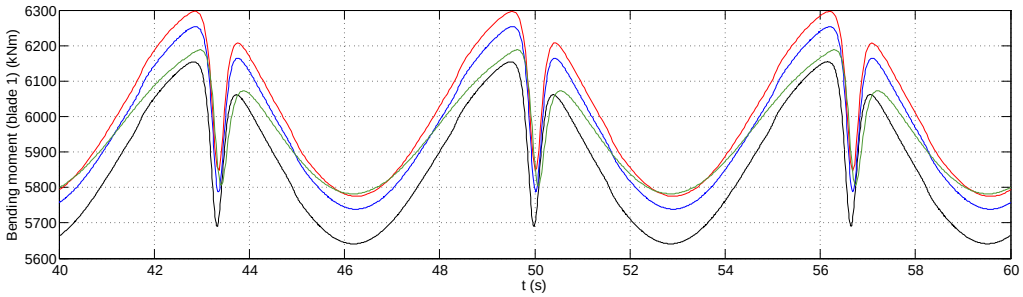

(b) Bending moment at blade root.

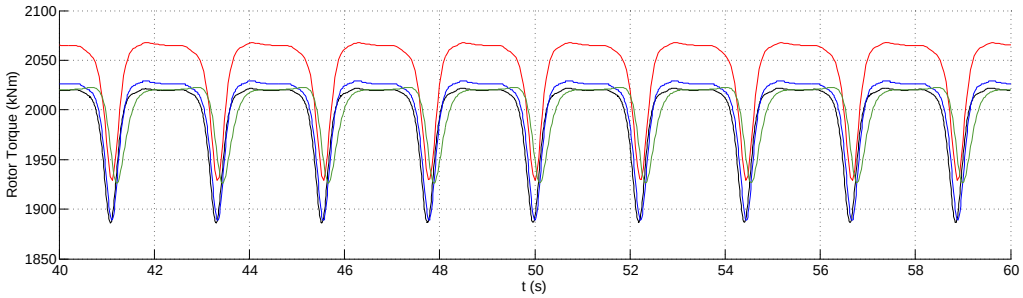

(c) Rotor torque.

Figure 3.7: *Comparison of load case 2.1a.*

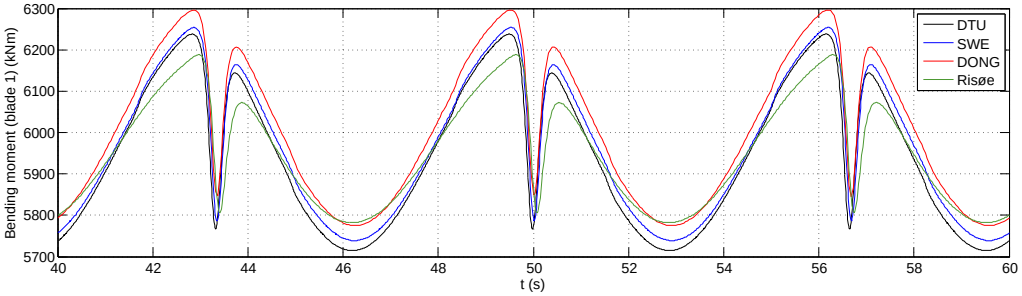

Figure 3.8: *Comparison of load case 2.1a, the bending moment from DTU are found 1 m from the root.*

In load case 3.1, all DOFs except those in the monopile are active, the wind speed is constant at 8 m/s and no waves are present. The shear force and the bending moment are again calculated 1 m from the blade root as shown in figure 3.9, and are very similar to the results from SWE. The curves are a little displaced due to the different starting position of the blades.

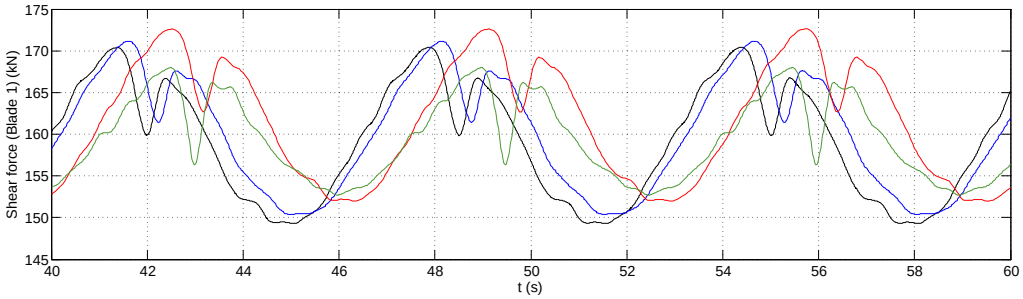

(a) Shear force at blade root.

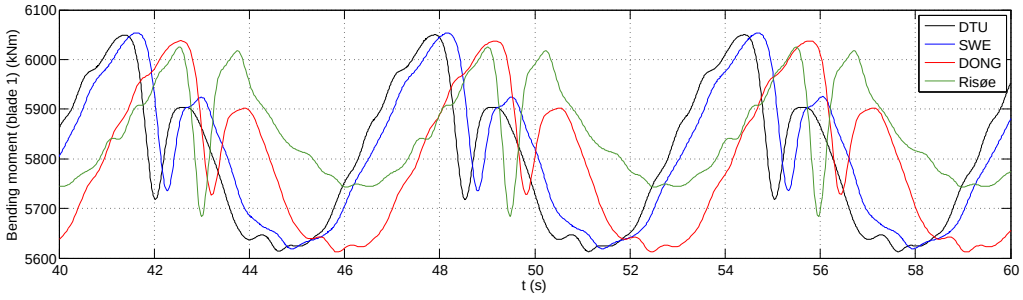

(b) Bending moment at blade root.

Figure 3.9: *Comparison of load case 3.1.*

In load case 4.1, the DOFs in the monopile and tower are active. The wind speed is zero and the wave is a regular linear wave shown in figure 3.10a. The fore-aft force in the bottom of the tower are not similar, figure 3.10b. In OC3 it is said that the results from load cases 4.X compare very well and since the force from DTU has the same magnitude as the other forces the difference is found to be acceptable.
The inline force and overturning moment at the sea bed compare on the other hand very well with the other codes, figure 3.10c and 3.10d.

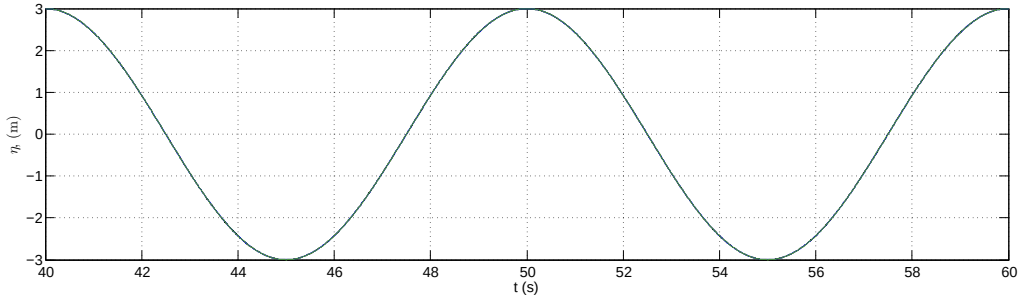

(a) Surface elevation.

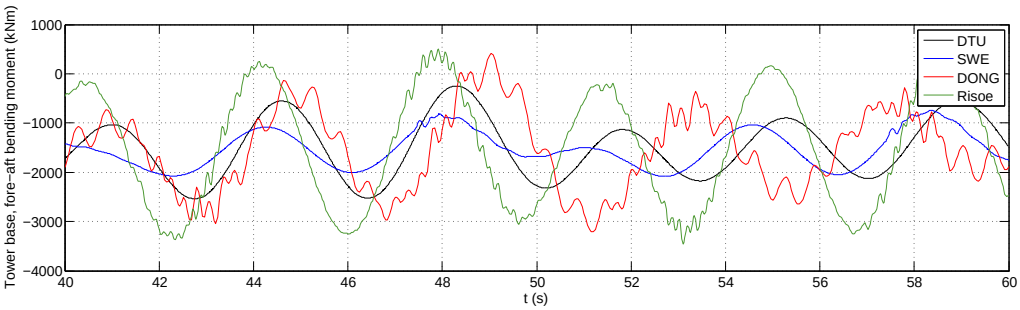

(b) Tower base fore-aft overturning moment.

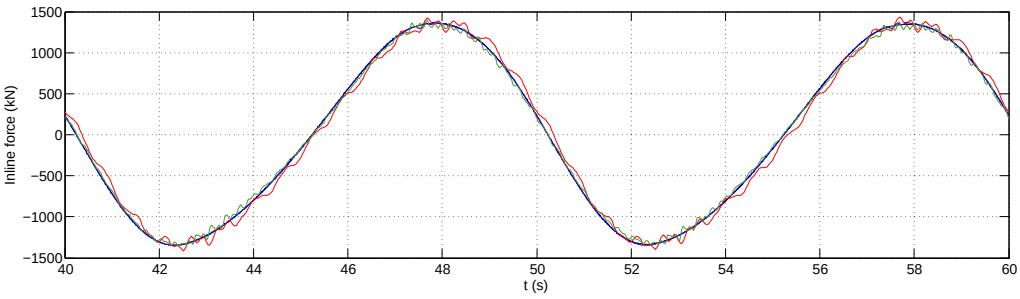

(c) Inline force at the sea bed.

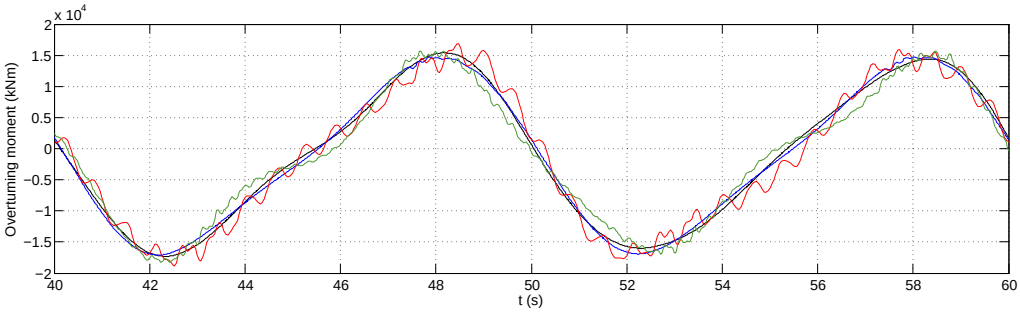

(d) Overturning moment at the sea bed.

Figure 3.10: *Comparison of load case 4.1.*

In load case 5.1, all DOFs are active, and both wind and waves are present. The shear force and bending moment are similar to those from SWE (figures 3.11a and 3.11b) as was seen in load case 3.1. The force and moment is found 1 m from the root, otherwise the bending moment would be smaller than the other codes as was seen in load case 2.1a.
The fore-aft force at the bottom of the tower is almost equal to that from SWE, figure 3.11c, and the oscillations of the force are more similar too unlike what was seen in load case 4.1. This might be due to the forcing and damping from the wind. The wave forcing causes some oscillations in the tower, which in load case 4.1 deviated much between the codes. The fore-aft overturning moment is a factor 10 larger in load case 5.1 compared to load case 4.1, which means that the effects from the wind are much stronger than the effects from the waves. The oscillations due to the wave forcing are therefore of a smaller magnitude and the differences are therefore too small to see.
The inline force and overturning moment at the sea bed are again very similar to SWE and Risøe, figures 3.12a and 3.12b.

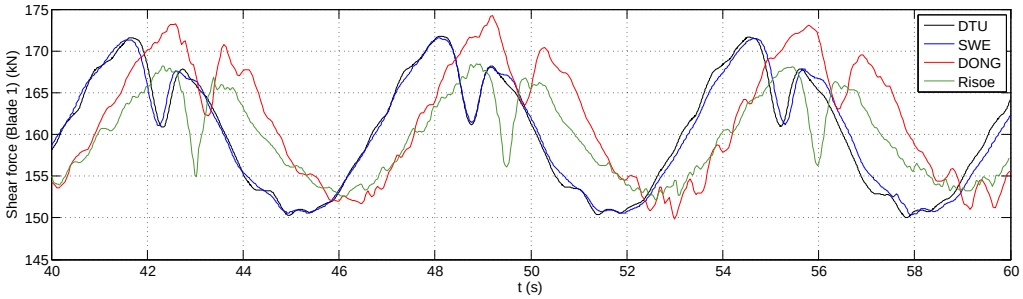

(a) Shear force at blade root.

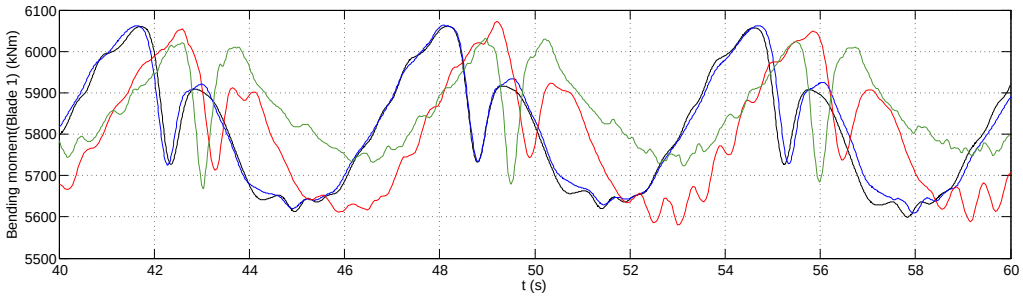

(b) Bending moment at blade root.

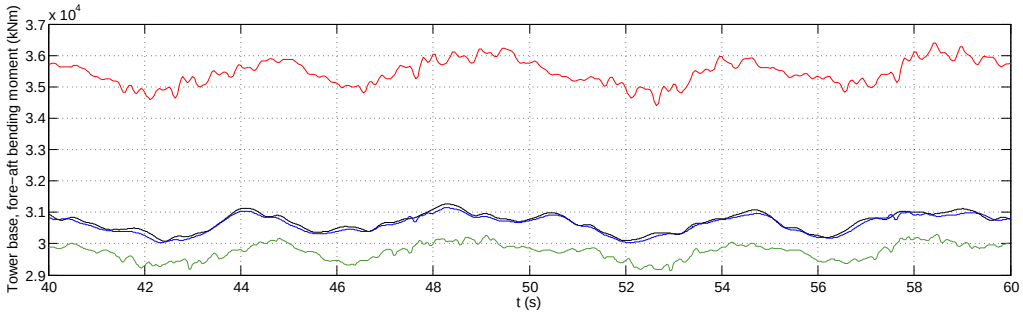

(c) Tower base fore-aft overturning moment.

Figure 3.11: *Comparison of load case 5.1.*

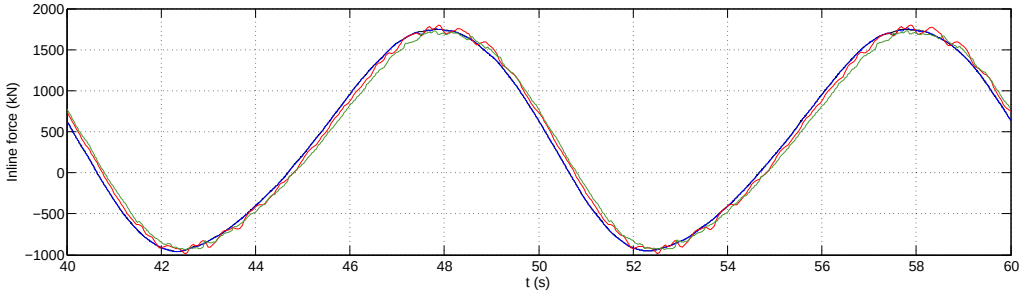

(a) Inline force at the sea bed.

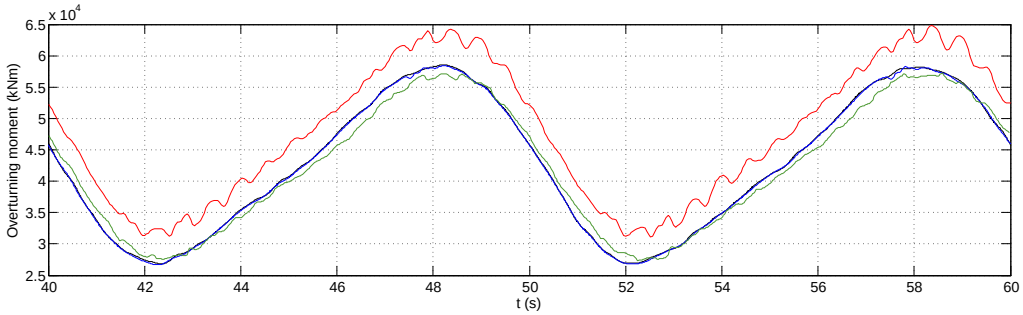

(b) Overturning moment at the sea bed.

Figure 3.12: *Comparison of load case 5.1.*

The comparison of the codes indicates that the implementation of the wind turbine into Flex5 is correct. There were some differences in the blades eigenfrequencies and some small deviations on load case 4.1 but that applied to all the codes and in general the results compared well with the other codes, in particular with SWE.

Chapter 4

Linear and fully nonlinear irregular wave forcing

In the first analysis, the linear and fully nonlinear irregular wave forcing are compared. The analysis is based on five representative sea states combined with a corresponding wind speed on four water depths. In first part of the chapter the metocean data is presented and the linear and nonlinear wave realizations are compared. Next the wave forcing on a fixed monopile is considered, and the difference between the linear and nonlinear wave forcing is therefore easy to compare. The last two sections are based on aeroelastic calculations. First the structural dynamic responses are analysed and in second part fatigue analysis is conducted. While a real fatigue design would involve a much larger set of wave climates, the chosen sea states provide a simplified basis for a first study of the influence on fatigue from wave nonlinearity. The analysis gives an idea of how important the nonlinear wave forcing is relative to the aerodynamic forcing which is dominating when the wind turbine is under operation.
The sea bed profile used in OceanWave3D to calculate the wave realizations is shown in figure 4.1. The sea bed has a slope of maximum 1:100. The generation - and absorption zones' inner boundaries are indicated with black lines. The four water depths where the wave realizations are considered are also indicated in the figure together with the slope of the sea bed at these four depths. To compare the wave realizations across the water depths it would have been preferred that the slopes were the same. However, the slope of the sea bed is rather small so the difference in the slope at the four depths is believed not to be important.

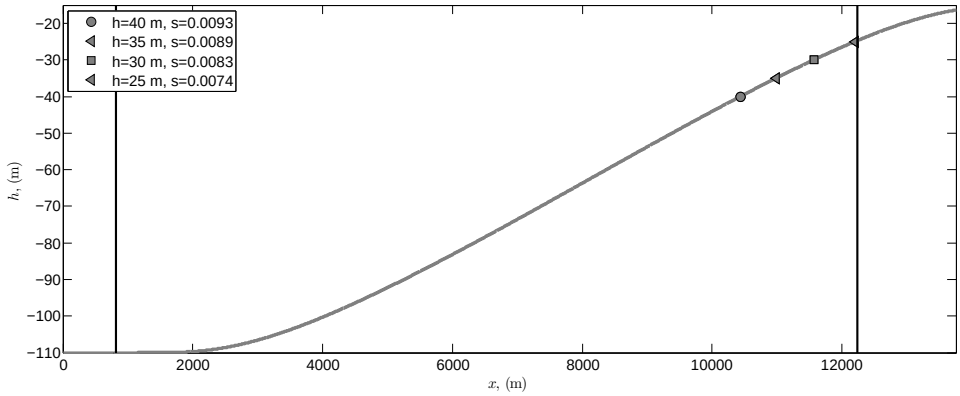

Figure 4.1: *The profile of the sea bed, the black lines indicate the inner boundaries of the relaxation zones.*

The NREL 5MW wind turbine is placed on four monopiles with varying diameter and thickness as stated in table 4.1. In this way it is ensured the structural first eigenfrequency of the wind turbine is $f = 0.27$ Hz at the four water depths and similar to OC3. 70% of the modal energy is distributed in the tower and 30 % in the monopile. The change in the diameter are not believed

to be important in the comparison of the forcing and response across the water depths, because the results primarily are presented as ratios between the linear and nonlinear realizations.

h (m)	40	35	30	25
D (m)	6.5	6.5	6.3	6.1
t (mm)	94	76	70	64

Table 4.1: *The diameter and thickness of the monopiles.*

4.1 The metocean data

The metocean data used in the analysis are representative data for the North Sea provided by DONG Energy. Six wind speeds, V, are considered. The smallest wind speed is below the wind turbine's cut-in wind speed and the largest wind speed is above the cut-out wind speed of the wind turbine. The last four wind speeds are chosen so that their probabilities, $\hat{P}$, describe the probability curve of the wind speed. The probability curve and the six wind speeds are shown in figure 4.2a.

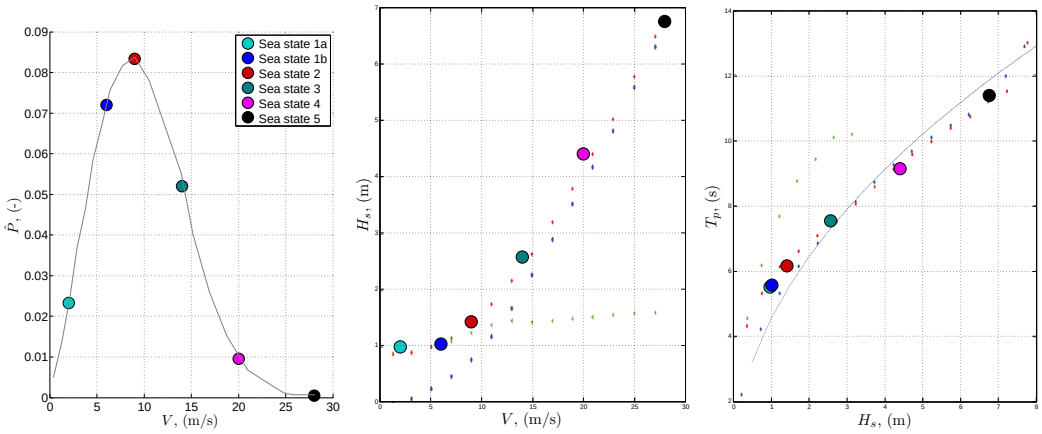

(a) Probability of occurrence and wind speed.

(b) Wave height and wind speed.

(c) Wave period and wave height.

Figure 4.2: *The probability of occurrence of the six wind speeds and the corresponding significant wave height and peak period. The figures are provided by DONG Energy.*

The significant wave heights corresponding to the six wind speeds are found from a scatter diagram which shows the relation between the wind and wave height as shown in figure 4.2b. Finally the peak wave periods can be found from a similar diagram with the relationship between the wave height and period, as shown in figure 4.2c. The sea states for the two smallest wind speeds are more or less identical and are therefore collapsed to one single sea state for the analysis. The five sea states and associated wind speeds and probability of occurrence are stated in table 4.2.
The turbulent wind is created by the IEC Turbulence Simulator in the WAsP Engineering model[1] using the Mann (1998) model. The turbulence intensity, I_t, is calculated according to IEC61400-1 (2006) using the normal turbulence model

$$I_t = \frac{\sigma_1}{V}, \quad \sigma_1 = I_{ref}(0.75V + 5.6\text{m/s}), \tag{4.1}$$

[1] `http://www.wasp.dk/Products/WEng/IECTurbulenceSimulator.aspx`

Wind and sea state		1a	1b	2	3	4	5
V	(m/s)	2	6	9	15	20	28
H_S	(m)	0.99	0.99	1.41	2.57	4.40	6.76
T_p	(s)	5.50	5.50	6.17	7.56	9.16	11.41
I_t	(-)	0.50	0.24	0.19	0.16	0.14	0.13
$\hat{P}_{rel}$	(-)	0.10	0.30	0.35	0.22	0.04	0.002

Table 4.2: *The six wind speeds and corresponding sea states, relative probability of occurrence and turbulence intensity.*

where $I_{ref} = 0.14$ is the expected value of the turbulence intensity at a wind speed of 15 m/s for medium turbulence characteristics (IEC61400-1 (2006)). The turbulence intensities of the six wind speeds are stated in table 4.2.
In order to carry out fatigue analysis with only these six wind speeds the relative probability of occurrence is considered

$$\hat{P}_{i,rel} = \frac{\hat{P}_i}{\sum_{i=1}^{N=6} \hat{P}_i}. \tag{4.2}$$

The relative probability of occurrence is stated in table 4.2. Wind and sea state *2* has the largest probability of occurrence of 0.35 while the largest wind and sea state has the lowest probability of occurrence of only 0.002.

4.2 The five sea states and their propagation

In the following, the five sea states are analysed in details with focus on a comparison between the linear and nonlinear sea states at the four water depths.

The sea states are based on the five JONSWAP spectra shown in figure 4.3, as described in DNV-OS-J101 (2010). In this formulation the peak enhancement factor increases as the ratio $T_p/\sqrt{(H_s)}$ decreases. The larger the peak wave period is compared with the significant wave height the more energy is contained around the peak frequency in the spectrum.
Below the spectra in figure 4.3 the first, second and third harmonic of the sea states are indicated. The grey line indicates the structural first eigenfrequency. The third and fifth sea state's second and third harmonics, respectively, are very close to the structural eigenfrequency.
The length of the time series of the wave realizations is four hours. The distance between $h = 110\,\text{m}$ and $h = 25\,\text{m}$ in the domain is 12300 m. A wave in the wave spectra with a frequency of 0.35 Hz has a wave period of $T = 2.86$ s and a wave length of $L = 12.75\,\text{m}$. The energy in the waves travels with the group velocity which in deep water is equal to half of the wave celerity, L/T, and in shallow water equal to the wave celerity. It takes therefore 6250 s for the wave energy of the wave to move from the left boundary of the domain and to a water depth of $h = 25\,\text{m}$. The analyses of wave the realizations are therefore only based on the two last hours of the wave realizations to ensure that the energy in the shortest waves in the part of the wave spectra which also cover the structural first eigenfrequency have reached the investigations points, when the analysis begins.

4.2.1 Convergence test

A regular linear wave should in OceanWave3D be resolved with 8-10 points per wave length to get a converged solution while for a very nonlinear wave up to 30 points is necessary per wave length. However for irregular waves it has not been investigated how many grid points, N_x, that are necessary in order to achieve converged results. It is therefore investigated whether the wave realizations used in the present analysis are converged.

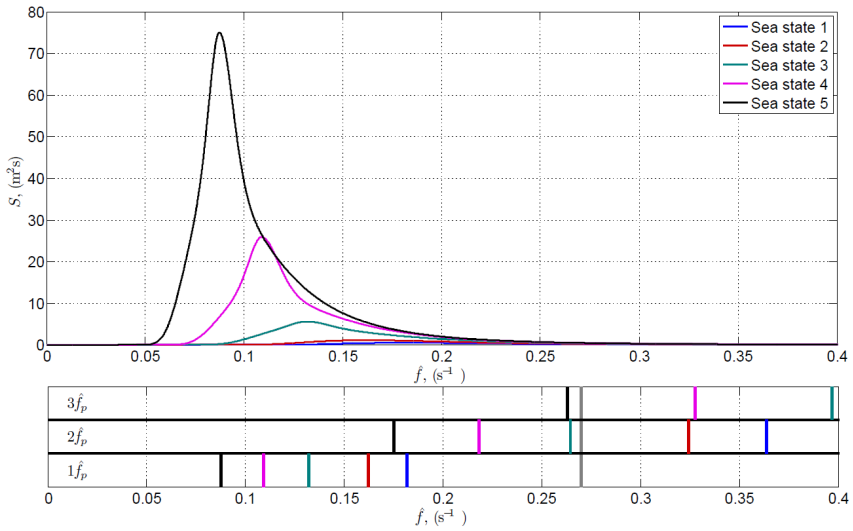

Figure 4.3: *JONSWAP spectrum of the five sea states at $h = 110\,m$. Below the figure the first, second and third harmonics of the sea states are indicated.*

The five linear and nonlinear wave realizations are calculated in the same domain. It is the smallest waves in the wave realizations that are resolved with fewest points per wave length. The smallest waves occur in the wave realization of the smallest sea state because this spectrum has energy at the highest frequencies. The convergence study is therefore done for the nonlinear wave realization of the smallest sea state with $H_s = 0.99$ and $T_p = 5.5\,\text{s}$.
Four calculations are performed with different grid spacing in the x-direction; 0.52 m, 0.78 m, 1.17 m and 1.56 m. It is the grid spacing of 0.78 m which are used in the analysis.
The spectrum of the surface elevation are shown in figure 4.4. The spectrum contains energy in the interval approximately 0.01–0.50 Hz. The energy content at 0.5 Hz is 2 % of the energy content at the peak frequency.

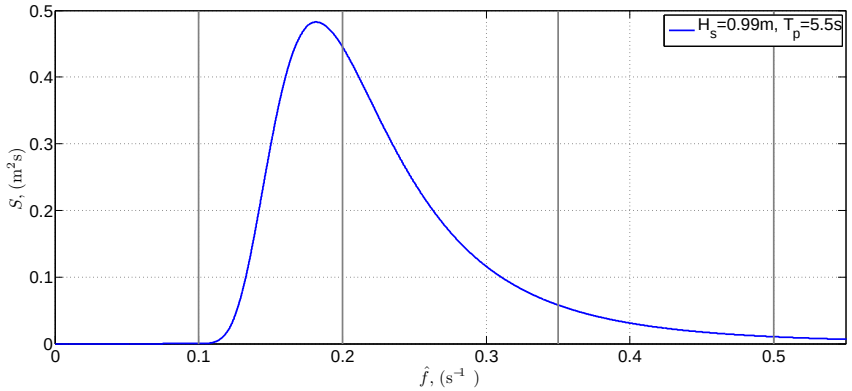

Figure 4.4: *Wave spectrum of the sea state with $H_s = 0.99\,m$ and $T_p = 5.5\,s$.*

The wave length of the four waves in the wave spectrum with different frequency and how many grid points these waves are resolved with using the four grid spacings, are stated in table 4.3. The frequencies are also indicated in figure 4.4
All four waves are resolved with enough grid points with the two smallest grid spacings, since the waves at the high frequencies are linear. The wave with $\hat{f} = 50\,\text{Hz}$ is not resolved with enough grid point with the two largest grid spacings.
The wave realizations are compared at the water depth 40 m, 35 m, 30 m and 25 m. These water depths are the same as those considered in the analysis of the sea states.
The length of the domain is 13758 m. The waves travel with the group velocity which in deep water

$\hat{f}$	L	N_x			
		$\Delta x = 0.39$m	$\Delta x = 0.78$m	$\Delta x = 1.17$m	$\Delta x = 1.56$m
0.50 Hz	6.25 m	12	8	5	4
0.35 Hz	12.7 m	24	16	10	8
0.20 Hz	38.9 m	75	50	35	25
0.10 Hz	121 m	300	200	133	100

Table 4.3: *Wave frequencies and the number of grid points per wave length with different grid spacing.*

is equal to half of the wave celerity (L/T). It takes therefore the smallest wave in the part of the spectrum which contains energy, $\hat{f} = 0.50\,\text{Hz}$, approximately 7900 s to move from the left boundary to a water depth of 25 m. The wave realizations are therefore compared between $t = 7900\,\text{s}$ and $t = 8100\,\text{s}$. The surface elevations of the four wave realizations are presented in figure 4.5 at the four water depths. The wave realizations with the three largest grid spacings are compared against the wave realization with the smallest grid spacing.
It is clear that the waves become more similar as the grid spacing decreases. Though, the wave realizations with $dx = 0.78\,\text{m}$ and $dx = 0.52\,\text{m}$ are not fully converged. Particular for the smallest waves in the time series they deviates.
To investigate how large the difference between the realization with the smallest grid spacing and the three other realizations are the absolute error, $Error_{abs}$, and the root mean square error, $Error_{rms}$, are calculated

$$Error_{i,abs} = \max(|\eta_{0.52} - \eta_i|), \quad \text{for} \quad t = 7900 - 8100s, \tag{4.3}$$

$$Error_{i,rms} = \sqrt{\frac{1}{N}\sum_{j=1}^{N}(\eta_{0.52} - \eta_i)^2}, \quad \text{for} \quad t = 7900 - 8100s. \tag{4.4}$$

Here N is the number of calculated η-values in the time sequence considered. The surface elevation with the smallest grid spacing is named $\eta_{0.52}$ and the three other surface elevations are named η_i. The errors are stated in table 4.4.

h	40 m		35 m		30 m		25 m	
Δx	$Error_{abs}$	$Error_{rms}$	$Error_{abs}$	$Error_{rms}$	$Error_{abs}$	$Error_{rms}$	$Error_{abs}$	$Error_{rms}$
0.78m	0.3630	0.1191	0.4769	0.1196	0.3656	0.1410	0.2456	0.0860
1.17m	0.6798	0.2081	0.5268	0.2142	0.6438	0.2302	0.5877	0.1860
1.56m	0.7016	0.2466	0.7455	0.2442	0.8062	0.2757	0.6014	0.2451

Table 4.4: *The error of the wave realizations with the three largest grid spacings relative to the wave realization with the smallest grid spacing.*

The error is smaller the smaller the grid spacing is. The root mean square error is more than halved when a grid spacing of 0.78 m is used compared to a grid spacing with 1.56 m, but the difference between $dx = 0.78\,\text{m}$ and $dx = 0.52\,\text{m}$ are still significant, even though the waves in the wave realization should be resolved with enough grid points. The reason for the difference can instead be found in the number of grid points in the vertical direction. 9 grid points is most often enough to get a converged solution as long as the wave number is below approximately $kh \sim 15$. However, for the present sea states the shortest waves in the spectra with frequencies between 0.45-0.50 Hz have wave numbers between $kh = 80$ to $kh = 110$ at $h = 110\,m$. For these short waves it is necessary with more points in the vertical direction to describe them properly. It is therefore investigated how many points that are necessary in the vertical direction to describe such a wave.
A linear regular wave with $H = 0.99\,\text{m}$ and $T = 2.22\,\text{s}$ is considered at $h = 110\,\text{m}$ which gives $kh = 80$. The wave is calculated with different grid spacing in the vertical and horizontal direction. The wave realizations are considered 15 m from the generation zone and it is ensured that potential reflection from the boundaries not has reached this point, when the wave realizations are analysed.

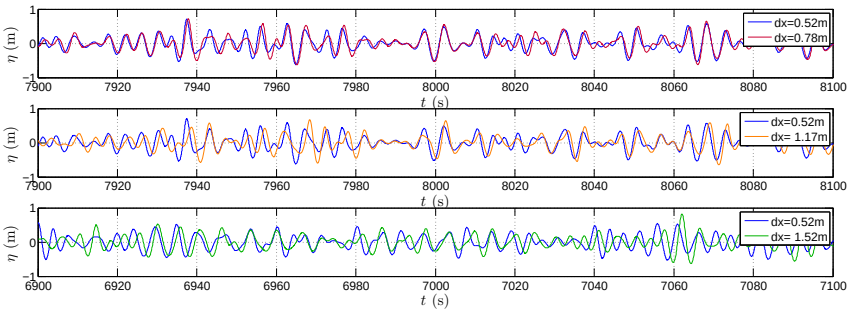

(a) η at $h = 40$ m.

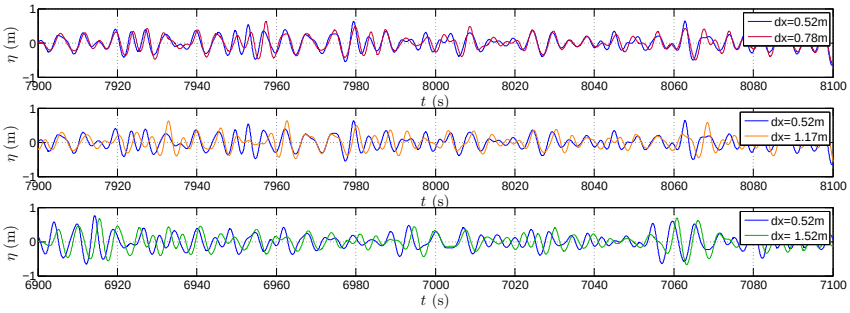

(b) η at $h = 35$ m.

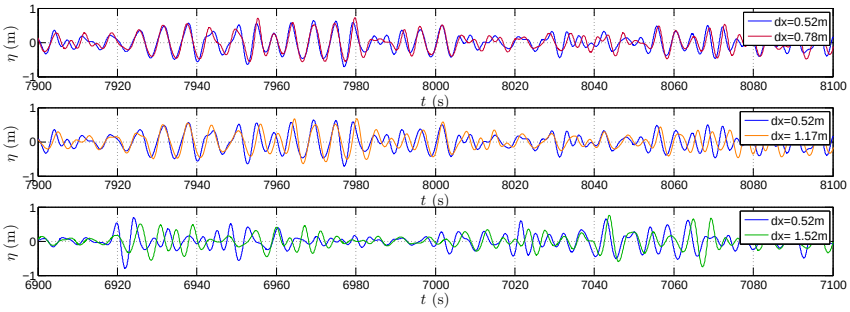

(c) η at $h = 30$ m.

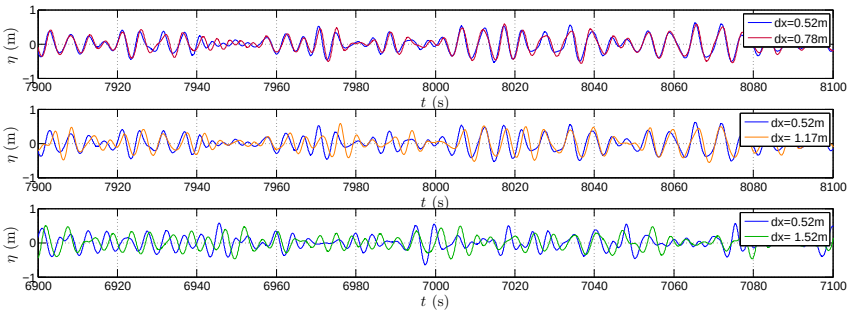

(d) η at $h = 25$ m.

Figure 4.5: *The surface elevation with different grid spacing of the small sea state.*

The amplitude of the wave realizations is calculated by considering the value of the wave spectrum at the frequency $\hat{f} = \frac{1}{T} = 0.45$ Hz based on five wave periods. Figure 4.6 shows the relative error between the calculated amplitude, $\hat{a}$, and the correct amplitude $H/2$ for different number of grid points in the vertical direction N_z and for different grid spacing dx. From $dx = 1.52\,\text{m}$ to $dx = 0.72\,\text{m}$ the rate of convergence is of $\text{O}(\Delta x^6)$. Here after the error is more or less constant for the different N_z-values. A grid spacing of $dx = 0.72\,\text{m}$ in the vertical direction seem therefore to be small enough to get a converged solution.
In the vertical direction the error is 100 % with $N_z = 9$ and $dx = 0.72\,\text{m}$, for $N_z > 13$ the error is less than 1 % and for $N_z = 25$ the error is 0.05 %. In the generation zone the relative error of the wave amplitude, just before the waves starts to be released, is 0.001. It can therefore not be expected that the error inside the domain is smaller than this.
Following the results in figure 4.6 the number of grid points in the vertical direction should be larger than approximately 15 for the smallest waves in the wave realization to be converged. As the number of grid points increases the computational time also increases. It is therefore always a balance in numerical calculations how accurate the calculations should be relative to computational time. With $N_z = 15$ it will take approximately 5 weeks to calculate a 4 hour long wave realization of the largest sea state considered in the analyses. This is still considered to be an acceptable computational time for the analysis here.
The wave with $H = 0.99\,\text{s}$ and $T = 2.22\,\text{s}$ is also calculated on a flat bed with $h = 25\,\text{m}$, to ensure that the wave also is converged in the shallow part of the domain when $dx = 0.72\,\text{m}$ and $N_z = 15$. Since $kh = 20$ at this depth, the number of grid points vertical should be enough. Only the size of the grid spacing is therefore investigated. Figure 4.7 shows the error in the amplitude for different dx-values. From $dx = 1.53\,\text{m}$ to $dx = 0.72\,\text{m}$ the rate of convergence is again of $\text{O}(\Delta x^6)$. For smaller grid spacings the error is close to be constant and smaller than 0.1 %. The error is therefore smaller at shallow water where the value of kh is smaller.
Finally a nonlinear stream function wave is considered to ensure that the largest waves in the wave realization of the sea state also is converged. Following DNV-OS-J101 (2010) the maximum wave height in a wave realization can be calculated from H_s and the number of waves N in the time series

$$H_{max} = \sqrt{\frac{1}{2}\ln(N)}H_s. \tag{4.5}$$

For a two hours time series with $T = 5.5\,\text{s}$ the number of waves is $N \sim 1300\,\text{s}$. The significant wave height in the sea state is $H_s = 0.99\,\text{m}$ which gives $H_{max} = 1.86\,\text{m}$. The wave period of the maximum wave is $T = 6.22\,\text{s}$ and is calculated from the definition of DNV-OS-J101 (2010)

$$11.1\sqrt{\frac{H_s V}{g}} \leq T \leq 14.3\sqrt{\frac{H_s V}{g}}. \tag{4.6}$$

The stream function wave is calculated in the domain where the wave realizations of the five sea states also are calculated with three different grid spacings, $dx = 1.04\,\text{m}$, $dx = 0.72\,\text{m}$ and $dx = 0.52\,\text{m}$.
The stream function wave is considered after approximately two hours, where the analysis of the sea states also begins. In figure 4.8 the surface elevations are shown in the top picture for 1700 s to show that the wave height for all three waves do not vary over time. The difference between the wave height of the wave realization with $dx = 1.04\,\text{m}$ and $dx = 0.52\,\text{m}$ is 0.11 % and the difference between the wave height of the wave with $dx = 0.78\,\text{m}$ and $dx = 0.52\,\text{m}$ is 0.03 %. In the bottom picture a few wave periods of the wave realizations are compared. It is seen that the phase of the wave with the largest grid spacing is wrong, while the surface elevation of the two other grid spacings are similar with a difference in the phase of ~ 0.8 %.
From the above analysis it is shown that with a grid spacing of $dx = 0.72\,\text{m}$ in the horizontal direction and with 15 grid points in the vertical direction both the smallest and largest waves in the wave spectrum are resolved with enough points to get an converged solution.
If the same analysis as above is done with $dx = 0.72\,\text{m}$ and $N_z = 9$ for a wave with a frequency of $\hat{f} = 0.35\,\text{Hz}$ and $kh = 54$ the relative error is ~ 8 % and for a wave with $\hat{f} = 0.25\,\text{Hz}$ and $kh = 27$ the relative error is ~ 3 %. In the present calculations the waves in the wave spectra with

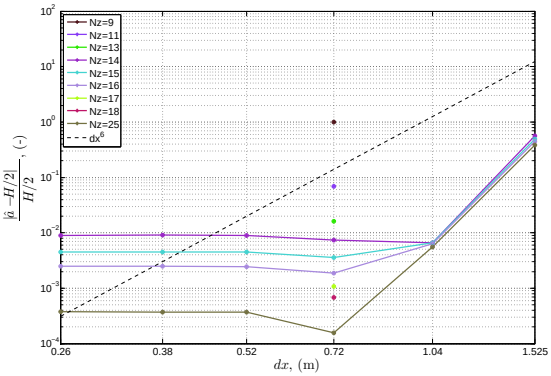

Figure 4.6: *The relative error for different number of grid points in the vertical direction N_z and for different grid spacing dx at a water depth of $h = 110\,m$.*

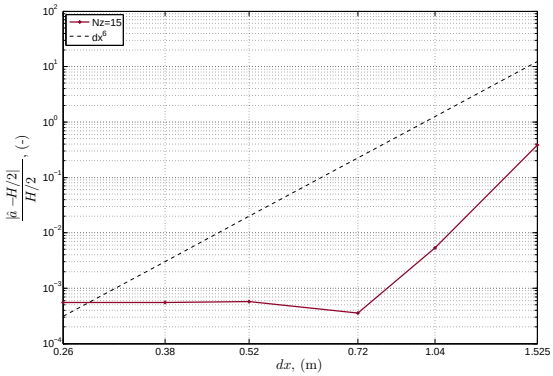

Figure 4.7: *The relative error for different grid spacings dx and $N_z = 15$ at a water depth of $h = 25\,m$.*

frequencies around the structural first eigenfrequency of $\hat{f}_p = 0.27\,\text{Hz}$ are therefore not resolved with enough grid point, but the error is smaller than for the wave with $\hat{f} = 0.50\,\text{Hz}$ which was considered in the analysis above. This means that the smallest waves in the wave realizations which are used in the following analysis are not described properly and that more grid points in the vertical direction should have been used in the calculations. For the static analysis this is not expected to be important because the waves in the part of the wave spectra with most energy is resolved with enough points, but in the dynamic analysis it can be important. It is expected that it will influence the broad band forcing, which must be smaller due to the lack of convergence. How it otherwise will influence the results is difficult to say, but errors exist both for the linear and nonlinear calculations. This is an uncertainty in the calculations which has to be remembered through the analysis and when the results are discussed.

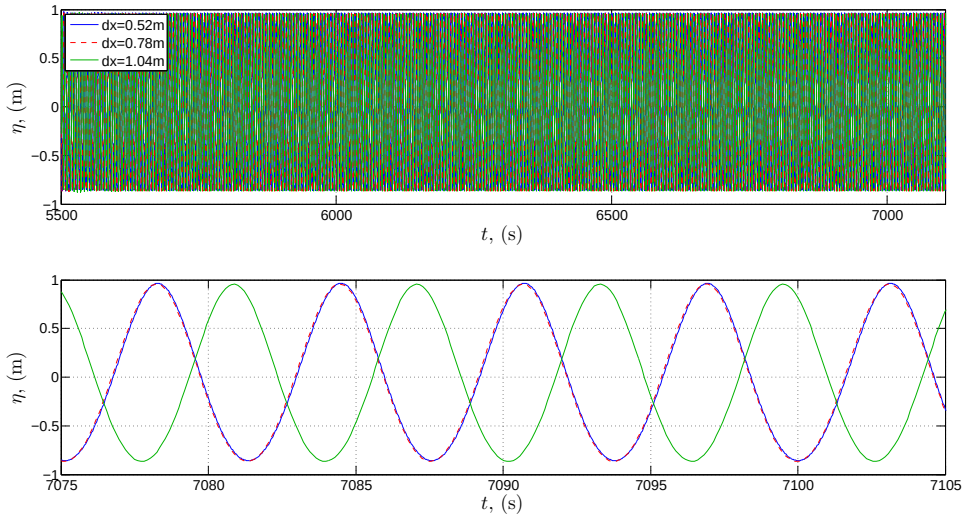

Figure 4.8: *Comparison of a stream function wave with $T = 6.22\,s$ and $H = 1.86\,m$ and different grid spacings, dx, at a water depth of $h = 25\,m$ after the waves have moved up the sloping sea bed shown in figure 4.1.*

4.2.2 Wave breaking

Although the breaking filter was applied, a few events in the two largest nonlinear wave realizations were identified as unrealistically large. By a closer analysis it was found that the vertical particle

acceleration, $\frac{dw}{dt}$, exceeded $-1g$. This indicates that the time scale of the dissipating breaking filter has been too small to limit the wave height and accelerations. These large steep waves will give unrealistically large forces and contribute unrealistic to the fatigue damage. The surface elevation and wave kinematics at these particular wave events were therefore dampened by adding a damping function (inverse cosh–function) to the results for η, u, a, w_z and η_x. This process was repeated until the particle acceleration was smaller than $1g$.
An example is shown in figure 4.9 where the nonlinear wave realization of the fourth sea state is considered at a time where $\frac{dw}{dt}$ is too large. The wave is therefore dampened in the time sequence $t \sim 11990 - 11992\,\text{s}$. The figure shows the surface elevation, the vertical particle acceleration and the horizontal particle velocity and acceleration before and after damping was considered. The surface elevation has a very narrow steep crest value before the damping, which gives some small oscillations in the particle accelerations. After the damping, the surface elevation and kinematics have smaller peak-values but are also more smooth and will thereby give more realistic contributions to the fatigue damage.
The damping is applied to 25 waves for the largest sea state at the four water depths and to nine waves for the fourth sea state.

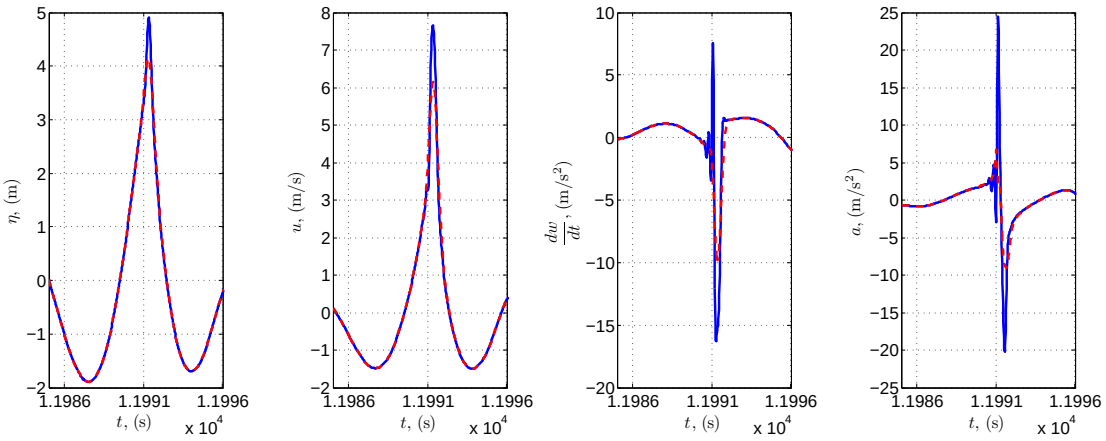

Figure 4.9: *surface elevation, the vertical particle acceleration and the horizontal particle velocity and acceleration. — before damping – – after damping.*

While this is a very non-physically approach to the problem it provides a simple solution. Actually there is no proven "correct" way of limiting the near-breaking waves from a potential flow solver. This extension of the flow models validity requires a calibrated damping and load model and is an area where further research is needed. As an example Marino *et al.* (2011) enhanced linear wave load calculations with intermittent application of the breaking wave load model of Wienke & Oumeraci (2005).

4.2.3 Comparison of linear and nonlinear wave realizations

The linear and nonlinear wave realizations of each sea states are generated by the same time series at the generation boundary. However the linear and nonlinear wave transformation are different and the significant wave heights are therefore not the same at the water depths where the wave realizations are studied. For a practically application the loads would always be based on a local value of the significant wave height. It was therefore decided to scale the results of the linear computation by multiplying the ratio between the nonlinear and linear significant wave heights at the water depths considered onto the linear wave elevations and kinematics. It should be noted that this is fully consistent with the linear nature of the solution. To compensate for the over prediction of the particle velocities above the mean water level of linear theory, Wheeler stretching is used in order to stretch the irregular linear wave kinematics from the mean water level and up to the real surface elevation. Although Wheeler stretching is only an alternative linear approximation for the velocity field, it is widely considered to give a more realistic description of the wave kinematics

between the still mean water level and the surface elevation. IEC61400-3 (2009) recommend among others Wheeler stretching to take account for varying height of the water surface.

Figure 4.10 shows the linear and nonlinear time series of the fifth sea state at a water depth of 30 m. The black line indicates at what time the analysis of the sea states begins. The wave groups of the nonlinear and linear sea state occur at approximately the same times, but besides this it is difficult to see a similarity between the two wave realizations in spite that they are based on the same time series at the generation boundary.

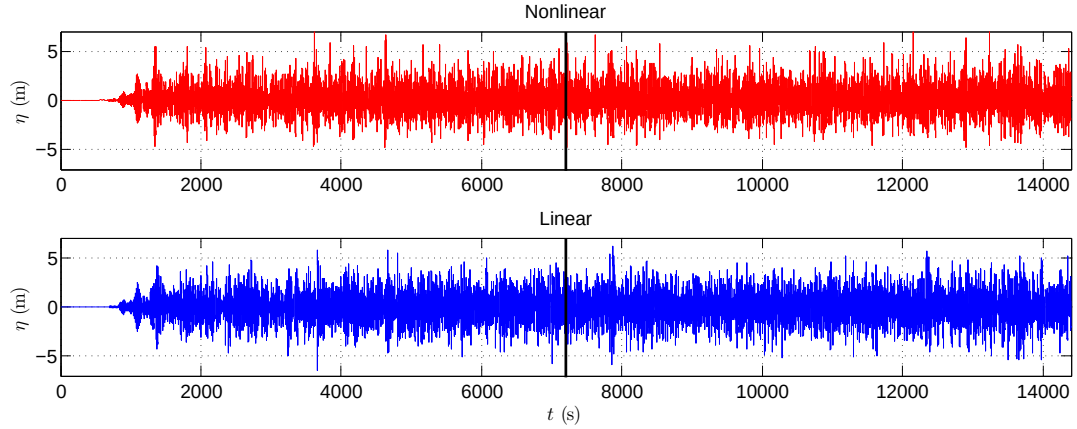

Figure 4.10: *The linear and nonlinear time series of the fifth sea state at a water depth of 30 m.*

The peak wave period and significant wave height of the five sea states at the four water depths investigated are stated in table 4.5. All five wave heights become smaller as the water depth decreases. This means that the sea states are in the part of the transformation from deep to shallow water where the wave height decreases before it begins to shoal and increase rapidly.

T_p (s)		5.50	6.17	7.56	9.16	11.41
H_s (m)	$h = 40\,\mathrm{m}$	0.93	1.36	2.48	4.11	6.29
	$h = 35\,\mathrm{m}$	0.93	1.36	2.46	4.08	6.27
	$h = 30\,\mathrm{m}$	0.92	1.36	2.44	4.04	6.28
	$h = 25\,\mathrm{m}$	0.92	1.34	2.41	4.01	6.26

Table 4.5: *The five sea state peak period and significant wave height values at the four water depths.*

Figure 4.11 shows the linear shoaling curve from deep to shallow water based on linear regular waves; At first the relative wave height decays to a minimum of 0.913, which is obtained for $k_0h = 1$, where the group velocity has its maximum. From there on the wave height rapidly increases for decreasing k_0h. The indices "0" indicates that it is the parameter at deep water, $kh > \pi$, where linear wave theory is valid. The shoaling of the sea states, which is based on H_s and T_p, is also shown in figure 4.11. Some deviation is seen relating to the linear regular shoaling. The two smallest sea states have a much larger reduction in the wave height at all water depths. The third and fourth sea state follow the linear shoaling curve quite well. The wave height of the fifth sea state decreases with decreasing wave height despite that the linear regular shoaling curve have started to increase again. The comparison shows that irregular and regular wave shoaling is uncomparable but also that the first and second wave realizations are at relative much deeper water, $k_0h > \pi$, than the other wave realizations. Further it is seen that the third and fourth sea state have the largest decrease in significant wave height.

The more nonlinear the waves in the wave realizations are the more steep the waves can be and the more energy has been relocated to higher and lower frequencies in the wave spectrum. Figure 4.12, from DNV-OS-J101 (2010), shows the relation between $\frac{h}{gT^2}$ and $\frac{H}{gT^2}$ for regular waves. The more to the left and the top of the figure the waves are placed, the more nonlinear they are. The

sea states position in the figure are based on H_s and T_p. All five sea states are in the limit between linear and nonlinear wave theory, but non of the sea states are described accurately by linear wave theory. The sea states become more nonlinear as T_p increases and the water depth decreases. From the figure it can therefore be expected that the difference between the linear and nonlinear wave realizations will increase with increasing T_p and decreasing water depth.
According to the theory the maximum wave height is for two hour times series 1.80-1.90 times the significant wave height, cf. Sumer & Fredsøe (2006). These values are below the breaking wave-curve in figure 4.12 for all sea states, even though the wave realizations of the fourth and fifth sea state during the calculations experience unrealistic steep waves, which were treated as wave breaking.

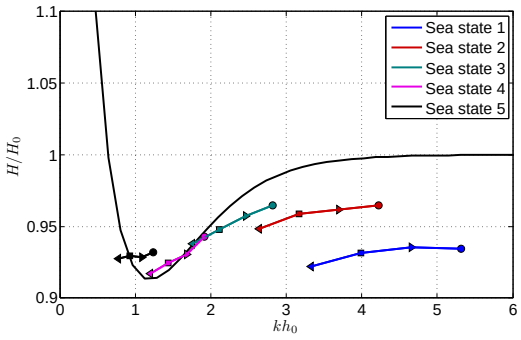

Figure 4.11: *The linear shoaling curve and the corresponding shoaling for the five sea states based on H_s and T_p at the four water depths: ∘ $h = 40\,m$, ▷ $h = 35\,m$, □ $h = 30\,m$, ◁ $h = 25\,m$.*

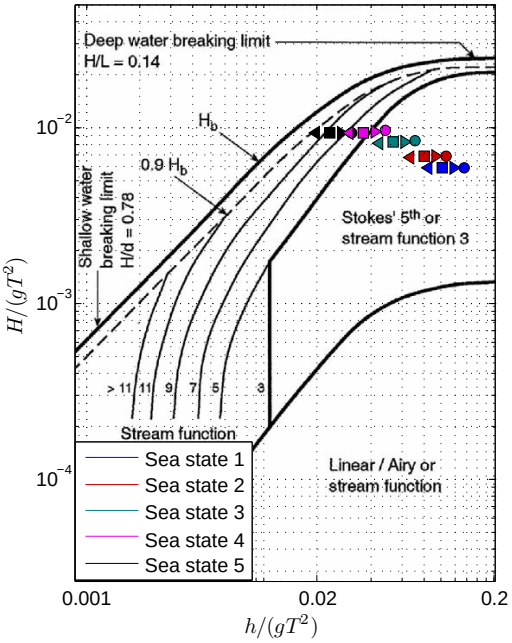

Figure 4.12: *The five sea states wave non-linearity at the four depths: ∘ $h = 40\,m$, ▷ $h = 35\,m$, □ $h = 30\,m$, ◁ $h = 25\,m$. The figure is from DNV-OS-J101 (2010).*

One way to compare the difference between the linear and nonlinear wave realizations is through the spectrum of the surface elevation.
The spectrum of the surface elevation of the first, third and fifth sea state are shown in figure 4.13 at a water depth of 30 m. The spectra at the other depths are similar.
The spectrum are calculated by dividing the surface elevations in 12 intervals of 600 s. The raw spectrum for each 600s episode was first smoothed by computing the running mean value along a 7 point moving stencil. The spectrum in the figures are the average of the 12 smoothen spectra. This is done to get a more smooth spectrum, the scattering would otherwise be very large, and it would be difficult to compare the linear and nonlinear spectrum. The spectra are amplitude spectra, so that it is easier to see the difference between the linear and nonlinear spectra at the frequencies with little energy. For all three sea states the total energy in the linear and nonlinear spectrum are the same. The differences in the spectra are therefore because the spectral energy in the nonlinear spectra has been relocated.
For the first sea state, figure 4.13a, the linear and nonlinear spectrum are quite similar but the nonlinear spectrum contains more energy at frequencies larger than 0.35 Hz. This energy must come from the peak of the spectrum. Same observations are done for the linear and nonlinear wave spectra of the second sea state.
The second harmonic of the third sea state are close to the structural first eigenfrequency of the

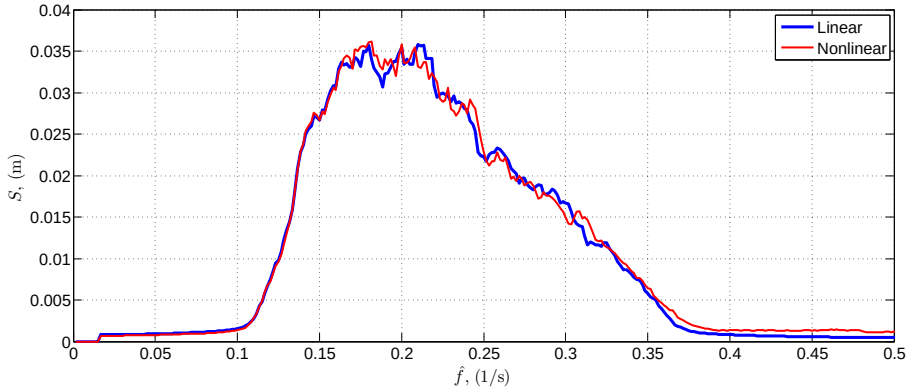

(a) The first sea state.

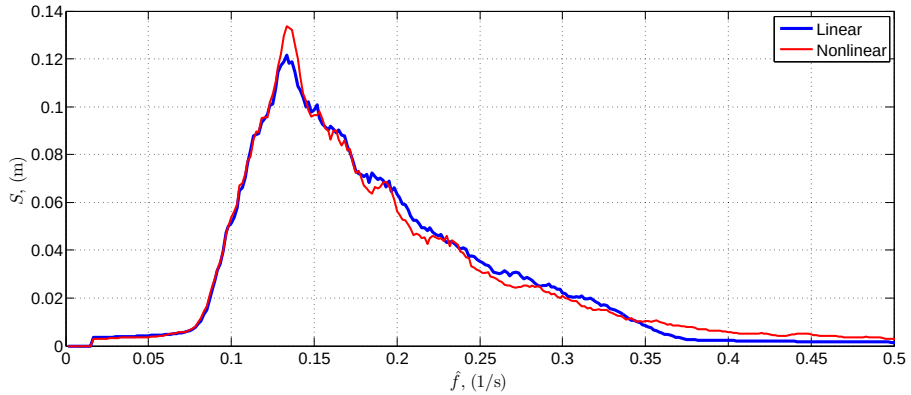

(b) The third sea state.

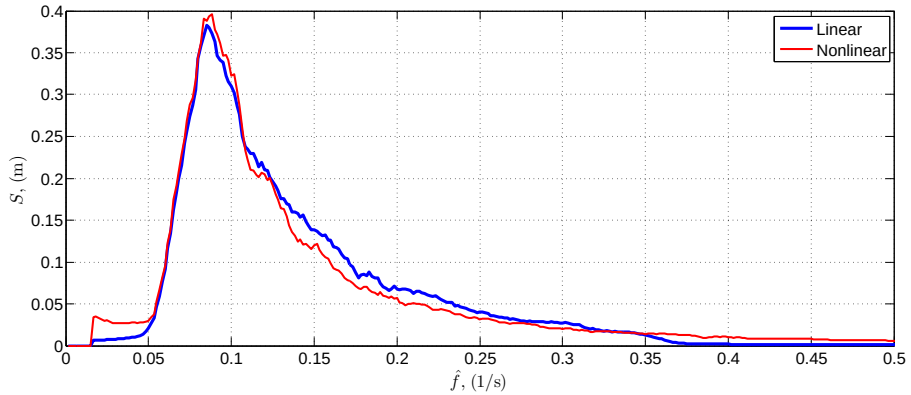

(c) The fifth sea state.

Figure 4.13: *Amplitude spectrum of the linear and nonlinear surface elevation at a water depth of 30 m.*

structure. However, it is not possible to identify the second harmonic in the nonlinear spectrum in figure 4.13b. Quite the reverse it is seen that the linear spectrum contains more energy at the frequencies between 0.18-0.34 Hz. At the peak frequency the nonlinear spectrum contains most energy. The energy which the nonlinear spectrum contains at frequencies larger than 0.35 Hz must therefore come from the part of spectrum between 0.18-0.34 Hz.
The observations from the third sea states are also seen for the forth and fifth sea state. Only the spectrum of the fifth sea state are repeated in figure 4.13c. The linear spectrum contains most energy between 0.12-0.34 Hz, while the nonlinear spectrum contains energy at both smaller and larger frequencies out side the range of the linear spectrum.
It therefore seems as the spectral energy that is moved to lower and higher frequencies in the nonlinear spectrum are taken from the high frequency part of the spectrum. It was expected that the spectral energy which is distributed would have been taken more from the peak of the spectrum. The wave breaking of the nonlinear waves could also influence that the nonlinear spectrum has less energy between 0.12-0.34 Hz. The wave breaking filter is a very simple filter, and it can not be controlled from which frequencies in the spectrum the energy is reduced.
This means that it actually is the linear spectra, which has most energy around the structural first eigenfrequency. To see higher harmonics in the wave spectra of the nonlinear waves realizations the waves therefore have to be more nonlinear.

Another way to compare the difference between the linear and nonlinear wave realizations is through the wave skewness. The larger the skewness is the shorter and more peaked the crest of the surface elevation is while the trough becomes wider and flatter.
The skewness is found to be close to zero for all the linear sea states while the nonlinear sea states all are skewed, as stated in table 4.6. For inertia-dominated structures as here, the Morison force depends on the particle acceleration and becomes therefore larger the more steep the waves are. The moment arm depends at the same time on the crest value and the overturning moment becomes therefore larger, the larger the crest value is. The difference in the skewness indicates therefore an important difference between the linear and nonlinear wave realizations

	Linear					Nonlinear				
h/Case	1	2	3	4	5	1	2	3	4	5
40 m	-0.02	0.00	-0.00	-0.00	-0.00	0.10	0.12	0.11	0.15	0.20
35 m	-0.02	0.01	0.01	-0.03	-0.02	0.10	0.10	0.16	0.13	0.18
30 m	-0.02	-0.03	0.01	0.00	-0.01	0.10	0.12	0.15	0.18	0.18
25 m	0.02	0.03	0.00	0.01	0.00	0.10	0.13	0.12	0.14	0.23

Table 4.6: *The five sea states wave skewness at all four depths.*

In table 4.6 it is further seen that the skewness increases in general with increasing sea state but it is difficult to see any trend or find any relationship in table 4.6 between the change in water depth and skewness. The wave realization of the smallest sea states has the same skewness at all four depths while the skewness of the wave realizations of the other four sea states varies in different ways. The skewness for the third and fourth sea states' wave realizations are smaller at $h = 25\,\mathrm{m}$ compared with some of the other depths, while the opposite is seen for the second and fifth wave realization.

4.2.4 Summary

In the above analysis the five sea states have been analysed. First a convergence test of the wave realizations showed that the waves are not fully converged. This is due to the number of grid points in the vertical direction which is too small. The missing convergence means that waves with frequencies around the structural first eigenfrequencies have errors of 3-8 %. This apply for both the linear and nonlinear waves. This can influence the broad band forcing which probably becomes smaller.
In spite of the wave breaking filter some large unrealistic steep wave events occurred in the two largest nonlinear wave realizations. These waves were therefore dampened to avoid unrealistic large forces.

In the comparison of the linear and nonlinear wave realizations, it was found that the wave transformation is different, and the linear wave realizations were therefore scaled to fit the significant wave heights of the nonlinear wave realizations. All five wave realizations are based on the significant wave height and peak wave period nonlinear. The skewness was found to be zero for the linear wave realization and non-zero for the nonlinear wave realizations and increases in general as the significant wave height increases. The skewness changes as the water depth changes, however no clear trend indicating that the skewness becomes larger as the water depth decreases is found. Finally, it was found that the spectrum of the surface elevation differs between the linear and nonlinear wave realizations, however not as expected. Instead of seeing higher harmonics in the nonlinear spectra the linear spectra of the three largest sea states contain most spectral energy close to the structural first eigenfrequency. The sea states have to be more nonlinear in order to see the higher harmonics in the wave spectra.

4.3 Morison force on fixed monopile

In the first part of the section a fixed monopile is considered and the forcing from the waves calculated by Morison's equation, (3.40) and (3.41). The diameter of the piles at the four water depths are the same as given in table 4.1. The analysis are interesting because they are independent of the structure and would represent a typical load-input to an arbitrary structural model. The difference between the linear and nonlinear wave forcing are therefore easy to compare.
In second part of the thesis two nonlinear irregular waves are compared to corresponding stream function waves.

4.3.1 Probability plots

In order to compare the sea states, the empirical probability of exceedance of surface elevation, η, inline force, F, and overturning moment, M, are calculated. In the time series the largest positive peak value between two zero down-crossings is found and sorted in increasing order. The probability of exceedance is then calculated as

$$P(X_i) = 1 - \frac{i}{N}, \tag{4.7}$$

where X_i is the i'th η,– F– or M-peak value sorted in increasing order and N is the number of peaks.
Figure 4.14-4.16 shows the probability of exceedance of the positive peaks of the surface elevation, inline force and overturning moment.
In order to compare the probability of exceedance, the data are fitted with probability distributions. The probability of exceedance of the surface elevation are fitted with the Rayleigh distribution, which is valid for linear narrow-banded spectra, while the force and moment are fitted with the Weibull distribution. The linear distributions are shown with a full line in the figures and the nonlinear distributions are shown with dashed lines in the figures. The extreme data (data which has a probability of exceedance smaller than 0.02) are compared with the Gumbel distribution. The Gumbel distribution is used as a model for values which are maxima of a large number of independent variables (WAFO-Tutorial (2011)). The Gumbel distributions are shown as dash/dotted lines in the figures.
The Rayleigh and Weibull distribution appear to represent the data well for probabilities larger than 0.1 while the extreme data are represented well by the Gumbel distribution.
In general the peak values for both the linear and nonlinear realizations in figure 4.14-4.16 increase with increasing sea state and the nonlinear peaks are larger than the linear peaks at the same probability of exceedance. The largest peaks of the force and moment reduce with decreasing water depth because the part of the monopile which is affected by the wave forcing reduces.
Figure 4.17 shows the relation between the linear and nonlinear quantiles at a probability of exceedance of 0.4 and 0.01 as function of the water depth. The 0.4-quantile is based on the Rayleigh/Weibull distributions while the 0.01-quantile is based on the Gumbel distribution

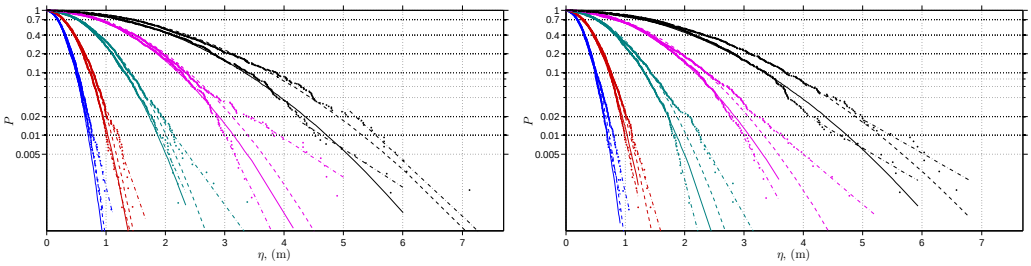

(a) $h = 40$ m. **(b)** $h = 35$ m.

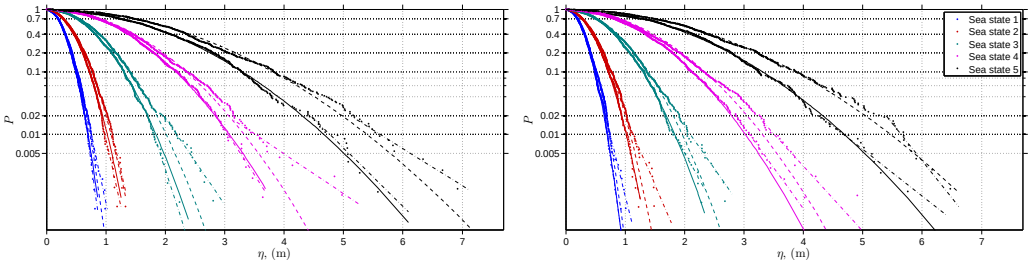

(c) $h = 30$ m. **(d)** $h = 25$ m.

Figure 4.14: *The probability of exceedance of the positive crest surface elevation. ·· Raw data, — Rayleigh distribution for linear peaks, – – Rayleigh distribution for nonlinear peaks, –·– Gumbel distribution for both linear and nonlinear peaks.*

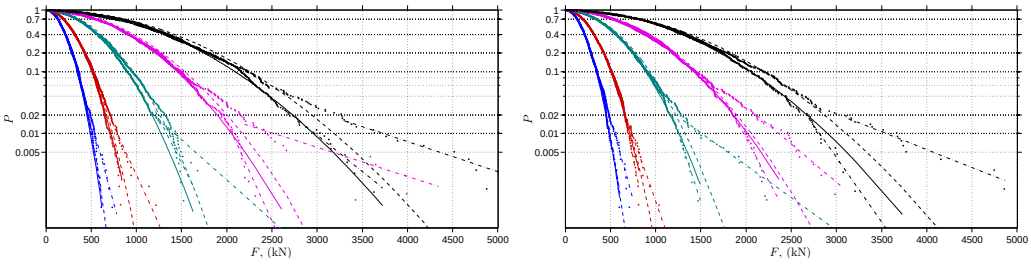

(a) $h = 40$ m. **(b)** $h = 35$ m.

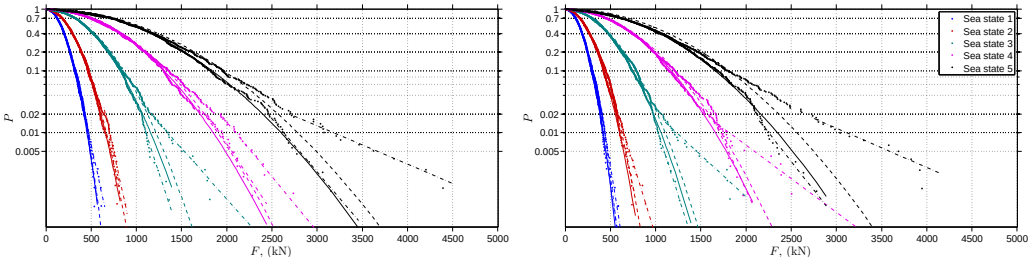

(c) $h = 30$ m. **(d)** $h = 25$ m.

Figure 4.15: *The probability of exceedance of the positive peak forces. ·· Raw data, — Weibull distribution for linear peaks, – – Weibull distribution for nonlinear peaks, –·– Gumbel distribution for both linear and nonlinear peaks.*

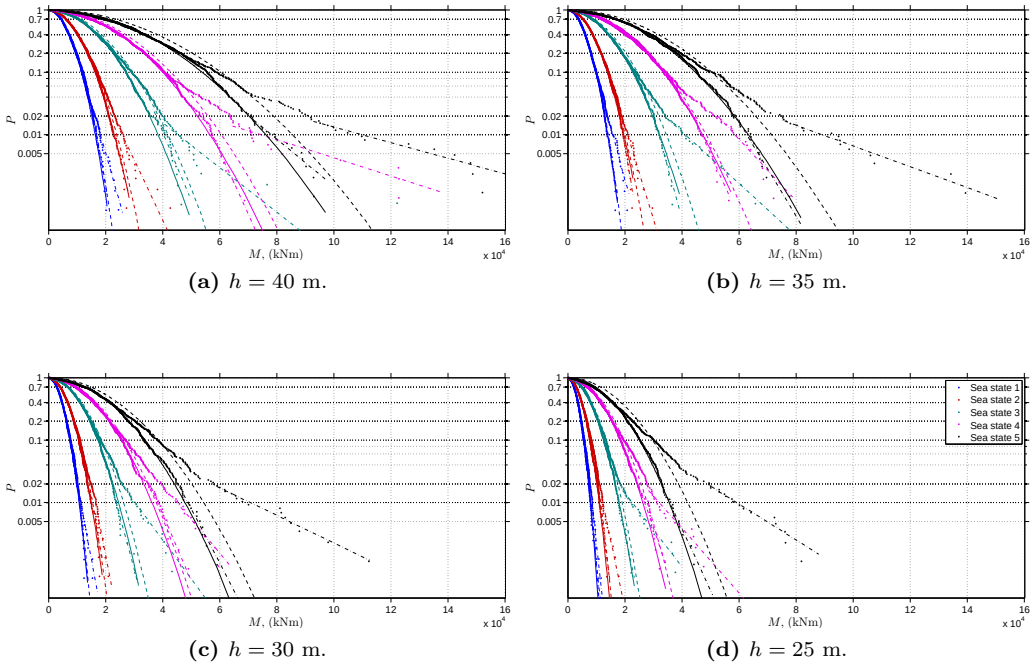

(a) $h = 40$ m. **(b)** $h = 35$ m.

(c) $h = 30$ m. **(d)** $h = 25$ m.

Figure 4.16: *The probability of exceedance of the positive peak moments. ·· Raw data, — Weibull distribution for linear peaks, – – Weibull distribution for nonlinear peaks, –·– Gumbel distribution for both linear and nonlinear peaks.*

The nonlinear quantiles are larger than the linear quantiles, which means that the nonlinear sea states result in the largest surface elevation, inline force and overturning moment both at the smaller and extreme probability of exceedance. This result confirms the expectations that the nonlinearity of the waves are important when large single events are considered.

The difference is largest for the 0.01-quantile which means that the nonlinearity is strongest for the extreme values of η, F and M. It is however interesting that there also is a significant difference between the linear and nonlinear values for the 0.4-quantile - also for the smallest sea states.

The difference between the linear and nonlinear quantiles of η, F and M increase in general as the sea states increase. This is observed for both the 0.4 and 0.01 quantile. However, for the second, third and fourth sea state there is some variation. At some depths the difference is largest for the fourth sea state and at other depths the difference is largest for one of the other two sea states.

If the 0.4 quantile is considered there is no clear change in the differences from water depth to water depth. The difference in the force are a little smaller than the difference in the surface elevation. The smaller difference is perhaps because the linear and nonlinear force profiles below the mean water level are similar and contribute more than the force profile above the mean water level for these small waves in the wave realizations. The largest differences are seen for the moment in particular for the largest sea state where the difference is doubled compared to the difference in the force. The increase in the moment must be because the nonlinear sea states have higher crest values that lead to larger moment arms.

For the 0.01 quantiles the difference in η, F and M deviates more from water depth to water depth. A clear trend is most obvious in the force and moment of the fifth sea state where the difference in general increases as the water depth decreases. The differences in the force are unlike the 0.4 quantile in general larger than the differences in the surface elevation. The larger difference must be because the wave crests of the nonlinear surface elevations are significant steeper, such that the force above the mean water level also becomes important. The largest differences are as in the 0.4 quantile found for the moments, again due to the larger moments arms in the nonlinear wave realizations.

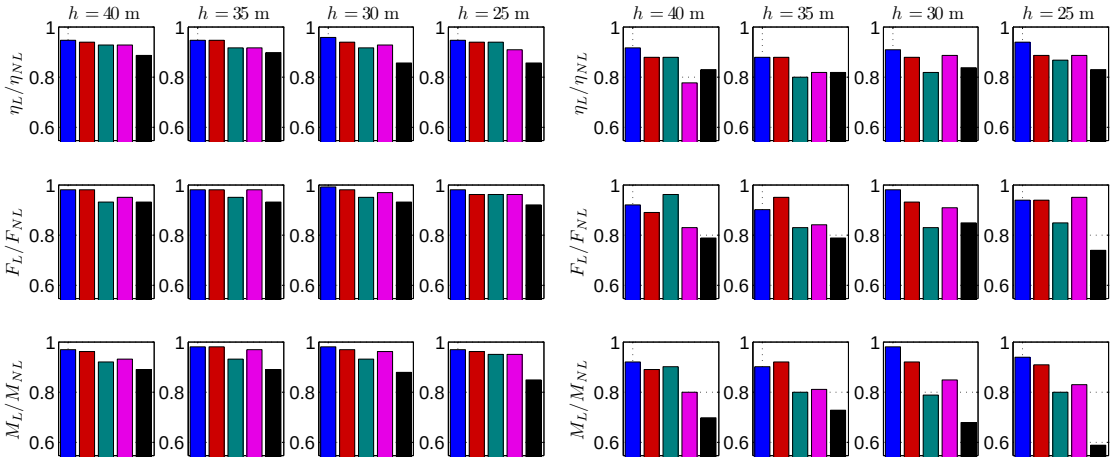

(a) 0.4-quantile. **(b)** 0.01-quantile.

Figure 4.17: *The difference between the linear and nonlinear peaks of the surface elevation, inline force and overturning moment at the probability of exceedance of 0.4 and 0.01.* *1* *2* *3* *4* *5*

4.3.2 Comparison between nonlinear irregular waves and stream function theory

The standards (eg. DNV-OS-J101 (2010)) require that stream function waves are used in the ultimate limit state (ULS). Based on the above analysis it is therefore interesting to compare fully nonlinear irregular waves with corresponding waves based on stream function theory.

The irregular waves are selected from the time series of nonlinear wave realization of the fifth sea state at a water depth of 30 m. The stream function waves are calculated with basis in the wave height and wave period for the selected irregular waves.

The two selected waves have a wave height- and period of $H = 6.53\,\text{m}$, $T = 10.85\,\text{s}$ and $H = 8.28\,\text{m}$, $T = 8.78\,\text{s}$, respectively. The crest of the waves have a maximum value of 3.7 m and 5.0 m and have therefore, according to figure 4.14c, a probability of exceedance of approximately 0.25 and 0.03, respectively.

The irregular surface elevation and corresponding stream function surface elevation are compared in figure 4.18. The irregular waves have a more narrow crest value than the corresponding stream function waves, particularly for the larger wave. The irregular waves are further lifted upwards vertically relative to the stream function waves. The irregular large wave looks rather steep but the slope of the surface elevation is not more than 22^o and the ratio $H/L = 0.07$. Waves are not said to break before $H/L \sim 0.16$, c.f Sumer & Fredsøe (2002). In the figure it is also indicated with a dashed line at what time the inline force of the different waves are largest. The stream function waves have the largest force close to when $\eta = 0\,\text{m}$, i.e. when the acceleration of the wave is largest. The irregular waves have the largest force closer to when η is largest, because the irregular waves are asymmetric around the peak value and therefore more steep closer to the peak-value, where the acceleration is largest.

The inline forces are shown in figure 4.19. The forces due to the smaller wave are quite similar while the forces due to the larger wave deviates. The force due to the irregular wave has a much stepper front than that due to the stream function wave because of the more narrow crest.

In figure 4.20 the corresponding force profiles are compared. The force profile due to the irregular waves and stream function waves are very different. The forces from the irregular waves are larger towards the top of the crest, because the wave is steeper resulting in a larger particle acceleration. Closer to the sea bed the stream function waves result in the largest distributed force. The difference between the irregular- and stream function wave is most pronounced for the larger wave. The differences in the force profiles result in different inline force and overturning moment, which

are stated in table 4.7. For the smaller wave the inline force and overturning moment are very similar, while the inline force due to the larger irregular wave is 40 % larger and the overturning moment twice as large at the inline force and the overturning moment due to the corresponding stream function wave.

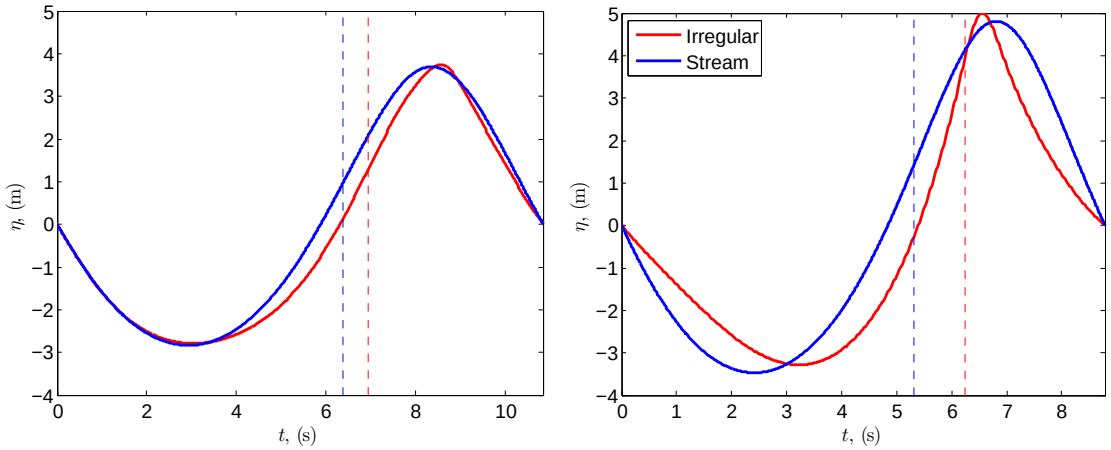

(a) $H = 6.53\,\text{m}$ and $T = 10.85\,\text{s}$. **(b)** $H = 8.28\,\text{m}$ and $T = 8.78\,\text{s}$.

Figure 4.18: *The nonlinear irregular wave compared with the corresponding stream function wave.*

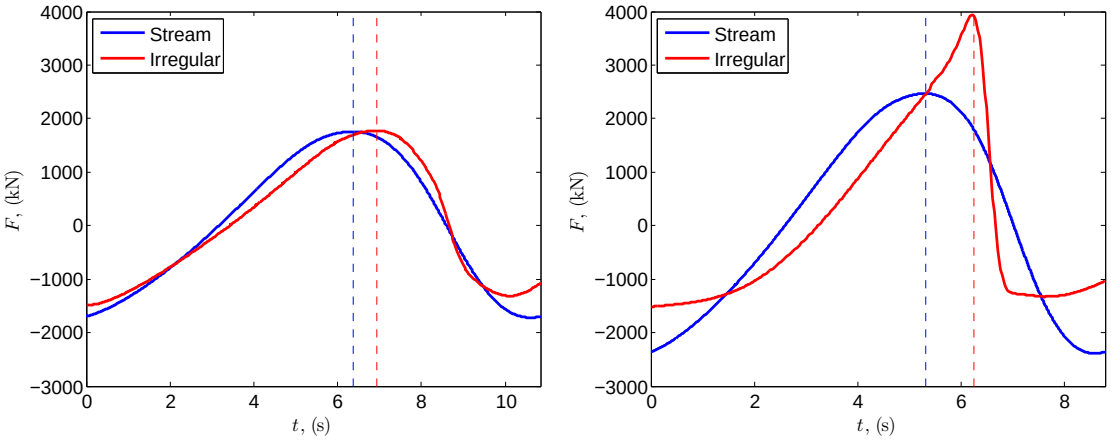

(a) $H = 6.53\,\text{m}$ and $T = 10.85\,\text{s}$. **(b)** $H = 8.28\,\text{m}$ and $T = 8.78\,\text{s}$.

Figure 4.19: *The inline force due to the nonlinear irregular wave compared with the corresponding stream function wave.*

4.3.3 Summary

In the present section the wave forcing on a fixed monopile has been investigated.
In the first analysis the peaks of the surface elevation, inline force and overturning moments due to the linear and nonlinear wave realizations were compared. In general the forces and moments decrease as the water depth decreases. This is both due to the smaller water column but also because the diameter of the monopiles decreases. Further, the nonlinear wave realizations result in both the largest positive peaks of the surface elevation, inline force and overturning moment. The

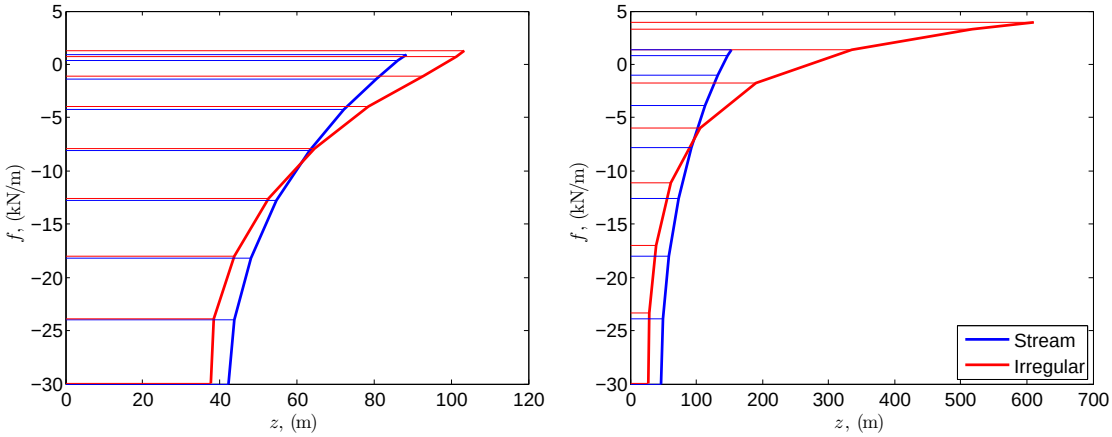

(a) $H = 6.53\,\text{m}$ and $T = 10.85\,\text{s}$. **(b)** $H = 8.28\,\text{m}$ and $T = 8.78\,\text{s}$.

Figure 4.20: *The forces due to the nonlinear irregular wave and the corresponding stream function wave.*

H (m)	T (s)	F_{irreg} (MN)	F_{stream} (MN)	M_{irreg} (MNm)	M_{stream} (MNm)
6.53	10.85	1.8	1.8	33	31
8.28	8.78	3.9	2.5	97	48

Table 4.7: *The inline force and overturning moment based on the waves shown in figure 4.18.*

difference between the linear and nonlinear wave forcing increases in general as the wave height increases and the water depth decreases. However, there is some variation, which must be due to the randomness of the wave realizations. The sea states are compared for two probabilities of exceedance, but the probabilities varies off cause a little from water to water depth and also between the sea states. The comparison indicates that the nonlinearity of the waves is important when the static wave forcing are considered, both for the small and large sea states and in particular for the largest waves in the wave realizations. It is not believed that the lack of convergence of the waves in high frequency part of the wave spectra influence the present results significantly, because the waves in the part of the spectrum with most energy are converged.

In the last part of the analysis two nonlinear irregular large waves from the largest sea state were compared with the corresponding waves based on stream function theory. The comparison shows that a fully nonlinear irregular wave can result in a larger inline force and overturning moment compared to stream function waves.

4.4 Dynamic analysis

The actually consequence of the hydrodynamic loads depend on the structure they are working on. To investigate this and to take the simultaneously aerodynamic loads and damping into account, the following analyses of the dynamic response of the tower and monopile are based on aeroelastic calculations.

The analysis is based on the sectional moment in the bottom of the tower and monopile because it most often is the moments that are important in the design.

For simplicity only wind and sea state *1a*, *1b*, *3* and *5* are considered at a water depth of $h = 30\,\text{m}$ and only time sequences of the last hour of the time series are presented. Before the actually analysis, a short discussion about the damping in a offshore wind turbine and a introduction to wavelet transformation is given.

4.4.1 Damping of the wind turbine

Besides aerodynamic damping there exist other types of damping in an offshore wind turbine; soil damping, hydrodynamic damping, structural damping in the tower and monopile and tower dampers. Aeroelastic damping is by far the most important damping effect and exist when the wind turbine is in operation. During stand still or when the wind turbine is idling the aeroelastic damping becomes insignificant and other types of damping therefore important.
According to Tarp-Johansen *et al.* (2009) these types of damping all in all have a logarithmic of decrement of 8% for the first structural mode. It is possible to include a constant damping ratio in Flex5 as explained in section 3.1.2.
In the following analysis the damping of the tower and monopile is therefore modeled by application of 8 % logarihmic decrement damping of the first structural eigenmode. As input the logarithmic decrements both in the tower (the first mode shape) and monopile is set to 9%. To check that this gives the correct damping a decay test is performed. In the test only the DOFs in the tower and monopile are turned on. The rest of the DOFs are stiff. The first eigenmode of the system still has a eigenfrequency of 0.273 Hz. The generator is turned off, the density of the air and water is zero and the blades are not rotating.
In order to make the decay test, the velocity of the DOFs are given an initial value equal to the eigenvector of the structural first eigenfrequency. For this case it means that the first DOF in the tower has a velocity of 1 and the first DOF in the monopile has a velcity of 0.117.
The decay of the displacement of the top of the tower and monopile are seen in figure 4.21. The

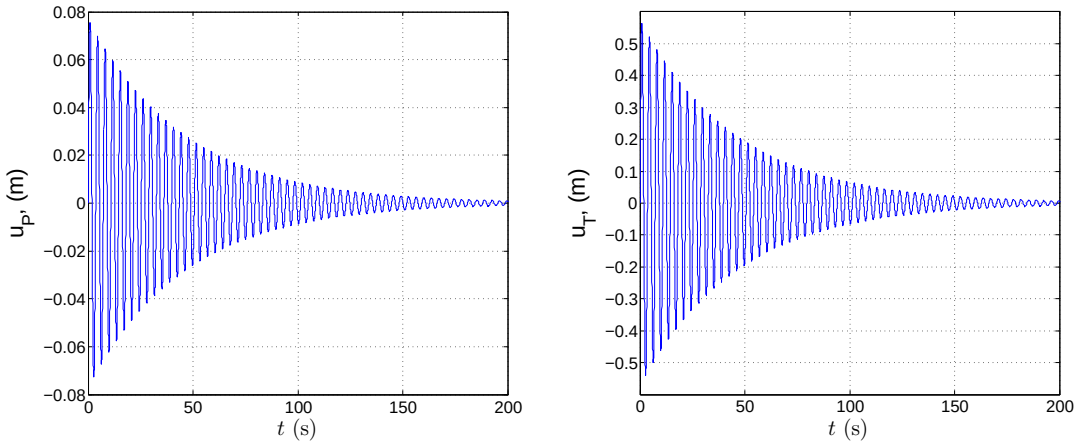

Figure 4.21: *Decay test of the displacement of top of the monopile,* u_P*, and tower,* u_T*.*

logarithmic decrement is calculated as

$$\delta = \frac{1}{j} \log \left(\frac{\hat{a}_i}{\hat{a}_{i+j}} \right), \quad j = 2, 3, ..., \tag{4.8}$$

where $\hat{a}_i$ is the first amplitude considered in the time series and a a_{i+j} is the j'th amplitude following $\hat{a}_i$.
The oscillations of the decay tests for the tower and monopile has a frequency of 0.274 Hz, so very close to the structural first eigenfrequency. The logarithmic damping for the first 20 amplitudes is found to be 8 % both in the tower and monopile.

4.4.2 Wavelet transformation

In the dynamic analysis wavelet transformations are used to identify at which frequencies in the times series in the energy content is large. Wavelet transformation is a method to localize special events in a signal both in time and frequency domain. In a Fourier transformation it is possible to investigate at what frequencies a signal contains energy. In a wavelet transformation it is further possible to investigate at what times the frequencies containing much energy. A wavelet transformation, WT, breaks the signal into its wavelets which are scaled and shifted versions of the mother wavelet

$$WT(\tau, b) = \int_{-\infty}^{\infty} x(t) g^*_{tb}(t; \tau, b) dt, \tag{4.9}$$

where x is the signal which is transformed and g_{tb} is the mother wavelet, which depends on the scale dilation parameter determining the width of the wavelet, b, and the position of the wavelet as it is shifted through the signal, τ. The asterisk denotes the complex conjugate quantity. The scale $b > 1$ stretches out the signal, whereas the scale $b < 1$ compresses the signal. The mother wavelet is, following the work of Massel (2001) the Morlet wavelet given as

$$g_{\tau b}(t; \tau, b) = \frac{1}{\sqrt{b}} \exp\left[-\frac{1}{2}\left(\frac{t-\tau}{b}\right)^2\right] \exp\left[ic\frac{t-\tau}{b}\right]. \tag{4.10}$$

The frequency parameter is here $c = 2\pi$ and the scale parameter b is given as

$$b = \frac{c + \sqrt{c^2+2}}{4\pi} \frac{1}{\hat{f}}. \tag{4.11}$$

With $c = 2\pi$ yields $b = \alpha = 1.0125\frac{1}{\hat{f}}$, which means that b and $1/\hat{f}$ is more or less equivalent. When the wavelet transformation is considered b therefore corresponds to the frequencies of the signal. Figure 4.22 shows the mother wavelets with $b = 0.5\,\mathrm{s}$ and $b = 1\,\mathrm{s}$ and $\tau = 0\,\mathrm{s}$.

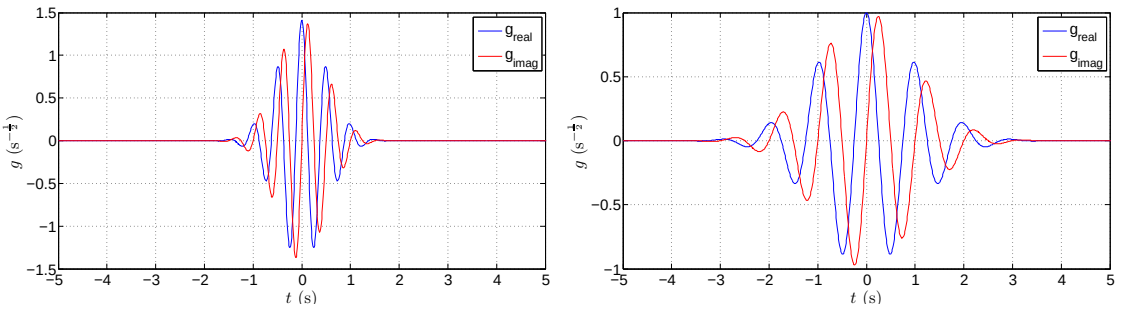

(a) $b = 0.5\,\mathrm{s}$. **(b)** $b = 1\,\mathrm{s}$.

Figure 4.22: *Two wavelets for $\tau = 0\,s$. — g_{real} — g_{imag}*

To calculate the wavelet transformation for one frequency $1/b$ and position τ the mother wavelet $g_{\tau b}(t : \tau, b)$ is calculated for this particular frequency and time. The mother wavelet is multiplied with the signal to get the wavelet. The wavelet transformation is then found by integrating the wavelet.

4.4.3 Wind and sea state *1a* and *1b*

In wind and sea state *1a* the wind speed is below the cut in wind speed. The wind turbine is therefore not producing energy and the blades are pitched 30 degrees. Case *1a* is therefore not affected by the aerodynamic forcing and damping to same extent as when the wind turbine operates and is a good example on how the dynamics of the tower and monopile works.
Figure 4.23 shows the wavelet transformation of the surface elevation and the moment in the bottom of the tower and monopile due to the nonlinear wave realizations for wind and sea state *1a* and *1b*. The y-axis shows the frequency and the x-axis shows the time.

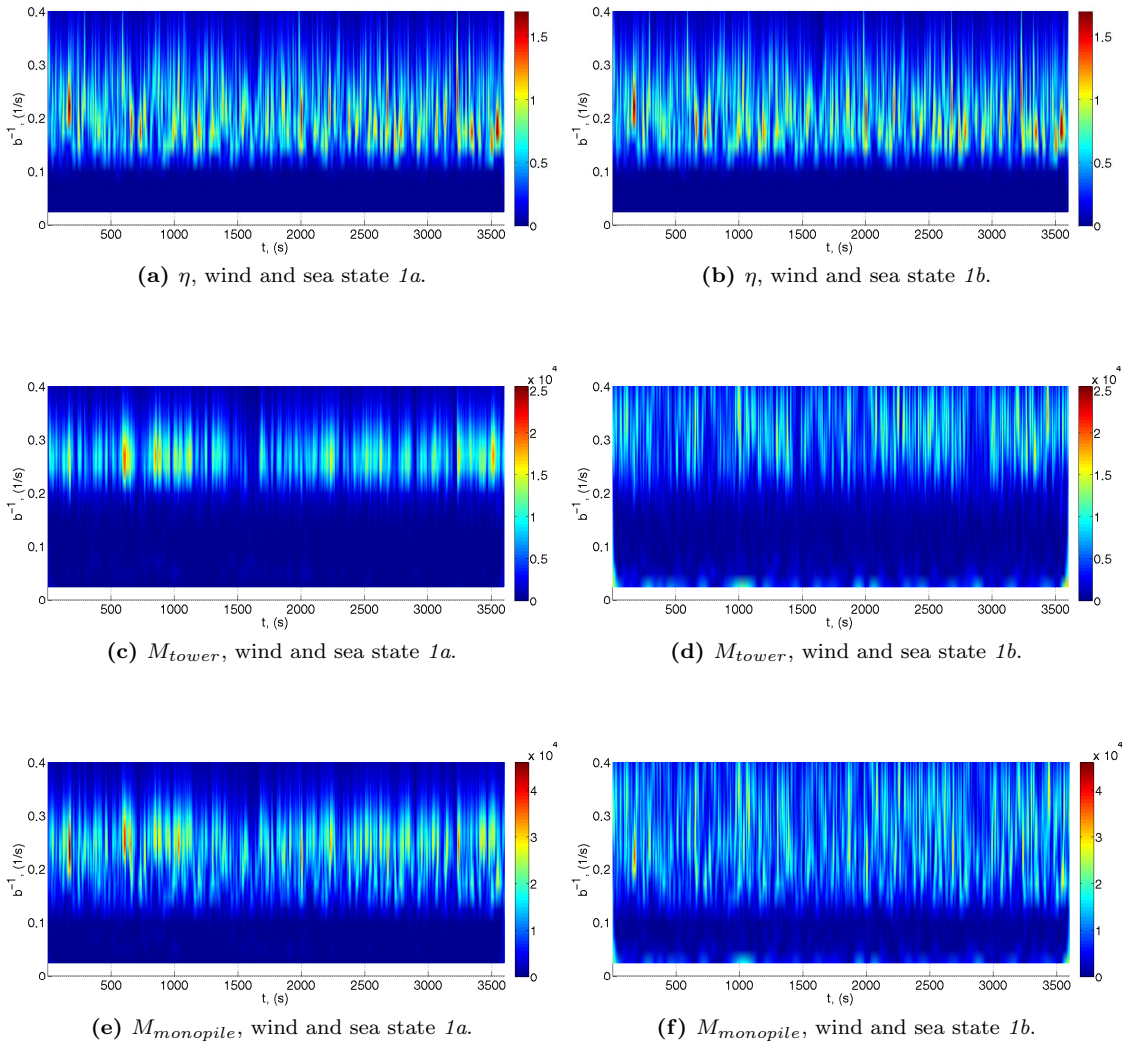

(a) η, wind and sea state *1a*.

(b) η, wind and sea state *1b*.

(c) M_{tower}, wind and sea state *1a*.

(d) M_{tower}, wind and sea state *1b*.

(e) $M_{monopile}$, wind and sea state *1a*.

(f) $M_{monopile}$, wind and sea state *1b*.

Figure 4.23: *The wavelet transformation of wind and sea state 1a and 1b due to the nonlinear sea states.*

The surface elevation contains most energy around the peak frequency of $\hat{f}_p = 0.18\,\text{Hz}$ but the energy is spread up to higher frequencies. The moment in the bottom of the tower, figure 4.23c, primarily contains energy around the structural first eigenfrequency, $\hat{f} = 0.27\,\text{Hz}$. It is further possible to see that when the surface elevation contains much energy at frequencies around $\hat{f} \sim 0.27\,\text{Hz}$, the amount of energy in the moment also increases, see for example at $t \sim 230\,\text{s}$ and $t \sim 3200\,\text{s}$. This means that the wave forcing turns on the first eigenmode of the tower.
The wavelet transformation of the moment in the monopile in case *1a*, figure 4.23e, is similar to the wavelet transformation of moment in the tower but the energy is spread to lower frequencies

closer to the peak frequency of the wave spectra. In the monopile the first eigenfrequency is also turned but not as much as in the tower.

In wind and sea state *1b* the wind turbine is producing energy and the wind turbine is therefore also affected by the aerodynamic forcing and aerodynamic damping. The moments in the bottom of the tower and monopile, figure 4.23d and 4.23f, deviate therefore much from case *1a*, despite that the wave realizations are the same.
The moment in the tower contains some energy around the structural first eigenfrequency but the energy is spread to larger frequencies due to the aerodynamic forcing. The moment contains compared to case *1a* also more energy at very small frequencies around 0.05 Hz also due to the aerodynamic forcing. The moment in the monopile contains energy around the peak frequency which also is seen for case *1a* but the energy is spread to frequencies above the structural eigenfrequency. The response due to the large wave at $t \sim 3200\,\text{s}$ is recognised both in the tower and in the monopile but the energy content is smaller than in case *1a*, which must be due to aerodynamic damping.
These above results are also representative for case *1a* and *1b* with the linear wave realizations.

The time series of the sectional moment in the bottom of the tower and monopile for wind and sea state *1a* in the time sequence $t = 3200 - 3400\,\text{s}$ are shown in figure 4.24 and 4.25, both due to the linear and nonlinear wave realizations. In the figure the linear and nonlinear surface elevation is also shown. The nonlinear surface elevation is relatively large at time $t \sim 3225\,\text{s}$ and $t \sim 3320\,\text{s}$. The moment in the bottom of the tower is also excited at $t \sim 3225\,\text{s}$ and dampens than slowly but get more energy again at $t \sim 3320\,\text{s}$. This can also be observed in the wavelet transformation of the moment in the bottom of the tower, figure 4.23c, where the energy increases abrupt at $t \sim 3225\,\text{s}$ and contains still much energy at $t \sim 3320\,\text{s}$, where the energy increases again.
The surface elevation of the linear wave realization of sea state *1a* increases at time $t \sim 3285\,\text{s}$, which excite the moment in the bottom of the tower. The moment increases over some wave periods and dampens afterwards slowly.
The moment in the bottom of the monopile is also excited at the same times as the moment in the tower is excited, for example at $t \sim 3225\,\text{s}$ for the nonlinear wave realizations and $t \sim 3285\,\text{s}$ for the linear wave realizations. However, the response dampens much faster in the monopile and is in general more static and follows the wave forcing more than the response in the tower. The difference between the response in the tower and monopile was expected since the tower is less stiff compared to the monopile.
The response due to the linear wave realization is larger than that due to the nonlinear wave realizations. This is observed at different places in the time series, even though the Morison forces were found to be largest for the nonlinear wave realization, described in section 4.3.1. A possible explanation for this could be that the spectral energy of the nonlinear wave realization is distributed from the peak of the spectrum to lower and higher frequencies. In section 4.2 it was observed that the nonlinear wave spectrum contains more energy at higher frequencies compared to the linear wave spectrum, however it was difficult to see if the energy was moved from frequencies close to the structural frequency.

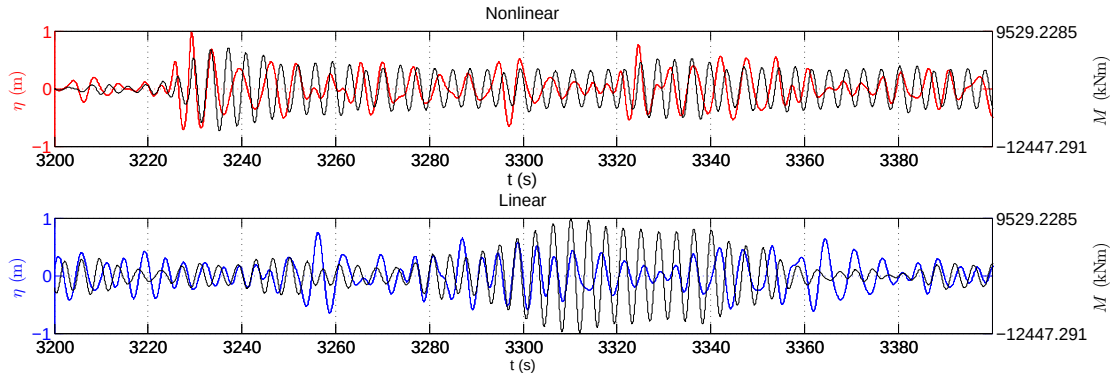

Figure 4.24: *Nonlinear and linear surface elevation for wind and sea state 1a and the corresponding moment in the bottom of the tower.*

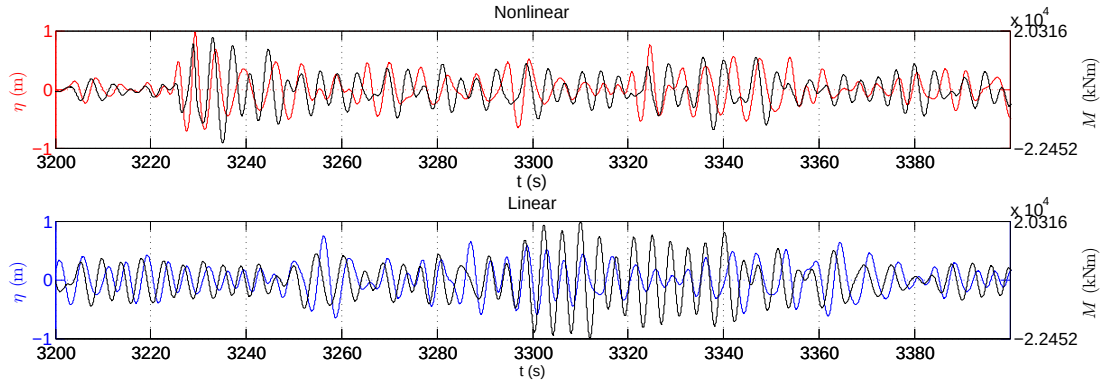

Figure 4.25: *Nonlinear and linear surface elevation for sea state 1a and the corresponding moment in the bottom of the monopile.*

If wind and sea state *1b* is considered the effects from the wind forcing becomes very obvious in the time series of the response. Figure 4.26 and 4.27 shows the sectional moment in the bottom of the tower and monopile in the same time sequence as case *1a*. The moment is now oscillating around a positive mean value due to the wind forcing but the magnitude is not larger than in case *1a*. The excitation of the tower and monopile caused by the wave forces is less pronounced due to the aeroelastic forcing and damping. It is difficult to identify the excitation of the moment of the tower which was observed for case *1a* due to the nonlinear wave realization at time $t \sim 3225\,\mathrm{s}$ and $t \sim 3320\,\mathrm{s}$ and for the linear wave realization at $t \sim 3285\,\mathrm{s}$. This is in accordance with expectations because the tower is wind dominated so the aerodynamic forcing and damping is stronger than the wave forcing in the tower when the wind turbine operates. However, when comparing the moment due to the linear and nonlinear wave realization it is possible to see that the responses deviate due to different wave forcing.

The moment in the monopile is not excited in the same way as in case *1a* neither for the linear nor for the nonlinear wave realization. Instead the response is very static and follows the oscillations of the wave forcing. This means that the aerodynamic damping also affect the dynamics of the monopile and not only the tower. On top of this static response it is possible to see some small high frequency oscillations. These high frequency oscillations are also observed in the wavelet transformation of the moment in the monopile, and must be due to the wind forcing.

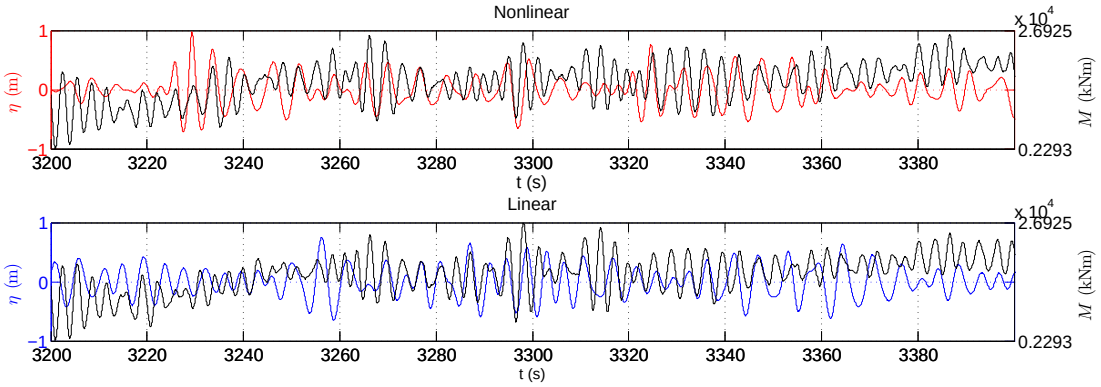

Figure 4.26: *Nonlinear and linear surface elevation for wind and sea state 1b and the corresponding moment in the bottom of the tower.*

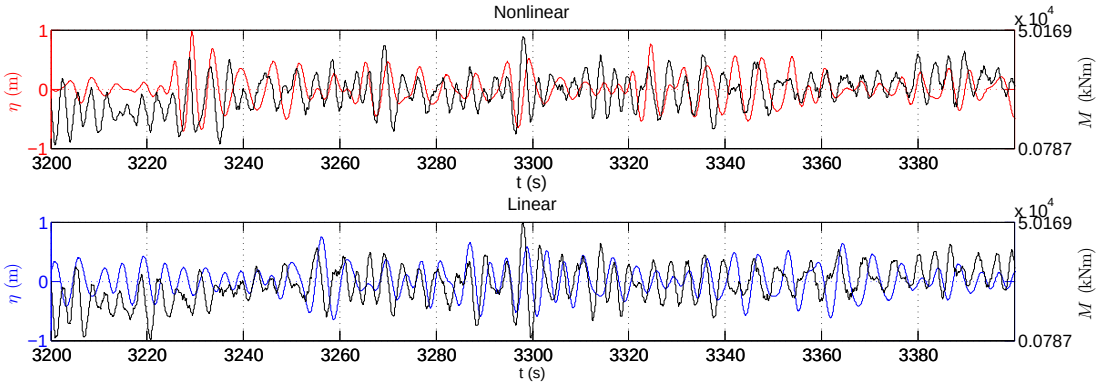

Figure 4.27: *Nonlinear and linear surface elevation for sea state 1b and the corresponding moment in the bottom of the monopile.*

4.4.4 Wind and sea state *3*

In wind and sea state *3* it is difficult to identify where in the time series the moments in the bottom of the tower and monopile is excited by the waves. The wavelet transformations are therefore used to identify some times where the surface elevation and moments contain energy around the first structural eigenfrequency. Figure 4.28 shows the wavelet transformation of the linear and nonlinear surface elevation and of the sectional moments in the bottom of the tower and monopile in the time sequence $t = 1850 - 2200\,\mathrm{s}$. The corresponding time series of the surface elevations and moments are seen in figure 4.29 and 4.30.
The wavelet transformation of the nonlinear surface elevation contains energy just below the first structural eigenfrequency at time $t \sim 1905\,\mathrm{s}$ and $t \sim 2000\,\mathrm{s}$. The same is seen in the wavelet transformation of the moment in the monopile. However no energy can be observed in the wavelet transformation of the moment in the tower at these two times, which must be due to the aerodynamic damping, which is stronger in the tower than in the monopile.

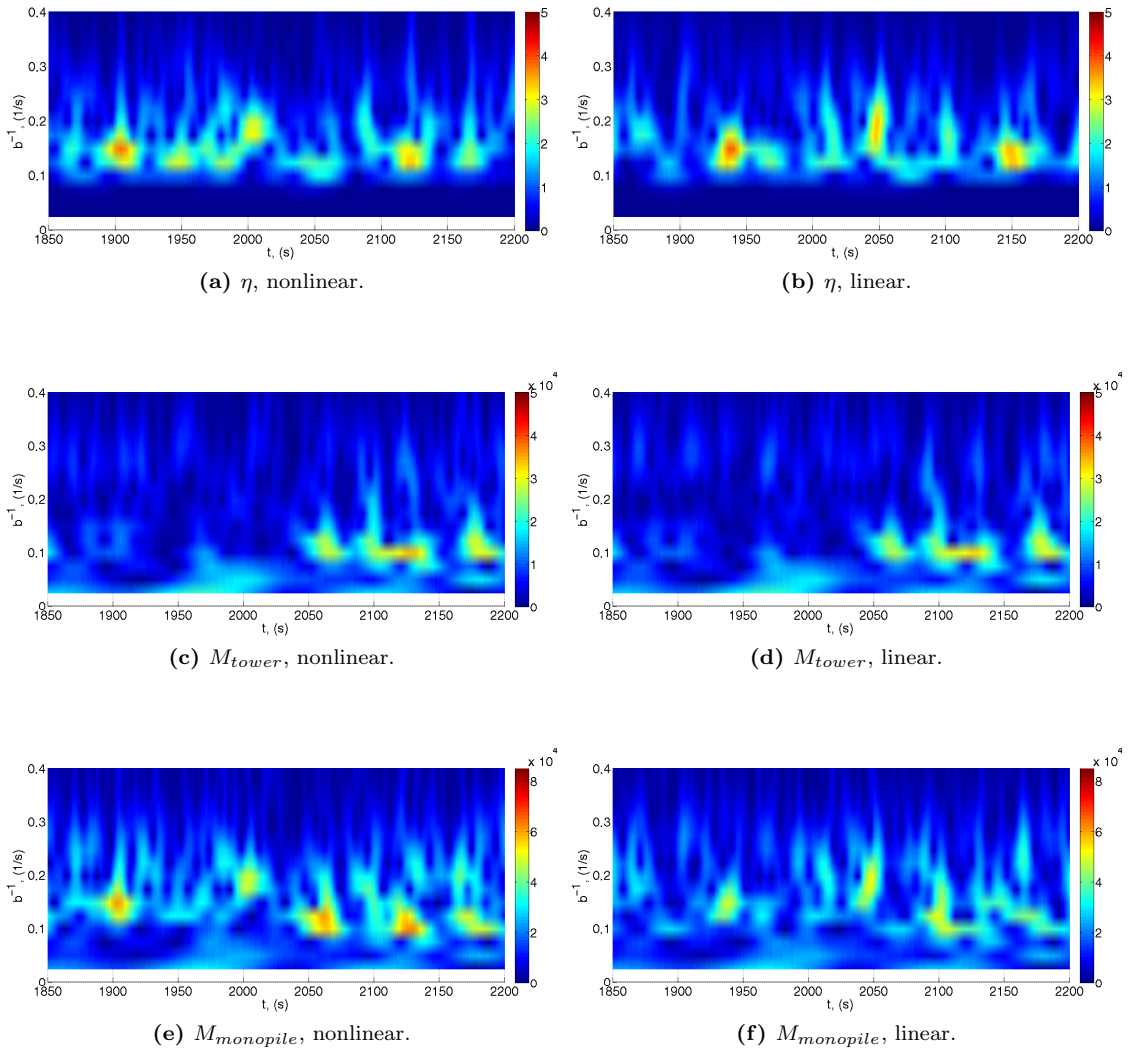

(a) η, nonlinear. **(b)** η, linear.

(c) M_{tower}, nonlinear. **(d)** M_{tower}, linear.

(e) $M_{monopile}$, nonlinear. **(f)** $M_{monopile}$, linear.

Figure 4.28: *Wavelet transformation for wind and sea state 3.*

Similar results are observed for the linear wave realization at time $t = 2010\,\mathrm{s}$ and $t = 2050\,\mathrm{s}$.
At time $t = 2065\,\mathrm{s}$ the energy in the wavelet transformations of the nonlinear and linear moment in the tower increases (due to the aerodynamic forcing). This increase in energy can also be observed

in the time series of the moment in the tower, figure 4.29 and 4.30, where it also is seen that the moment due to the nonlinear wave realization increases more than the moment due to the linear wave realization. This is because the nonlinear surface elevation at the same time increases and contains energy up to $\hat{f} = 0.2\,\text{Hz}$. If the moments in the monopile are considered it is also seen that it only is the nonlinear moment which increases at this time. This again indicates that the aerodynamic forcing affects the dynamics of the tower more than the dynamics of the monopile. Instead the moments in the monopile, both due to the linear and nonlinear wave realizations, follow the static forcing from the waves most of the time. On the top of the static response the moments in the monopile contain high frequency oscillations, which must be due to the aerodynamic forcing. The analysis indicate that it is a complex task to identify the source of the response in the tower and monopile because it depends on so many factors. The tower is more exposed to the aerodynamic forcing and aerodynamic damping compared to the monopile, and it is therefore difficult to find the difference in the response due to the linear and nonlinear wave forcing in the tower.

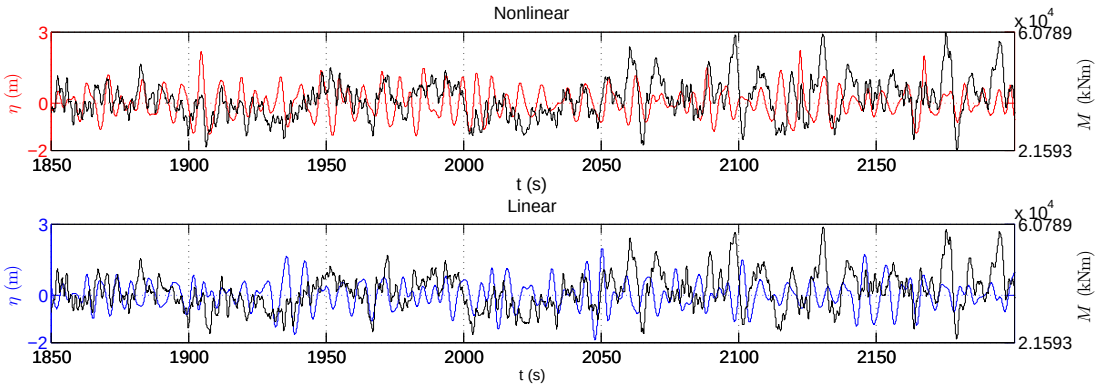

Figure 4.29: *Nonlinear and linear surface elevation for sea state 3 and the corresponding moment in the bottom of the tower.*

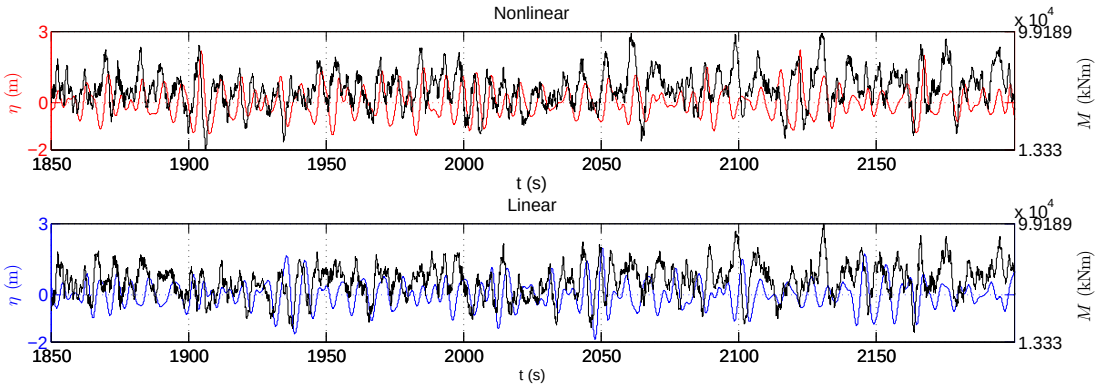

Figure 4.30: *Nonlinear and linear surface elevation for sea state 3 and the corresponding moment in the bottom of the monopile.*

4.4.5 Wind and sea state *5*

In wind and sea state *5* the wind speed is above the cut-out wind speed of 25 m/s and the wind turbine blades are pitch 87 degrees. The aerodynamic damping is therefore insignificant in the fore-aft direction, and it is possible to see the effects from the wave forcing both in the tower and monopile.

The wavelet transformation of the surface elevation for both the linear and nonlinear sea state and the corresponding moments in the bottom of the tower and monopile are shown in figure 4.31. The surface elevations primarily contain energy at the peak frequency of $\hat{f} = 0.9\,\text{Hz}$. However the energy is spread as in threads up to higher frequencies, particular for the nonlinear wave realization

at $t \sim 1400\,\text{s}$, $t \sim 2100\,\text{s}$ and $t \sim 2450\,\text{s}$.
The moments in the tower contain energy around the structural first eigenfrequency, while the moments in the monopile contain energy at the wave peak frequency but also at the structural first eigenfrequency at the same times as the moments in the tower are excited. It is interesting to see that the excitation of the structural first eigenfrequency in the tower is just as pronounced for the linear as for the nonlinear sea state.

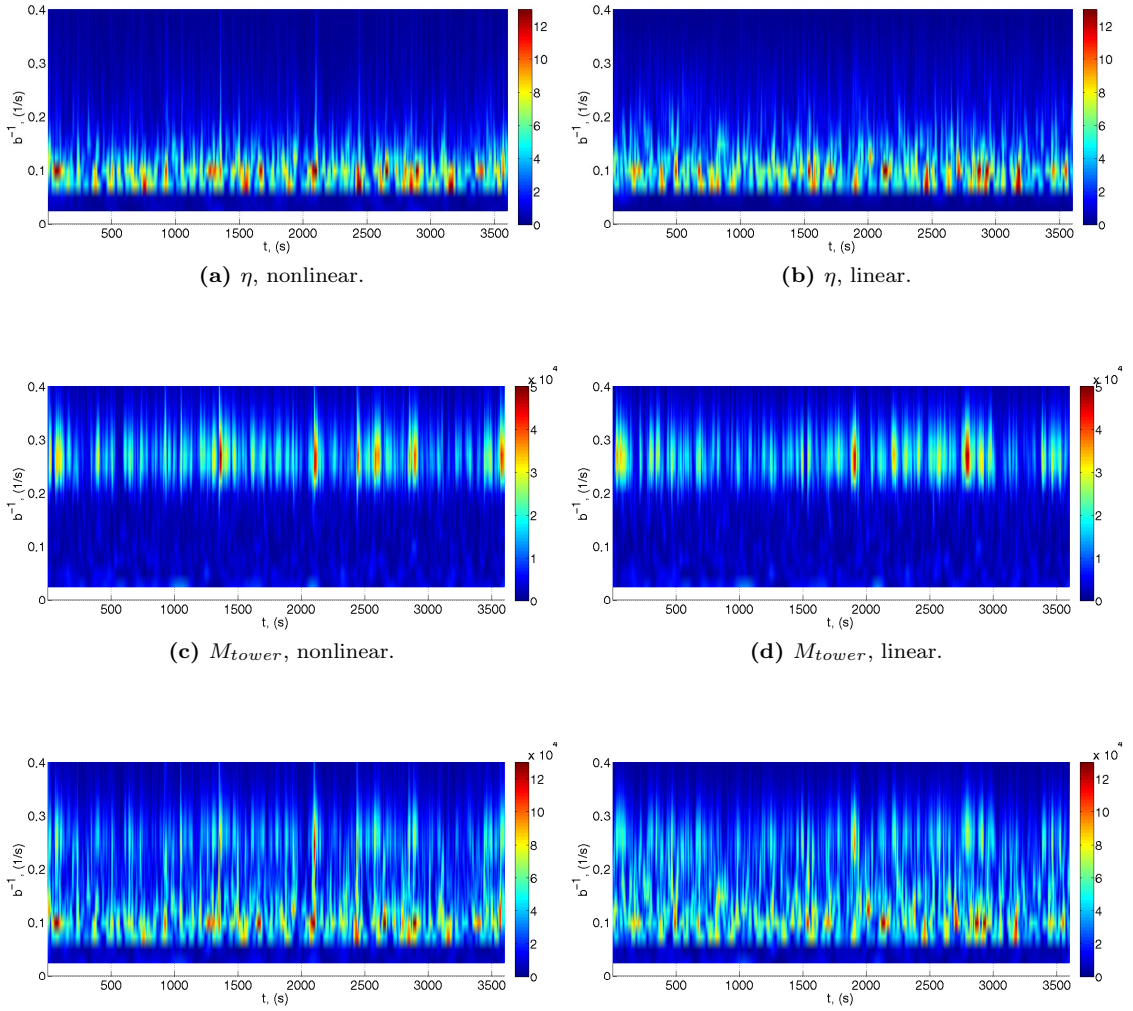

(a) η, nonlinear.

(b) η, linear.

(c) M_{tower}, nonlinear.

(d) M_{tower}, linear.

(e) $M_{monopile}$, nonlinear.

(f) $M_{monopile}$, linear.

Figure 4.31: *Wavelet transformation for wind and sea state 5.*

The time series of the sectional moments in the bottom of the tower and monopile are shown in figure 4.32 and 4.33 in the time sequence $t = 2400 - 2800\,\text{s}$. At $t \sim 2575\,\text{s}$ and $t \sim 2650\,\text{s}$ the moment in the tower due to the nonlinear wave realization is excited. At $t \sim 2430\,\text{s}$ the surface elevation has as sudden increase in energy, and the response in the tower looks like a impulsive response. The wavelet transformation of the moment, figure 4.31c, also have a sudden increase of energy at this time and the energy is spread from 0.2 Hz-0.4 Hz.
The linear surface elevation contains a large amount of energy at $t = 2750\,\text{s}$ which excite the moment in the tower significantly. The response is also excited at $t \sim 2400\,\text{s}$ and $t \sim 2550\,\text{s}$.
The reason the excitation of the structural first eigenfrequency in the tower seems to be just as pronounced for the linear as for the nonlinear sea state must be because the linear spectrum of the surface elevation considered in section 4.2 contains more energy around the structural frequency

compared to the nonlinear spectrum. The excitation due to the linear wave realizations are therefore caused by the broad band forcing. For the nonlinear wave realization the excitation can both be due to nonlinear effects such as springing, ringing and broad band forcing.
Impulsive responses as is seen for the nonlinear wave realization in the tower and monopile at $t = 2430\,\mathrm{s}$ is observed several times for the nonlinear wave realization only. This is because the linear wave are not steep enough to generate such responses.
The moments in the monopile follows the wave forcing in a quasi-static manner but are also excited at the same times as the moments in the tower, particular at $t = 2430\,\mathrm{s}$ for the nonlinear wave realization.
For the nonlinear wave realizations it is not easy to distinguish between the response due to springing and broad band forcing, but it is expected that springing occurs due to the nonlinear wave realization. Ringing may also occur, but it has not been possible to identify this response in the moments in the tower and monopile due to the nonlinear wave realization.

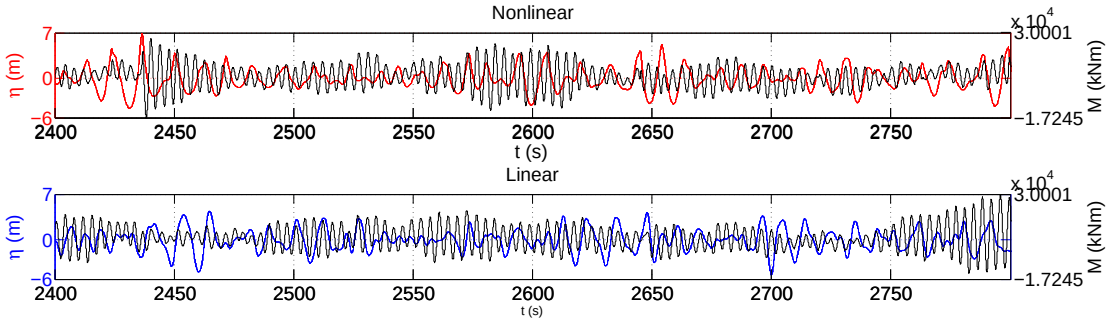

Figure 4.32: *Nonlinear and linear surface elevation for sea state 5 and the corresponding moment in the bottom of the tower.*

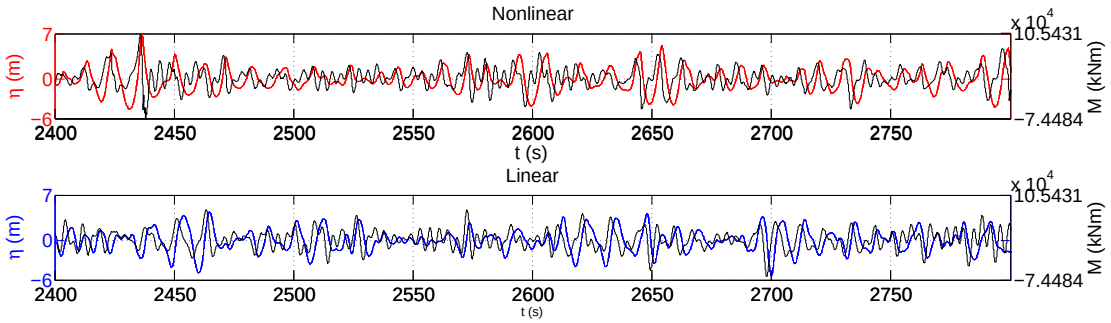

Figure 4.33: *Nonlinear and linear surface elevation for sea state 5 and the corresponding moment in the bottom of the monopile.*

4.4.6 Summary

In the above analysis the dynamic response of a wind turbine exposed to hydrodynamic and aerodynamic forces was considered. The analysis was based on aeroelastic calculations. 8 % of damping in logarithmic decrement was added to the first eigenfrequency of the tower and to the monopile and represent soil damping, hydrodynamic damping, structural damping in the tower and monopile and tower dampers.
Wavelet transformations, which were used in the analysis, are a convenient method that gives an overview of where in the times series special events take place.
In the dynamic analysis it was found that the effects from the wind are very important in the structural response of the tower and monopile.
The tower is wind dominated, it only feels the waves because the monopile is moving. The monopile works therefore as a "force transmitter", which transmit the static wave forcing to the tower. The response in the tower is very dynamic and primarily due to excitation of the first structural

eigenfrequency. The effects from the waves are difficult to identify in the tower when the wind turbine operates, both because the wind forcing is dominating but also because the response due to the waves is dampened by the aerodynamic damping.
The monopile is relative stiff and exposed directly by the waves. The monopile reacts therefore mainly quasi-static to the wave forces. However, in cases where the aerodynamic damping is insignificant the wave loads induced structural excitation of the structural first eigenfrequency, which both was seen in the tower and in the monopile.
The excitation due to the linear wave realizations, which was seen in the monopile and tower when the wind turbine blades were pitch and the effects from the wind insignificant, was similar to the excitation due to the nonlinear wave realizations. For the linear wave realization the excitation is caused by broad band forcing. For the nonlinear wave realizations the excitation must be caused by both springing and broad band forcing.
For the largest wind and sea state it was possible to see impulsive excitation due to the nonlinear waves. This is a nonlinear effect. The waves in the linear wave realization do not become steep enough to cause such a response.
The lack of convergence of the waves in the high frequency part of the wave spectra, can therefore influence the present results. If the waves were converged it would most likely cause larger broad band forcing.

4.5 Fatigue analysis

Fatigue analysis is a simple method to study the accumulated effects of the wave nonlinearity. The fatigue calculations are based on the time series of the sectional moments in the bottom of the tower and monopile which are rainflow counted using the method defined in the IEA "Recommended Practices for Wind Turbine Testing and Evaluation; 3. Fatigue Loads", IEA (1990). The two hours time series of the wave realizations are divided in two. The aeroelastic calculations are performed for each 1 hour time series where the corresponding two 1 hour wind fields are based on different seed-values. This is done to keep the output data on a reasonable size, such that the data was easy to handle and analyse. The transient from the first part of the time series to the nex part is of course missing with this method. However, for times series of 1 hour each it is not believed to be very important. The two 1 hour aeroelastic calculations for each wind and sea state are rainflow counted and the rainflow counting for each wind and sea state is added up. Norton (2003) found that for loads driven by both the wind and waves time simulations of 60 min are necessary in order to get the correct equivalent loads. The two hours time series considered here should according to Norton (2003) therefore be sufficient.
The fatigue analyses are based on all six wind and sea states at the four water depths $h = 40\,\mathrm{m}$, $h = 35\,\mathrm{m}$, $h = 30\,\mathrm{m}$ and $h = 25\,\mathrm{m}$.

4.5.1 Rainflow counting

Often rainflow counting are explained by rotating the load time series so that the time axis is pointing vertical downwards and connecting the peaks in the time series by straight lines, such that the lines look like a roof. The cycles are then counted by considering rainflow that begins inside the peaks and slides along the roof as illustrated in figure 4.34. For more details see for example Downing & Socie (1982), Rychlik (1987) and Twidell & Gaudiosi (2009).
In IEA (1990) another rainflow counting method is used, where all the peaks in the load time series are identified, as illustrated in figure 4.35a. The first four peaks, P_1, P2, P3 and P4, are as a start considered. A cycle is counted if the two inner peaks, P_2 and P_3, are inside the two outer peak and therefore fulfil one of the two requirements

$$\begin{aligned} \mathsf{P}_{i+1} > \mathsf{P}_i \quad \text{and} \quad \mathsf{P}_{i+2} \geq \mathsf{P}_i \quad \text{and} \quad \mathsf{P}_{i+3} \geq \mathsf{P}_{i+1} \quad \text{or} \\ \mathsf{P}_{i+1} < \mathsf{P}_{i+2} \quad \text{and} \quad \mathsf{P}_{i+2} \leq \mathsf{P}_i \quad \text{and} \quad \mathsf{P}_{i+3} \leq \mathsf{P}_{i+1}, \end{aligned} \tag{4.12}$$

where $i = 1$ for the example where we consider P_1, P_2, P_3 and P_4 in figure 4.35a. The two inner peaks are afterwards removed from the time series and the magnitude of the cycle, $|\mathsf{P}_2 - \mathsf{P}_3|$, are

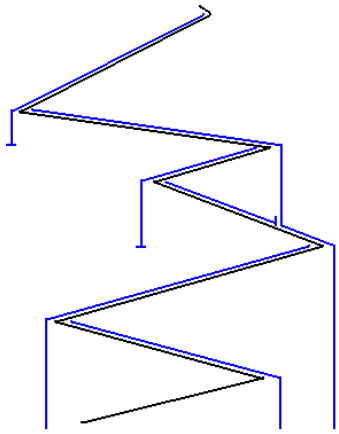

Figure 4.34: *Example of of rainflow counting.*

saved together with the corresponding number of occurrences. For peak P_2 and P_3 which is a full cycle the number of occurrence is 1.
The next four peaks, P_1, P_4, P_5 and P_6, are afterwards considered as indicated in figure 4.35b. The two inner peaks do not fulfil the criteria in equation (4.12). A step forward is therefore taken so peak P_4, P_5, P_6 and P_7 are considered. The procedure continuous until all cycles in the load times series are identified, the magnitude of the cycles saved and the peaks in the cycle removed. Afterwards the load time series consist of peaks which are converging until the largest peak, P_7, is reached and afterwards diverging as illustrated in figure 4.35c.
The remaining peaks are counted as half cycles with the magnitude $|\mathsf{P}_1 - \mathsf{P}_4|$, $|\mathsf{P}_4 - \mathsf{P}_5|$ ect. The number of occurrence for these magnitudes are 0.5, since the peaks only results in half cycles . The amplitudes are saved in a vector $\underline{\hat{S}}$ and the corresponding numbers of occurrence are saved in a vector $\underline{N_s}$ as illustrated in equation (4.13).

$$\underline{\hat{S}} = \begin{bmatrix} |\mathsf{P}_2 - \mathsf{P}_3| \\ |\mathsf{P}_8 - \mathsf{P}_{15}| \\ \vdots \\ |\mathsf{P}_1 - \mathsf{P}_4| \\ \vdots \end{bmatrix} \quad \text{and} \quad \underline{N_s} = \begin{bmatrix} 1 \\ 1 \\ \vdots \\ 0.5 \\ \vdots \end{bmatrix}. \tag{4.13}$$

4.5.2 Equivalent loads

Equivalent load range can be used as a reference loading. The equivalent load range, L_{eq}, represent one load-value that for a certain number of cycles, N_{eq}, results in the same damage level as the history of fatigue loads which are investigated. The fatigue analysis is with this method reduced to one number so it is easy to compare different load situations.
The equivalent loads depend on the S-N-curves. A S-N-curve gives the relation between the magnitude of a cyclic stress, $\hat{S}$, against the logarithmic scale of cycles to failure N_s

$$N_s = \hat{S}^{-\mathsf{m}}. \tag{4.14}$$

The curves are found from experiments, and m is a function of the material. For steel m is often between 3 and 5. The larger m is the larger is the stress for a certain number of cycles.
The damage caused by $N_{s,i}$ cycles with the corresponding stress ranges $\hat{S}_i$ is

$$D_{fat} = \sum_i \frac{N_{s,i}}{\hat{S}_i^{-\mathsf{m}}}. \tag{4.15}$$

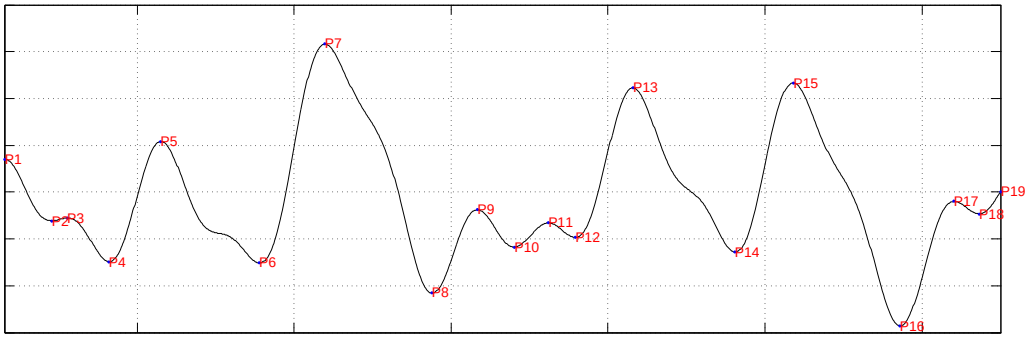

(a) All the peaks are identified.

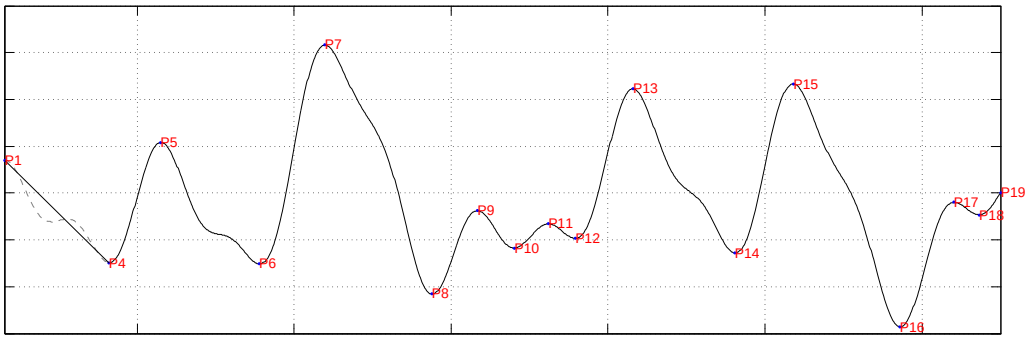

(b) One load cycle P_2–P_3 are counted and removed.

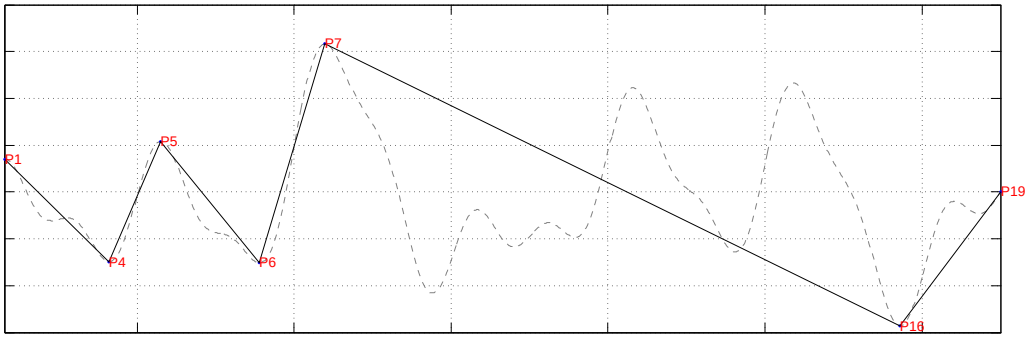

(c) All the cycles are counted and removed. The remaining peaks are half cycles.

Figure 4.35: *A load time series, which is rainflow counted with the method in IEA (1990).*

The equivalent loads are found by considering the damage caused by N_{eq} constant amplitude cycles with the stress range L_{eq} which equals equation (4.15)

$$\frac{N_{eq}}{L_{eq}^{-\mathsf{m}}} = \sum_i \frac{N_{s,i}}{\hat{S}_i^{-\mathsf{m}}} \Leftrightarrow L_{eq} = \left(\sum_i \frac{N_{s,i}(\hat{S}_i)^{\mathsf{m}}}{N_{eq}} \right)^{\frac{1}{\mathsf{m}}}. \tag{4.16}$$

The value of N_{eq} are often chosen to be between 10^6 and 10^7 or it is assumed that the frequency of the loading L_{eq} is constant. In the present thesis a fixed frequency of 1 Hz is chosen, so that for a one hour time series $N_{eq} = 3600$.
According to Norton (2003) an appropriate value of the S-N-slope is $\mathsf{m} = 4$ in the wind turbine tower. The equivalent load range is here calculated with damage exponents of $\mathsf{m} = 3$ and $\mathsf{m} = 5$. The larger m is, the more sensitive the fatigue damage is to the largest moments in the time series.

Figure 4.36 compares the linear and nonlinear equivalent loads for all wind and sea states at the four water depths. The differences between the wind and sea states equivalent loads are largest for $\mathsf{m} = 5$, because it is for the largest moments in the time series that the biggest differences between the wind and sea states are and the larger m is the more sensitive the equivalent loads are to the largest moments. The equivalent loads are further largest in the monopile because the moments here both have the contributions from the wind and waves.

The equivalent loads both in the tower and monopile decrease as the water depth decreases, because the water column where the wave forces are working decreases but also because the moment arm decreases as the length of the monopile decreases. Further, the diameter of the monopile also decreases as the water depth decreases, which also results in smaller wave forces.

The equivalent loads due to wind and sea state *1a* are larger than the equivalent loads due to wind and sea state *1b* at the largest water depth. At deep water the wave forcing is relative to the aerodynamic forcing large and the response from the waves are in case *1a* not exposed to the same amount of aerodynamic damping as the response in the case *1b* is. At the smaller water depths the opposite is seen because the wave forcing becomes smaller relative to the aerodynamic forcing as the water depth decreases and the aerodynamic forcing contribute therefore more to the equivalent loads.

In the tower the equivalent loads due to wind and sea state *3* are larger than those due to wind and sea state *4* and the equivalent loads due to wind and sea state *2* similar to those due to wind and sea state *4*. This is because the wind speeds in case *2* and *3* are close to the rated wind speed compared to the wind speed in case *4*. The trust and therefore the aerodynamic forcing is therefore larger.

The largest wind and sea state results in the largest equivalent loads in the tower for $h = 40\,\mathrm{m}$. At $h = 25\,\mathrm{m}$ the equivalent loads due to wind and sea state *5* is smaller than those due to wind and sea state *3* and *4*. This is again because the wave forcing becomes smaller relative to the aerodynamic forcing as the water depth decreases.

In the monopile the equivalent loads are much more dependent on the wave forcing compared to the tower. The equivalent loads increases as the sea state increases and as the water depth increases. This is in agreement with the results which was found when the static wave forces were compared in section 4.3.

Both in the tower and monopile it is also possible to see a difference in the equivalent loads due to the linear and nonlinear wave realizations.

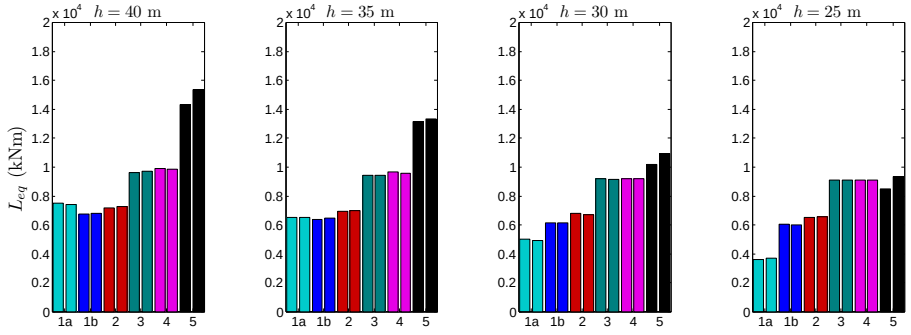

(a) Tower, m = 3.

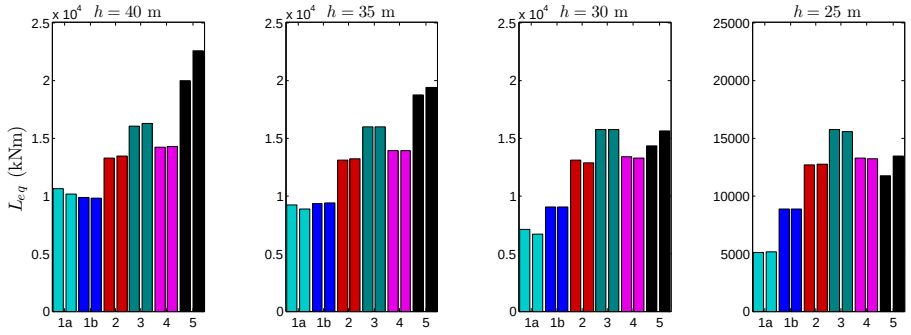

(b) Tower, m = 5.

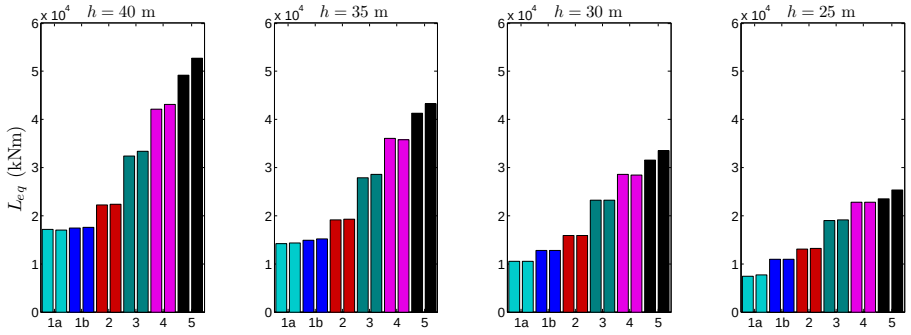

(c) Monopile, m = 3.

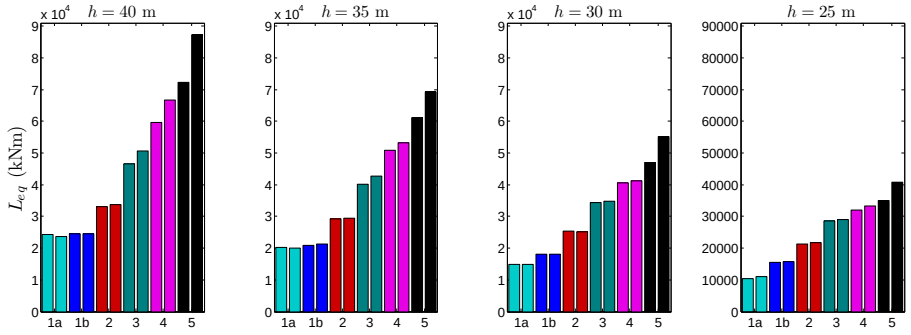

(d) Monopile, m = 5.

Figure 4.36: *The linear and nonlinear equivalent loads for each wind and sea state and water depth. For each wind and sea state both the linear (left bar) and the nonlinear (rigth bar) is given.* *1a* *1b* *2* *3* *4* *5*

Figure 4.37 shows the ratio between the linear and nonlinear equivalent loads for all six wind and sea states at the four water depths. The difference between the linear and nonlinear equivalent loads are largest for $\mathsf{m} = 5$, which, in agreement with expectations, indicates that it particular is the largest moments that differs between the linear and nonlinear sea states. In the following focus is on the equivalent loads based on $\mathsf{m} = 5$.
There is no clear linkage between the difference in the equivalent loads in the tower and the difference in the probability of exceedance of the surface elevation, inline force and overturning moment discussed in section 4.3.1. The missing linkage must primarily be due to the aerodynamic forcing and aerodynamic damping. In the monopile the differences between the linear and nonlinear equivalent loads increase as the sea states increase, which also was observed in the probability of exceedance analysis. The trend is most clear for $h = 40\,\mathrm{m}$, where the wave forcing provides the largest contribution to the total forcing. At the smaller water depths the trend is less consistent.
The linear equivalent loads for wind and sea state *1a* are larger than the nonlinear equivalent loads except for $h = 25\,\mathrm{m}$ both in the tower and monopile. The waves in the realizations are very small and the wind turbine is not exposed to any significant aerodynamic forcing or aerodynamic damping. Further it was found in section 4.3.1 that the Morison forces are largest for the nonlinear sea state. The equivalent load would therefore be expected to be the same or largest for the nonlinear sea state. However, when analysing the dynamic responses in section 4.4 the linear moments in the tower and monopile were also found to be largest. This was explained with the possibility that the linear wave spectrum contains more energy at the structural frequency. The current analysis of the equivalent loads contribute to this theory.

The ratio between the linear and nonlinear equivalent loads for wind and sea state *1b* to *4*, where the wind turbine operates, are quite similar in the tower. This must be due to effects from the wind which erases the difference between the linear and nonlinear wave forcing. It is difficult to see any trend in how the differences between the linear and nonlinear equivalent loads varies from water depth to water depth
The reason that the linear equivalent loads for wind and sea state *1b* to *4* some times are largest must be due to the broad band forcing which is largest for the linear wave realizations because the linear spectra contain more energy around the structural first eigenfrequency. This was seen for the third sea state in section 4.2. The tower is therefore excited more due to the linear wave realizations despite that the nonlinear wave forcing is strongest.
In the monopile the nonlinear equivalent loads of wind and sea state *1b* to *4* are in general largest. This is because the response in the monopile is more static, and the structural first eigenfrequency is therefore not excited in same manner as in the tower.

For wind and sea state *5* the difference between the equivalent loads due to the linear and nonlinear wave realizations are significant. In the tower the nonlinear wave realization results in equivalent loads $5 - 10$ % larger than the corresponding loads due to the linear wave realization, simply because the effects from the wind are insignificant. The response in the tower was excited both due to the linear and nonlinear wave realization but the nonlinear wave realizations also resulted in impulsive responses, which therefore must be the main cause to the difference. In the monopile the difference is 10-20 %. The larger difference in the monopile emphasis that the response in the monopile reflects the wave forcing more directly, and was in section 4.3.1 found to be significant larger for the nonlinear wave realization compared to the linear wave realization.

In the monopile and for the largest wind and sea state in the tower the difference between the linear and nonlinear equivalent loads in general decreases from $h = 40\,\mathrm{m}$ to $h = 30\,\mathrm{m}$ even though the nonlinear wave forcing is largest. This can be because the broad band forcing of the nonlinear wave realizations decreases because more energy is moved to higher and lower frequencies. This do not apply for the linear wave realizations. From $h = 30\,\mathrm{m}$ to $h = 25\,\mathrm{m}$ the difference between the linear and nonlinear equivalent loads increases again which can because the steep wave excitation increases as the water depth decreases and is much stronger for the nonlinear wave realizations.

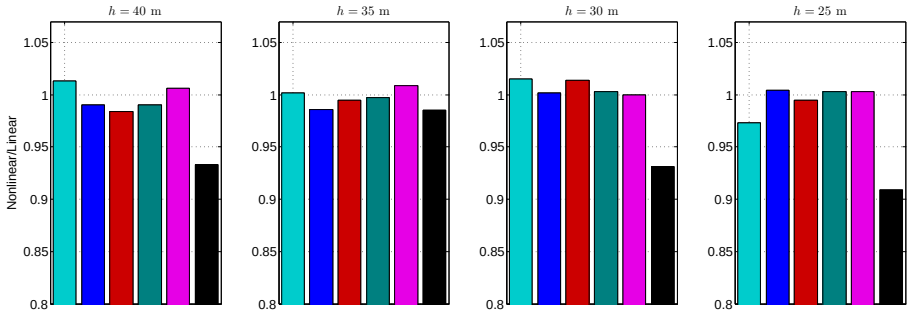

(a) Tower, m = 3.

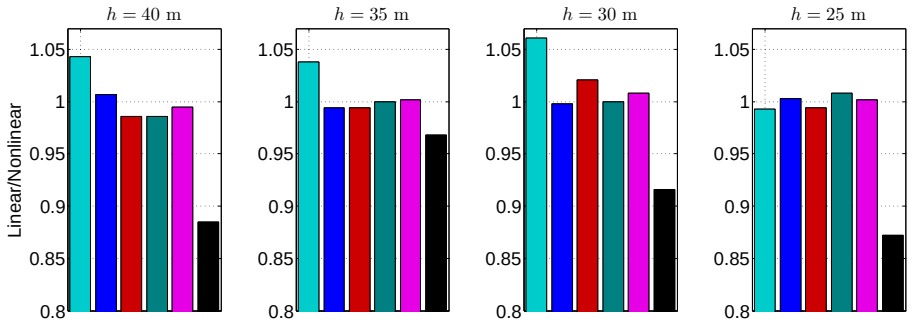

(b) Tower, m = 5.

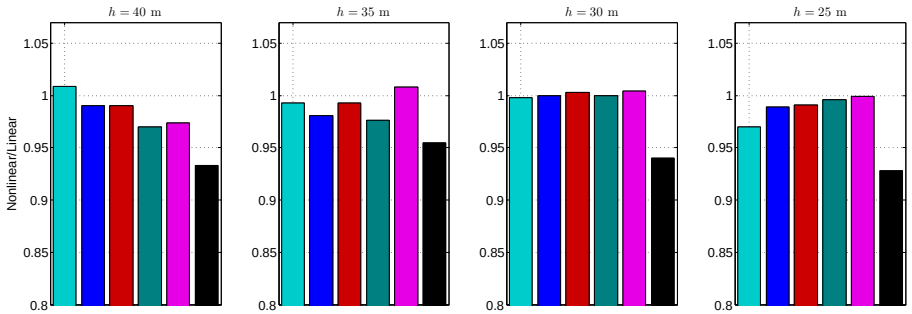

(c) Monopile, m = 3.

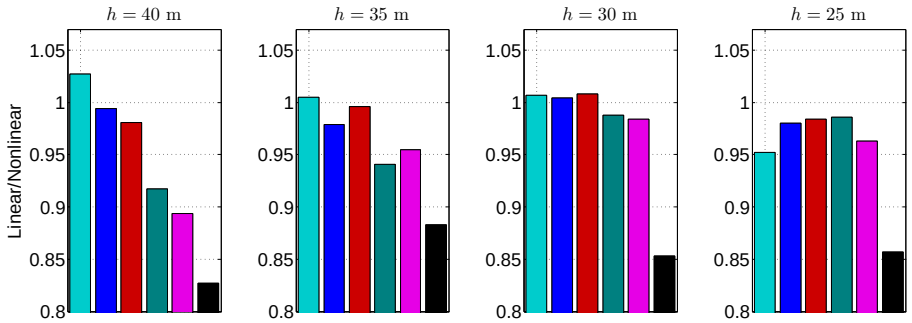

(d) Monopile, m = 5.

Figure 4.37: *The ratio between the linear and nonlinear equivalent loads for each wind and sea state and water depth.* *1a* *1b* *2* *3* *4* *5*

4.5.3 Accumulated equivalent loads

In the accumulated fatigue analysis the probability of occurrence of the wind and sea states are considered and the analysis indicates therefore whether the large difference in the linear and nonlinear equivalent loads of the largest sea states is important in the design of the wind turbine. The accumulated equivalent load, $L_{eq,acc}$ is based on the relative probability of occurrence of the six wind and sea states as stated in table 4.2 and is calculated as

$$L_{eq,acc} = \left(\sum_j L_{eq,j}^{\mathsf{m}} \frac{T_j}{T} \right)^{\frac{1}{\mathsf{m}}}, \tag{4.17}$$

where the jth load case occur the time T_j and T is the total time.
The accumulated equivalent load due to the linear and nonlinear wave realizations are compared in figure 4.38 at the four water depths. The accumulated equivalent load decreases as the water depth decreases both in the tower and in the monopile, which also was seen for the equivalent loads in figure 4.36 and is because the wave forcing and moment arm decreases as the water depth decreases.
The ratio between the accumulated equivalent load due to the linear and nonlinear sea states are stated in figure 4.39 for both damage exponents and at the four depths. The differences are as for the equivalent loads largest for $\mathsf{m} = 5$. The similarity in the accumulated equivalent load in the tower for $\mathsf{m} = 3$ and $\mathsf{m} = 5$ indicates that the accumulated equivalent load here is due to the smaller moments in the time series with high probability of occurrence. In the monopile there is a significant difference between the accumulated equivalent load for $\mathsf{m} = 3$ and $\mathsf{m} = 5$ and indicates that the accumulated equivalent load here depends on the large moments in the time series.
In the tower the linear and nonlinear accumulated equivalent load is more or less the same at the four water depths. The accumulated equivalent load due to the nonlinear wave realizations is a few percent larger at $h = 40\,\text{m}$ for $\mathsf{m} = 5$. The opposite is seen at $h = 30\,\text{m}$. In the monopile the accumulated equivalent load due to the nonlinear wave realizations is largest. The largest different is 9 % at $h = 40\,\text{m}$ and the smallest different is 2 % at $h = 30\,\text{m}$.
The fact that the linear accumulated equivalent load relative to the nonlinear accumulated equivalent load increases from $h = 40$ to $h = 30\,\text{m}$ and decreases again from $h = 30\,\text{m}$ to $h = 25\,\text{m}$ agrees with the explanation given above when the equivalent loads were analysed. The broad band forcing of the nonlinear wave realizations decreases as the water depth decreases, while it is more constant for the linear wave realizations. However, as the water depth decreases the steep wave excitation increases and begins to be dominating for $h = 25\,\text{m}$.
If the waves were fully converged the broad band forcing of both the linear and nonlinear wave realization is expected to be stronger, which would result in larger accumulated equivalent load. However, the problem apply both to the linear and nonlinear wave realizations and the differences between the linear and nonlinear wave realizations are therefore believed not to change significantly. Yet, it is an uncertainty in the results.
Opposite to this, if the inertia coefficient in the calculations of the hydrodynamic forces was corrected for the diffraction effects, it is expected that the broad band forcing would decease. For example, if the correction was included for a wave with frequency of 0.30 Hz on a water depth of 30 m the inertia coefficient would be reduced with ~ 40 % following the MacCamy-Fuchs-diagram shown in Sumer & Fredsøe (2006). For a wave with 0.25 Hz the inertia coeffecient would be reduced with ~ 12 %. Further, if the correction only is applied on the free waves in the wave spectrum, the reduction would be the same for linear and nonlinear wave forces. This would cause the high frequency waves to be less important in the accumulated equivalent load and could imply that the larger waves would be more important in the accumulated equivalent load, where the nonlinearity of the waves is stronger.

In figure 4.40 the relative contribution from each wind and sea state to the accumulated equivalent load is presented for $\mathsf{m} = 5$ only. With this figure it becomes more clear which of the five sea states that are important in the accumulated equivalent load.

In the tower wind and sea state *2* and *3* contribute more than 90 % to the accumulated equivalent load even though these two wind and sea states only occur 57 % of the time. In the monopile it is wind and sea state *3* and *4* that contribute most to accumulated equivalent load, approximately 75–80 %. This is interesting because wind and sea state *4* only occur 4 % of the time.
From figure 4.40 it is also seen that wind and sea state *4* contribute significant more to the accumulated equivalent load in the monopile than in the tower which can be explained with the aerodynamic damping which affects the tower more than the monopile.
For the largest sea state the contribution from the nonlinear wave realization is twice as large as the contribution from the linear wave realization. The largest wind and sea states contribution to the accumulated equivalent load increases with increasing water depth because the contribution from the wave forcing to the total forcing increases with the water depth and become larger relative to the wind forcing. This means that the wind and sea state with no aerodynamic damping where the wind turbine is parked become more important the larger the water depth is. This can also be seen in the tower for the smallest wind and sea state which contribute most for $h = 40\,\mathrm{m}$. Further it is seen that wind and sea state *5* contribute significant more to the accumulated equivalent load than its probability of occurrence of 0.2 %, particular in the monopile, which indicate that the largest sea states can be important in the accumulated equivalent load. Contrary, wind and sea state *1b* contribute significant less than the largest wind and sea state, even though it occur 50 times more.

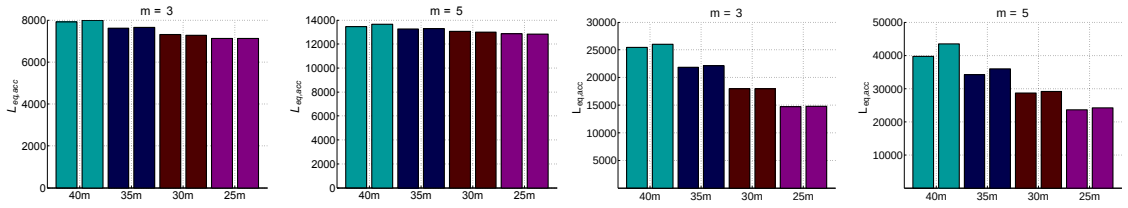

(a) Tower. **(b)** Monopile.

Figure 4.38: *The total accumulated equivalent load for all four water depths. For each water depth both the accumulated equivalent load due to the linear wave realizations (left bar) and the nonlinear wave realizations (rigth bar) are given.*

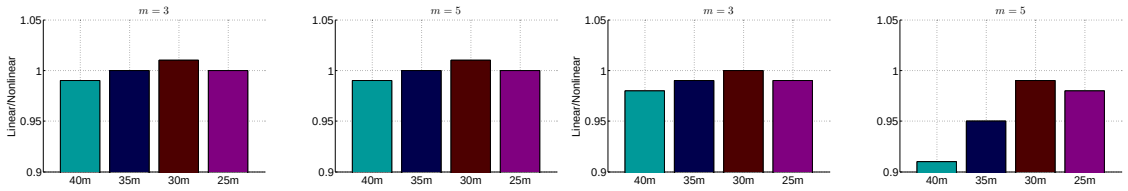

(a) Tower. **(b)** Monopile.

Figure 4.39: *The ratio between the linear and nonlinear total accumulated equivalent load for all four water depths.*

4.5.4 Summary

In the present section the linear and nonlinear equivalent loads have been compared. Also the accumulated equivalent load based on the six wind and sea states were calculated and compared. The equivalent loads increase as the sea states increase. The trend is most clear in the monopile, where the effects from the wind are less significant. Further, the equivalent loads decrease as the

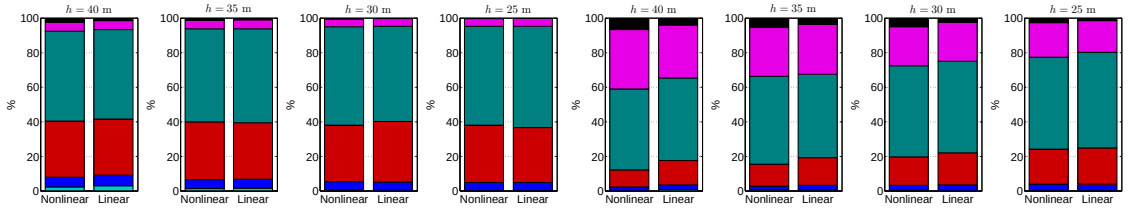

(a) Tower, $\mathsf{m} = 5$. **(b)** Monopile, $\mathsf{m} = 5$.

Figure 4.40: *The wind and sea states contribution to the total accumulated equivalent load for both the linear and nonlinear sea states and all four water depths.* *1a* *1b* *2* *3* *4* *5*

water depth decreases. Again the trend is most clear in the monopile and in the tower for the wind sea states where the wind turbine is parked.

The response in the tower depends primarily on the effects from the wind. The difference between the linear and nonlinear equivalent loads in the tower is therefore quite small when the wind turbine operates. It was only for wind and sea state *1a* and *5* where the effects from the wind are insignificant that a significant difference between the linear and nonlinear equivalent loads was seen. For wind and sea state *1a* the linear equivalent load is largest, which can be due to the broad band forcing which perhaps is largest for the linear wave realization. For wind and sea state *5* the nonlinear wave realization results in the largest equivalent loads due to the larger wave forcing and impulsive excitation.

In the monopile the response depends more on the wave forcing and the equivalent loads due to the nonlinear wave realizations are therefore largest for all wind and sea states except for wind and sea *1a*.

In the accumulated equivalent load it was also seen that the difference between the linear and nonlinear wave realizations are small in the tower. In the monopile for the largest water depths the nonlinear accumulated equivalent load is 5-8 % larger than the linear accumulated equivalent load. The effect of the broad band forcing appear to be an important factor in the accumulated equivalent load. If the broad band forcing is largest for the linear wave realizations it can cancel out the effect from the nonlinear wave forcing in the tower and almost also in the monopile. In this result it should be remembered that the waves in the high frequency part of the wave spectra are not fully converged, which perhaps causes the broad band forcing to be smaller than if the waves were converged. Opposite to this, the inclusion of diffraction effects could lead to smaller broad band forcing, which could imply that the larger waves in the wave realizations, where the nonlinearity is stronger, would contribute more to the accumulated equivalent load.

As the water depth decreases the steep wave excitation appears to increase. It can further seem as this effect begins to be stronger than the linear broad band forcing for $h = 25\,\mathrm{m}$.

It is further found that the largest wind and sea states despite their low probability of occurrence can be important for the accumulated equivalent load both when the linear and nonlinear waves are considered.

Chapter 5

Wind-wave misalignment

Aerodynamic damping is the main damping factor in offshore wind turbines, but exists primarily in the direction of the wind. The wind-wave-misalignment is therefore recognized to be an aspect which could be of great importance in the fatigue analysis, because of the small amount of aerodynamic damping in the direction of the waves. According to DNV-OS-J101 (2010) the misalignment between the wind and waves shall be included in the design if relevant. Stand-still conditions both below and above the cut-out wind speed, which was also considered in the previous chapter, are also an important aspect because the aerodynamic damping is small and in case of storm events the co-existing wave conditions are harsh.
Fischer *et al.* (2011) considered all power and idling load cases from IEC61400-3 (2009) and calculated the non-lifetime weighted equivalent loads when the angle between the wind and wave directions went from 0°-360°. They compared the overturning moment at mudline both in the fore-aft and side-to-side direction. The moment in the fore-aft direction was 30 % larger when the waves were in this direction compared to when they were in the side-to-side direction. The moment in side-to-side direction was 5 times larger when the waves were in side-to-side direction compared to when they were in the fore-aft direction. The analysis indicated that at sites with extreme misalignment it is important to to take the directionality of the waves into account.
Norton (2003) also investigated the effects of misalignment on the fatigue damage. 1386 ten minutes simulations were carried out based on 7 years data from the Dutch sea, including the probability distribution of misalignment between the wind and waves. To investigate the effects of the misalignment 205 ten minute calculations were also carried out with aligned wind and waves. The equivalent loads in the bottom of the tower were then calculated in intervals of 15 degrees for each load case and summed including probabilities of occurrence of each load case. The difference in the fatigue damage was up to 3% when the misaligned and aligned calcualtions were compared. Afterwards Norton (2003) considered the same load cases but where the misalignment was increased by 60° for each load case. The difference in the fatigue damage increased significantly and was up to 15% when the misaligned and aligned calcualtions were compared.
In this chapter the misalignment between the wind and waves are included in the analysis. The analysis is based on the same wind and sea states as in chapter 4 and focus is again on comparing the effects from the linear and the nonlinear wave realizations.
van der Meulen *et al.* (2012) simulated all the load cases required by the IEC-standards with both linear and second order nonlinear irregular waves. The equivalent fatigue load increased with 7 % in the foundation when the second order loads were considered. The increase in the fatigue damage was due to the waves perpendicular to the wind direction and during high wind speeds where the turbine was idling. It is therefore expected that the difference in the response and fatigue damage due to the linear and nonlinear waves will differ from what was found in previous chapter with aligned wind and waves. From these analysis it should be remembered that the broad band forcing may be a little too small because the waves are not fully converged. However the broad band forcing might also be too large because the diffraction effects are neglected.
In first part of the chapter the probability distribution for wind, waves and misalignment are found, based on data from the UPWIND-project[1]. Hereafter dynamic analysis are performed and

[1] `http://www.upwind.eu/`

the response in the bottom of the tower and monopile investigated for cases where the waves are in the side-to-side direction. This is followed by an analysis of the equivalent loads and accumulated equivalent load. In the last section of the present chapter a small misalignment study with larger waves is considered.

5.1 The probability of occurrence

In order to find a reasonable probability distribution for wind, waves and misalignment the environmental data from the UPWIND-project is used. In the UPWIND-project, design bases for three different sites were defined. The site considered here is located in the Dutch North Sea and has a water depth of 25m and is presented in more detail in Fischer *et al.* (2010). Assuming that the metocean data from section 4.1 and the wind-wave-misalignment-distribution can be combined should be acceptable because both data come from the North Sea.

In the report of Fischer *et al.* (2010) directional scatter diagram for all wind speeds are stated. The wind bins cover 2 m/s in such a way that the bin for $V = 1-3$ m/s covers all the wind observations in the interval $1 \leq V < 3$ m/s. The 12 directional bins each cover 30 degrees in such a way that the bin for $D = 30°$ covers all the data in the interval $15 \leq D < 45$. The misalignment between the wind and waves considered in the present report is therefore based on the scatter diagrams for the wind intervals where the six wind speeds from chapter 4 belong.

In the scatter diagram the probabilities for all combinations of wind- and wave directions are stated. In the present analysis the focus is on the misalignment between the wind and waves and not their individual direction. The scatter diagram is therefore reorganised so that the wind direction always is zero degrees and the wave direction is re-located relatively to the wind direction. The reorganisation results in a vector with probabilities of how often the angle between the wind and wave direction is in the interval 345°–15°, 15°–45° and up to 315°–345°.

The analysis is simplified more, by ignoring whether the waves have a positive or negative direction, so the probability of the interval 15°–45° are added to the interval 315°–345°, etc.

The probabilities stated in the scatter diagrams in Fischer *et al.* (2010) are the probabilities in relation to all wind bins and directions. To use the probabilities in the present analysis the relative probability of occurrence of the different directions for each wind bin are found

$$\hat{P}_{rel,i,j} = \frac{\hat{P}_{i,j}}{\sum_i \hat{P}_{i,j}}. \tag{5.1}$$

The index i represents the seven wave directions $(0°, 30°, 60°, ..., 180°)$ and j the six wind speeds considered.

Finally the relative probabilities, $\hat{P}_{rel,i,j}$, are multiplied with the probability of occurrence of the corresponding wind speed, $\hat{P}_{rel,j}$, used in in the fatigue analysis in section 4.5 and repeated in table 5.1. In this way the sum of the relative probabilities is equal to one, $\sum_{i=1}^{7}\sum_{j=1}^{6} \hat{P}_{rel,i,j} = 1$. The wind-wave-misalignment-distribution for the six wind speeds and sea states are stated in table 5.1.

V	H_s	T_p	$\hat{P}_{rel,j}$	$\hat{P}_{rel,i,j} \cdot 10^2$						
(m/s)	(m)	(s)		0°	30°	60°	90°	120°	150°	180°
2	0.99	5.50	0.1	1.038	2.247	1.803	1.515	1.247	1.218	0.587
6	0.99	5.50	0.3	6.595	10.074	5.683	3.162	1.994	1.688	0.741
9	1.41	6.17	0.35	11.103	14.269	5.210	2.004	1.074	0.666	0.288
14	2.57	7.56	0.22	9.131	9.603	1.878	0.528	0.223	0.144	0.105
20	4.40	9.16	0.04	2.028	1.722	0.190	0.013	0.015	0.010	0.000
28	6.75	11.41	0.002	0.121	0.076	0.007	0.000	0.002	0.000	0.000

Table 5.1: *The probability of occurrence of the six wind and sea states including the misalignment between the wind and wave directions.*

The probability of occurrence decreases as the angle between the wind and waves increases for all six wind speeds. The angle between the wind and waves are below 45 degrees 68 % of the time. As the wind speed increases the probability of large misalignments decreases. For the largest wind speed for example the probability of misalignment only exits for angles of 30°, 60° and 120°. This is because the larger the wind speeds are the larger the probability that the wind and sea state are due to the same weather regime.

5.2 Dynamic analysis

The focus in this analysis is to investigate the response due to the waves in the tower and monopile in the direction perpendicular to the wind direction (side-to-side direction), where the aerodynamic loads and damping are expected to be insignificant. Further, this response is compared to the response in the fore-aft-direction for the situation where the waves also are in fore-aft direction. A drawing with the fore-aft and side-to-side directions is shown in figure 5.1.

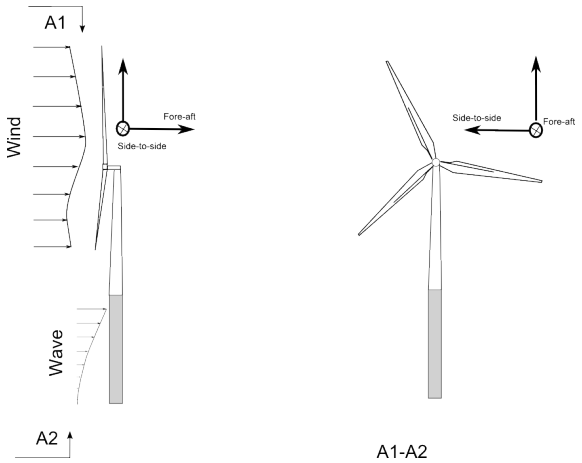

Figure 5.1: *A sketch of a wind turbine seen from the front and the side. In the figure the fore-aft and side-to-side direction are given.*

The overturning moment in the bottom of the tower and monopile is considered in the side-to-side direction for the same wind and sea states as was analysed in section 4.4, i.e. wind and sea state *1a*, *1b*, *3* and *5* at a water depth of $h = 30\,\text{m}$. In the present analysis, however, the waves are also in the side-to-side direction so perpendicular to the wind direction.

5.2.1 Wind and sea state *1a* and *1b*

The overturning moments in the bottom of the tower and monopile for wind and sea state *1a* in the side-to-side direction are shown in figure 5.2a and 5.2b in the same time sequence which was considered in section 4.4. Both the moment due to the linear and nonlinear wave realizations and the linear and nonlinear surface elevations are shown in the figures. In the figure the moments in the bottom of the tower and in the bottom of the monopile in the fore-aft direction for the case with aligned wind and waves from section 4.4, figure 4.24 and 4.25, are also indicated with a grey line for comparison.
Both the linear and nonlinear moment in the tower and the monopile are very similar to the case with waves in the fore-aft direction. The structural first eigenfrequency is excited both due to the linear and nonlinear wave realizations. In the tower the excitation is a little smaller when the waves are in the fore-aft direction and the excitation also dampens faster. In figure 5.4 a cross section of two blades with pitch angles of 0° and 30°, respectively, are shown. It is seen that if the blade is pitch 30° the projected area of the blade in the fore-aft direction still is significant. There can therefore still be some some aerodynamic damping in the fore-aft direction, when the blades are pitched to an angle of 30°.
Similar results are seen in the monopile.

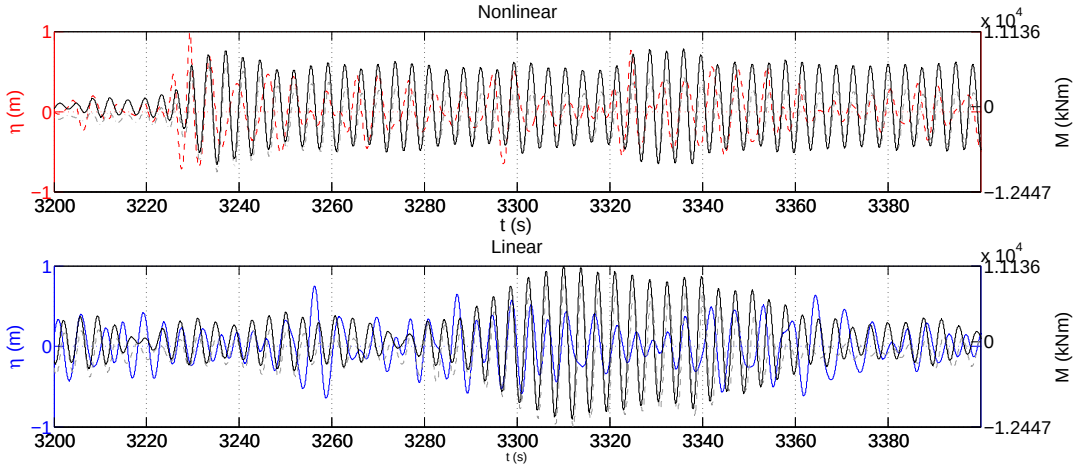

(a) Tower.

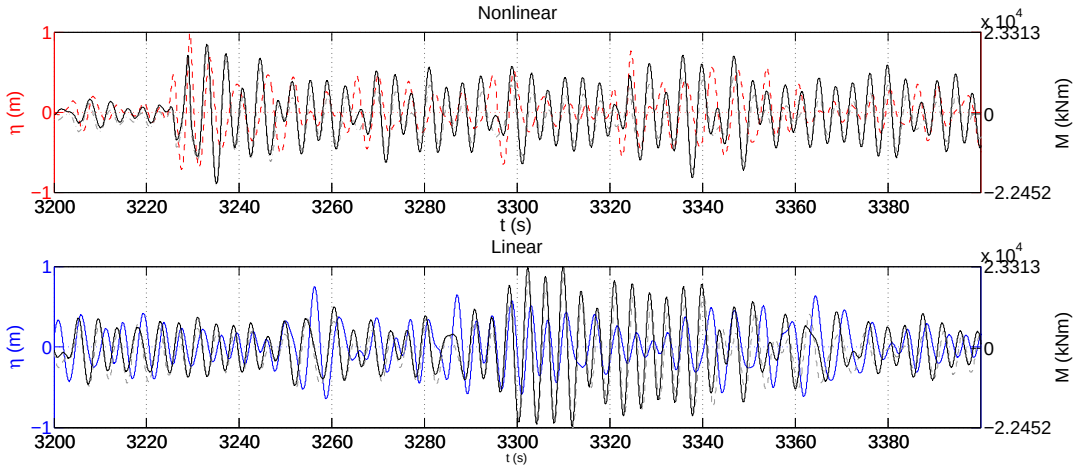

(b) Monopile.

Figure 5.2: *Nonlinear and linear surface elevation for sea state 1a and the corresponding moment in the bottom of the tower and in the bottom of the monopile in the side-to-side direction for a situation where the waves also are in the side-to-side direction. The grey dashed line show the moment in the bottom of the tower and in the bottom of the monopile in the fore-aft direction for the case with aligned wind and waves from figure 4.24 and 4.25, respectively.*

The overturning moments due to case *1b* in the side-to-side direction are shown in figure 5.3a-5.3b both due to the linear and nonlinear wave realizations. The moment in the bottom of the tower and in the bottom of the monopile in the fore-aft direction for the case with aligned wind and waves from figure 4.26 and 4.27, respectively, are indicated in the figures with grey lines.

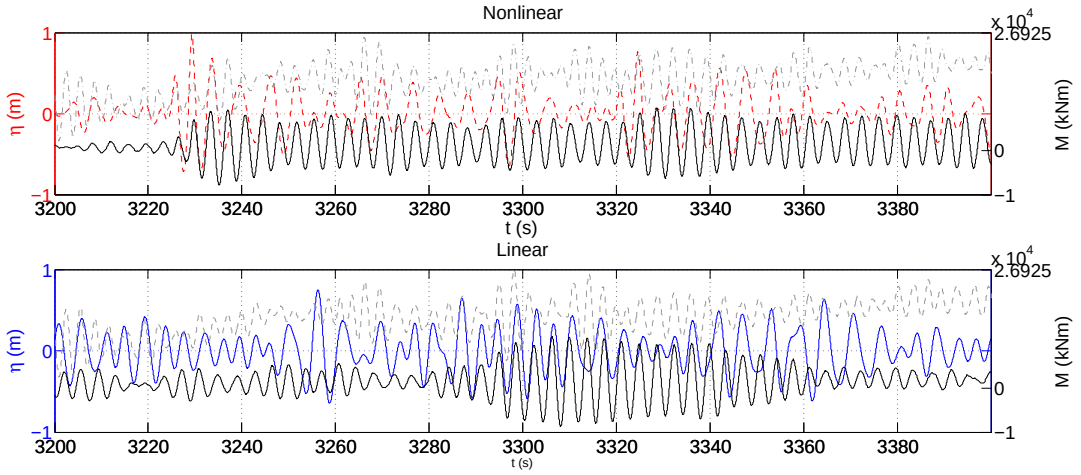

(a) Tower.

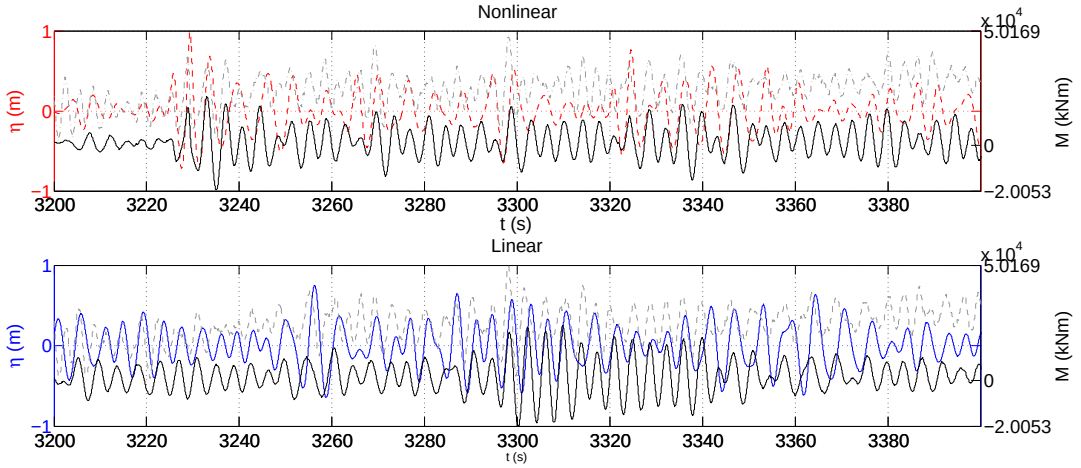

(b) Monopile.

Figure 5.3: *Nonlinear and linear surface elevation for sea state 1b and the corresponding moment in the bottom of the tower and in the bottom of the monopile in the side-to-side direction for a situation where the waves also are in the side-to-side direction. The grey dashed line show the moment in the bottom of the tower and in the bottom of the monopile in the fore-aft direction for the case with aligned wind and waves from figure 4.26 and 4.27, respectively.*

It is clear that the effects from the wind are insignificant in the side-to-side direction. There is a large difference between the moments in the side-to-side direction and the moments in fore-aft direction. The moments in the fore-aft direction oscillate around a larger mean value, due to the aerodynamic forcing. Both the linear and nonlinear overturning moments in the side-to-side direction are very similar to the moments of case *1a*.

Although difficult to see from the figure, the magnitude of the excitations is sometimes a little smaller compared to case *1a* (figure 5.2a-5.2b). In case *1a* the blades are pitched to 30° which perhaps results in larger aerodynamic forcing in the side-to-side direction due to the turbulent wind and therefore larger excitation.

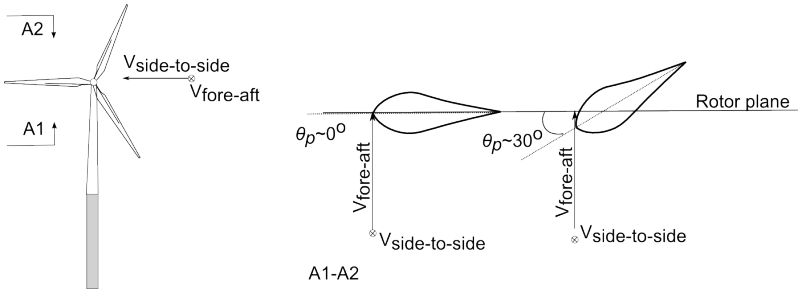

Figure 5.4: *A cross section of a blade with different pitch angle.*

5.2.2 Wind and sea state *3*

In section 4.4 where the wave realizations of the third sea state were considered in the fore-aft direction it was difficult to identify the response due to the waves in the overturning moments both in the tower and monopile. This changes when the waves are in side-to-side direction as shown in figure 5.5a-5.5b, where the overturning moments in the bottom of the tower and monopile due to the linear and nonlinear wave realizations are shown and compared to the moments in the bottom of the tower and in the bottom of the monopile in the fore-aft direction for the case with aligned wind and waves. The moments in the fore-aft direction both in the tower and monopile oscillate around a larger mean value, due to the aerodynamic forcing, while the amplitude of the oscillations are similar in the two directions.
In the tower in the side-to-side direction, the structural first eigenfrequency is excited all the time. Further it is seen that the excitation due to the linear and nonlinear wave realization is of the same magnitude. If the full time series of 7200 s is considered (not shown here) it appears as the linear wave realization results in most excitation. This is in accordance with expectations, since it was found in chapter 4.4 that the broad band forcing is largest for the linear wave realization.
The overturning moments in the monopile are also excited but are more static than in the tower and is to a larger extent dominated by the wave forcing.

5.2.3 Wind and sea state *5*

For wind and sea state *5* the angle between the wind and waves are only 60° because the probability of a 90° angle is zero. The moments in the bottom of the tower and bottom of the monopile due to the linear and nonlinear wave realizations, shown in figure 5.6a-5.6b, are still in the side-to-side direction. The moments are compared to the moments in the bottom of the tower and in the bottom of the monopile in the fore-aft direction for the case with aligned wind and waves from figure 4.32 and 4.33.
In the tower in the side-to-side direction the overturning moment due to the linear and nonlinear wave realization are very similar. The excitation of the structural first eigenfrequency occur at the same instance of time and the oscillations are very similar, for example at time $t = 2525\,\text{s}$ and $t = 2650\,\text{s}$. The excitations are not connected to the large waves in the time series and are therefore primarily due to effects from the turbulent wind in the side-to-side direction. The wind forcing in the side-to-side direction becomes significant because the blades are pitched to 87°. The projected area of the blades are therefore turned against the turbulent wind in the side-to-side direction. The magnitude of the moment in the tower is of same size as the moments in the fore-aft direction (grey curves in the figure), where the excitation is due to the forcing from the waves.
The response in the tower due to the waves is not as apparent as was seen in the fore-aft direction in section 4.4. This is probably both because the angle between the wind and wave direction only is 60° but also because the aerodynamic damping is stronger in the side-to-side direction due to the pitching of the blades.
In the monopile the response from the waves is seen more clearly than in the tower, because the monopile to a larger extent is dominated by the waves, and the response is more static. However, the response from the waves in the monopile is not as dramatical as was seen in section 4.4, where the waves were in the fore-aft direction, because the angle of the waves only are 60°. The

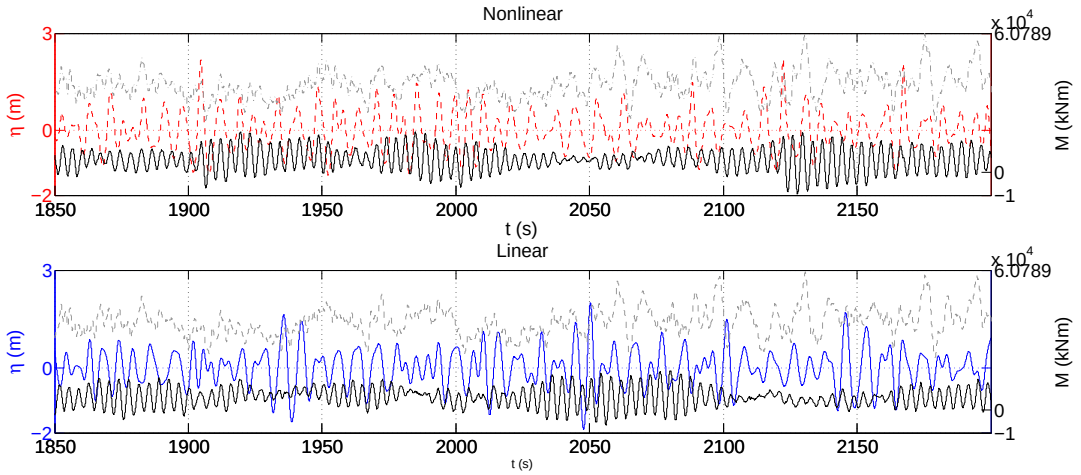

(a) Tower.

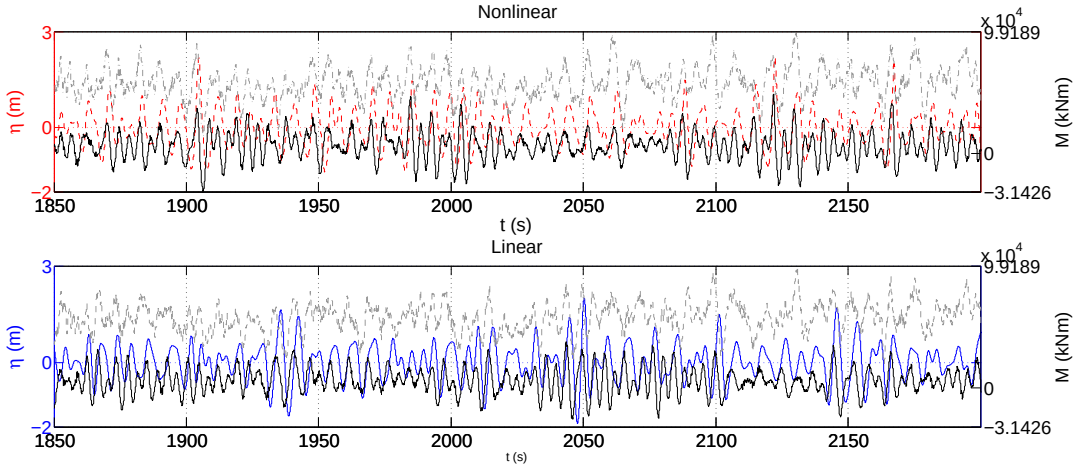

(b) Monopile.

Figure 5.5: *Nonlinear and linear surface elevation for sea state 3 and the corresponding moment in the bottom of the tower and in the bottom of the monopile in the side-to-side direction for a situation where the waves also are in the side-to-side direction. The grey dashed line show the moment in the bottom of the tower and in the bottom of the monopile in the fore-aft direction for the case with aligned wind and waves from figure 4.29 and 4.30, respectively.*

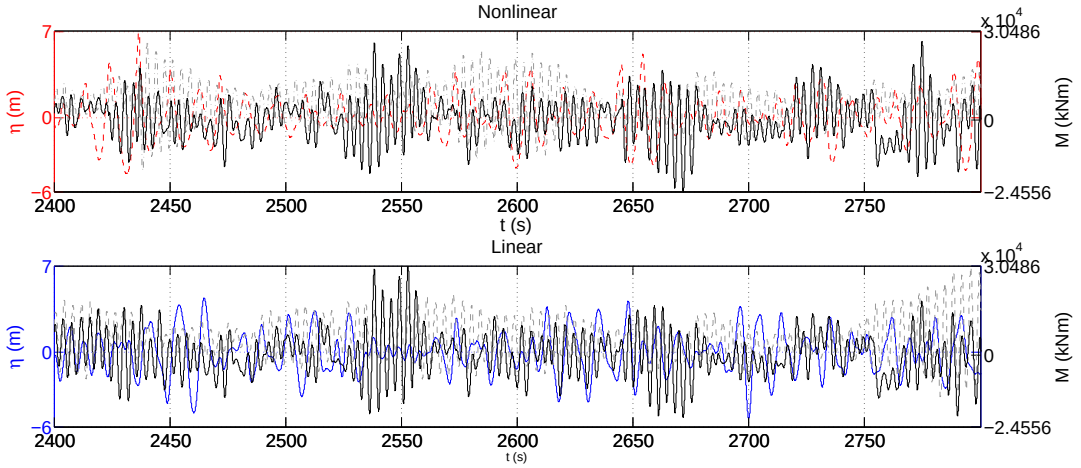

(a) Tower.

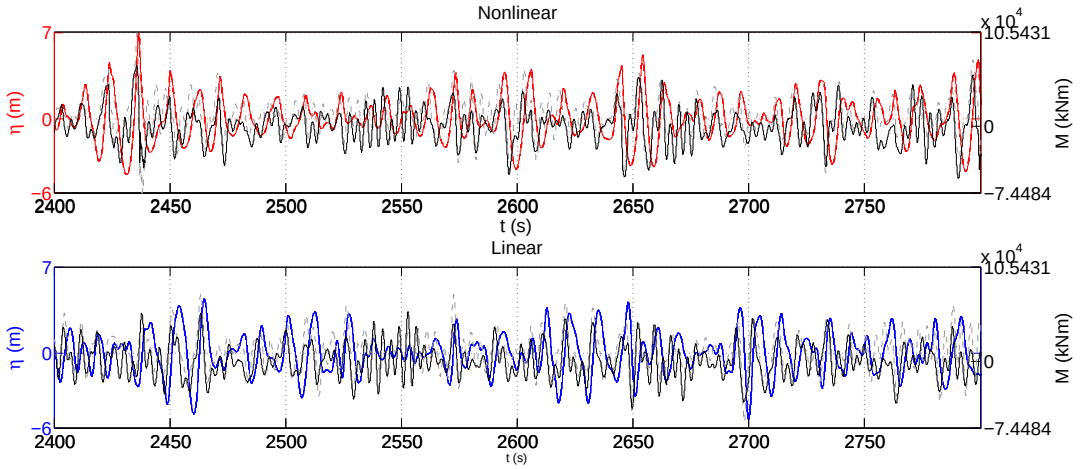

(b) Monopile.

Figure 5.6: *Nonlinear and linear surface elevation for sea state 5 and the corresponding moment in the bottom of the tower and in the bottom of the monopile in the side-to-side direction for a situation where the waves also are in the side-to-side direction. The grey dashed line show the moment in the bottom of the tower and in the bottom of the monopile in the fore-aft direction for the case with aligned wind and waves from figure 4.33 and 4.33, respectively.*

impulsive responses which occur due to large steep nonlinear waves in the fore-aft direction are therefore difficult to identify in the time series of the overturning moments in the side-to-side direction. Further, the response due to the aerodynamic forcing is also recognised in the monopile particular at time $t = 2525\,\mathrm{s}$ due to the turbulent wind in the side-to-side direction and because the blades are pitched to 87°.

5.3 Fatigue analysis

The fatigue analyses are similar to those in section 4.5 but now the misalignment between the wind and wave direction is included. The equivalent loads and accumulated equivalent load are only calculated for $\mathsf{m} = 5$, because it was found in section 4.5 that the differences between the linear and nonlinear loads were most pronounced for this case.
The equivalent loads and accumulated equivalent load are based on the overturning moments in the bottom of the tower and monopile both in the fore-aft and side-to-side directions and are calculated for the same four water depths, which were considered in chapter 4, $h = 40\mathrm{m}$, $h = 35\mathrm{m}$, $h = 30\mathrm{m}$ and $h = 25\mathrm{m}$.

5.3.1 Equivalent loads

The equivalent loads for each wind and sea state are calculated for each direction of the waves (from 0°-180°). The equivalent loads due to the linear and nonlinear wave realizations are compared in figure 5.7-5.10.
In the fore-aft direction the linear and nonlinear equivalent loads must be the same when the wave direction is 90° and in the side-to-side direction they must be the same when the wave directions are 0° and 180°, because the response in these cases is only due to the aerodynamic forcing. This is also seen in the figures. In the fore-aft direction the equivalent loads decrease as the waves become perpendicular to the wind direction, which is expected because the forcing in the fore-aft direction thereby reduces. However, in the tower this effect is very small for the cases where the wind turbine operates, where the effects from the waves are negligible relatively to the contribution from the wind.
In the monopile the nonlinear equivalent loads are larger or equal to the linear equivalent loads for almost all wind and sea states at the four depths, because the monopile is relative stiff and exposed directly by the waves, and because the nonlinear wave forcing is largest. The difference between the linear and nonlinear equivalent loads are not that significant in the side-to-side direction. This can be due to the broad band forcing which is largest for the linear waves, and even though the response in the top of the monopile mainly is quasi-static there also is a dynamic response.
In the tower the effects of the broad band forcing are also seen. At the three largest depths the linear equivalent loads of wind and sea state *1a* to *4* are larger than the nonlinear equivalent loads in the side-to-side direction. For these sea states the linear broad band forcing is therefore a stronger effects than the nonlinear wave forcing. However, for $h = 25\,\mathrm{m}$ the effects of the nonlinear wave steepness is might seen, because the nonlinear equivalent load for wind and sea state *4* here is larger than the linear equivalent loads.
For wind and sea state *5* the nonlinear equivalent loads in the tower are largest. However in the side-to-side direction for the three largest water depths it is seen that the linear and nonlinear equivalent loads for this wind and sea state are very similar. This is due to the turbulent wind which results in a large aerodynamic forcing in the side-to-side direction because the blades are pitched 87°. The aerodynamic damping is also stronger in this direction, so the effects from the wave realizations are dampened more in the side-to-side direction than in the fore-aft direction.

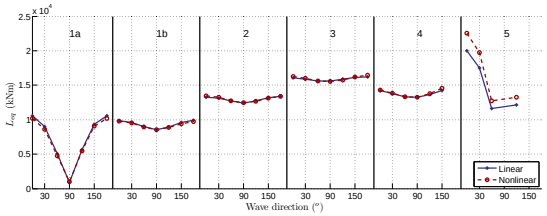

(a) Tower, fore-aft.

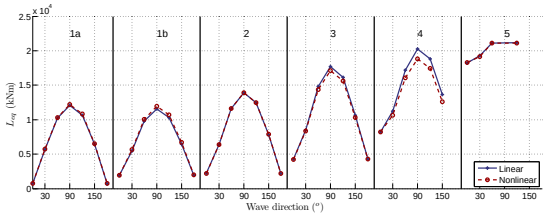

(b) Tower, side-to-side.

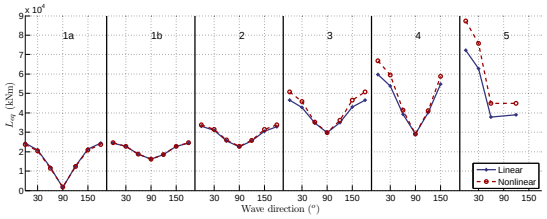

(c) Monopile, fore-aft.

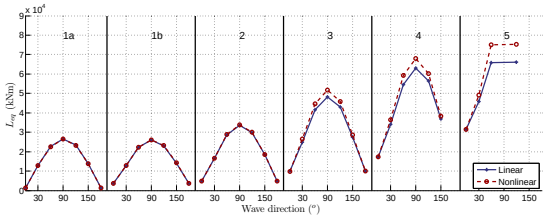

(d) Monopile, side-to-side.

Figure 5.7: *The linear and nonlinear equivalent loads for $h = 40$ m in the fore-aft and side-to-side direction for $\mathsf{m} = 5$. The wave direction changes from being aligned with the wind direction (0°) to be in the opposite direction of the wind direction (180°).*

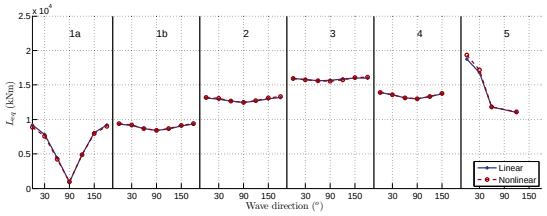

(a) Tower, fore-aft.

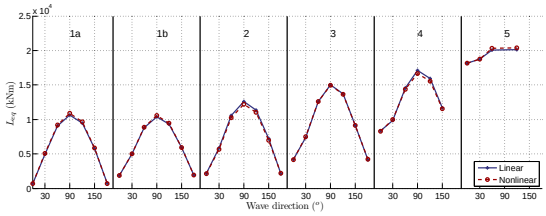

(b) Tower, side-to-side.

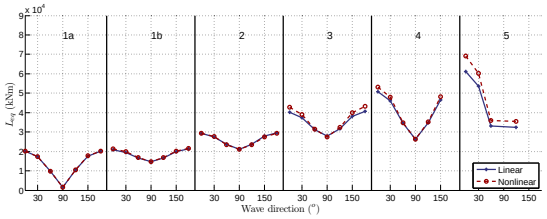

(c) Monopile, fore-aft.

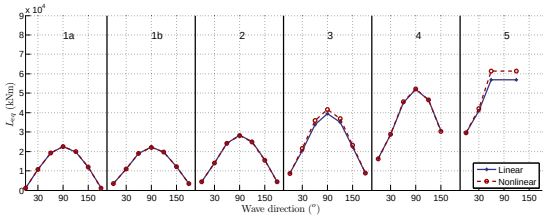

(d) Monopile, side-to-side.

Figure 5.8: *The linear and nonlinear equivalent loads for $h = 35$ m in the fore-aft and side-to-side direction for $\mathsf{m} = 5$. The wave direction changes from being aligned with the wind direction (0°) to be in the opposite direction of the wind direction (180°).*

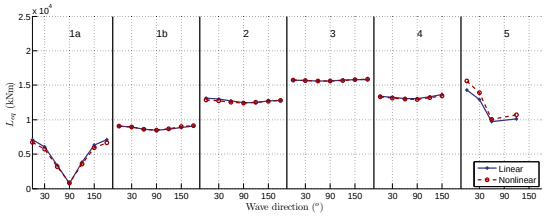

(a) Tower, fore-aft.

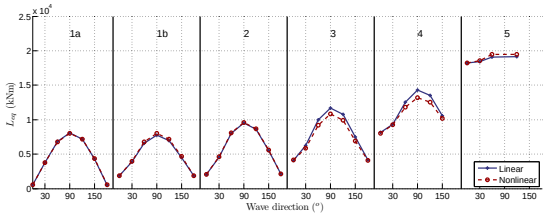

(b) Tower, side-to-side.

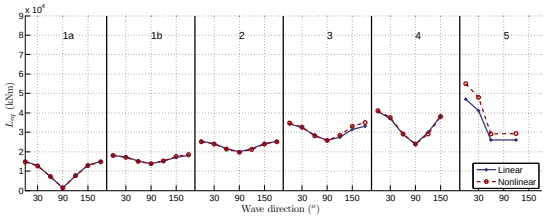

(c) Monopile, fore-aft.

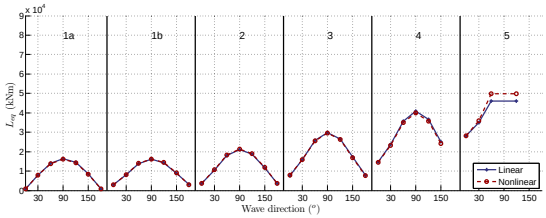

(d) Monopile, side-to-side.

Figure 5.9: *The linear and nonlinear equivalent loads for* $h = 30$ *m in the fore-aft and side-to-side direction for* $\mathsf{m} = 5$*. The wave direction changes from being aligned with the wind direction (*$0°$*) to be in the opposite direction of the wind direction (*$180°$*).*

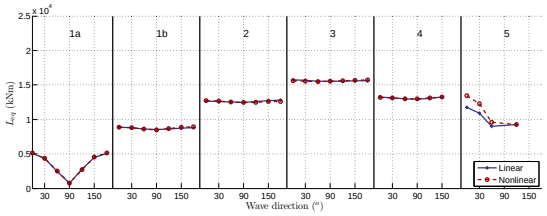

(a) Tower, fore-aft.

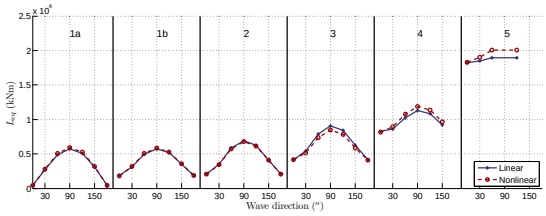

(b) Tower, side-to-side.

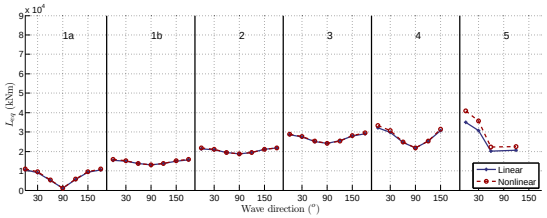

(c) Monopile, fore-aft.

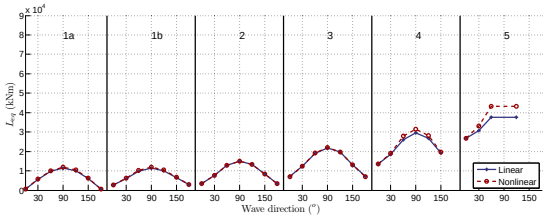

(d) Monopile, side-to-side.

Figure 5.10: *The linear and nonlinear equivalent loads for* $h = 25$ *m in the fore-aft and side-to-side direction for* $\mathsf{m} = 5$*. The wave direction changes from being aligned with the wind direction (*$0°$*) to be in the opposite direction of the wind direction (*$180°$*).*

5.3.2 Accumulated equivalent load

The accumulated equivalent load due to the linear and nonlinear wave realization are calculated where the misalignment between the wind and waves is included.
In figure 5.11 the total accumulated equivalent load both due to the linear and nonlinear wave realizations is shown in the fore-aft and side-to-side direction. In the fore-aft direction the accumulated equivalent load is a little smaller than was obtained in section 4.5 where the waves and wind were aligned. This is because the dominating direction of the waves is still in the fore-aft direction and because the aerodynamic forcing results in the largest contribution to the accumulated equivalent load. In the side-to-side direction the accumulated equivalent load is smaller than in the fore-aft direction, because the aerodynamic forcing is almost absent in this direction. The difference between the equivalent loads in the fore-aft and side-to-side direction increases as the water depth decreases which must be because the contribution from the waves to the accumulated equivalent load reduces as the water depth decreases and in the side-to-side direction the effects from the wind is less significant.

Figure 5.12 shows the ratio between linear and nonlinear accumulated equivalent load both in the fore-aft and side-to-side direction for all four water depths. In the fore-aft direction the difference in the accumulated equivalent load is similar to section 4.5 where the wind and waves were aligned. In the present analysis it is therefore not so important whether the misalignment between the wind and waves are included in the fore-aft direction, when the effects from the linear and nonlinear wave realizations are compared.

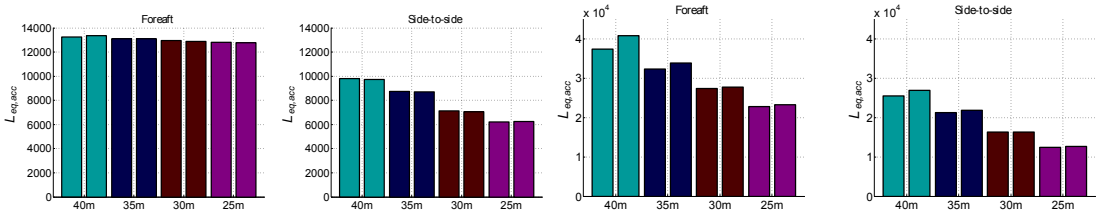

(a) Tower **(b)** Monopile

Figure 5.11: *The total accumulated equivalent load for all four water depths. For each water depth both the accumulated equivalent load due to the linear wave realizations (left bar) and the nonlinear wave realizations (rigth bar) are given.*

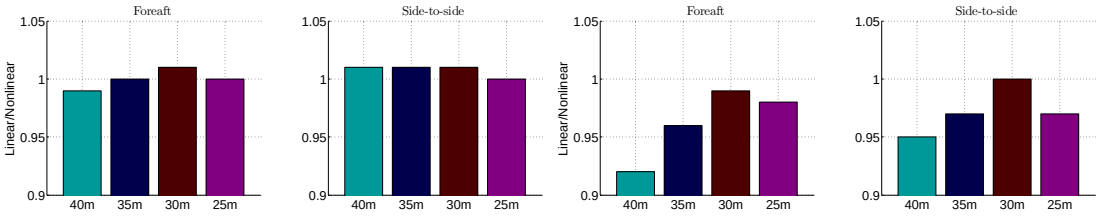

(a) Tower **(b)** Monopile

Figure 5.12: *The ratio between the linear and nonlinear accumulated equivalent load in case of misaligned wind and waves both in the fore-aft and side-to-side direction for* $\mathsf{m} = 5$.

The linear accumulated equivalent load becomes larger relative to the nonlinear accumulated equivalent load for $h = 40\,\mathrm{m}$ to $h = 30\,\mathrm{m}$ both in the tower and in the monopile in the fore-aft direction and in the monopile in the side-to-side direction. This has already been explained by the fact that the broad band forcing of the nonlinear wave realizations decreases as the water depth decreases

because more energy is moved to higher and lower frequencies which does not apply for the spectra of the linear wave realizations. Another factor that can influence the decrease in the nonlinear accumulated equivalent load relative to the linear accumulated equivalent load from $h = 40\,\text{m}$ to $h = 30\,\text{m}$ can be that in section 4.5 it was seen that the largest wind and sea state contribute less to the accumulated equivalent load the smaller the water depth is. It was also seen that for the largest wind and sea state the contribution from the nonlinear wave realization was twice as large as the contribution from the linear wave realization. This can also explains why the difference between the linear and nonlinear accumulated equivalent load in the tower in the side-to-side direction is constant for $h = 40\,\text{m}$ to $h = 30\,\text{m}$. The probability that the largest wind and sea state occur in the side-to-side direction is very small, and the contribution from the largest sea states to the accumulated equivalent load in the side-to-side direction is therefore also very small. The difference which was seen between the linear and nonlinear contribution to the accumulated equivalent load for the largest wind and sea state at the largest water depths in the fore-aft direction is therefore insignificant in the side-to-side direction.
For $h = 30\,\text{m}$ to $h = 25\,\text{m}$ the nonlinear accumulated equivalent load becomes larger relative to the linear accumulated equivalent load both in the tower and in the monopile and both direction. This has also already been explained by the fact that the nonlinearity of the waves increases as the water depth decreases. The nonlinear waves therefore become more steep compared to the linear waves.

The tower is wind dominated, and feels only the waves because the pile is moving, so the difference between the linear and nonlinear accumulated equivalent load is smaller in the tower than in the monopile, because the effects from the wind are stronger. Further, the dynamic response in the tower is stronger compared to the dynamic response in the monopile. Since the broad band effects are found to be largest for the linear wave realizations this explain why the difference between the linear and nonlinear accumulated equivalent load in the tower is so small and why the linear accumulated equivalent load actually is largest at some water depths also in the side-to-side direction where the aerodynamic damping for most cases are insignificant.

The monopile is relatively stiff and exposed directly by the waves, which explains why the nonlinear accumulated equivalent load is larger than the linear accumulated equivalent load. The trend in the fore-aft and side-to-side direction is the same, though there are some variations. In the fore-aft direction the difference between the linear and nonlinear accumulated equivalent load is larger than in the side-to-side direction for $h = 40 - 30\,\text{m}$. This is both due to the broad-band excitation which is stronger in the side-to-side direction due to the lack of aerodynamic damping but also because the probability for the largest sea states to occur in the side-to-side direction is very small and the difference between the linear and nonlinear wave forcing is largest for the largest waves. For $h = 25\,\text{m}$ the difference between the linear and nonlinear accumulated equivalent load is larger in the side-to-side direction compared to the fore-aft direction. This can as discussed previously be because the wave steepness increases as the water depth increases and the nonlinear waves become more steep compared to the linear waves. This trend is off cause more obvious in the side-to-side direction where the aerodynamic forcing and damping are less significant.

5.4 Structural analysis with larger waves

In the analysis of chapter 4 and first part of chapter 5 the nonlinearity of the wave realizations was found not to be that important for accumulated equivalent load of the aeroelastic calculation. This was due to the broad band forcing which was largest for the linear waves. For other conditions it can be the nonlinear waves which result in the largest excitation of the structures first natural frequency and which generate the largest accumulated equivalent load.
In Schløer *et al.* (2012), similar analyses as seen in section 4.4 and 4.5 were done but for some other wind and sea states. The analysis of Schløer *et al.* (2012) suggested that the wave nonlinearity can change the wave induced accumulated equivalent load level significantly. The analysis was based on five representative JONSWAP sea states with increasing significant wave height. The significant wave heights were larger relative to the wind speed than for the wind-wave climates of chapter 4

and previous in the present chapter. These sea states are therefore applied here to investigate the effect from wave nonlinearity to the accumulated equivalent load when the misalignment between the wind and stronger waves are included in the analysis.
The relationship between the significant wave height and the peak periods was given by a simple relation

$$T_p = \tilde{\kappa}\sqrt{H_s}. \tag{5.2}$$

For the present sea states $\tilde{\kappa} = 4.38$. The relationship is given in DNV-OS-J101 (2007) to be used in deep water and has been used in many studies (e.g. Gravesen *et al.* (2003), who used $\tilde{\kappa} = 4.7$ and Walter (1999), who used $\tilde{\kappa} = 2.12$). For comparison the $\tilde{\kappa}$-value for the sea states considered in chapter 4 are between 4.4 and 5.3.
The significant wave height and peak wave period are stated in table 5.2. The waves were generated in a water depth of 135 m and moved up along a sloping sea bed with a slope of 1:25 and were considered in a water depth of 40 m. In Schløer *et al.* (2011) it was found that an increase in the steepness of the sea bed slope can resulte in larger extreme forces, in particular for the nonlinear forces. This can be because the steepness of the waves increases as the slope increases. Hence relative to the waves of chapter 4 and previous in the present chapter the waves are both larger and on a steeper slope. Both effects are expected to enhance the wave forcing.
In the aeroelastic computations in Schløer *et al.* (2012), two situations were considered for each of the five sea states. One where a single constant and small wind speed was applied for all five sea states and one where the wind was turbulent and the wind speed increased with increasing significant wave height. In the present analysis only the cases with the turbulent "more realistic" wind are considered. The five turbulent wind velocities were found by use of the joint probabilistic model of Johannessen *et al.* (2002), based on data from the northern North Sea with the wind velocity as the primary parameter

$$\hat{P}(V, H_s, T_p) = \hat{P}(V) \cdot \hat{P}(H_s|V) \cdot \hat{P}(T_p|V, H_s). \tag{5.3}$$

The wind speeds probability of occurrence were also based on this joint density distribution model as stated in table 5.2. All wind speeds are in the range where the wind turbine operates.
The diameter and the thickness of the monopile is $D = 6.8\,\mathrm{m}$ and $\mathtt{t} = 0.105\,\mathrm{m}$. The diameter is therefore larger than the monopile in a water depth of 40 m in chapter 4 and previous in the present chapter. However, the first structural eigenfrequency is the same, $\hat{f} = 0.27\,\mathrm{Hz}$.
It should further be noted that for the present calculations the number of grid points in the vertical direction, $N_z = 9$, is also too small to describe the waves in the high frequency part of the spectrum. The same problem with the convergence which was found for the wave realizations in chapter 4, is therefore also expected to exist for the present wave realizations.
In Schløer *et al.* (2012) it was found that the nonlinear effects were strong for all five sea states. The structural response was compared for cases where the wind speed was constant and small. The excitation from the nonlinear wave realizations were significantly larger than the excitation from the linear wave realizations. Impulsive responses were further seen even for the second smallest nonlinear wave realization.

In the present analysis the misalignment between the wind and waves are included in the fatigue analysis. The misalignment are found in the same way as explained in section 5.1 using the scatter diagrams in Fischer *et al.* (2010). The misalignment between the wind and wave directions and their probability of occurrence are stated in table 5.2. The probability is largest for the smallest wind velocity (53 %) and smallest for the largest wind speed (0.2 %). It is further seen that as the wind speed increases the probability of large misalignments decreases and that the probability of occurrence is largest when the angle between the wind and waves are 30° for the three smallest wind speeds.
The equivalent loads and accumulated equivalent load is calculated in the same way as explained in section 4.5 and is based on one hour time series.
The linear and nonlinear equivalent loads of the overturning moment in the bottom of the tower and monopile are compared in figure 5.13 both in the fore-aft and side-to-side direction.

T_p (s)	H_s (m)	V (m/s)	I_t (-)	$\hat{P}_{rel}$ (-)	0^o	30^o	60^o	90^o	120^o	150^o	180^o
6.8	2.3	6.7	0.22	0.53	0.11	0.17	0.095	0.053	0.033	0.028	0.012
7.9	3.0	8.5	0.20	0.35	0.096	0.140	0.066	0.030	0.020	0.012	0.006
10.5	4.5	13.4	0.16	0.10	0.041	0.047	0.012	0.004	0.002	0.001	0
12.3	6.8	18.1	0.15	0.014	0.011	0.009	0.001	0	0	0	0
14.2	9.3	23.5	0.14	0.002	0.001	0.001	0	0	0	0	0

Table 5.2: *The five sea states and corresponding wind speed, turbulence intensity and relative probability of occurrence. Further is the wind-wave-misalignment-distribution for the five sea states stated.*

The nonlinear equivalent loads are largest both in the tower and monopile in both directions.

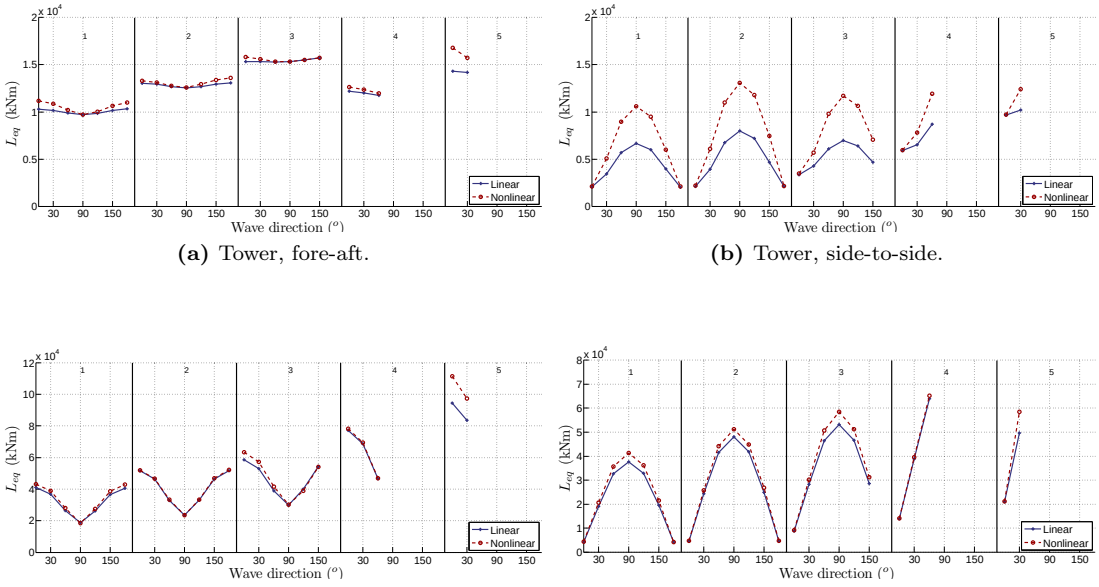

(a) Tower, fore-aft. **(b)** Tower, side-to-side.

(c) Monopile, fore-aft. **(d)** Monopile, side-to-side.

Figure 5.13: *The linear and nonlinear equivalent loads for $h = 40$ m in the fore-aft and side-to-side direction for $m = 5$. The wave direction changes from being aligned with the wind direction ($0°$) to be in the opposite direction of the wind direction ($180°$).*

In the fore-aft direction the difference between the linear and nonlinear equivalent loads are small, but for the largest wind and sea state a significant difference is seen.
The largest differences between the linear and nonlinear equivalent loads are seen in the tower in the side-to-side direction. In this direction the aerodynamic forcing and damping is insignificant and the impulsive responses due to the nonlinear waves significant. This was observed in Schløer *et al.* (2012) when the sea states were combined with a constant small wind in the aeroelastic calculations. In the monopile the difference between the linear and nonlinear wave realizations are much smaller. The monopile does not experience the impulsive responses in the same manner as the tower but mainly reacts in a quasi-static manner to the wave forces.
To illustrate the difference in the response due to the linear and nonlinear wave realizations, the overturning moment in the bottom of the tower and monopile in the side-to-side direction due to the third wind and sea state are shown in figure 5.14 for a situation where the waves are in an angle of $90°$ to the wind direction. It is clear to see that the nonlinear wave realization excite the structural first eigenfrequency in the tower more than the linear wave realization. This is representative for the whole time series. In the monopile the response is more static and the moments due to the linear and nonlinear wave realizations of the same size.
The accumulated equivalent load are based on the equivalent loads shown in figure 5.13 and the

probabilities stated in table 5.2. The differences between the linear and nonlinear accumulated equivalent load are shown in figure 5.15. In the tower the linear and nonlinear accumulated equivalent load is almost the same in the fore-aft direction while the nonlinear accumulated equivalent load is 35 % larger in the side-to-side direction.
The present analysis confirms the findings in chapter 4, that the wind is dominating in the tower in the fore-aft direction. The differences in the linear and nonlinear wave realizations do not change the accumulated equivalent load much. In the side-to-side direction the contribution from the waves is more important in the tower. For the analysis here it is the nonlinear wave realizations which results in the largest excitation of the structural first eigenfrequency and therefore the largest accumulated equivalent load.
In the monopile the nonlinear accumulated equivalent load is 5 % and 8 % larger in the fore-aft and side-to-side direction, respectively. The increase in the difference in the side-to-side direction is, as in the tower, due to the missing effects from the wind.

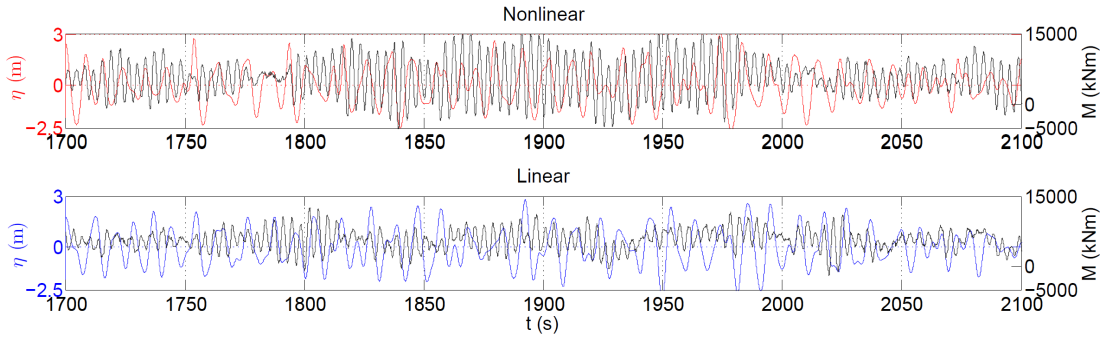

(a) Tower

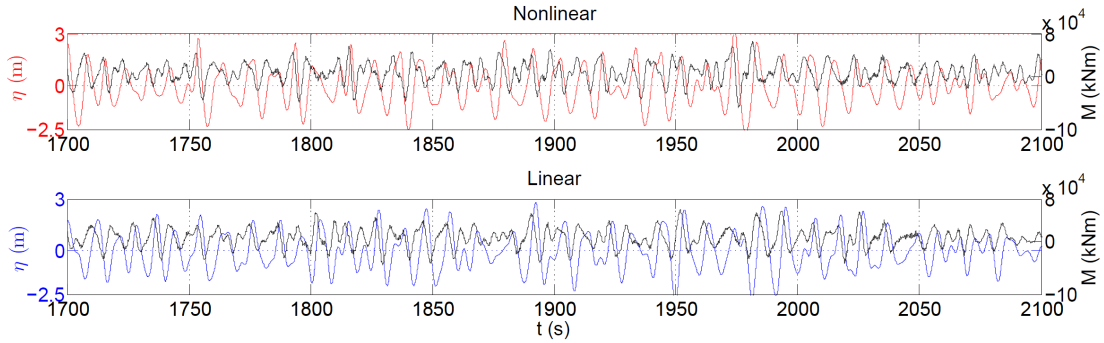

(b) Monopile

Figure 5.14: *Nonlinear and linear surface elevation for sea state 3 and the corresponding moment in the bottom of the monopile in the side to side direction for a situation where the waves also are in the side-to-side direction.*

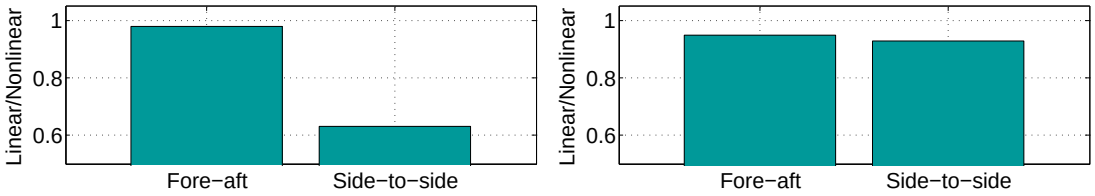

(a) Tower **(b)** Monopile

Figure 5.15: *The ratio between the linear and nonlinear accumulated equivalent load in the fore-aft and side-to-side direction for* $m = 5$.

5.5 Summary

In the present chapter it has been investigated how the nonlinearity of the waves affects dynamic response and the fatigue in misaligned conditions. The misalignment between the wind and waves was based on data from Fischer *et al.* (2010).
The dynamic analyses showed that in situations where the effects from the wind are insignificant the properties of the wave realizations and the energy in the wave spectra becomes very important. For wind and sea states *1a*, *1b* and *3* the excitations in the tower due to the linear and nonlinear wave realizations are of same magnitude. The larger nonlinear wave forcing are in the linear wave realization compensated by the larger broad band forcing.
For the largest wind and sea state the effects from the waves are reduced in the side-to-side direction. This is both because the waves only are misaligned with an angle of 60^o but also because the aerodynamic forcing and damping is stronger in the side-to-side direction when the blades are pitch to 87°.
In the fatigue analysis it was found that the linear accumulated equivalent load becomes larger relative to the nonlinear accumulated equivalent load in the side-to-side direction. This is due to the broad band forcing which is largest for the linear waves and this excitation increases in the side-to-side direction due to the lack of aerodynamic damping. However, for the water depth of $h = 25\,\text{m}$ the analysis indicated that the nonlinearity begins to be important due to the increase in the steepness of the nonlinear waves as the water depth decreases. The discussion about the larger broad forcing which is expected if the waves were fully converged and the reduction of the broad forcing if the diffraction effects were included in the Morison forces applies also for the results in the present analysis.
The analyses were based on wave realizations where the linear wave realizations contain most energy around the structural first frequency. Therefore sea states which for a given wind speed are stronger compared to the previous analysis are considered in the last part of the present chapter. The waves are larger due to the larger H_s-value and the larger sea bed slope of 1:25. The relative importance of the wave forcing and the waves contribution to the accumulated equivalent load is therefore larger. Also the nonlinearity of the waves becomes more important. This is seen in the results, particular of the accumulated equivalent load in the tower and particular in the side-to-side direction. The small study thus show that the nonlinearity of the waves can be important in the accumulated equivalent load. It should be noticed that the problem with convergence of the waves in the high frequency part of the wave spectrum applies also for these wave realizations.

Chapter 6

Hydrodynamic damping

Besides aerodynamic damping there exist other types of damping in an offshore wind turbine; soil damping, hydrodynamic damping, structural damping in the tower and the monopile and tower dampers. According to Tarp-Johansen *et al.* (2009) these types of damping all in all have a logarithmic decrement of 8% for the first structural mode.
To calculate the hydrodynamic damping Tarp-Johansen *et al.* (2009) considered a 3.5 MW wind turbine placed on a monopile with diameter 4.7 m in a water depth of 20 m. Using the radiation/diffraction program WAMIT, they found that the radiation damping corresponded to a logarithmic decrement of 1.4 %. The shape functions used to represent the displacement of the pile, were the riged body modes which already excist in WAMIT; a unit deflection of the whole pile and a rotation of the pile around its top, as shown in figure 6.1. When the two shapes are merdged it gives a linear deflection which is zero at the sea bed and one at the mean water level.

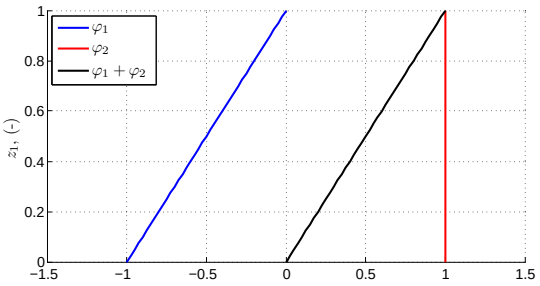

Figure 6.1: *The shape functions defined in WAMIT.*

In the following a more accurate description of the shape functions is used to calculated the radiation damping of a beam in WAMIT, and it is investigated if that changes the magnitude of the hydrodynamic damping. By comparison Cook & Vandiver (1982) calculated the radiation damping using potential flow theory and an approximated expression to be 0.69% in logarithmic decrement, so the only half of what Tarp-Johansen *et al.* (2009) found.
WAMIT is a program used to analyse the interaction between ocean waves and offshore structures. The model is based on potential flow theory and solves the Laplace equation by the of boundary integral equation method, also known as the panel method. The boundary conditions at the free surface and boundaries at the sea bed and on the structure are of first order, which means that the model solution only are valid up to mean water level.
For a rigid body the equation of motion reads

$$\sum_{j=1}^{N} \left((\rho \mathscr{A} + \mathsf{A}_{ij})\ddot{\mathsf{u}}_j + (\mathsf{B}_{ij} + \mathsf{c}_{ij})\dot{\mathsf{u}}_j + ((EI\mathsf{u}_{xx})_{xx} + \mathsf{C}_{\mathsf{R}ij})\mathsf{u}_j \right) = F_j, \tag{6.1}$$

where N is the number of degrees of freedom. The added mass, A, and the damping, B, are hydrodynamic forces calculated in WAMIT and are functions of the angular frequency ω. The restoring force, C_R, is also calculated in WAMIT but is in the present analysis considered to be

zero. The structural mass, $\rho\mathscr{A}$, and the structural stiffness, $(EI\mathsf{u}_{xx})_{xx}$, are calculated in Flex5. The damping of the structure, c, is set to zero because it is the hydrodynamic damping which is investigated in the present analysis. The excitation force F represents the Froude-Krylov force and diffraction forces, Faltinsen (1993).
The added mass and hydrodynamic damping are hydrodynamic forces due to forced harmonic rigid body motions. Faltinsen (1993) explains that the forces are found in WAMIT by forcing the structure to oscillate with a wave frequency with no impact from waves and therefore no excitation forces. The forced motion results in a oscillating fluid pressure on the body. This pressure can be calculated by the Bernoulli equation by solving for the velocity potential in the Laplace equation. For a harmonic oscillation with the amplitude $\hat{a}$, $\mathsf{u} = \hat{a}cos(\omega t)$, the force F is given as $F = \mathsf{A}\cos(\omega t) + \mathsf{B}\sin(\omega t)$ where first term can be seen as the added mass and second term as the hydrodynamic damping. The added mass and hydrodynamic damping can therefore be found by integrating the pressure over the body

$$F_j = -\mathsf{A}_{j,i}\ddot{\mathsf{u}} - \mathsf{B}_{j,i}\dot{\mathsf{u}}. \tag{6.2}$$

6.1 Hydrodynamic damping of a beam

In section 3.1 it was explained that the deflection of u_j can be expressed by a shape function and generalised coordinate, $\mathsf{u}_j = \varphi_j\alpha_j$. It was also explained how the equation of motion, (6.1), can be simplified by multiplying each term with φ_i and integrating along the length of the beam, L. Equation (6.1) can then be written as

$$\mathbf{GM}\underline{\ddot{\alpha}} + \mathbf{GK}\underline{\alpha} = -\mathbf{GA}\underline{\ddot{\alpha}} - \mathbf{GB}\underline{\dot{\alpha}}, \tag{6.3}$$

where

$$\begin{aligned} GM_{ij} &= \int_{-h}^{0} \rho\mathscr{A}\varphi_i\varphi_j dx, \\ GK_{ij} &= \int_{-h}^{0} EI\varphi_{i,xx}\varphi_{j,xx} dx, \\ GA_{ij} &= \int_{-h}^{0} \mathsf{A}\varphi_i\varphi_j dx, \\ GB_{ij} &= \int_{-h}^{0} \mathsf{B}\varphi_i\varphi_j dx. \end{aligned} \tag{6.4}$$

In the present analysis it is the damping ratio of the structural first eigenmode of the whole structure which should be found. The equation of motion therefore has to be solved for the whole structure; monopile, wind turbine tower and wind turbine, which gives 24 degrees of freedom. The generalised coordinate is therefore a vector of size 24, and the matrices in equation (6.3) are of size 24x24. The forcing from the added mass and damping only exist in the water, i.e. for the two first shape functions. It is therefore only the first 2x2 elements which are nonzero in the added mass matrix and hydrodynamic damping matrix

$$\mathbf{GA}_{24} = \begin{bmatrix} \mathsf{A}_{1,1} & \mathsf{A}_{1,2} & 0 & \dots & 0 \\ \mathsf{A}_{2,1} & \mathsf{A}_{2,2} & 0 & \dots & 0 \\ 0 & 0 & 0 & \dots & 0 \\ \vdots & \vdots & \vdots & \ddots & \vdots \\ 0 & 0 & 0 & \dots & 0 \end{bmatrix} \quad \text{and} \quad \mathbf{GB}_{24} = \begin{bmatrix} \mathsf{B}_{1,1} & \mathsf{B}_{1,2} & 0 & \dots & 0 \\ \mathsf{B}_{2,1} & \mathsf{B}_{2,2} & 0 & \dots & 0 \\ 0 & 0 & 0 & \dots & 0 \\ \vdots & \vdots & \vdots & \ddots & \vdots \\ 0 & 0 & 0 & \dots & 0 \end{bmatrix}. \tag{6.5}$$

If it is assumed that the hydrodynamic forcing on the right hand side of equation (6.3) is zero an eigenvalue problem occur with the solution $\alpha = x_0 e^{i\omega t}$.

$$\begin{aligned}
&\mathbf{GM}_{24}\ddot{\underline{\alpha}} + \mathbf{GK}_{24}\underline{\alpha} = 0 \Leftrightarrow \\
&-\mathbf{GM}_{24}\omega^2 x_0 e^{i\omega t} + \mathbf{GK}_{24} x_0 e^{i\omega t} = 0 \Leftrightarrow \\
&\mathbf{GM}_{24}^{-1}\mathbf{GK}_{24} x_0 = \omega^2 x_0,
\end{aligned} \tag{6.6}$$

where x_0 is an eigenvector and ω^2 is an eigenvalue. The generalised coordinates $\underline{\alpha}$ can therefore be expressed by the eigenvector of the first structural eigenmode (since it is the one that are solved for), x_0, and a scalar, α_0, which again is a function of time

$$\alpha(t) = \alpha_0(t) x_0. \tag{6.7}$$

Equation (6.3) now reads

$$\mathbf{GM}_{24}\ddot{\alpha_0}\underline{x}_0 + \mathbf{GK}_{24}\alpha_0\underline{x}_0 = -\mathbf{GA}_{24}\ddot{\alpha_0}\underline{x}_0 - \mathbf{GB}_{24}\dot{\alpha_0}\underline{x}_0. \tag{6.8}$$

Equation (6.8) is a system of force equations. By multiplying each term with the transposed of the eigenvector, $\underline{x}_0^T$, the system of equations is reduced to one equation of motion

$$\tilde{\mathsf{M}}\ddot{\alpha_0} + \tilde{\mathsf{K}}\alpha_0 = -\tilde{\mathsf{A}}\ddot{\alpha_0} - \tilde{\mathsf{B}}\dot{\alpha_0}, \tag{6.9}$$

where

$$\begin{aligned}
\tilde{\mathsf{M}} &= \underline{x}_0^T \mathbf{GM}_{24}\underline{x}_0, \\
\tilde{\mathsf{K}} &= \underline{x}_0^T \mathbf{GK}_{24}\underline{x}_0, \\
\tilde{\mathsf{A}} &= \underline{x}_0^T \mathbf{GA}_{24}\underline{x}_0, \\
\tilde{\mathsf{B}} &= \underline{x}_0^T \mathbf{GB}_{24}\underline{x}_0.
\end{aligned} \tag{6.10}$$

In equation 6.10 $\tilde{\mathsf{M}}$ and $\tilde{\mathsf{A}}$ are modal masses and $\tilde{\mathsf{K}}$ and $\tilde{\mathsf{B}}$ are modal stiffness and modal damping. From equation (6.9) is is possible to calculate the damping ratio, ζ, and logarithmic decrement, δ, as explained in section 3.1

$$\zeta = \frac{\tilde{\mathsf{B}}}{2\sqrt{(\tilde{\mathsf{M}} + \tilde{\mathsf{A}})\tilde{\mathsf{K}}}}, \tag{6.11}$$

$$\delta = \frac{2\pi\zeta}{\sqrt{1-\zeta^2}}. \tag{6.12}$$

The mass, $\tilde{\mathsf{M}}$, is calculated in Flex5 without including the added mass, $-\rho C_m \mathscr{A}\ddot{\alpha}$, where $C_m = 1$ is the added mass coefficient. This is done because the added mass from WAMIT is added to the mass, $\tilde{\mathsf{M}}$, in equation (6.11). The stiffness and the eigenvector are on the other hand calculated in Flex5 with the added mass, because the logarithmic decrement should represent a situation where the added mass is included.

6.2 The shape functions

As standard WAMIT has six rigid-body modes, displacement in- and rotation around three directions equal to the Cartesian coordinates. Instead of solve for one to six of the standard degrees of freedom it is possible to solving for user-defined flexible-body modes.
In the present analysis the shape function used to describe the displacement of the pile is the same which describes the displacement of the monopile in Flex5, described in more detail in section 3.1.1. The two shape functions are seen in figure 6.2 for a case where the monopile is 40 m placed in a water depth of 30 m.
In WAMIT the shape functions are defined by the non-dimensional coordinate $z_1 = 1 + z/h$, maps $z = [-h; 0]$ to $z_1 = [0; 1]$. Since WAMIT is a linear model, the pile is only considered up to mean

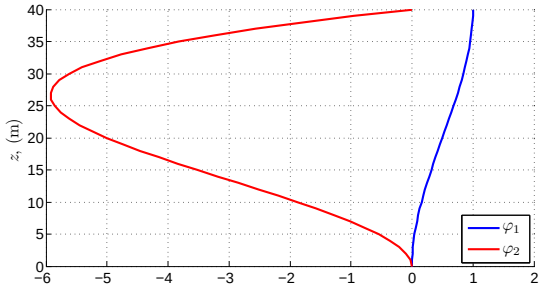

Figure 6.2: *The shape functions used in monopile in Flex5 for the pile.*

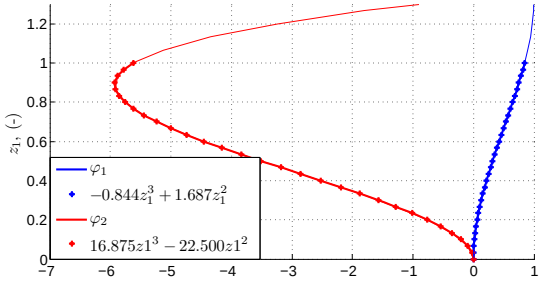

Figure 6.3: *The shape functions used in WAMIT for a monopile with a length of 40 m placed in a water depth of $h = 30\,m$. The functions are only considered up to the mean water level, i.e. $z_1 = 1$.*

water level. For the NREL wind turbine considered here the pile reaches 10 m above the mean water level. Only the part of the shape functions below the mean water level is therefore defined in WAMIT as shown in figure 6.3. In WAMIT the shape functions can be described by polynomials. The polynomials which describe the shape functions up to mean water level are also stated in the figure. The polynomials were found by the Matlab function "polyfit.m". Third order polynomials were found to describe the shape functions very accurate, the fourth order coefficients were close to be zero to machine accuracy.

6.3 The results

The four monopiles considered in chapter 4 are also considered in the present analysis. The four monopiles geometrical data are repeated for convenience in table 6.1.

h (m)	40	35	30	25
D (m)	6.5	6.5	6.3	6.1
t (mm)	94	76	70	64
L (m)	50	45	40	35

Table 6.1: *The four monopiles with the diameter, D, thickness t and length, L in four water depths, h.*

The damping matrix was as a start calculated for 7 wave periods $T = 2, 3, 3.7, 4, 5, 6, 7\,s$. It was found that the damping ratio and logarithmic decrement was largest for $T = 3.7\,s$ which is equal to the period of the structural first eigenfrequency. The dynamic amplification factor, $\mathsf{H} = \frac{\mathsf{u}}{\mathsf{k}\hat{a}}$, is a parameter which says how large a body's deflection u is relative to the amplitude of the forcing $\hat{a}$. The dynamic amplification factor is largest when the frequency of the forcing is equal to the eigenfrequency of the body. If the expression for H is combined with the expression for the damping $\mathsf{c} = \frac{\delta \mathsf{k}}{\pi \omega_0}$ it is found that the logarithmic decrement, δ, is largest when H is largest and therefore when the eigenfrequency of the body and the frequency of the force is equal. Only the period of 3.7 s is therefore considered in the following. In the discussion about ringing, which concerns the

structural excitation at the natural modes, it is also most relevant to consider the damping at the structural first eigenfrequency.
The damping ratio and logarithmic decrement for the four monopiles are stated in table 6.2.
The logarithmic decrement is largest for the largest water depth because the water column which dampens the structural displacement is larger and also the diameter of the pile is larger. The logarithmic damping is significant smaller than the one in Tarp-Johansen *et al.* (2009). In Tarp-Johansen *et al.* (2009) they considered a pile with a length of $\mathsf{L} = 80$ m and a diameter of $D = 4$ m, which represented the monopile and tower. The water depth was $h = 20$ m. In the top of the pile, it had a top mass which represented the nacelle and blades of the wind turbine. The shape functions were as already mentioned the rigged body modes shown in figure 6.3. However the shape functions did only represent the wetted part of the pile. So if the pile had a unit deflection in the top of the pile the deflection at the mean water level was L/h. The reason that the method used in Tarp-Johansen *et al.* (2009) gives a larger damping, must be because the shape functions are rigid. So the integrated deflection of the wetted part of the pile is larger than if the flexible shape functions from Flex5 are considered.
If the damping of a wind turbine besides the aerodynamic damping gives a logarithmic decrement of 8%, the contribution from the radiation damping is small but not small enough to be insignificant. However the damping is not found to be large enough to incorporate the radiation damping in Flex5 in the previous or following analysis.

h (m)	40	35	30	25
ζ (%)	0.07	0.06	0.04	0.04
δ (%)	0.42	0.38	0.27	0.25

Table 6.2: *The damping ratio and logarithmic decrement for the four monopiles.*

However, it is possible to include a constant logarithmic damping ratio corresponding to the radiation damping in Flex5 as explained in section 3.1.2. Figure 6.4 shows a decay test where the structural first eigenfrequency is given a logarithmic decrement of 0.42 % and calculated in same manner as in the decay test in section 4.4.1. The degrees of freedom are given a start velocity corresponding to the structural first eigenvector. The logarithmic decrement of the monopile's deflection is 0.37 % and the frequency of the oscillation is 0.269 Hz. The constant damping terms which are given as input therefore have to be adjusted a little to get the correct damping. This might be because the radiation damping that is calculated is for the structural first eigenfrequency of the whole structure, while the damping which is given as input in Flex5 is for the DOFs in the monopile and the tower's first DOF only.

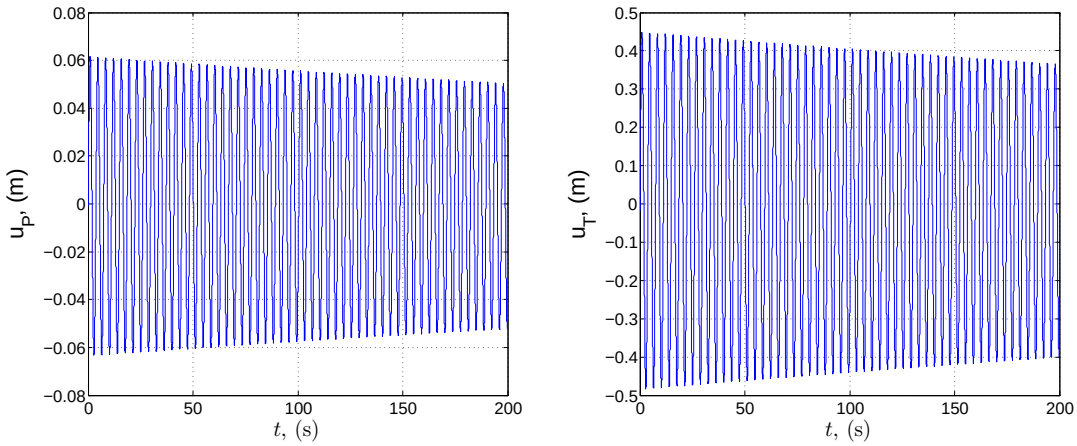

Figure 6.4: *Decay test of the displacement of top of the monopile, u_{mp}, and tower, u_t at $h = 40\,m$. The monopile and tower are given constant damping ratio corresponding 0.42 % in logarithmic decrement.*

6.4 Summary

The magnitude of the hydrodynamic radiation damping from the waves has been investigated in the present chapter. The hydrodynamic forces in terms of the added mass and damping are calculated in the radiation/diffraction program WAMIT. The shape functions used to calculated the forces in WAMIT are the same as used in Flex5 to describe the deflection of the monopile.
When the equation of motion is solved it is solved for the whole structure; monopile, wind turbine tower and wind turbine. The generalized stiffness and mass matrix is therefore taken from Flex5. The hydrodynamic radiation damping is found to be between 0.2-0.5 % in logarithmic decrement. The damping is found to increase as the water depth increases due to the larger water column. It is further found that the radiation damping is largest at the same frequency as structural eigenfrequency. The calculated hydrodynamic damping is smaller than predicted by Tarp-Johansen *et al.* (2009) due to differences in the description of the shape functions and the system which is solved for.

Chapter 7

Soil damping by a new soil model

Next to aerodynamic damping, soil damping gives the largest contribution to the overall damping of the wind turbine and the monopile. Unfortunately, this type of damping is the most complex damping mechanism, Gujer (2005), and is very difficult to model. Today usually only monotonic p-y curves are used to describe the nonlinear soil stiffness in aerodynamic calculations, which describes the nonlinear elastic relations between the lateral displacement of the monopile, y, and the soil pressure, p, at a given vertical level. The p-y-curves are original intended for static analysis and do therefore not contain effects of hysteresis that leads to a change in the loading the second time the pile is loaded to a certain deflection. The standards (e.g. DNV-OS-J101 (2010)) also recommend the p-y curves to be used in the analyses of the piles lateral pile capacity.
Even simpler models are sometime also used. The soil stiffness can be represented by coupled or uncoupled springs at the sea bed, where the pile therefore is not extended into the soil. Another simple model is where the properties and the length of the pile below the sea bed are changed so that the response above the sea bed are similar to the response using the more accurate p-y model. These more simplified models are explained in more detail in Jonkman *et al.* (2009) or Passon & Kühn (2005). One problem with these simpler models compared to the p-y-model is according to Passon & Kühn (2005) that the loads are under predicted because the largest bending moment occurs below the sea bed, where the pile in the simple models is not described correct, if described at all. It is possible to describe the soil more correct with FEM-models. However, these models are very time consuming computationally and are according to Passon & Kühn (2005) only used in the final stage and for certification.
To model the soil damping a constant damping ratio are included in the aeroelastic models either in the springs in the soil or in same manner as was done in the analysis in chapter 4 and 5.
To get a better description of the soil's interaction with the pile displacement and of the soil damping the soil model from Hededal & Klinkvort (2010) and Klinkvort (2012) is implemented in Flex5. The model offers a description of the cyclic pile-soil interaction and includes hysteretic damping from the soil.
In first part of the present chapter the soil model is presented and the implementation in Flex5 is described. Next the response of the monopile and wind turbine tower using this soil model is compared against the response obtained with classical p-y curves combined with a constant damping factor. The dynamic consequences of including the new soil model is analysed including the effects on the fatigue.

7.1 The model

The soil model is a Winkler model, which is a model where the pile is described as a beam and the soil is described by uncoupled nonlinear cycling springs, as indicated in figure 7.1. The model is based on observations from rigid pile tests, which according to Klinkvort (2012) makes the model suitable for monopiles supporting wind turbines.
The soil model consists of two forces which are active in different phases during a cycle, f_{face} and f_{drag}. In figure 7.2 the relation between the force in a spring in the soil, f_s, and the corresponding displacement of the pile, u, during two cycles are shown.

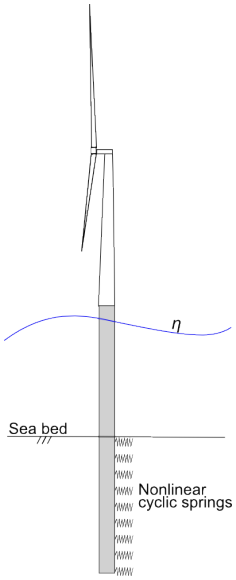

Figure 7.1: *A sketch of the wind turbine, where the monopile is extended into the soil. The interaction between the soil and pile are described by uncoupled nonlinear cycling springs.*

The force f_{face}, represent the loading phase, when the soil is loaded to a new extent. The pile pushes the soil and creates a gap behind the pile. Klinkvort (2012) found from centrifugal tests that the sand falls back into the created gap but it will not fill the gap totally. In the model of Klinkvort (2012), the pile moves in the gap until it reaches the mean of the two extremities of the pile displacement, where after the soil resistance starts to build up again. This represents the back-filling of the soil in the model. This part of the model is not implemented in Flex5, to keep the model simple as a start. Instead the method of Hededal & Klinkvort (2010) is used where the resistance starts to build up when the pile reaches the extremities in the gap in each direction, indicated with $\alpha_{\hat{max}}$ and $\alpha_{\hat{min}}$ in figure 7.2.
The build-up of the resistance is a linear elastic process, since the pile has been in that area before. The face force becomes active when the soil is loaded to a new extent. The maximum loading in the two cycles in figure 7.2 is indicated with u_{max} and u_{min}. The build-up of resistance and loading to a new extent can be combined in one equation

$$f_s(\mathsf{u}) = \begin{cases} (S_t(x)-1)\, f_{u,virgin}(\mathsf{u}) + S_t(x)\,(-f_{u,virgin}(\mathsf{u}_{min}) + \mathsf{k}_s(\mathsf{u}-\mathsf{u}_{min})) \\ \qquad \text{for } \mathsf{u} < \alpha_{min} + \frac{\Delta\mathsf{u}}{|\Delta\mathsf{u}|}\frac{f_{drag}}{\mathsf{k}_s} \\ S_t(x) f_{u,virgin}(\mathsf{u}) + (1-S_t(x))\,(f_{u,virgin}(\mathsf{u}_{max}) + \mathsf{k}_s(\mathsf{u}-\mathsf{u}_{max})) \\ \qquad \text{for } \mathsf{u} > \alpha_{max} + \frac{\Delta\mathsf{u}}{|\Delta\mathsf{u}|}\frac{f_{drag}}{\mathsf{k}_s} \end{cases} \tag{7.1}$$

where $\Delta\mathsf{u}$ is the change in the displacement from previous to the present time step and the term $\frac{\Delta\mathsf{u}}{|\Delta\mathsf{u}|}$ therefore indicate whether the change in the displacement is positive or negative. The slope of the elastic loading is equal to the elastic soil stiffness k_s. The step function S_t indicates whether the loading of the soil is linear elastic or determined from the virgin curve and is given by

$$\begin{aligned} S_t(x) &= \frac{1}{1+e^{-2\beta x}}, \quad \text{where} \\ x &= \begin{cases} \mathsf{u}-\mathsf{u}_{min} & \text{for } u < \alpha_{min} + \frac{\Delta\mathsf{u}}{|\Delta\mathsf{u}|}\frac{f_{drag}}{\mathsf{k}_s} \\ \mathsf{u}-\mathsf{u}_{max} & \text{for } u > \alpha_{max} + \frac{\Delta\mathsf{u}}{|\Delta\mathsf{u}|}\frac{f_{drag}}{\mathsf{k}_s}. \end{cases} \end{aligned} \tag{7.2}$$

If $x \geq 0$ the step function is $S = 1$, if $x = 0$ the step funtion is $S = 0.5$ and for $x > 0$ the step function is $S = 0$. The larger the parameter β is in equation (7.2) the more abrupt is the change of the step function from zero to one. According to Hededal & Klinkvort (2010) a typical value of β is $1 \cdot 10^6$ and is therefore used here.

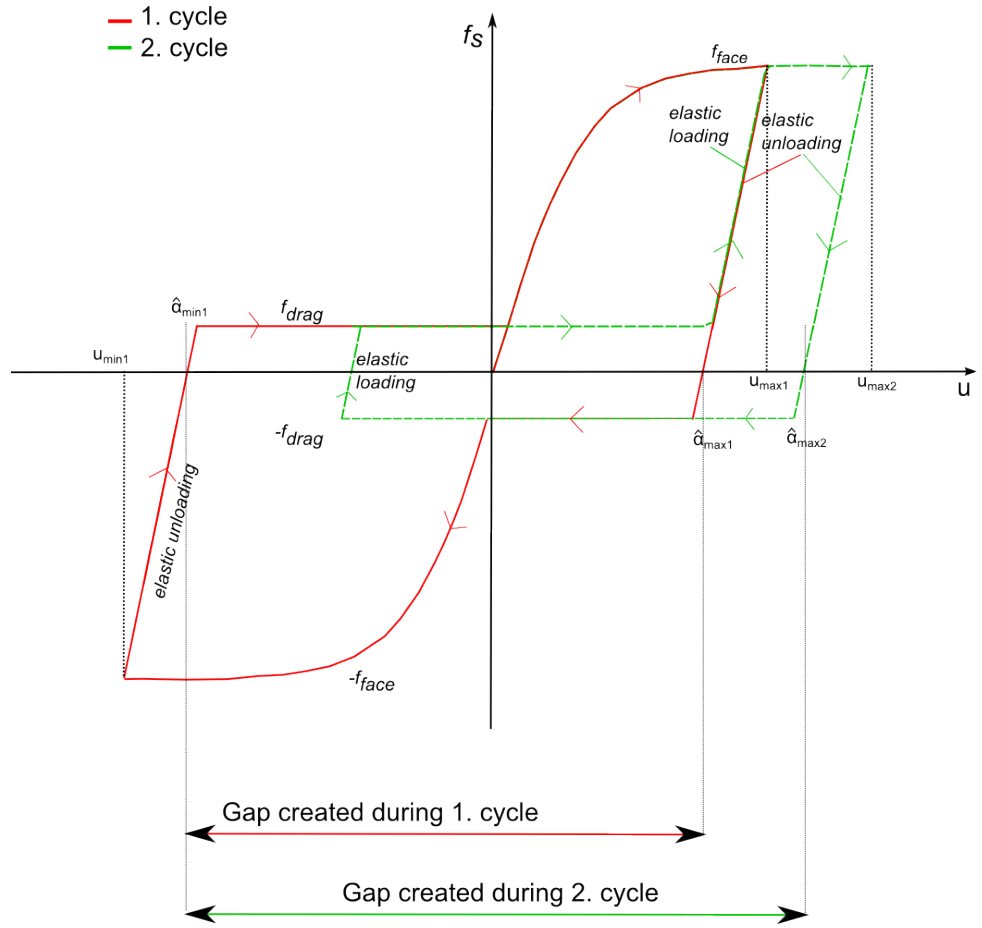

Figure 7.2: *The spring element and the relation between the displacement and the force. Index "1" refer to the first cycle and index "2" to the second cycle.*

Hededal & Klinkvort (2010) use the API (2010) definition of the $p-y$ curves for sand to define the virgin curve, $f_{u,virgin}$. This is the same definition as given in DNV-OS-J101 (2010). The virgin curve describes the relation between the force and the displacement first time the soil is loaded to a new extent

$$f_{u,virgin} = A_s f_u \tanh\left(\frac{k_m z}{A_s f_u}\mathsf{u}\right). \tag{7.3}$$

Here $A_s = \max\left(0.9, 3 - \frac{0.8z}{D}\right)$ is a strength reduction parameter, f_u the ultimate bearing capacity, k_m the soil modulus parameter, z the depth below the sea bed and u the displacement.
When the pile moves in the gap created behind the pile, a drag force, f_{drag}, or friction along the sides of the pile exists. This process is plastic and the drag force is therefore constant. Klinkvort (2012) found from cyclic tests that the friction was in the range 10 % smaller than the maximum capacity of the soil. The drag force is therefore calculated as

$$f_s = \frac{A_s f_u}{10}\frac{\Delta\mathsf{u}}{|\Delta\mathsf{u}|}. \tag{7.4}$$

When the pile changes direction the unloading of the soil occurs linear-elastic. The slope of the elastic unloading is also equal to the elastic soil stiffness k_s and the soil force is calculated as

$$f_s = f_{s,old} + \Delta\mathsf{u}\mathsf{k}_s, \tag{7.5}$$

where $f_{s,old}$ is the soil force at previous time step.

7.1.1 Incorporation into Flex5

In the implementation in Flex5 the soil model only calculates the force due to the displacement in the fore-aft direction. The displacement in the side-to-side direction is assumed small and therefore neglected. This is consistent with the present utilization of the model where wind and waves are assumed to be co-aligned. In Hededal & Klinkvort (2010) the force is calculated as a point force in each spring, but when the model is implemented in Flex5 the force is converted to a distributed force.

When a monopile is moving in the soil, it rotates around a point between the bottom of the pile and the sea bed as illustrated in figure 7.3. Instead of considering the whole pile, a more simple solution is made to keep the implementation of the model simple as a start. Therefore the last part of the pile, L_{P2}, is represented by a liner rotating spring, also illustrated in figure 7.3. It is assumed that the forces below the rotating spring are not important. This is the reason for the omission of the pile and the associated forces below the rotating point.

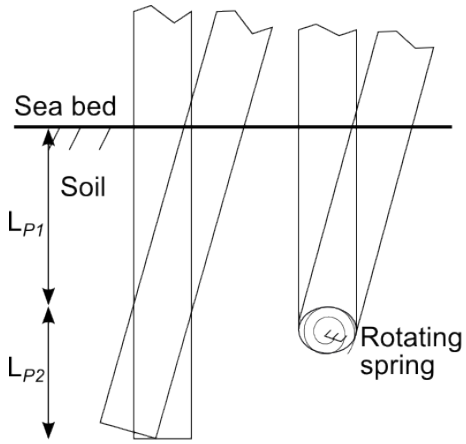

Figure 7.3: *A sketch of how a pile rotates around a point in the soil, and how the pile is simplified in the soil model in Flex5 by representing the last part of the pile* L_{P2} *with a rotating springs.*

Further, if only the part of the pile above the rotating point is considered, the displacement of the monopile in the soil can be described by a shape function rather easily. Therefore a new shape function is introduced in Flex5. This is further done to maintain the modal scheme used in Flex5. Alternative the foundation module in Flex5 could be replaced by a finite element model, which for example has been done by Vestas Technology, Hald & Høgedal (2005).

The two first shape functions in the monopile are almost identical to those explained in section 3.1.1 and are still used to describe the displacement of the monopile above the sea bed. However, instead of being rigidly supported in the bottom, the shape functions now have an angular deflection corresponding to the moment resulting from the stiffness of the rotating spring.

The deflection and angular deflection of the third shape function in the top of the pile are both zero, since the shape function only is used to describe the deflection in the soil. The shape depends on a prescribed force, f_{ref}, which is given as input and shall represent the expected force distribution in the soil. The shape function therefore only works optimally if the prescribed force corresponds to the exact force in the soil. At the bottom the third shape function also has an angular deflection corresponding to the moment resulting from the stiffness of the rotating spring. The new shape function has not been validated against any other soil models. This is left for future work. In figure 7.4 the three shape functions are shown for two different distributions of f_{ref} also shown in the figure. It is seen that the third shape function are very similar for the two load examples despite that f_{ref} are not the same.

To calculate the soil forces and the corresponding displacement of the pile at each time step a iteration takes place. This is necessary, since the relation between the pile displacement and the soil force is nonlinear. First the current displacement of the soil is calculated based on the two first degrees of freedom

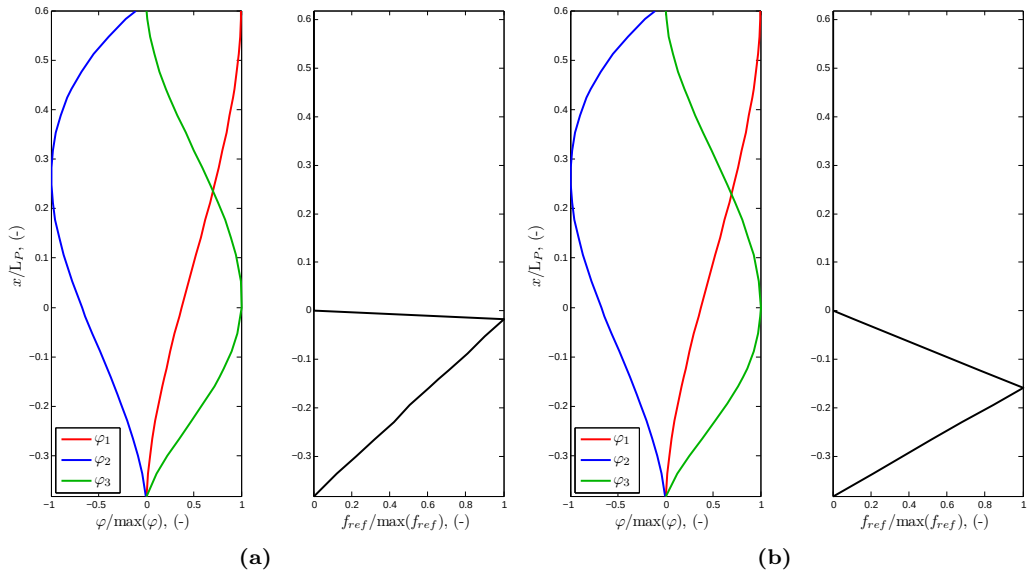

Figure 7.4: *The three mode shapes for two different distributions of* f_{ref}.

$$\mathsf{u} = \sum_{i=1}^{2} \varphi_i \alpha_i. \tag{7.6}$$

Hereafter the iteration starts. The force, f_s, in each spring element in the soil are calculated. In this calculation the force and displacement from the previous time step and the calculated displacement in equation (7.6) are used.
The generalised force, GF_3, in the soil and the generalised coordinate α_3 is afterwards calculated with a relaxation

$$GF_3 = \int_{z_{min}}^{-h} f_s(z) dz, \tag{7.7}$$

$$\alpha_3 = K_{relax} \frac{GF_3}{GK_3} - (1 - K_{relax})\alpha_3, \tag{7.8}$$

where z_{min} and $-h$ are the z-coordinate in the bottom of the pile and at the seabed, respectivly. The relaxation are necessary to ensure a numerical stable solution. The generalised stiffness GK_3 is found from the predefined force f_{ref} as

$$GK_3 = \int_{z_{min}}^{-h} f_{ref} dz. \tag{7.9}$$

Finally, the displacement of the pile is updated based on all three degrees of freedom. A new force is than calculated based on this new displacement

$$\mathsf{u} = \sum_{i=1}^{3} \varphi_i \alpha_i. \tag{7.10}$$

The iteration stops when α_3 is converged. The displacement and the soil force are updated at the full time step in the Runga-Kutta integration scheme.
The present soil model is donated the "cyclic model" in the following. It will later be compared to a traditional p-y model with parametrised damping.

7.2 Test case parameters

In all the analysis of the cyclic soil model the same test case is considered. The properties of the monopile and the soil of the test case are presented below.
The wind turbine is placed in a water depth of 25 m. The monopile is therefore the same as used in the analysis in chapter 4 and 5 for $h = 25\,\mathrm{m}$, with a diameter of $D = 6.1\,\mathrm{m}$ and $t = 64\,\mathrm{mm}$. In the second task in the Offshore Code Comparison Collaboration, Jonkman & Musial (2010), a flexible monopile is considered which is penetrated 36 m into the soil and placed in a water depth of 20 m. The same penetration depth is assumed in the present analysis. Klinkvort (2012) made centrifugal experiments where it was found, that for a load case similar to the one considered here, the distance from the sea bed to the rotating point, L_{P1} in figure 7.3, is approximately 3/5 of the whole length of the pile in the soil, $\mathsf{L}_{P1} + \mathsf{L}_{P2}$. The rotating spring in the bottom of the pile in FLex5 is therefore placed 21.6 m below the sea bed. The structural first eigenfrequency is 0.24 Hz and is therefore smaller compared to a monopile fixed at the sea bed, which was considered in chapter 4 and 5. This was expected since the eigenfrequency of a cantilever beam is inversely proportional to the length of the beam squared, $\hat{f} = \frac{1.8751^2}{2\pi}\sqrt{\frac{EI}{m\mathsf{L}^4}}$.
The stiffness of the rotating spring is found by considering a pile with the same properties as above which penetrates 36 m into the soil and with a rotating point 21.6 m below the sea bed. The pile is loaded by a force at the mean water level to fracture using the Winkler-model presented in Klinkvort (2012). By considering the relation between the bending moment and rotation of the pile in the rotating point the stiffness of the rotating spring is found to be $E \sim 3 \cdot 10^8\,\mathrm{kNm/rad}$.
The soil is assumed to be sand with the same soil properties along the full extent of the pile. A friction angle of $\phi = 38.5^o$ is used. The same value has been used in one of the soil layers considered in Jonkman & Musial (2010). The soil modulus parameter is a function of ϕ and is according to API (2010) equal to $k_m = 36440\mathrm{kN/m^3}$. The effective weight is $\gamma = 10\,\mathrm{kN/m^3}$. The ultimate bearing capacity and therefore also the drag force are functions of the depth. As an example their values 9 m below the sea bed are calculated to be $f_u = 5466\,\mathrm{kN/m}$ and $f_{drag} = 491\,\mathrm{kN/m}$.
In the previous chapters a logarithmic decrement damping of 8 % to represent the damping in the wind turbine besides aerodynamic damping has been used. Following the work of Tarp-Johansen *et al.* (2009) the structural damping and tower dampers contribuate approximately with 3.2 % to the logarithmic decrement damping. In chapter 6 the hydrodynamic damping is found to be 0.2-0.5 % in logarithmic decrement. The last approximately 4 % out of the total logarithmic decrement damping is therefore due to the damping from the soil. In the present analysis this 4 % of logarithmic decrement is therefore omitted, because the soil damping now is included in the cyclic soil model. Further it can be questioned whether the 8 % of logarithmic decrement damping which has been used in the previous chapters is too much. Therefore, the logarithmic damping to represent the structural damping, tower dampers and hydrodynamic damping is reduced and only 2 % of logarithmic decrement is used in the present analysis. The damping is added to the towers first eigenfreqyence and to the monopile.

7.3 Decay tests

In this section the properties of the cyclic model and how it affects the monopile is analysed.
In a decay test where the soil does not experience extra loading after the first cycle and the pile therefore moves in the gap, it can be shown that the logarithmic decrement damping is equal to $\frac{1}{2}\frac{\mathsf{W}}{\max(E_{kin})}$, where W is the work done by the soil during a cycle, T, and $\max(E_{kin})$ is the maximum kinetic energy during the cycle. The result can be found by considering the equation of motion with the undamped solution $\mathsf{u} = \mathsf{u}_0\cos(\omega t)$

$$\mathsf{m}\ddot{\mathsf{u}} + \mathsf{k}\mathsf{u} + \mathsf{c}\dot{\mathsf{u}} = 0. \tag{7.11}$$

The work done by the damping term during a cycle $T = \frac{2\pi}{\omega}$ is given as

$$\mathsf{W} = \int_0^T \mathsf{c}\dot{\mathsf{u}}d\mathsf{u} = \int_0^T \mathsf{c}\dot{\mathsf{u}}^2 dt = \int_0^T \mathsf{c}(-\omega)^2\mathsf{u}_0^2\sin^2(\omega t)dt = \mathsf{c}\omega^2\mathsf{u}_0^2\frac{1}{2}T = \mathsf{c}\omega\mathsf{u}_0^2\pi. \tag{7.12}$$

The maximum kinetic energy in the system during the cycle is found as

$$\max\left(E_{kin}\right) = \max\left(\frac{1}{2}\mathsf{m}\dot{\mathsf{u}}^2\right) = \frac{1}{2}\mathsf{m}(-\omega)^2\mathsf{u}_0^2 \max\left(\sin^2(\omega t)\right) = \frac{1}{2}\mathsf{m}\omega^2\mathsf{u}_0^2. \tag{7.13}$$

The ratio between the work and the kinetic energy is found to be

$$\frac{\mathsf{W}}{\overline{E_{kin}}} = \frac{\mathsf{c}\omega\mathsf{u}_0^2\pi}{\frac{1}{2}\mathsf{m}\omega^2\mathsf{u}_0^2} = \frac{\mathsf{c}\pi}{\frac{1}{2}\mathsf{m}\sqrt{\frac{k}{m}}} = 2\frac{\mathsf{c}\pi}{\sqrt{\mathsf{mk}}}, \tag{7.14}$$

which is twice the logarithmic decrement, $\delta = \frac{\mathsf{c}\pi}{\sqrt{\mathsf{mk}}}$
The work done by the force during a cycle can also be described as

$$\mathsf{W} = \int_t^{t+T} f d\mathsf{u}. \tag{7.15}$$

If the pile only moves in the gap in figure 7.2 and it is assumed that the soil is very stiff such that the trajectory in the diagram has approximately vertical sides, the soil force equals either f_{drag} or $-f_{drag}$ and equation (7.15) can be rewritten

$$\mathsf{W} = -2f_{drag}\int_0^{T/2} -\mathsf{u}_0\omega\sin(\omega t)dt = -2f_{drag}\mathsf{u}_0\omega\left[\frac{1}{\omega}\cos(\omega t)\right]_0^{T/2} = 4f_{drag}\mathsf{u}_0. \tag{7.16}$$

Combining equation (7.13), (7.14) and (7.16) gives

$$\delta = \frac{1}{2}\frac{\mathsf{W}}{\max(E_{kin})} = \frac{1}{2}\frac{4f_{drag}\mathsf{u}_0}{\frac{1}{2}m\dot{\mathsf{u}_0}^2\omega^2} = \frac{4f_{drag}}{m\mathsf{u}_0\omega^2}. \tag{7.17}$$

From equation (7.17) it is seen that the smaller the amplitude of the displacement is the larger is the logarithmic damping. This is in the following demonstrated where it also is investigated whether the relation $\delta = \frac{1}{2}\frac{W}{\max(E_{kin})}$ can be found by the cyclic model in Flex5.

7.3.1 Decay test I

In the present section it is investigated whether it is true that the damping is largest for the small amplitudes of the displacement. Two decay tests are applied in Flex5 where the only external force is the forcing from the soil. The density of the water and air are set to zero to avoid hydrodynamic and aerodynamic damping. Further, only the degrees of freedom in the monopile are active, to ensure that it only is the pile-soil interaction which is considered.
In the first decay test the first degree of freedom in the monopile has a start velocity of $\dot{\alpha_1} = 1$ and in the second decay test the start velocity is $\dot{\alpha_1} = 4$. In figure 7.6 the logarithmic decrement as function of time is shown together with the displacement of the top pile. For both tests the first couple of cycles are affected by elastic deformation as can be seen from the free curves in figure 7.6. The undisturbed decay test thus starts at $t \sim 7\,\mathrm{s}$ for the small-amplitude test and for $t \sim 10\,\mathrm{s}$ for the large-amplitude test.
First off all it is seen that the small-amplitude decay test with the smallest amplitude as a start has the largest logarithmic decrement. Also, the logarithmic decrement increases for this small-amplitude decay test the first 20 s and for the large-amplitude decay test the first 55 s. In these time sequences the logarithmic decrement therefore increases as the amplitude of the displacement decreases, which is in accordance with equation (7.17). After 100 s the logarithmic decrement is 12 % and 16 %, respectively. The reason that the logarithmic decrement starts to decease again after 20 s and 55 s respectively, is that the displacement of the pile begins to be so small that the soil force is between -f_{drag} and f_{drag}. Therefore only the linear elastic loading and unloading exist. This effect occur first in the bottom of the pile. In figure 7.5 the soil force in the depth 8 m below the sea bed is shown as function of time and as function of the pile displacement in the same depth. It is seen that the force only experience elastic loading and unloading after $t \sim 30\,\mathrm{s}$ with $\dot{\alpha_1} = 1$ and after time $t \sim 55\,\mathrm{s}$ with $\dot{\alpha_1} = 4$.

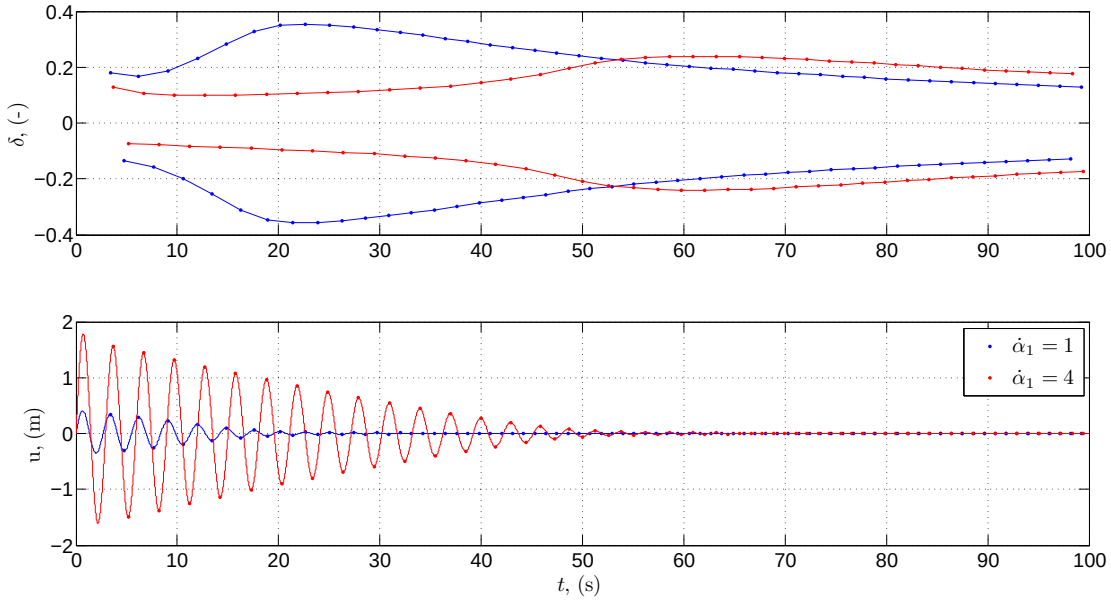

Figure 7.5: *The logarithm decrement (top figure) as function of time for the two decay tests with different start value (bottom figure).*

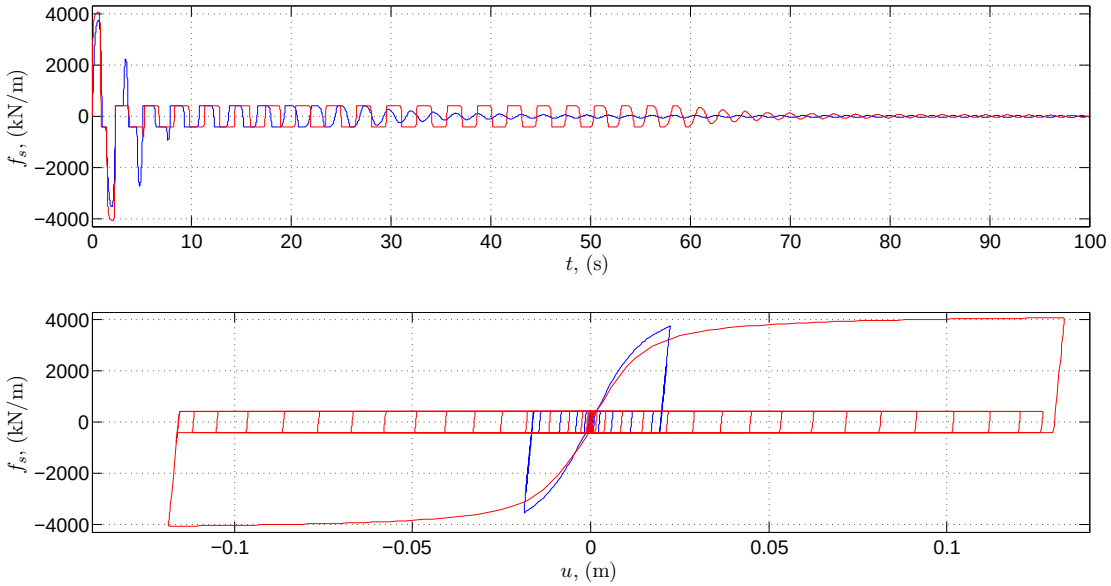

Figure 7.6: *The soil force 8 m below the sea bed as function of time and displacement for two decay test.*

7.3.2 Decay test II

The present analysis are to show that the cyclic model removes the expected energy during a cycle. In the following three decay tests similar as those above are considered, and the work and kinetic energy during one cycle are calculated and compared against the logarithmic decrement.
To simplify the analysis and to calculate the kinetic energy only the mass of the nacelle and hub, M_{top}, is considered. The mass of each blade is therefore set to 0.062kg and the density of the tower and monopile is 0.001 kg/m^3 in the calculation.
The total work done by the soil during a cycle is calculated as

$$\mathsf{W} = \int_{z_{min}}^{-h} \int_{t}^{t+T} f_s(z,t)\mathsf{u}(z,t)d\mathsf{u}dz = \int_{z_{min}}^{-h} \int_{t}^{t+T} f_s(z,t)\dot{\mathsf{u}}(z,t)dtdz. \tag{7.18}$$

The deflection is given as $\mathsf{u}(z,t) = \alpha_1\varphi_1 + \alpha_2\varphi_2 + \alpha_3\varphi_3$. The kinetic energy is found as

$$\max(E_{kin}) = \frac{1}{2}\max(\dot{\mathsf{u}}^2\mathsf{M}_{top}), \tag{7.19}$$

where $\dot{\mathsf{u}}$ here is the velocity of the nacelle. The start velocity, $\dot{\alpha}$, of the first DOF in the monopile is 1, 4 and 6 respectively. The decay test with $\dot{\alpha_1} = 4$ is shown in figure 7.7 to illustrate how W and $\max(E_{kin})$ are calculated. The cycle where the work and kinetic energy are calculated is chosen so that the displacement of the pile in all depths moves in created gap in figure 7.2. The cycle is indicated with black lines in figure 7.7. The kinetic energy is largest at the red star in the figure where the velocity $\dot{\mathsf{u}}$ is largest. The logarithmic decrement is calculated for the negative, δ_1, and positive peak, δ_2 surrounding the peak where the kinematic energy is largest.
The logarithmic decrement and the value of $\frac{1}{2}\frac{W}{\max(E_{kin})}$ of the three decay tests are compared in table 7.1. The value of the logarithmic decrement and the value of $\frac{1}{2}\frac{W}{\max(E_{kin})}$ compare well for all three tests. The smallest decay test with $\dot{\alpha_1} = 1$ results in the worse comparison. This is because the soil in the bottom of the monopile already after a few cycles only is exposed to elastic loading and unloading while the soil in the top of the pile still is moving on the virgin curve. It is therefore difficult to find a cycle where the relation $\delta = \frac{1}{2}\frac{W}{\max(E_{kin})}$ is valid along the full extent of the pile.

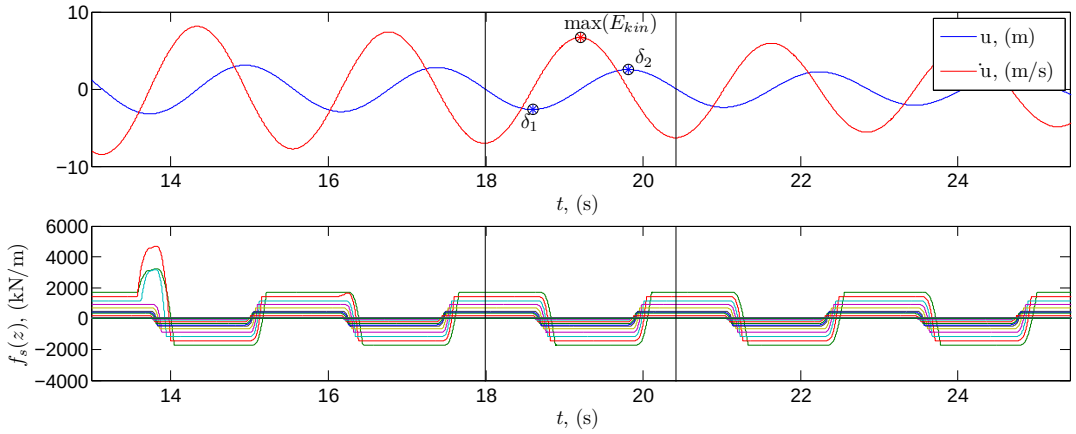

Figure 7.7: *The decay test with $\alpha_1 = 4$. The two blue stars in the top figure show where δ_1 and δ_2 in table 7.1 are calculated. The red star indicates where $\max(E_{kin})$ is calculated and the black lines indicate the cycle where the work is calculated. The bottom figure shows the soil force in the spring elements.*

α_1	δ_1	δ_2	$\frac{1}{2}\frac{W}{\max(E_{kin})}$
1	0.26	0.37	0.38
4	0.10	0.10	0.10
6	0.065	0.065	0.073

Table 7.1: *The logarithmic decrement for the three decay tests and the corresponding value of* $\frac{1}{2}\frac{W}{\max(E_{kin})}$.

7.4 A nonlinear elastic spring model

To investigate the effects of the cyclic model in the aeroelastic calculations, the model is compared to a nonlinear elastic spring model, which in the following is named the "elastic model". In the elastic model the soil force is calculated using equation (7.3) as described in DNV-OS-J101 (2010), and therefore follows the virgin curve of figure 7.2. The description of the third shape function in the monopile and the rotating spring in the bottom of the pile is the same as with the cyclic model.
To compare the elastic model with the cyclic model a constant logarithmic damping which represents the soil damping as well as possible is included in the elastic model. The amount of damping which should be added the elastic model is in the following investigated.
In the cyclic model 2 % of logarithmic damping is added to the first eigenfrequence in the tower and the monopile to represent structural damping, tower dampers and hydrodynamic damping. The same is done for the elastic model. The constant damping to represent the soil damping, which shall give the same damping rate as the cyclic model, is further added to the monopile in the elastic model, since the damping due to the soil in the cyclic model works on the monopile.
To find the amount of damping which should be added to the monopile a decay test where the start displacement is representative for a aeroelastic calculation is considered. In the calculation with the 5th sea state in chapter 4 the displacement in top of the monopile is ~ 0.04 m, which therefore is used in the present decay test. In the decay test all DOFs in Flex5 are active but the wind speed is zero and no waves are present. If 40 % logarithmic decrement is added to the monopile in the elastic model the decay tests with the cyclic model and the elastic model show simlar amounts of damping. The decay tests are shown in figure 7.8. A logarithmic damping of 40 % seems very large, but it results in a logarithmic decrement of 12 % of the first structural eigenfrequency. For comparison Klinkvort (2012) found a logarithmic decrement of 8-10% for a decay test with a displacement of the pile at the sea bed of 0.04 m. The soil and structural properties were not the same as considered here, however it still indicates that the soil models give reasonable results.

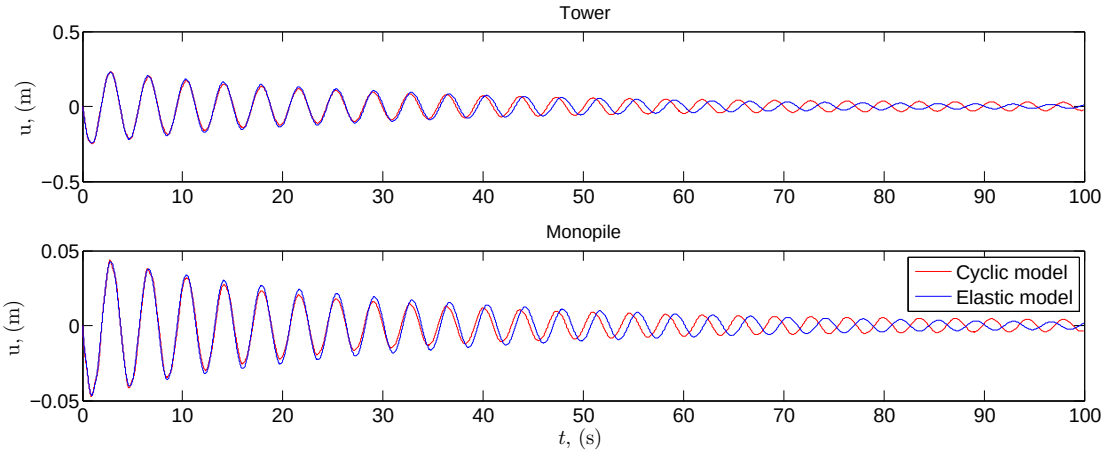

Figure 7.8: *Decay test where the cyclic model and the elastic model are compared.*

In the decay tests it is seen that the frequencies of the displacement of the monopile and tower differ slightly in the two models. The frequency of the cyclic model is a little larger.

In figure 7.9 the cyclic and elastic models are compared for two cases. In picture (a) both forces are loading on the virgin curve, while the unloading is different for the two models. The stiffness of the soil is therefore not the same for the two models. In picture (b) the cyclic model is moving in the gap while the elastic model still is loading and unloading on the virgin curve. The cyclic model has in this figure a larger efficient stiffness. Since the frequency is defined as $\omega = \frac{k}{m}$ it is clear that the larger k is the larger is the frequency.

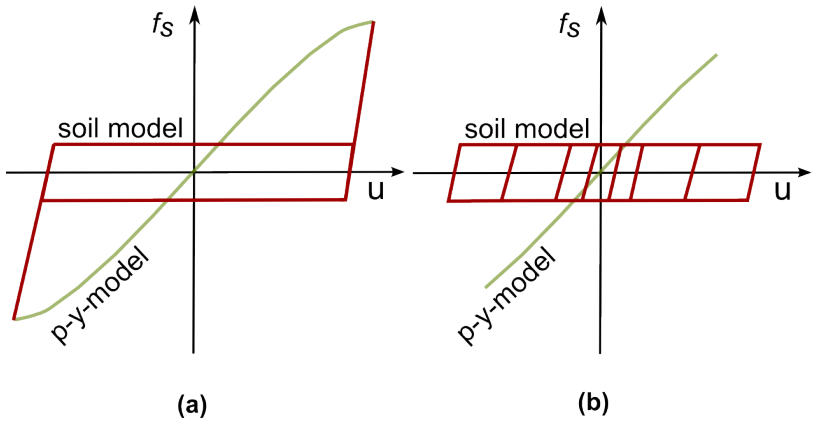

Figure 7.9: *The elastic model and cyclic model for two different situations.*

7.5 Dynamic analysis

The damping of the elastic model is now adjusted to the cyclic model. Next the importance of the cyclic model in the structural dynamics is investigated. It is expected that the creation of the gap with the cyclic model can cause some extra excitation when the pile hits the edge of the gap. Further, it is interesting to see whether the damping of the two soil models are the same, when the structure is exposed to irregular forcing.

Three wind and sea states, *2*, *4* and *5*, from chapter 4 are considered. The wind speed, turbulence intensity, significant wave height and peak wave period of the three wind and sea states are repeated in table 7.2. Only the nonlinear wave realizations are considered and only the last hour of the time series is used in the present analysis.

V (m/s)	H_s (m)	T_p (s)	I_t (-)
9	1.41	6.17	0.19
20	4.40	9.16	0.14
28	6.75	11.41	0.13

Table 7.2: *Wind and sea state 2, 4 and 5 from chapter 4, which also are considered here.*

The aeroelastic calculations are carried out in Flex5 both with the cyclic model and the elastic model. Focus is on the deflections in the top of the monopile and in the top of the tower and the overturning moments in the bottom of the monopile and tower.

The calculations are run in 200 s before the analysis starts. At the start of a calculation in Flex5, an iteration is done before the first time step, where the initial structural deflection is calculated based on the starting loads. This iteration is not combined with the soil models yet. Therefore, if the calculations start with full forcing from the first time step, the start deflection with the cyclic model and the elastic model will not be the same. To ensure that the start conditions are the same for the two models, the surface elevations and wave kinematics and the wind speed were ramped up from zero to their full magnitude go from being zero to fully developed during the first 200 s using a sinusoidal function for the wave kinematic and a linear function for the wind speed.

7.5.1 Response

In figure 7.10 the deflection in the top of the monopile the first 1000 s of all three wind and sea states are shown. The cyclic model and elastic model are compared against each other. For wind and sea state *2* and *4* the wind turbine operates and the wind turbine is therefore exposed to a positive trust force. This explains why the deflection is positive for these two cases. For wind and sea state *5* the blades are pitched to an angle of 87° and the aerodynamic forcing is therefore small. The deflection of the monopile is therefore in this case also negative sometimes due to the wave forcing.

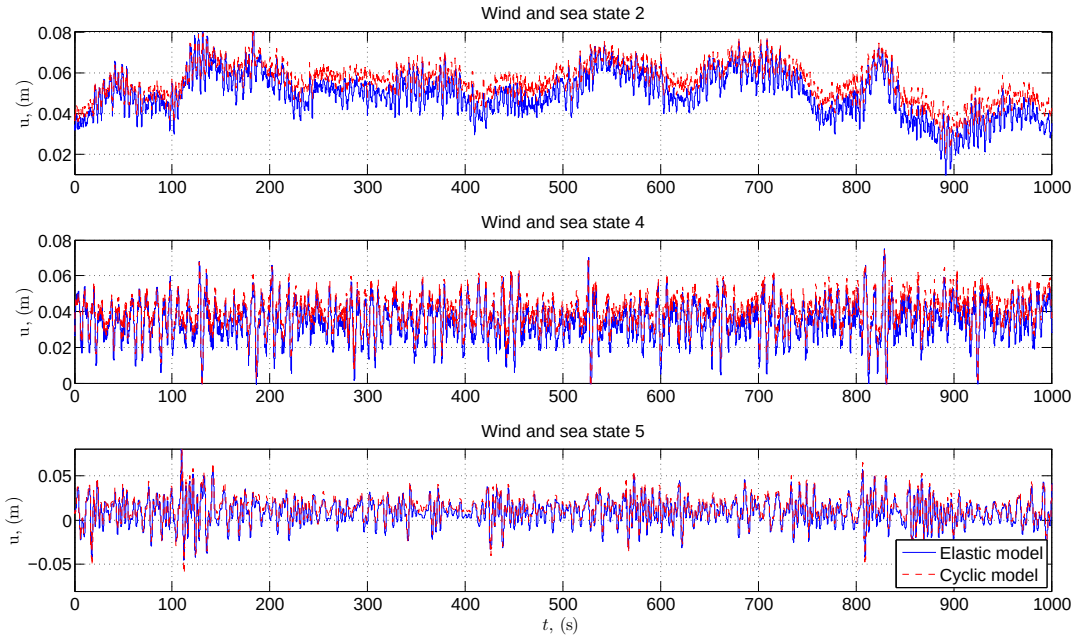

Figure 7.10: *The deflection of the top of the monopile for wind and sea state 2, 4 and 5.*

For wind and sea state *2* it is clear that the difference between the deflection due to the soil-model and the elastic model increases from the start to the end of the time series. This is because the gab in the soil becomes larger and larger in the cyclic model every time the forcing from the wind and waves increases to a new extent. The deflection of the pile increases therefore also, and rotates around a larger and larger mean value. In reality the gab would off course increase sometimes but there would also be backfilling of the gab, which is missing in this cyclic model. The effect is also seen for wind and sea state *4* but is not a pronounced, because the trust force is smaller for wind and sea state *4* compared to wind and sea state *2*. For wind and sea state *5* the aerodynamic forcing is very small and it is therefore not possible to see an increase in the difference between the deflections because the gap only increases when a new largest wave force occur.
Besides the increasing gab the deflections due to the two models are very similar.

In figure 7.11a a time sequence of the deflection in the top of the tower and the overturning moment in the bottom of the tower is shown for wind and sea state *2*. The cyclic model and the elastic model is compared in the figure. The deflection of the tower is the deflection relative to the bottom of the tower, so the deflection of the monopile is not added to the deflection in the figure. Both the deflection and the moment due to the two models are very similar. The response both of the deflection and the moment are some time largest for the elastic model and sometimes for the cyclic model. In the deflection it is possible to identify a high frequency oscillation at for example time $t \sim 2820\,\text{s}$. The frequency is $\hat{f} \sim 1.3$ Hz and is the eleventh global structural eigenfrequency with 35 % of the model energy in the monopile and 43 % of the model energy in the tower. The rest of the model energy is distributed in the nacelle with 2 % and in the blades with 18 %. In figure 7.11b the deflection of the top of the monopile and the overturning moment in the bottom of the monopile due to wind and sea state *2* are shown in same time sequence as for the tower. The

shift which exists between the two model's deflection of the pile is not seen on the overturning moment. In the monopile the high frequency oscillation of $\hat{f} \sim 1.3$ Hz is also recognised both in the deflection and in the moment with the cyclic model. The reason that the oscillations are more obvious in the moment in monopile is that the moment arm is larger. The excitations which occur in the tower and further up in the wind turbine are therefore amplified in the moment-signal in the monopile. It is further seen that the high frequency oscillations continues from $t = 2820 - 2850$ s before they starts to dampen. The amplitude of the main moment-signal is not large in this time period which means that the soil force in some springs during this time are moving on the elastic loading/unloading curve where f_{face} also are active and the monopile therefore hits the edge of the gab again and again. For small forces it is therefore also possible to excite the eleventh structural frequency.

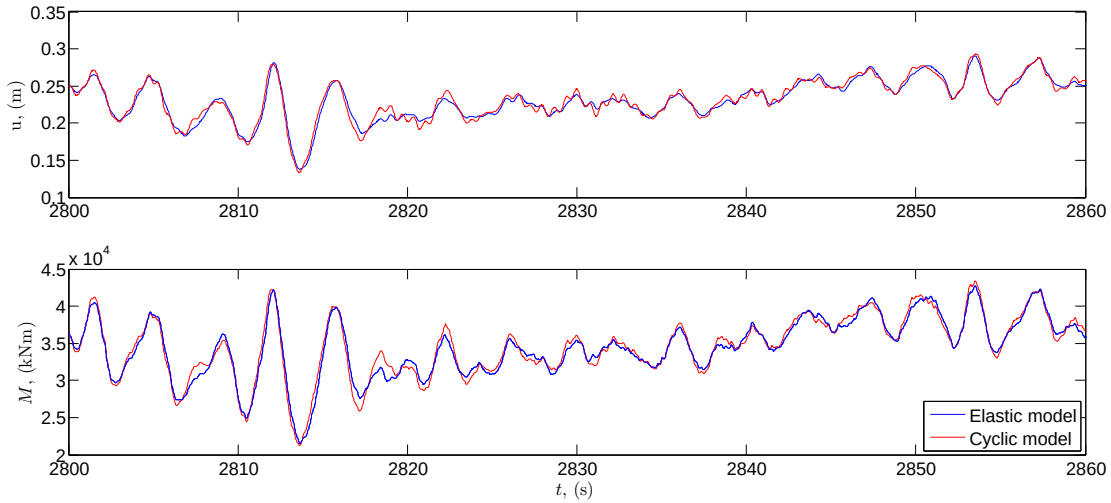

(a) Tower.

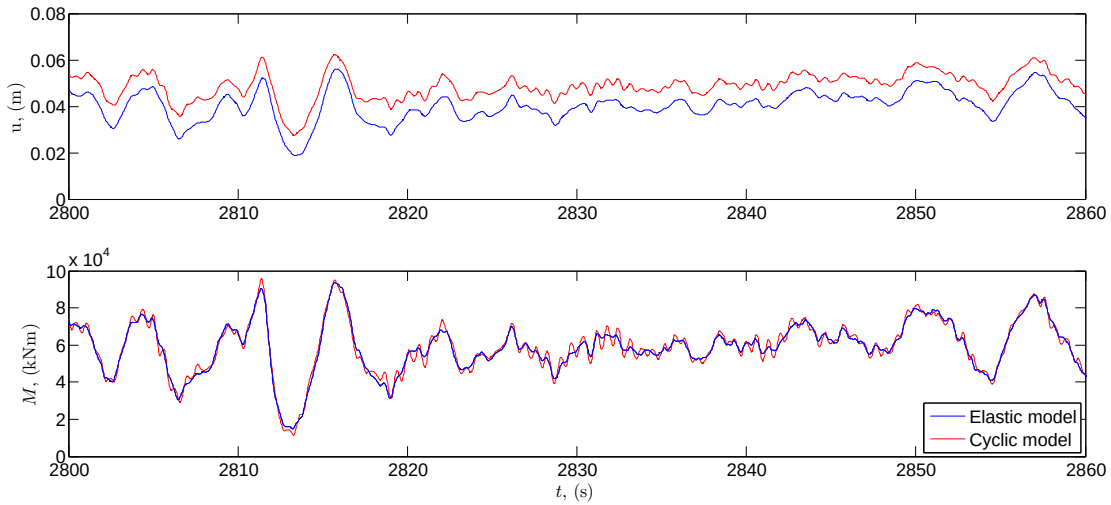

(b) Monopile.

Figure 7.11: *The deflection in the top of the tower and in the top of the monopile and the overturning moment in the bottom of the tower and in the bottom of the monopile. Wind and sea state 2.*

In figure 7.12 the deflection of the top of the tower and monopile and the overturning moment in the bottom of the tower and monopile for wind and sea state *4* are shown in a time sequence. The curves are similar to wind and sea state *2*. The structural eleventh eigenfrequency is also excited

for wind and sea state *4*, and the excitation is largest in the monopile, which for example can be seen at $t = 830\,\text{s}$. The structural eleventh frequency is also excited in the elastic model in the overturning moment in particular in the bottom of the monopile. However, the excitation is not as large as for the cyclic model. Since some of the modal energy is distributed in the blade, it can be excitation of the blade which is repeated in the moment in the monopile. The position of the blades over time is the same for the two models. It can therefore not be a phase difference in the position of the blades, which causes the larger excitation in cyclic model. Also, if the constant damping in the monopile is reduced from 40 % of logarithmic damping to 2 % in the elastic model the exciation is still not as large in the elastic model as is seen with the cyclic model (this is not presented in a figure). This indicates that the larger excitation of the cyclic model is caused by the cyclic description of the soil and is not due to differences in the size of damping of the two models.

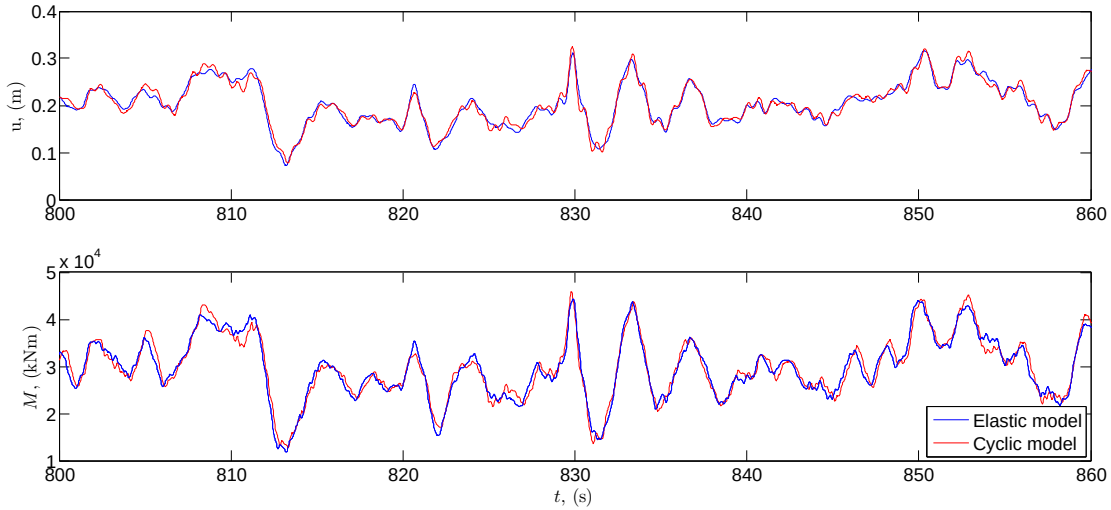

(a) Tower.

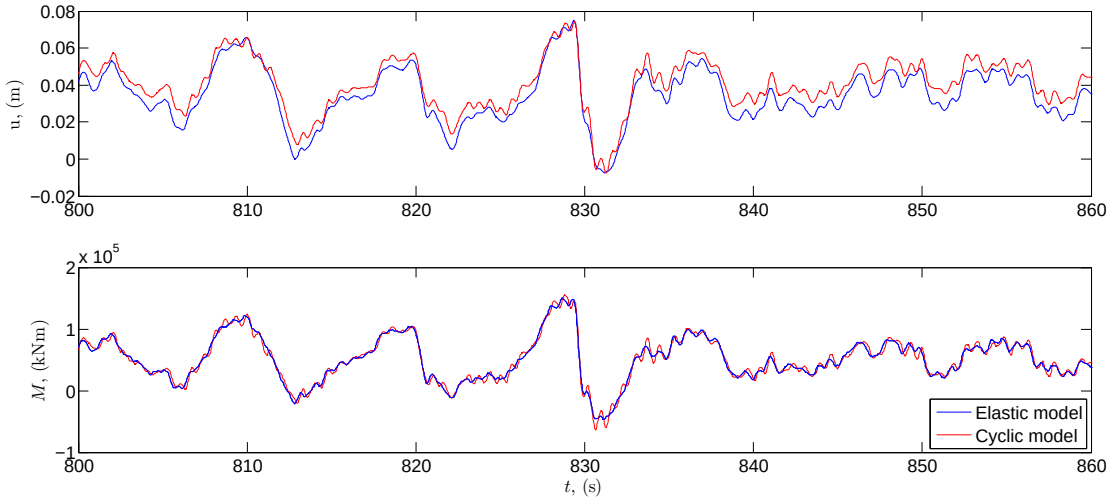

(b) Monopile.

Figure 7.12: *The deflection in the top of the tower and in the top of the monopile and the overturning moment in the bottom of the tower and in the bottom of the monopile. Wind and sea state 4.*

The deflections and moments in the tower and monopile due to the fifth wind and sea state are considered in 7.13 in a time sequence where two large waves at $t \sim 1725\text{s}$ and $t \sim 1738\,\text{s}$ occur and cause impulsive responses. In the tower, primarily the structural first eigenfrequency is excited. In

the monopile both the structural first and eleventh frequencies are excited with both models, but the eleventh eigenfrequency is excited most with the cyclic model. The excitation of the eleventh frequency dampens after approximately 20 s whereafter the moment in elastic model and the cyclic model are very similar. For wind and sea state *5* the structural eleventh frequency is only excited when a large wave occur and the monopile thereby hits the edge of the gap.

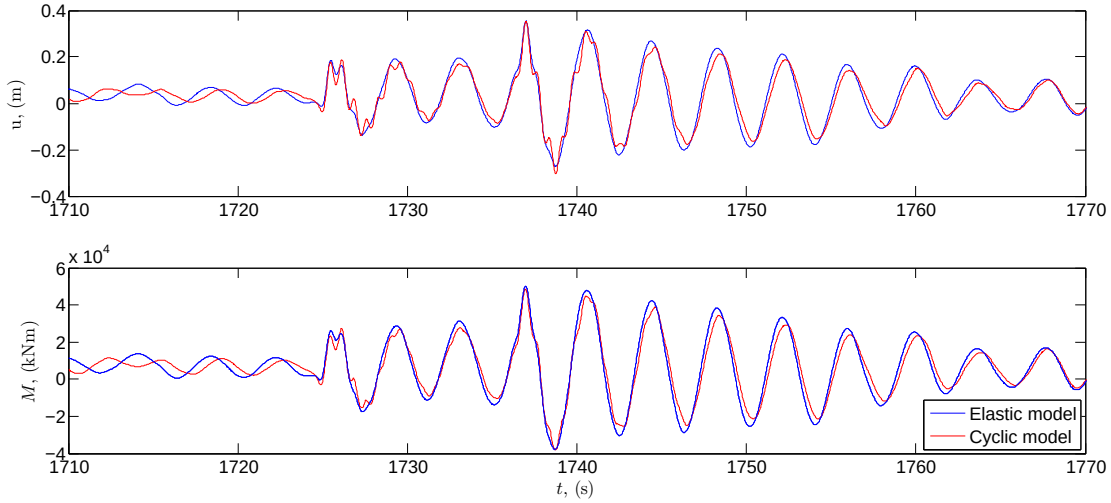

(a) Tower.

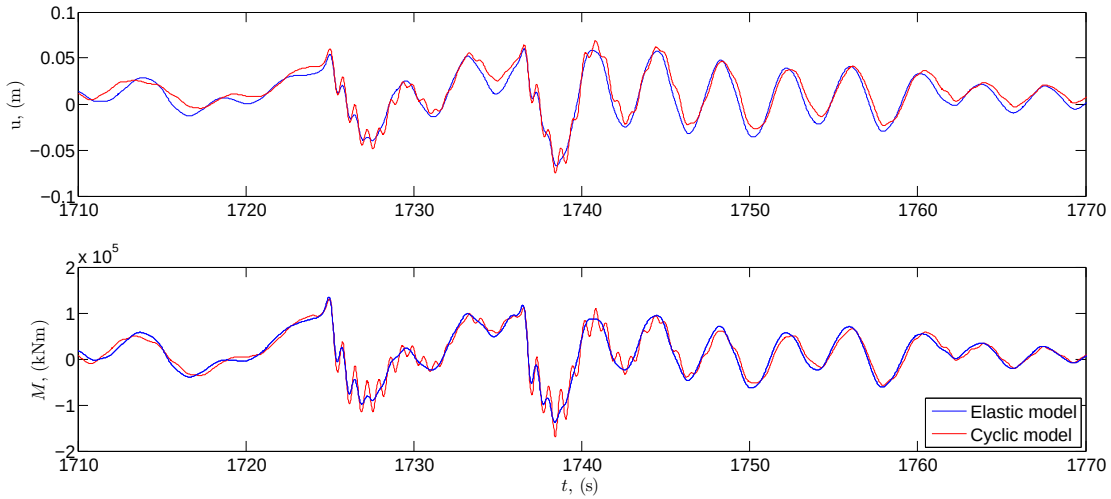

(b) Monopile.

Figure 7.13: *The deflection in the top of the tower and in the top of the monopile and the overturning moment in the bottom of the tower and in the bottom of the monopile. Wind and sea state 5.*

7.5.2 Equivalent loads

The equivalent loads based on the overturning moments in the bottom of the tower and monopile due to wind and sea state *2*, *4* and *5* are calculated for both models. This is done to quantify the long-term effect of the observed dynamic differences in the two models. The equivalent loads are compared in figure 7.14 both for $m = 3$ and $m = 5$.
The equivalent loads are consistent with the results of chapter 4. The loads are largest for the fifth wind and sea state and smallest for the second wind and sea state. Further the loads due to the

elastic model (left bar) and the soil-model (right) bar are generally very similar. The cyclic model results in the largest equivalent loads except for the equivalent loads due to the wind and sea state *2* and *4* in the tower, where the loads due to the elastic model are largest.

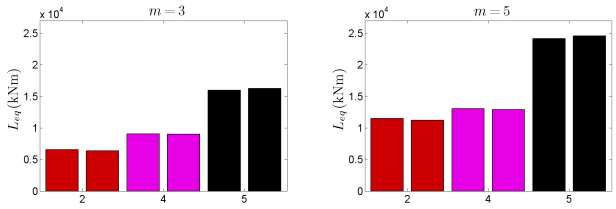

(a) Tower.

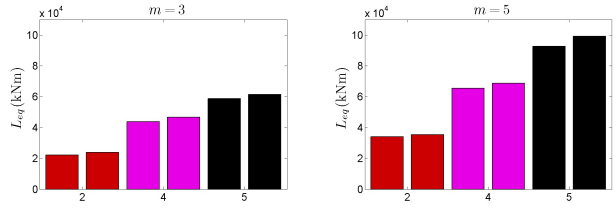

(b) Monopile.

Figure 7.14: *The equivalent loads for wind and sea state 2, 4 and 5 when the elastic model (left bar) and the cyclic mode (right bar) are used.*

In figure 7.15 the ratio between the equivalent loads due to the elastic model and the cyclic model are shown. In the monopile the equivalent loads due to the soil-model are approximately 5 % larger than those due to the elastic model. This must be due to the excitations of the structural eleventh eigenfrequency. For $m = 3$ the difference is largest for case *2* while the opposite is seen for $m = 5$. The larger m is the more important the extremes are when calculating the equivalent loads. For wind and sea state *2* and *4* it was seen that the high frequency oscillations occurred for smaller forces when the monopile was moving close to the edge of the gap. This can explain why the equivalent loads with the cyclic model are relative larger than the equivalent loads with the elastic model for $\mathsf{m} = 3$. For wind and sea state *5* the high-frequency oscillations occurred when a large wave force occurred and was most prenounced for the cyclic model. This can then explain why the equivalent loads of the cyclic model here are relative larger than the equivalent loads with the elastic model for $\mathsf{m} = 5$.
In the tower the difference between the two models are smaller. For wind and sea state *2* and *4* the equivalents loads are 1-2 % smaller in the cyclic model while the equivalent loads for wind and sea state *5* are 2 % larger in the cyclic model. The high-frequency oscillations which in the monopile lead to larger equivalent loads with the cyclic model is not as pronounced in the tower, which can explain that the difference between the equivalent loads are smaller in the tower. Further, the constant damping in the elastic model is based on a representative deflection from wind and sea state *5*. This damping value might be a little too small when the two other sea states is considered. This can explain why the equivalent loads with the elastic model is largest for wind and sea state *2* and *4*.

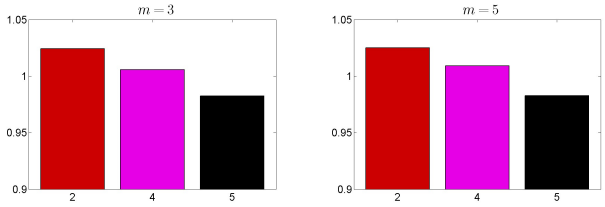

(a) Tower.

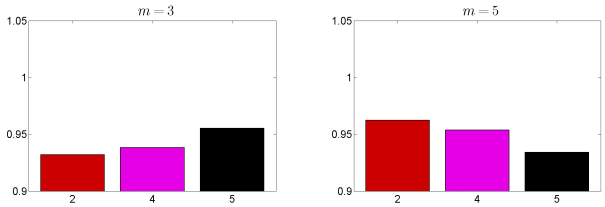

(b) Monopile.

Figure 7.15: *Difference between the equivalent loads for wind and sea state 2, 4 and 5 with the elastic model and the cyclic model.*

7.6 Summary

In the present chapter a soil model containing effects like hysteresis and creation of gaps between the pile and soil at reversed loading has been implemented in Flex5. The implementation was simplified by only considering a part of the pile below the sea bed. The last part of the pile was represented by a rotating spring. In this way the displacement of the pile in the soil could be described by an "internal" shape function.
Two simple decay tests were considered to investigate the properties of the cyclic soil model and validate that the model was working as expected. It was found that the damping is largest for the small amplitudes of the displacement and that the cyclic model removes the expected energy during a cycle.
Finally, the cyclic soil model was compared against a elastic model based on classical p-y curves combined with a constant damping factor. To represent the soil damping 40 % of logarithmic damping was added to the monopile in the elastic model. In a decay test this resulted in a logarithmic decrement of 12 % of the structural first eigenfrequency for both models. In the decay test it was further seen that the frequency of the displacement of the pile differed slightly in the two models. This is due to differences in the efficient stiffness of the soil.
The comparison of the two models in the dynamic analysis indicated that it is possible to represent the soil damping by a constant damping added to the system. However, it it is necessary to change the damping according to the conditions that are investigated.
Further it was seen that the cyclic model results in larger excitations of structural eigenfrequency of 1.3 Hz and that these excitations leads to larger equivalent loads. That means, that even if the constant damping is chosen correctly it may still be non-conservative to use the elastic model because as the detailed and sometimes rapidly varying soil force is not included in that model.

Chapter 8

Aeroelastic response to CFD wave loads

The potential flow model, OceanWave3D, can as discussed earlier not handle wave breaking. Further, all the analyses have so far been based on Morison equation where the undisturbed wave kinematics are utilized. Effects as wave run- up on the cylinder and detailed diffraction are therefore also ignored. One method to handle these effects is through the CFD-solver OpenFOAM, in combination with the wave generation toolbox, waves2Foam (Jacobsen et al., 2012), which solves the Navier-Stokes equations. The equations are solved by the finite volume method and the free surface is handled by a variant of the volume of fluid method, Hirt & Nichols (1981).

It is through OpenFOAM possible to calculated the wave kinematics around a cylinder exposed to waves and the corresponding pressure acting on the cylinder. The wave kinematics around and forcing on the cylinder from OpenFOAM are considered to be more correct than the wave kinematics and forcing based on OceanWave3D and Morison's equation. It is therefore of interest to compare the results of the aeroelastic calculations when the wave loads are based on the potential flow and Morison's equation and to similar computations when the wave loads are calculated by OpenFOAM.
To do the calculations in OpenFOAM a combined solver described in Paulsen *et al.* (2012) and Paulsen *et al.* (2013*b*) is used. In the combined solver the undisturbed wave kinematics are calculated by OceanWave3D in the entire domain. OceanWave3D further works as boundary conditions for OpenFOAM, which calculate the wave kinematics and corresponding pressure on the cylinder in a smaller area just around the cylinder. The two models are coupled via generalized coupling zones. With this method the calculation time in OpenFOAM is reduced significantly.

In the first part of the present chapter the wave realization is considered and how it is calculated is presented. Afterwards it is explained how the forces are derived from OpenFOAM and the wave kinematics and the surface elevation from OceanWave3D and OpenFOAM are compared. Hereafter a static comparison of the inline force and overturning moment based on the potential flow and Morison's equation and the forces from OpenFOAM is performed, to find the optimal values of the inertia coefficient, C_M and the drag coefficient, C_D. Finally, a dynamic analysis is utilized where the forces are included in the aeroelastic calculations in Flex5. The importance of the "Rainey terms" in Morison's equation, (3.40 and 3.40), is further investigated in the aeroelastic calculations. The following analyses are based on the calculations Paulsen *et al.* (2013*a*). The calculations are kindly provided by Bo Terp Paulsen.

8.1 The model set-up

In Paulsen *et al.* (2013*a*) the forces based on OceanWave3D and Morison's equation were compared against the forces from OpenFOAM and laboratory experiments. In the experiments a fixed cylinder on a sloping sea bed exposed to irregular waves were considered. The experiments were

carried out at DHI and consisted also of experiments with a flexible cylinder and multi-directional waves. The experiments are made as part of the larger Danish Wave Loads Project and are described in more details in Nielsen *et al.* (2012) and Bredmose *et al.* (2013).
The calculations in the present study are based on an experiment where the cylinder has a diameter of $D = 0.164\,\mathrm{m}$ and is placed in a water depth of $h_{cyl} = 0.55\,\mathrm{m}$. The waves are generated at a water depth of $h_d = 0.82\,\mathrm{m}$. At the downstream end of the domain the water depth is 0.46 m. The ratio between model scale and full scale is 1:36.6. The nonlinear irregular wave realizations are in the experiments based on unidirectional JONSWAP spectrum with the target values $H_s = 0.23\,\mathrm{m}$ and $T_p = 1.68\,\mathrm{s}$ at the cylinder. The data are repeated in table 8.1. A sketch of the profile used in the calculations is shown in figure 8.1. The inner boundaries of the relaxation zones in OceanWave3D and the coupling zones are also indicated in the figure.
In the calculations the incident wave realization from the model test was reconstructed by application of a linear reflection analysis applied for the first three wave gauges which were placed between 1m and 1.35 m from the wave maker.

	D (m)	h_{cyl} (m)	h_d (m)	H_s (m)	T_p (s)
Model scale	0.164	0.5765	0.82	0.23	1.68
Full scale	6.00	21.10	30.01	8.3	10.2

Table 8.1: *Experimental data in model and full scale.*

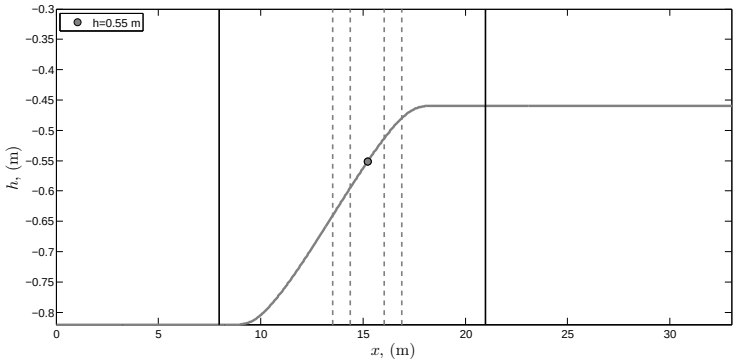

Figure 8.1: *The profile of the sea bed. The black lines indicates the inner boundaries of the relaxation zones. The dashed lines indicate the coupling zones.*

The calculations in OceanWave3D and in OpenFOAM are also in model scale and afterwards scaled to full scale by Froude scaling. In the Froude scaling the acceleration of gravity is keept constant and a scaling factor, $\tilde{\lambda}$, between the length scales in model and full scale is assumed. This leads to the relation, $\sqrt{\tilde{\lambda}}$, between the time scales in model and full scale. The potential flow solver is inviscid and therefore perfect to Froude-scaling. In OpenFOAM viscosity of the fluid is included in the calculations. However, the viscous boundary layer at the cylinder is neglected and instead a slip condition is applied at the surface of the cylinder. By making the calculations in model scale but the analyses in full scale can lead to scale effects. However, since this flow and the forces are inertia dominated, the scale effects are assumed to be small.
The length of the time series which is compared is 99.2 s in model scale which gives 600 s in full scale.
The grid spacing of the domain in model scale is $dx = 0.05$ m. A wave with a frequency 0.32 Hz in full scale is therefore resolved with 8 points in the horizontal direction. This should be sufficient to get a converged solution, and the waves in the wave realization with frequencies smaller than 0.32 Hz are therefore expected to be resolved with enough points in the horizontal direction. However, waves with frequencies larger than 0.32 Hz in full scale are resolved with to few points to ensure a converged solution. A wave with a frequency of 0.32 Hz in a water depth of 0.82-0.55 m is a liner wave. The non-dimensional wave number is $kh = 12$, and nine grid points in the vertical direction is therefore sufficient to describe the wave in OceanWave3D. However, for waves with

larger frequencies more grid points in the vertical direction is perhaps necessary to get a converged solution. Since the peak frequency of the considered sea state is 0.1 Hz, it is expected that most of the waves in the wave realization in the present analysis are converged.
All data are in the following in full scale if nothing else is stated. Also, in the following when forces and moments are said to be based on Morison's equation it implies that the wave kinematics are from OceanWave3D.

8.2 The wave loads from OpenFOAM

The pressure on the cylinder, p, calculated in OpenFOAM is at each time step converted into a single distributed force by spatial integration of the pressure on the wetted area of the cylinder by the following procedure.
The total pressure over the cylinder is first multiplied with the factor, $\tilde{\alpha}$, which is the local volume ratio of water of each cell. If $\tilde{\alpha} = 1$ the cell only consists of water and if $\tilde{\alpha} = 0$ the cells only consists of air. The pressure on each cell on the cylinder is afterwards converted to a force, F, by multiplying the pressure with the face area of the cell against the wall.
The total force matrix is projected into a force matrix in same direction as wave propagation , F_x, and perpendicular to this direction, F_y. The forces on each cell on the cylinder, F_x, are then converted to distributed forces in the z-direction by dividing the force with the distance the force works on in the z-direction (the height of the cell)

$$f_x = F_x/\Delta z. \tag{8.1}$$

The cylinder is placed on a sloping sea bed. The forces are therefore not found in the same depths on the front and rear side of the cylinder. The distributed forces on the cylinder is therefore interpolated to the vector $z = [z_{min}; z_{top}]$, where z_{min} is the lowest point on the cylinder and z_{top} is the top point on the cylinder as indicated in figure 8.2. The forces around the cylinder for each z-value are afterwards summed to one distributed force working along the cylinder.

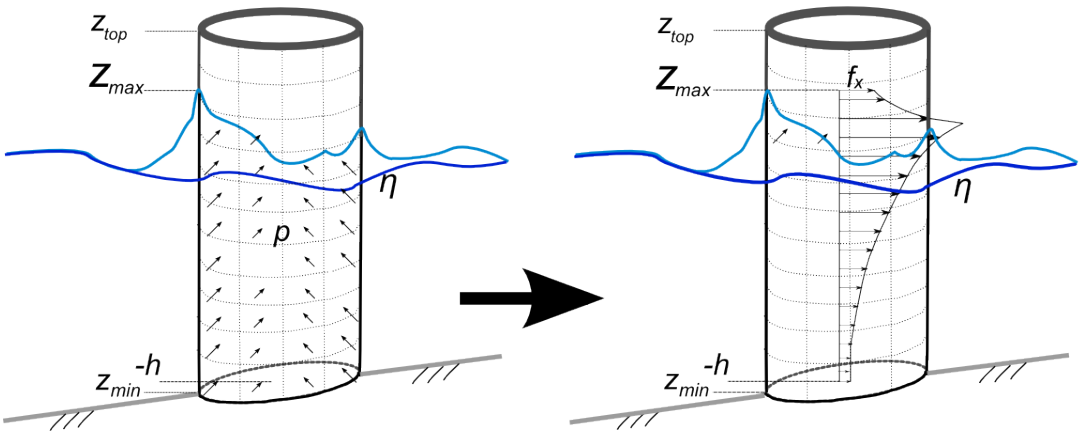

Figure 8.2: *A sketch of the cylinder in OpenFOAM. In the figure the definitions of z_{min}, z_{max} and Z_{max} are stated. The pressure on the cylinder p are converted to a single distributed force, f_x, from $-h$ to Z_{max}.*

In Flex5 the wave kinematics are given as input in some defined points from the sea bed and up to the undisturbed surface elevation. When the forces from OpenFOAM are considered the surface elevation is defined as the highest point on the cylinder which the water reaches and is calculated as

$$Z_{max} = \int_{z_{min}}^{z_{top}} z\lambda dz + z_{min}. \tag{8.2}$$

The distributed force is next interpolated to a vector from the cylinders centerline at the sea bed, $-h$, and up to Z_{max} which is input to Flex5

$$z_i = \sigma_i i(Z_{max} + h) - h, \quad i = 1, 2, ..., N_z. \tag{8.3}$$

This vector is based on the σ-coordinate, equation (2.5), with $N_z = 20$. The force vector is shown in figure 8.2.
The force from the CFD-calculations corresponds to a situation where the cylinder is not moving, i.e. $\dot{\mathsf{u}} = 0$. The forces from the CFD-calculations are in Flex5 therefore corrected for the displacement of the monopile by considering the terms in the Morison equation, (3.40), where the velocity of the monopile appears, i.e. the drag term, f_D, and the axial divergence correction term, f_{dc}

$$\begin{aligned} f_D(z,t) =& \frac{1}{2}\rho C_D D \left(u(z,t) - \dot{\mathsf{u}}(z,t)\right) \left|u(z,t) - \dot{\mathsf{u}}(z,t)\right| \\ =& \text{sign}\left[u(z,t) - \dot{\mathsf{u}}(z,t)\right] \cdot \frac{1}{2}\rho C_D D \left(u(z,t)^2 + \dot{\mathsf{u}}(z,t)^2 - 2u(z,t)\dot{\mathsf{u}}(z,t)\right), \end{aligned} \tag{8.4}$$

$$f_{dc}(z,t) = \rho \mathscr{A} C_m w_z(z,t) \left(u(z,t) - \dot{\mathsf{u}}(z,t)\right). \tag{8.5}$$

Comparing equation (8.4) to Morison's equation, (3.40), it is seen that the velocity of the monopile in the side-to-side-direction is neglected in the drag force to simplify the equation.
In the Flex5 calculations presented in the following sections in the present chapter, the largest velocity of the monopile is $\dot{\mathsf{u}} \sim 0.05$ m/s, while the horizontal particle velocity of the waves is up to $u \sim 8$ m/s. It applies therefore that $\dot{\mathsf{u}} << u$ and the second term in the drag force $\dot{\mathsf{u}}^2$ is therefore ignored. The correction of the displacement of the cylinder in the CFD-force, f_{CFD} therefore gives

$$f_{CFD} = f_{CFD} + \text{sign}\left[u(z,t) - \dot{\mathsf{u}}(z,t)\right] \cdot \frac{1}{2}\rho C_D D \left(-2u(z,t)\dot{\mathsf{u}}(z,t)\right) - \rho \mathscr{A} C_m w_z(z,t)\dot{\mathsf{u}}(z,t). \tag{8.6}$$

The point force, equation (3.41), and repeated here fore convenience

$$F_s = -\frac{1}{2}\rho \mathscr{A} C_m \eta_x \left(u(z,t) - \dot{\mathsf{u}}(z,t)\right)^2,$$

is relative small. Further, it is a third-order force and therefore a order larger than f_D and f_{dc}. The CFD-force is therefore not corrected for the structures contribution to the point force.
The velocities u and w are extracted from OpenFOAM in the same depth but half a meter from the cylinder, because the velocities around the cylinder are to disturbed to use. The velocities are therefore only defined from $-h$ to η and not to Z_{max} in figure 8.2. The derivative w_z is calculated as post-processing using the midpoint rule on a 5 point stencil which is accurate to fourth order.

8.3 The wave kinematics

The wave kinematics from OpenFOAM and OceanWave3D are compared in the following.
In figure 8.3 the surface elevation from OceanWave3D are compared against the surface elevation extracted next to the cylinder in OpenFOAM and the surface elevation found at the front of the cylinder, Z_{max}. The surface elevations from the two calculations compare well, while Z_{max} is larger due to wave run-up on the cylinder.
The amplitude spectra of the surface elevations are also shown in the figure and are also comparable. The spectrum is smoothened by computing the running mean value along a 7 point moving stencil for the whole spectrum. The peak frequency is the same for the two surface elevations and Z_{max}, but the surface elevation from OpenFOAM and Z_{max} contains more energy just above the peak frequency compared to the surface elevation from OceanWave3D. Further, Z_{max} contains more energy below the peak frequency compared to the two surface elevations.

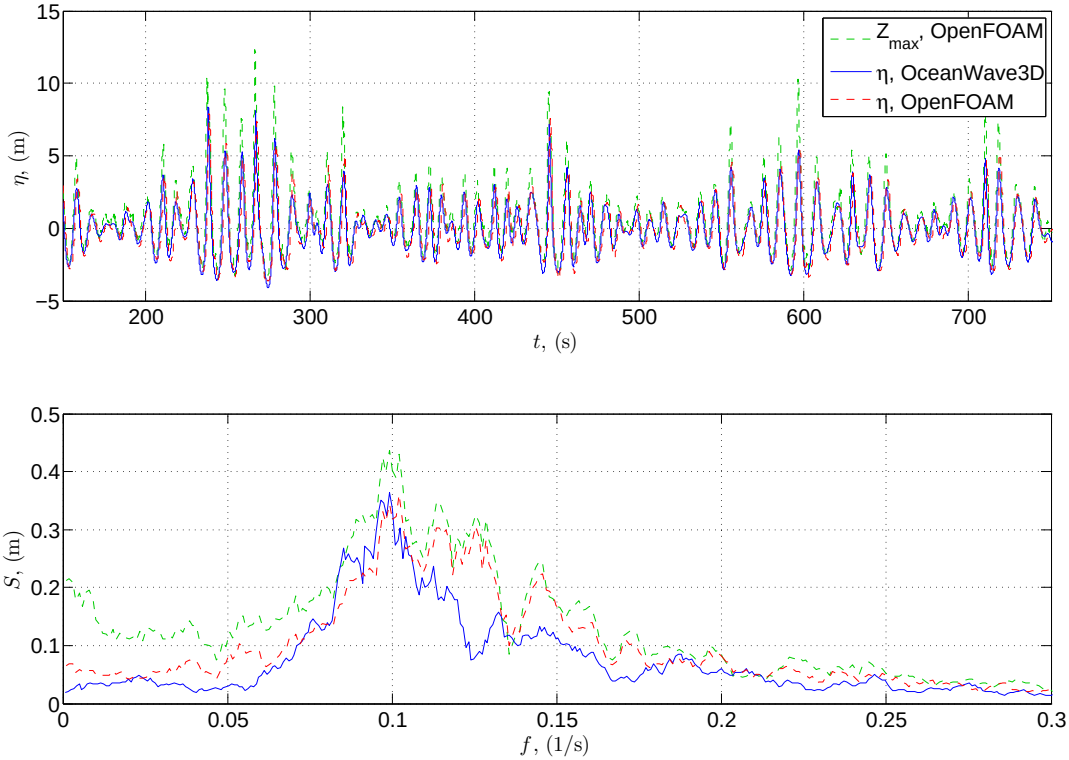

Figure 8.3: *The time serioes and wave spectra of the surface elevations from OceanWave3D and OpenFOAM. Further is the surface elevation found on the cylinder in OpenFOAM (Z_{max})a also shown.*

The surface elevations of the first waves in the wave group in the interval $t = 220 - 320\,\mathrm{s}$ are compared in figure 8.4 and it is seen that the crests of the largest waves from OceanWave3D have the largest crest and have more steep peaks than the crests of the waves from OpenFOAM. This is because the large waves in OpenFOAM have some white capping and a little overturning, which round off the peaks.

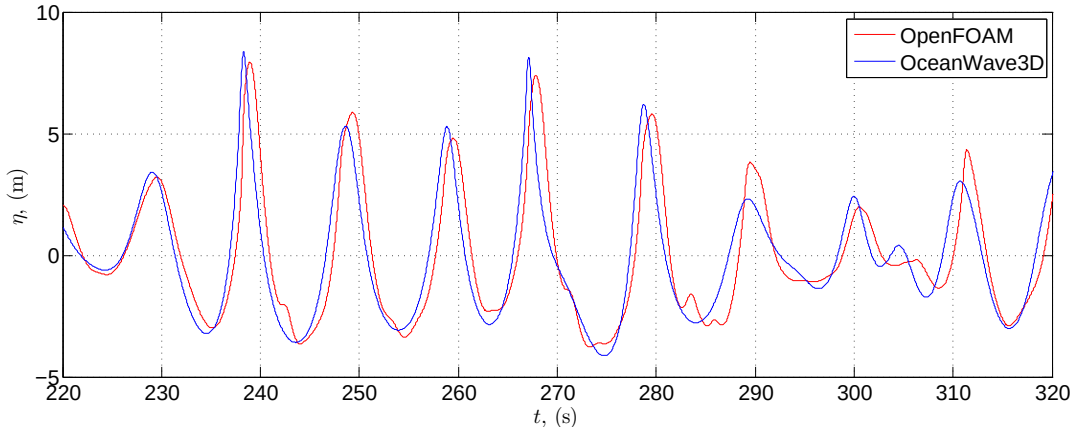

Figure 8.4: *The surface elevation from OceanWave3D and OpenFOAM in a time interval with some large waves.*

In figure 8.5a-8.5f the wave which passes the cylinder around $t \sim 239\,\mathrm{s}$ are shown for 6 different instants. The wave is seen to show some white capping in front of the cylinder in figure 8.5a-8.5d. In figure 8.5e and 8.5f the wave passes the cylinder and illustrates the wave runup on the cylinder. In figure 8.5g and 8.5h the wave which passes the cylinder at time $t =\sim 259.5\,\mathrm{s}$ is shown during its propagation towards the cylinder. It is seen that the wave is overturning. The wave breaking filter was not activated in the OceanWave3D-calculations even though the limit for when the filter applied the calculations was reduced to $\frac{dw}{dt} < -0.2g$. No energy has therefore been extracted from the large waves in the present wave realization in OceanWave3D. The reason that the filter is not activated can be that it does not cover this type of wave breaking, where the waves have some white capping and experience a small overturning.
It does not apply for all waves in the wave realization that the crests are largest in the waves from OceanWave3D, which also is seen in figure 8.4 at $t \sim 290\,\mathrm{s}$ and $t \sim 310\,\mathrm{s}$.

The probability of exceedance of the positive and negative peaks in the surface elevations are compared in figure 8.6. It is seen that the curves are similar but also that the surface elevation in OpenFOAM has larger positive peaks for all probabilities of exceedance except for the two smallest probabilities. So even though the crests of the surface elevation are more narrow in OceanWave3D they are not larger. For the negative peaks the two curves varies more. For some probabilities of exceedance the surface elevation from OceanWave3D has the largest negative peaks and for other probability of exceedance it is the surface elevation from OpenFOAM which results in the largest negative peaks. Particular for the lowest probabilities of exceedance, OpenFOAM results in the largest negative peaks.

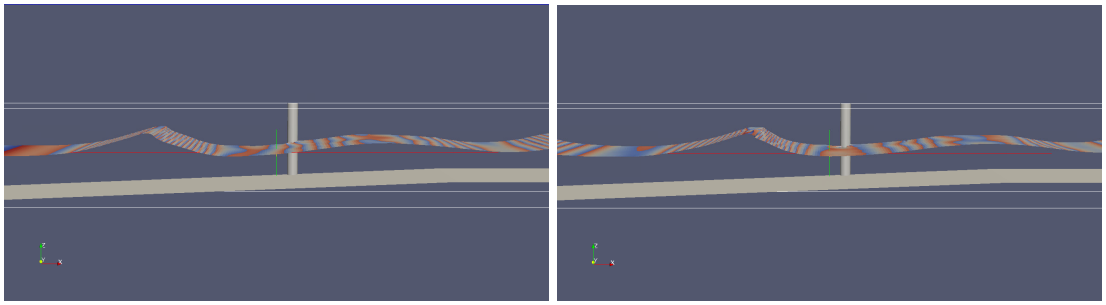

(a) $t = 231.7\,\mathrm{s}$.

(b) $t = 234.7\,\mathrm{s}$.

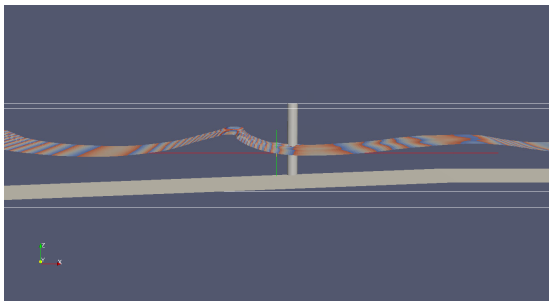

(c) $t = 235.9\,\mathrm{s}$.

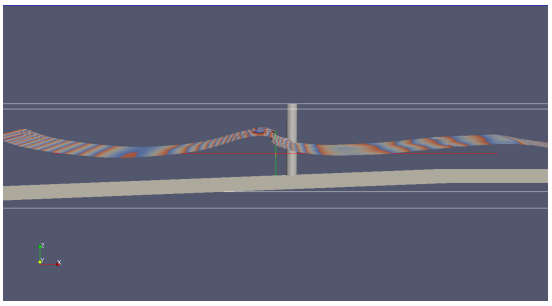

(d) $t = 237.1\,\mathrm{s}$.

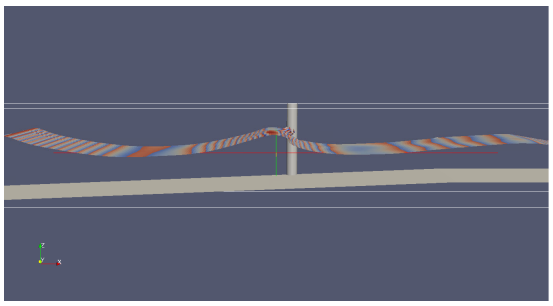

(e) $t = 237.7\,\mathrm{s}$.

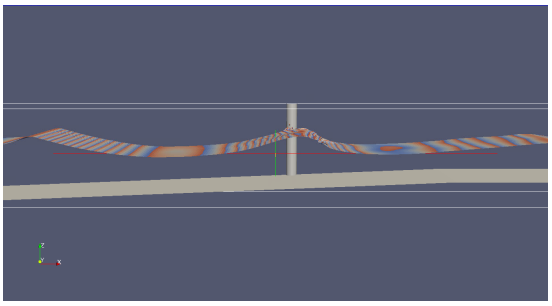

(f) $t = 239.0\,\mathrm{s}$.

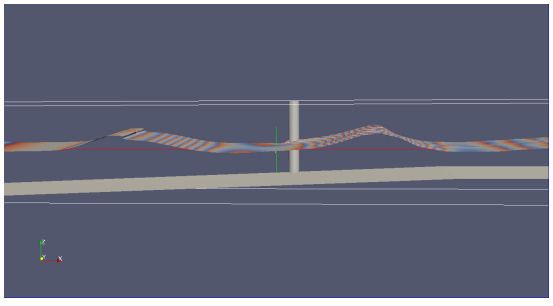

(g) $t = 251.1\,\mathrm{s}$.

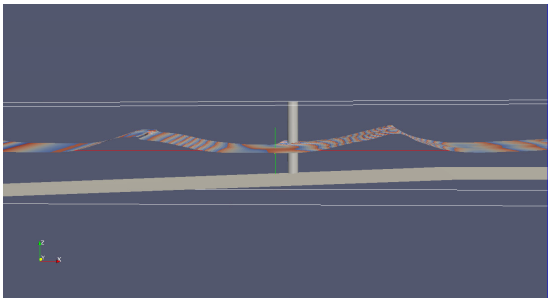

(h) $t = 252.3\,\mathrm{s}$.

Figure 8.5: *Illustrations of the surface elevation in OpenFOAM. The waves experience some white capping and overturning.*

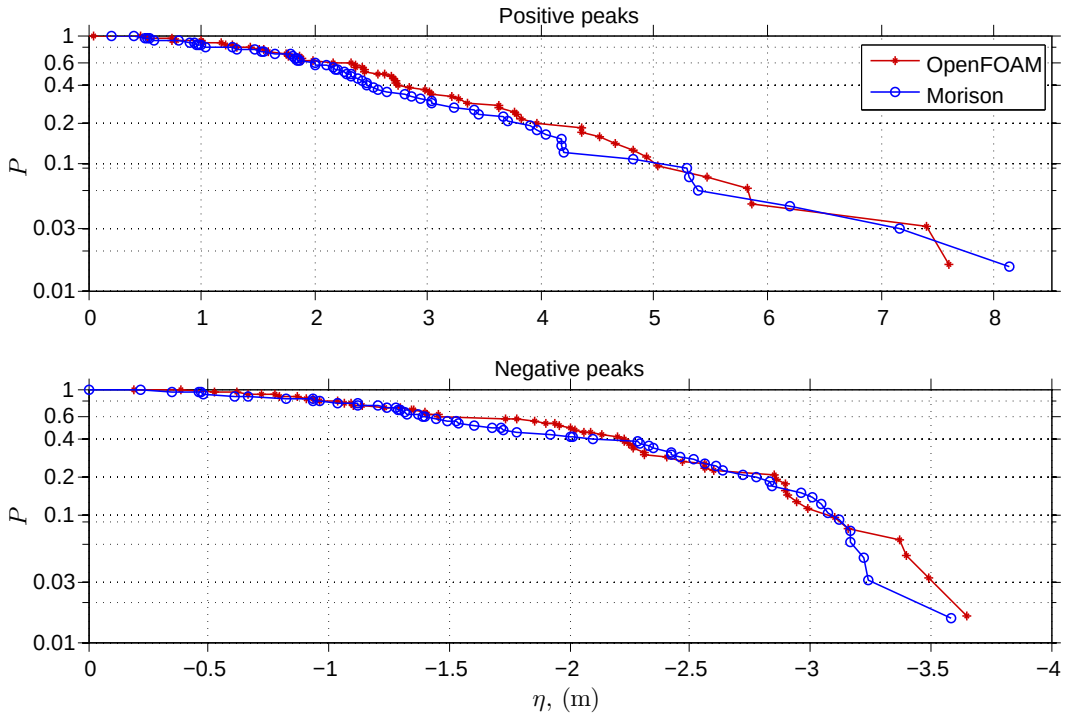

Figure 8.6: *The probability of exceedance of the positive and negative peaks in the surface elevation.*

The wave kinematics u and w_z from the OpenFOAM and OceanWave3D calculations are compared in figure 8.7 and 8.8 in the interval $t = 250 - 350\,\text{s}$. The velocities from OpenFOAM are not well described close to the surface elevation because of the interfering with the air. The comparison of the velocities is therefore done below the surface elevation for $z = -5$. Both the horizontal velocity and the term w_z from OpenFOAM and OceanWave3D compare reasonably, although there is some deviation between the signals, particular for the signal of w_z.

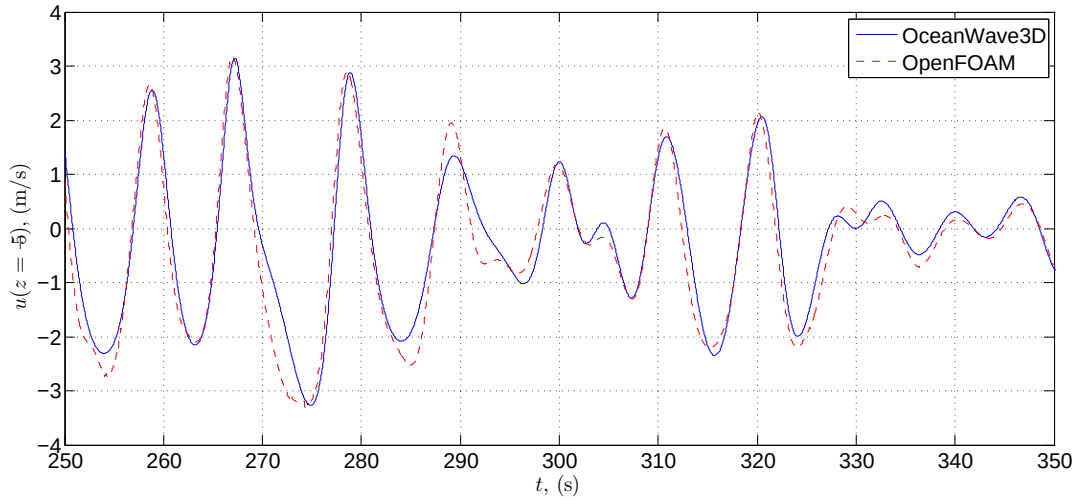

Figure 8.7: *The horizontal velocity below the surface elevation at $z = -5\,m$.*

The two models calculate the wave kinematics by two different methods. Further, it is shown above that the waves in OpenFOAM experience wave breaking. It can therefore not be expected that the wave kinematics from the two calculations are equal. The differences should be remembered when the forces are compared in the following.

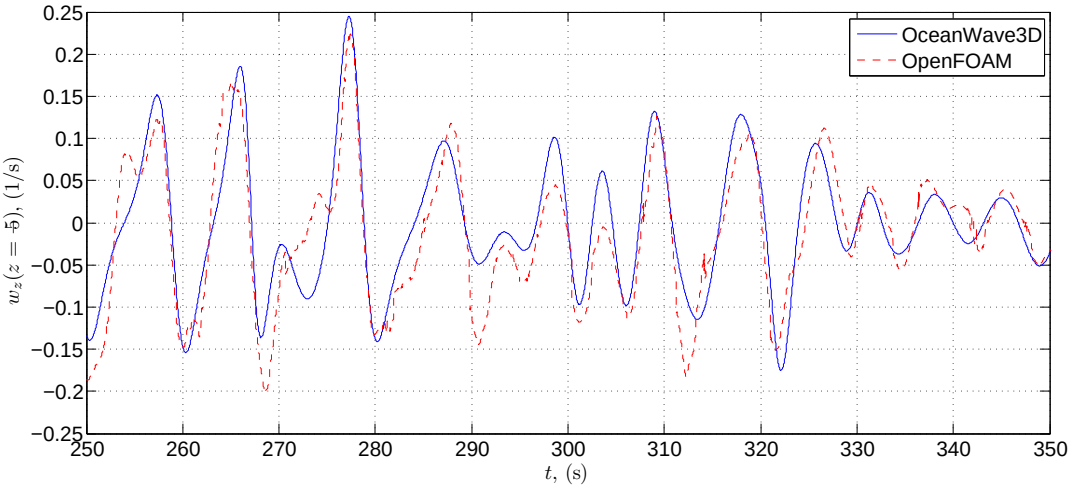

Figure 8.8: *The vertical velocity gradient below the surface elevation at $z = -5\,m$.*

8.4 Inline force and overturning moment

The Morison force depends on the two force coefficients $C_M = C_m + 1$ and C_D. The coefficients are functions of the Keulegan-Carpenter number, KC, and the Reynolds number, Re, which in case of irregular waves can be calculated from the standard deviation of the horizontal velocity $\hat{\sigma}_u$ and the mean wave period based on zero up-crossings, T_z. According to Sumer & Fredsøe (2006) the standard deviation should be calculated from the velocity at still water level. Since the calculations here are nonlinear, the velocity at still water is not know. Instead Re and KC is based on the particle velocity at the free surface. This results in a too large standard deviation, but is used as a first estimate to calculate the force coefficients. Based on the present calculations in model scale the coefficients are found to be

$$KC = \frac{\sqrt{2}\hat{\sigma}_u T_z}{D} = 3.35, \tag{8.7}$$

$$Re = \frac{\sqrt{2}\hat{\sigma}_u D}{\nu} = 5.99 \cdot 10^3. \tag{8.8}$$

In Sumer & Fredsøe (2006) the relation between KC and the force coefficients are given for irregular wave experiments with a Reynolds number equal to $Re = 7.78 \cdot 10^3$, which is close to the value here. The figure should therefore be representative for the present analysis and gives force coefficients equal to $C_M = 1.6$ and $C_D = 0.5$. In Froude scaling the KC-number is preserved, while the Re-number changes. When the force coefficients in full scale is based on the Reynold's number in equation (8.8) there can be scale effects. However, since the forces from OpenFOAM are calculated in model scale it is most consistent to calculate the Morison forces in model scale also. Further, the forces are inertia-dominated, and the forces can therefore be expected to be less scale-sensitive. To investigate the values of the force coefficients the wave forcing on a fixed monopile is considered. The probability of exceedance, equation (4.7), of the positive and negative peaks in the time series of the inline force and overturning moment based on the Morison forces and the forces from OpenFOAM are compared in figure 8.9-8.10.

For probabilities of exceedance larger than $P \sim 0.04$ the forces and moments from OpenFOAM result in the largest positive peaks. For the two smallest probability of exceedance the inline force and overturning moments based on the Morison forces are largest. This is explained with the wave breaking, which reduces the wave steepness of the largest waves in OpenFOAM. The forces are inertia dominated and depend therefore much on the acceleration of the waves and therefore on the steepness of waves.

For the negative peaks of the forces it is only for the smallest probability of exceedance that the force based on Morison's equation is largest, while for the negative moments Morison's equation

results in the largest negative moments for probabilities smaller than 0.15. This can be due to the moment arm which perhaps is largest in OceanWave3D when the largest moments are calculated. When the peaks of the surface elevations were compared in figure 8.6 it was seen that the negative largest peaks were smallest in the OceanWave3D which gives a larger moment arm.

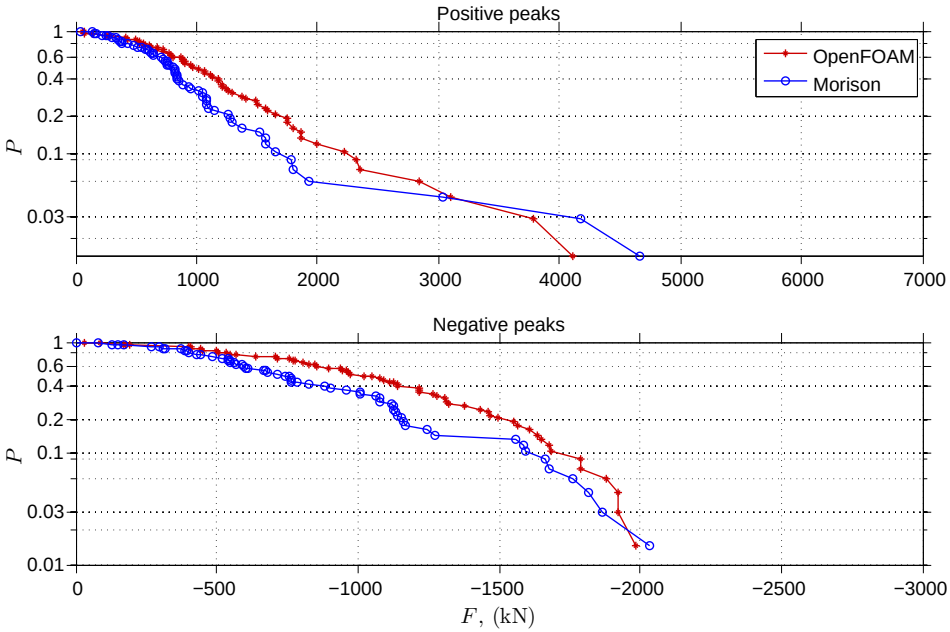

Figure 8.9: *The probability of exceedance of the inline force with $C_M = 1.6$ and $C_D = 0.5$. Top picture is for the positive peaks and bottom picture is for the negative peaks.*

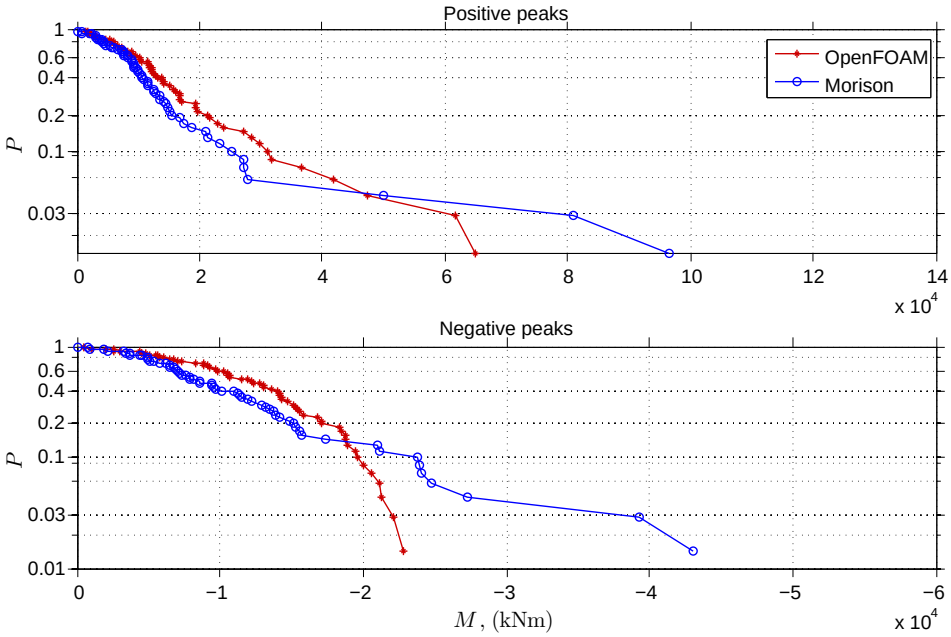

Figure 8.10: *The probability of exceedance of the overturning moment force with $C_M = 1.6$ and $C_D = 0.5$. Top picture is for the positive peaks and bottom picture is for the negative peaks.*

8.4.1 The force coefficients C_M and C_D

The figures of the probabilities of exceedance clearly show that with the chosen values of the coefficients, $C_M = 1.6$ and $C_D = 0.5$, the forces based on Morison's equation do not result in the same probability of exceedance as the forces from OpenFOAM. It is further seen that it is not possible to find values of the coefficients which gives the same peak values for each probability of exceedance. If the Morison force and moment are equal to the CFD-force and moment for the smallest probabilities of exceedance the Morison force and moment are too small for the larger probabilities of exceedance and vice versa.
The most optimal values of C_M and C_D are therefore found by considering C_M-values between [1.5;2.2] and C_D-values between [0;2.0]. The probability of exceedance is calculated for each combination of the two coefficients and the error of the Morison forces and moments for each combination calculated as

$$Error = \int_0^1 \frac{(X_{CFD} - X_{Morison})^2}{(\hat{\sigma}_{X_{CFD}})^2} dP, \tag{8.9}$$

where X_{CFD} and $X_{Morison}$ are the positive or negative peaks of the inline forces or overturning moments based on the forces from OpenFOAM and Morison forces, respectively, and $\hat{\sigma}_{X_{CFD}}$ is the standard deviation of the peaks considered from OpenFOAM.
Contour plots of the errors are shown in figure 8.11. It is seen that both the inline force and overturning moment is relative insensitive to changes in C_D. The contour-lines are rather parallel with the C_D-axis. The contour-plots are based on the peaks in the inline force and the overturning moments. Since the forces are inertia dominated the drag force is small at the peaks, which can explain the small dependence on C_D. For C_M the error is smallest in the interval $C_m \sin 1.5 - 2$ but with variation. For the positive peaks the error becomes smaller as C_M decreases and as C_D increases. While for the negative peaks the error becomes smaller as C_M decreases and as C_D decreases. If the contour plots of both the negative and positive peaks is considered the optimal values of coefficients are approximately $C_D = 1$ and $C_M = 1.65$. The C_M value based on the Reynolds number and Keulegan-Carpenter number are therefore very close to be optimal. Considering the drag coefficient the error can be reduced a little by changing it from $C_D = 0.5$ to $C_D = 1.0$ particular for the negative peaks in the overturning moments.

Figure 8.12-8.13 show the probability of exceedance of the peaks of the inline forces and overturning moments with $C_D = 1.0$ and $C_M = 1.65$ and compared them to the probability of exceedance of the peaks of the inline forces and overturning moments based on the forces from OpenFOAM. It is seen that the difference between the smaller forces with high probability of exceedance is smaller with the new force coefficients. However, the difference in the largest positive peaks of both the forces and moments are larger with these force coefficients. It is further seen that the largest peaks of the negative forces and moments becomes smaller with the new force coefficients. In the choice of force coefficients it is decided to choose the force coefficients that represent all the peaks the best. Instead focus could have been on the peaks with probability of exceedance larger than for example 0.1. In such a situation the force coefficients should be larger, while for the peaks with probability of exceedance smaller than approximately 0.1 the force coefficients should have been smaller.

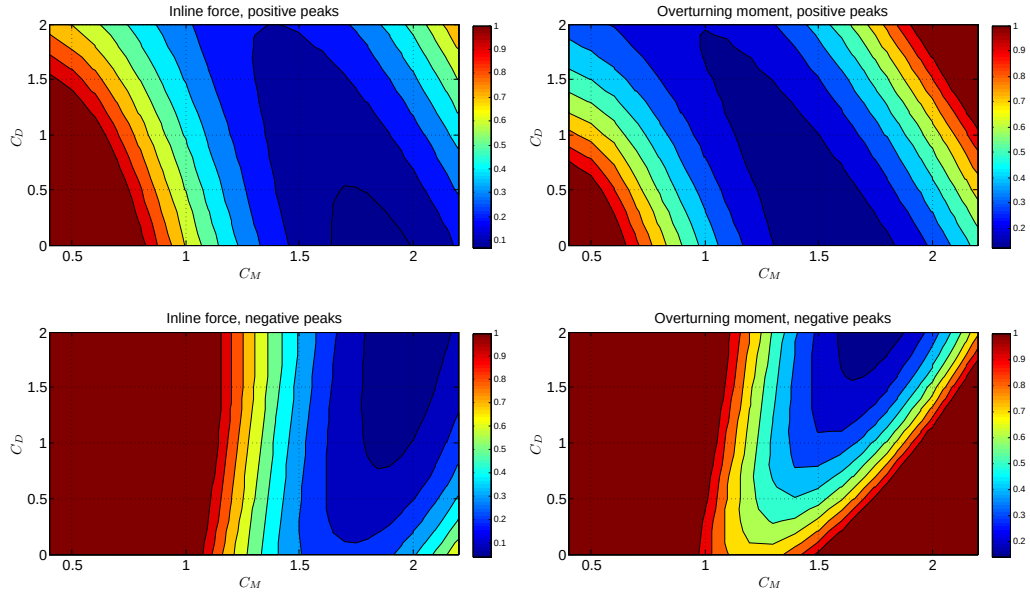

(a) Inline force **(b)** Overturning moment

Figure 8.11: *Error of inline force and overturning moment as function of C_M and C_D.*

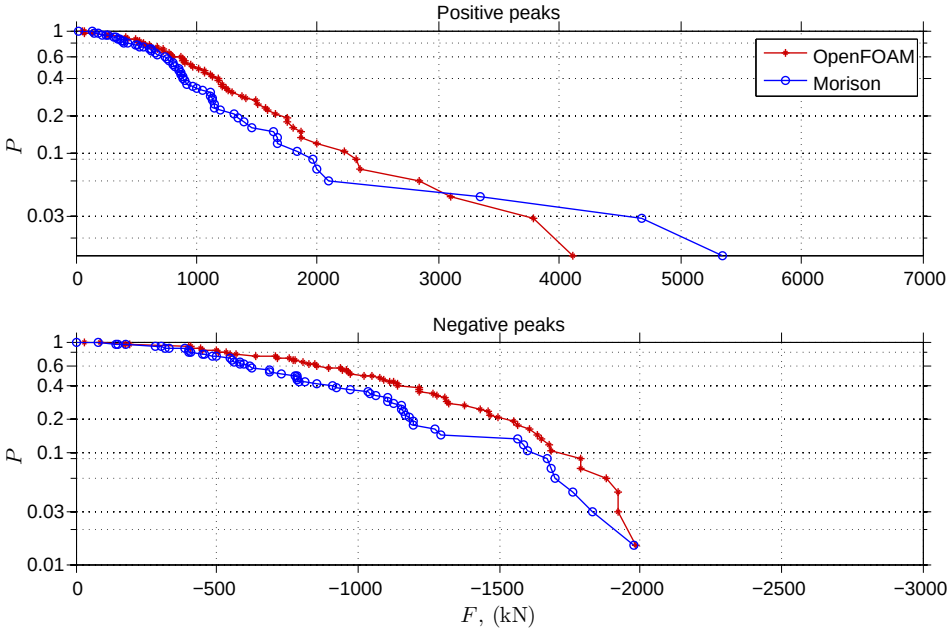

Figure 8.12: *The probability of exceedance of the inline force with $C_M = 1.65$ and $C_D = 1.0$. Top picture is for the positive peaks and bottom picture is for the negative peaks.*

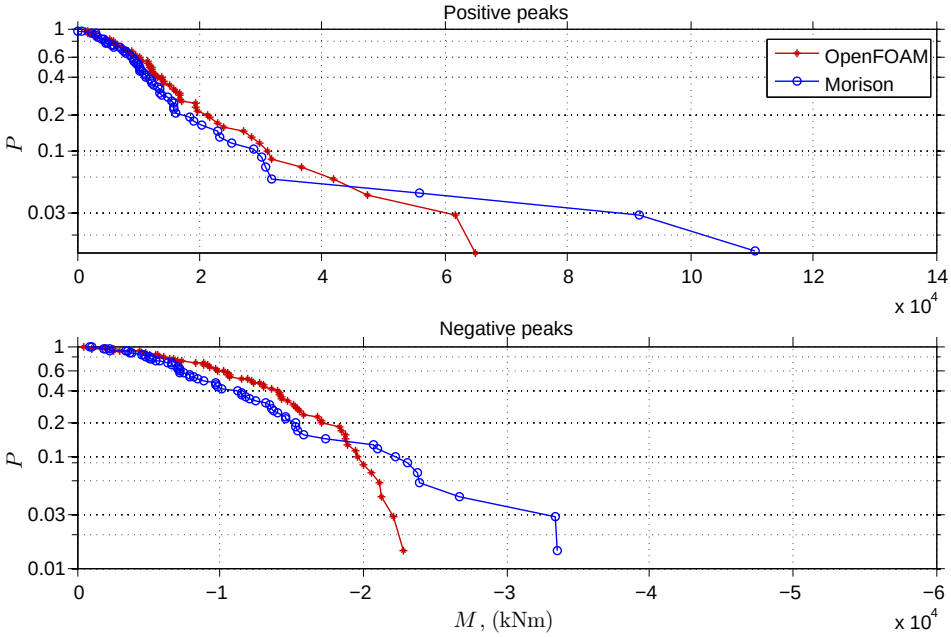

Figure 8.13: *The probability of exceedance of the overturning moment force with* $C_M = 1.65$ *and* $C_D = 1.0$. *Top picture is for the positive peaks and bottom picture is for the negative peaks.*

8.5 Dynamic analysis

In the previous section focus was to find the optimal values of C_M and C_D in Morison's equation. In the present section the dynamic response due to the Morison forces and the forces from OpenFOAM is compared. Further, the importance of the "Rainey-terms" in Morison's equation is investigated. The force coefficients are the optimal values of $C_M = 1.65$ and $C_D = 1$.

The sea state considered in the present analysis is relatively strong and if the relation between the significant wave height and wind velocity considered in figure 4.2 in chapter 4 are used here it is seen that the wind speed that matches the present sea state is above 30 m/s and therefore above the cut-out wind speed. In the dynamic analysis here the wind turbine is therefore parked and the blades pitched 87 degrees. To simplify the effects from the wind, the turbulence is disregarded and a constant wind speed of 30 m/s is used. The 8 % of logarithmic decrement damping explained in section 4.4.1 to represent soil damping, hydrodynamic damping, structural damping in the tower and monopile and tower dampers, is also applied in the present analysis.

The probability of exceedance of the peaks in the time series of the forces and moments in the bottom of the tower and monopile are again calculated. In the design focus is most often based on the positive peaks. To keep the analysis more simple only the positive peaks are considered in the following.

Due to the wind forcing the forces and moments are shifted to larger values above zero. In the following analysis the positive peaks are therefore defined as peaks larger than the mean of the signals.

Four descriptions of Morison's equation are used to calculate the wave forcing. The first force (Morison_1) both Rainey-terms are included. This version of the force is the force which is used in all other analyses in the present thesis. In the second force (Morison_2) only the axial divergence terms is included. In the third (Morison_3) only the point force is included and in the fourth force (Morison_4) both the axial divergence terms and the point force are disregarded. In figure 8.14 the sectional forces and moments in the bottom of the tower due to the four descriptions of Morison's equation are compared and in figure 8.15 the sectional forces and moments in the bottom of the monopile are compared. The largest difference in the probability of exceedance are seen for the largest peaks. In the tower the four types of Morison's equation starts to deviate for $P \sim 0.2$ and in the monopile for $P \sim 0.05$. It is the point force that contributes most to the differences which

can be explained by the fact that it has η_x as a direct factor, and that η has the largest changes in space for the largest waves with a large steepness. The vertical acceleration also increases as the steepness of the waves increases, which explains that the contribution from the axial divergence term also increases as the peaks of the forces increases.
The reason that the difference between the four types of Morison's equation starts to deviate for smaller probabilities in the tower must be due to the excitations of the structural first eigenfrequency. The larger and more steep the waves are, the larger is the dynamic excitation and the wave forcing leading to the dynamic response is further amplified when particular the point force is included.
In figure 8.14-8.15 the sectional forces and moments based on Morison's equation are also compared against the sectional forces and moments due to the forces from OpenFOAM. In Flex5 when the forces from OpenFOAM are considered, the calculations are made with and without the correction of the axial divergence term. However, the sectional forces do not change whether the correction is included or neglected. In the figures only the calculation with the axial divergence terms is therefore shown.

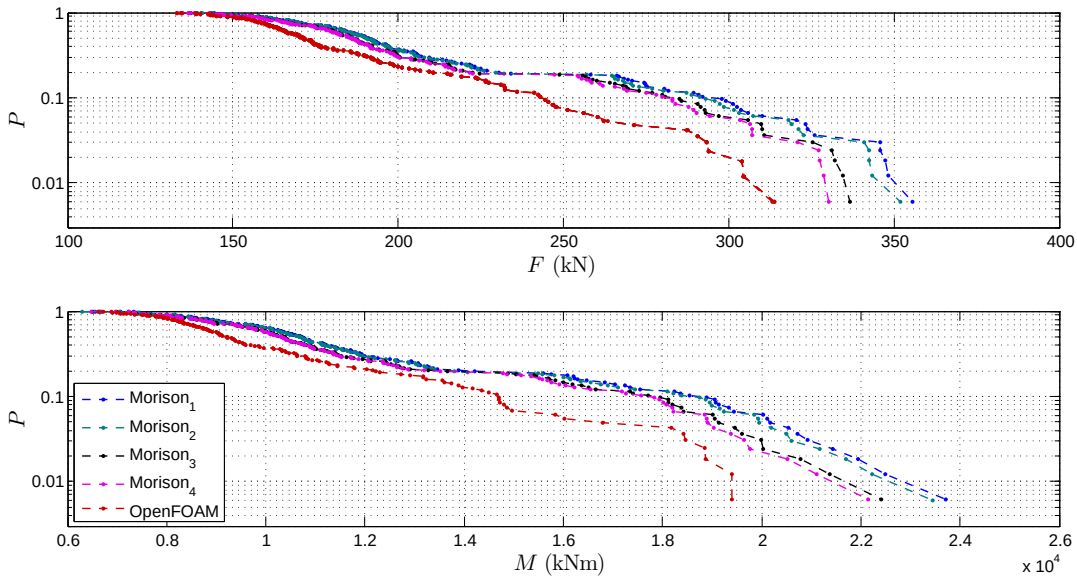

Figure 8.14: *Probability of exceedance of the inline force and overturning moment in the bottom of the tower.*

In the monopile, 8.15, the difference between the sectional forces and moments due to forces from OpenFOAM and Morison's equation are similar to the differences which was seen for the static analysis in figure 8.12 and 8.13. For the positive peaks of the forces, OpenFOAM results in the largest values except for probabilities smaller than 0.05. For the moments the probability of exceedance are similar for $P < 0.02$. OpenFOAM results in the largest peaks for $0.05 < P < 0.2$, while for probabilities of exceedance smaller than this, the Morison forces results in the largest moments.
In the tower the peaks of both the sectional forces and moments based on the forces from OpenFOAM are smallest for all probabilities of exceedance. The large deviation in the tower between the two types of forces are believed to be due to the steepness of the waves which is largest for the waves from OceanWave3D. A time interval of the inline force in the bottom of the tower and monopile based on the Morison forces and the forces from OpenFOAM are compared in figure 8.16. It is the fourth version of the Morison's equation without the Rayney terms which is considered. It is seen that the structural excitation in the tower is largest for the Morison force. If the sectional forces in the monopile are compared it is also seen that the inline forces from OceanWave3D has steeper crests than the forces from OpenFOAM. These steep forces result in more impulsive responses in the tower. In the sectional force in the tower a high frequency oscillation is seen at $t \sim 240$ and $t \sim 267$ for both signals. The frequency of the oscillations is equal to the structural

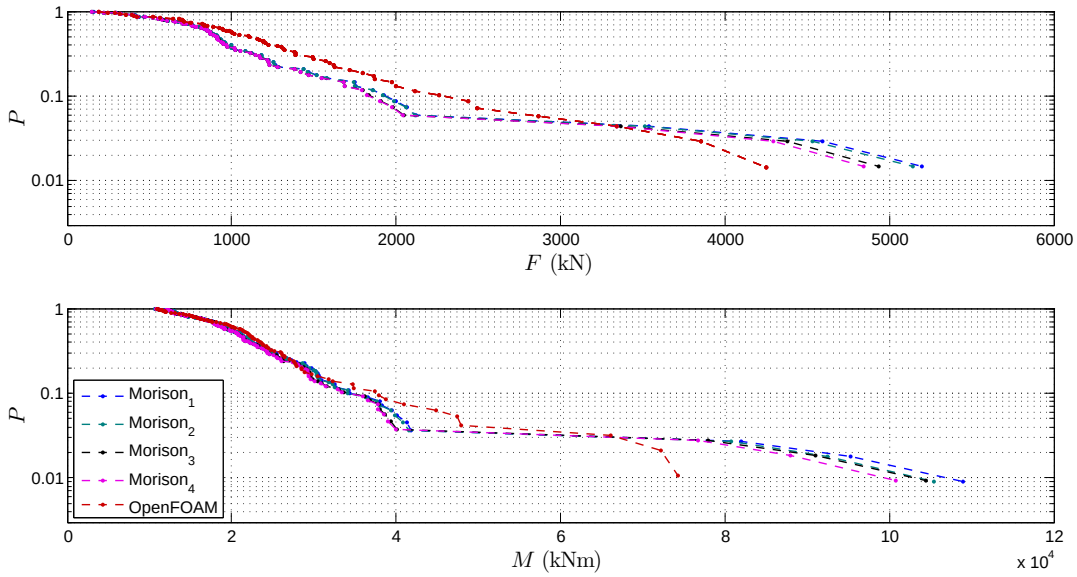

Figure 8.15: *Probability of exceedance of the inline force and overturning moment in the bottom of the monopile.*

13th global frequency of 2.27 Hz. The excitation looks a little stronger when the sectional force due to forces from OpenFOAM are considered.

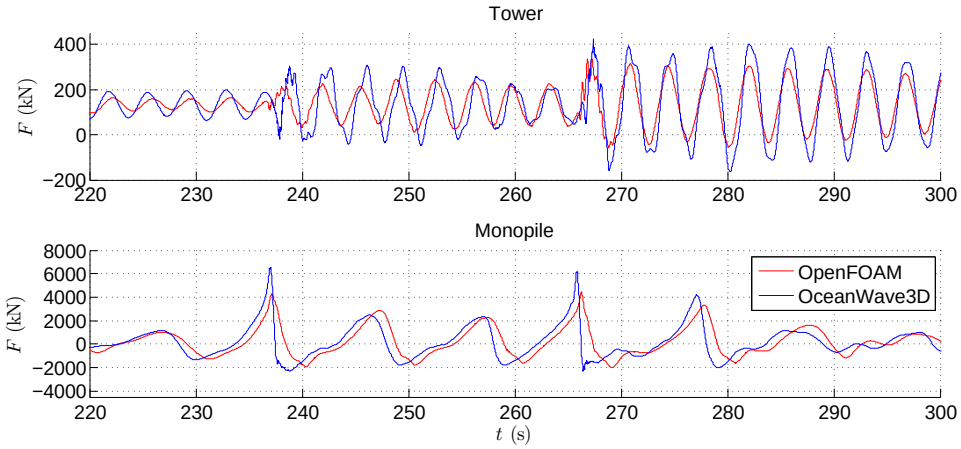

Figure 8.16: *The inline force in the bottom of the tower and monopile.*

8.6 Summary

In the present chapter the forces and moments in the tower and monopile based on OceanWave3D and Morison's equation have been compared against forces and moments based on CFD-calculations. The CFD-solver has a more detailed description of the waves and is therefore assumed to be more correct. Since the peak frequency of the sea state is 0.1 Hz, it is not believed to be significant for the results that the waves with frequencies larger than 0.32 Hz are not fully converged. Even though the waves in OpenFOAM experience wave breaking the wave breaking filter was not activated in OceanWave3D. The lack of wave breaking for the largest waves of OceanWave3D leads to a larger steepness for these waves relative to the results from OpenFOAM.
The static analyses showed that Morison's equation can describe the hydrodynamic fores well. However, it is difficult to find force coefficients to represent both the smaller and largest waves in a

wave realization. With the same force coefficient the difference between the peaks of the Morison's equation and the forces from OpenFOAM are almost the same for the negative and positive peaks. However, for the largest peaks there is some deviation. The difference between the largest negative moments based on Morisons's equation and from OpenFOAM is much larger than the difference of the largest positive peaks. This is can be due to the moment arm which for the negative peaks is largest in the waves from OceanWave3D. In the forces the largest positive peaks are also much larger than the largest peaks based on forces from OpenFOAM than what is seen for the negative peaks. This is due to the larger steepness of the waves in OceanWave3D.
In the static analysis it was further seen that the peaks of the inline force and overturning moment are less sensitive to the drag coefficient because the forces are inertia dominated at the peaks.
In the dynamic analysis the Rainey terms in Morison's equation were found to change the forces, particular for the large steep waves the point force influences the value of the forces.
Finally, it was found, that even though the Morison forces result in the smallest peaks of the sectional forces and moments in the monopile the opposite is seen in the tower. In the tower the peaks of the forces and moments due to the Morison forces are largest and was explained with the larger steepness of the waves in OceanWave3D. This result indicates that even if the peaks of the hydrodynamic forces based on Morison's equation are correct the dynamic analysis can still result in different sectional forces due to dynamic excitation of the structure.

Chapter 9

3D load effects

So far in the thesis only unidirectional waves have been considered. Ocean waves, however, are generally multi-directional. When directional wave realizations are considered the waves affect the structure in more directions at the same time. According to Quarton *et al.* (2005), this can in some cases have an important influence on the loads acting on the structure. How important it is to include the directionality of the waves depends on the site considered and also on the structure. Many investigations emphasise that the wave forcing is reduced when the spreading of the waves is taken into account. Schaumann & Böker (2007) analysed measurements on the FINO1-Research Platform and found also that the wave spreading in short-term sea states can reduce the resulting fatigue loads of a monopile significantly. Sharma & Dean (1981) calculated both uni- and multi-directional irregular wave realizations of second order. The total force on a single pile was reduced by a factor of 0.61 as the directional spreading of the energy in the waves increased.

Following the standard DNV-OS-J101 (2010), the directionality of the waves shall be considered if the directionality has an impact on the design of the wind turbine structure.

It is therefore interesting to investigate how the wave directionality for fully nonlinear waves reduces the forces. Further, the dynamic response to directional waves is also interesting to look into, as the real structural stresses are associated with the response and not the external forces alone. In the present chapter the wave statistics of a unidirectional wave realization and a multi-directional wave realization is first compared. The CPU time for 3D-calculations in OceanWave3D is time demanding. To get a longer time series, the analysis of the wave statistics is therefore based on experiments from the Wave Load Project, also mentioned in chapter 8.

A part of the multi-directional wave realization from the experiments is afterwards reproduced numerically in OceanWave3D. This calculation is kindly provided by Bo Terp Paulsen, who presents the calculations in Paulsen *et al.* (2013*b*). The wave realizations are compared against a unidirectional wave realization, which is generated by a JONSWAP-spectrum at the generation zone which is adjusted iteratively until the significant wave height at the location of the cylinder is the same in two calculations. The effects of multi-directional wave realizations on the structural dynamics can thereby be analysed and compared to unidirectional wave realizations.

Before the analyses a short description is given on how multi-directional irregular wave realizations can be calculated.

9.1 Directional irregular waves

The wave spectrum in a three-dimensional wave field is not only a function of the frequency but also of the directionality. In the following it is explained how a three dimensional spectrum can be calculated. The spectrum can be described as the product of the frequency spectrum and a directional spectrum

$$S(\hat{f},\hat{\varphi}) = S(\hat{f})D_s(\hat{f},\hat{\varphi}) \quad \text{where} \tag{9.1}$$

$$S(\hat{f}) = \int_{-\pi}^{\pi} S(\hat{f},\hat{\varphi})d\hat{\varphi}, \tag{9.2}$$

$$\int_{-\pi}^{\pi} D_s(\hat{f},\hat{\varphi})d\hat{\varphi} = 1. \tag{9.3}$$

Different forms of the directional spreading functions exist, here the cosine-power function is here given as example

$$D_s(\hat{f},\hat{\varphi}) = \cos\left(\frac{\hat{\varphi}-\hat{\varphi}_m}{2}\right)^{2\beta}, \tag{9.4}$$

where $\hat{\varphi}_m$ is the mean direction of the wave components. The spreading parameter β is often chosen to be a function of the frequency. In figure 9.1a three examples of the spreading parameter of Sand & Mynett (1987), Klinting & Sand (1987) and Mitsuyasu *et al.* (1975) are given. In figure 9.1b the directional spreading function with β defined from Mitsuyasu *et al.* (1975) is shown. It is seen that the spreading function is most narrow for $\hat{f} = \hat{f}_p$. Hereby the waves around the frequency are most directionally focused, while frequencies away from $\hat{f}_p$ will have a stronger spreading.
The discrete representation of a directional spectrum can both be prescribed by a single or a double summation. With the double summation there can be problems with the phase locking, because different directional components has the same frequency. This can lead to the socalled 'checker board effect' where the effective wave height varies systematically in space. With the single summation it is ensured that each frequency component has one and only one random direction. This is used in the example here. In complex form, the surface elevation is written as

$$\begin{aligned}\eta(x,y,t) &= \sum_{n=1}^{N} \hat{A}_n e^{i(\omega_n t - k_{nx}x - k_{ny}y)} = \sum_{n=1}^{N} \hat{A}_n e^{i(-k_{nx}x - k_{ny}y)} e^{i\omega_n t} = \sum_{n=1}^{N} \hat{C}_n e^{i\omega_n t} \\ &= \sum_{n=1}^{N} \hat{A}_n(\cos(\omega_n t - k_{nx}x - k_{ny}y) + i\sin(\omega_n t - k_{nx}x - k_{ny}y)),\end{aligned} \tag{9.5}$$

where

$$\hat{A}_n = \hat{a}_n + i\hat{b}_n, \quad \text{and} \quad \theta_n = \omega_n t - k_{nx}x - k_{ny}. \tag{9.6}$$

The values k_{nx} and k_{ny} are found from the wave number k_n and the dispersion relation

$$\omega_n^2 = gk_n \tanh(k_n h), \tag{9.7}$$

$$k_{nx} = k_n \cos\varphi_n, \tag{9.8}$$

$$k_{ny} = k_n \sin\varphi_n. \tag{9.9}$$

Combining equation (9.5) and (9.6) gives

$$\begin{aligned}\eta(x,y,t) &= \sum_{n=1}^{N} (\hat{a}_n + i\hat{b}_n)(\cos\theta_n + i\sin\theta_n) \\ &= \sum_{n=1}^{N} \hat{a}_n\cos\theta_n + \hat{a}_n i\sin\theta_n + i\hat{b}_n\cos\theta_n + \hat{b}_n i^2\sin\theta_n \\ &= \sum_{n=1}^{N} (\hat{a}_n\cos\theta_n - \hat{b}_n\sin\theta_n) + i(\hat{b}_n\cos\theta_n + \hat{a}_n\sin\theta_n).\end{aligned} \tag{9.10}$$

The coefficients $\hat{a}_n$ and $\hat{b}_n$ are given as

$$\hat{a}_n = \sqrt{2S(\hat{f}_n)\Delta\hat{f}}\cos(2\pi\epsilon_n), \quad \hat{b}_n = \sqrt{2S(\hat{f}_n)\Delta\hat{f}}\sin(2\pi\epsilon_n). \tag{9.11}$$

The variable ϵ_n is a random number between zero and unity and gives the phase-angle of each wave-component in time.
The directional accumulated distribution is used to determine the direction of each frequency component,

$$P_s(\hat{\varphi}, \hat{f}) = \int_{-\pi/2}^{\pi/2} D_s(\hat{\varphi}, \hat{f}) d\hat{\varphi}. \tag{9.12}$$

Examples of P_s are shown in figure 9.1c for three different $\hat{f}$-values. The equation

$$P_s(\hat{\varphi}_n, \hat{f}_n) = \psi_n, \quad n = 1, 2, ...N, \tag{9.13}$$

is solved to determine one random direction, $\hat{\varphi}_n$, for each of the frequencies, where ψ_n is a random number between zero and unity. Examples of the method to determine a direction of each frequency are shown in figure 9.1c.

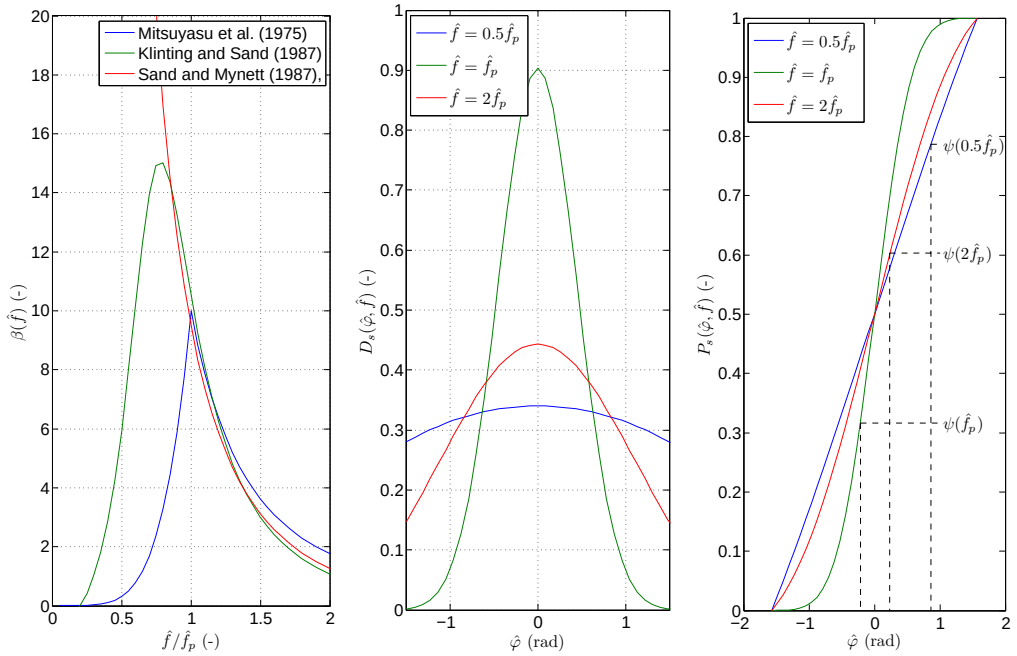

(a) Different distributions of the spreading parameter, β.

(b) The cosine-power directional spreading function when β of Mitsuyasu *et al.* (1975) is used.

(c) Method to determine a direction for each frequency in the spectrum.

Figure 9.1: *Different functions to be used in the directional spectrum.*

An example of a directional JONSWAP-spectrum is shown in figure 9.2. The spectrum is based on the cosine power directional spreading function where the spreading parameter of Mitsuyasu *et al.* (1975) is used, as shown in figure 9.1a and 9.1b. The significant wave height, $H_s = 8.3\,\text{m}$, and peak period, $T_p = 12.6\,\text{s}$, of the spectrum are equal to the wave realizations considered in the following.

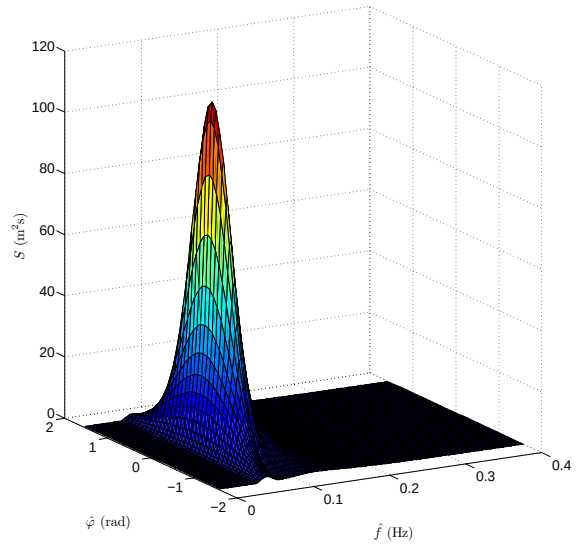

Figure 9.2: *A multi-directional JONSWAP-spectrum using the consine power derictional spreading function together with the spreading parameter of Mitsuyasu* et al. *(1975).*

9.2 Analysis of data from model tests

In this section the model tests are first described and afterwards the unidirectional and multi-directional wave realization from the model tests are compared.
The model tests were carried out at DHI in a basin area measuring 18 x19 and 1 m in depth. A sketch of the model setup from Nielsen *et al.* (2012) is shown in figure 9.3. The model tests considered in the present study were for a fixed cylinder placed on the sloping part of the sea bed in a water depth of 0.55 m. The slope was 1:25 and the waves were generated in a water depth of 0.82 m. At the bottom of the cylinder a force transducer was placed to measure the total wave force acting on the cylinder in both horizontal directions and also the vertical direction.

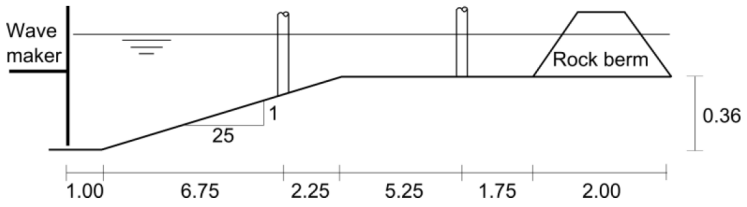

Figure 9.3: *A sketch of the model set-up. The figure is from Nielsen* et al. *(2012).*

The sea states of the unidirectional and multi-directional wave realizations in the model tests are relative extreme with a significant wave height of 0.22 m and a peak wave period of 2.08 s, which gives a non-dimensional wave number $kh = 0.78$ at the cylinder. The wave is therefore in intermediate water depth. The sea states are defined by a JONSWAP-spectrum. The spreading factor of the multi-directional sea state which defines how much of the wave energy that travels in the main wave direction is 0.875 following the definition of Forristall & Ewans (1997). For a unidirectional sea state the spreading factor is 1 and for a omni-directional sea state the spreading factor is 0.71. The model tests are Froude-scaled to full scale with the factor 1:36.6. In table 9.1 the diameter of the cylinder, the water depths and the wave properties are stated in model scale and full scale. In the following if nothing else is stated all data are in full scale.
The time series of the multi-directional wave realization is three hours long. In figure 9.4 the time series of the surface elevation at a wave gauge at same depth as the cylinder but 15 cm to the left of the cylinder is shown. From the signal it is seen that it takes around 2000 s before the wave realization is fully developed. The analysis of the wave realization begins therefore after the

	D (m)	h_{cyl} (m)	h_d (m)	H_s (m)	T_p (s)
Model scale	0.164	0.55	0.82	0.22	2.08
Full scale	6.00	21.10	30.01	8.3	12.6

Table 9.1: *Model data in model and full scale.*

first 2000 s and is based on a time series of 8800 s. The time series of the unidirectional wave realization is 24 hours long. The part of the time series which is compared to the multi-directional wave realization is chosen such that the difference between the two significant wave heights is as little as possible but such that the length of the time series are the same. The part of the unidirectional wave realization considered is from 5600-14400 s and shown in figure 9.4. From the graphical view, it is difficult to see whether the surface elevations of the two wave realizations stand out from each other. The largest crest values are in both time series around 10 m and the smallest trough values just below -5 m. The significant wave height, H_s, and wave skewness, Sk, of the two wave realizations are stated in table 9.2. The significant wave height for both wave realizations are 3 % smaller than the desired significant wave height. The wave-signals are calibrated in the laboratory, but the wave signals are random which makes it difficult to obtain the exact same statistical data. The unidirectional wave realization results in the largest H_s and Sk. For H_s the difference is not larger than 0.16 % while the skewness is 12 % larger. This is accordance with Toffoli *et al.* (2006) who compared a second order surface elevation in unidirectional and multi-directional seas. They found that the skewness reduces for multi-directional waves except for wave realizations in shallow water, which is not the case here, where the skewness was found to increase. The larger skewness of the unidirectional wave realization indicates that the crest of this wave realization is shorter and more peaked while the trough is wider and flatter compared to the multi-directional wave realization. The skewness is often used as an indicator on how nonlinear a wave is. The unidirectional waves are therefore most nonlinear. This may be explained by the unidirectional waves have longer time to develop the wave nonlinearity. If two wave components in the unidirectional wave realization add up and focus, they can only be separated again due to differences in the phase velocity. In the multi-directional wave realization they can add up shortly but also separate again because they have different direction.

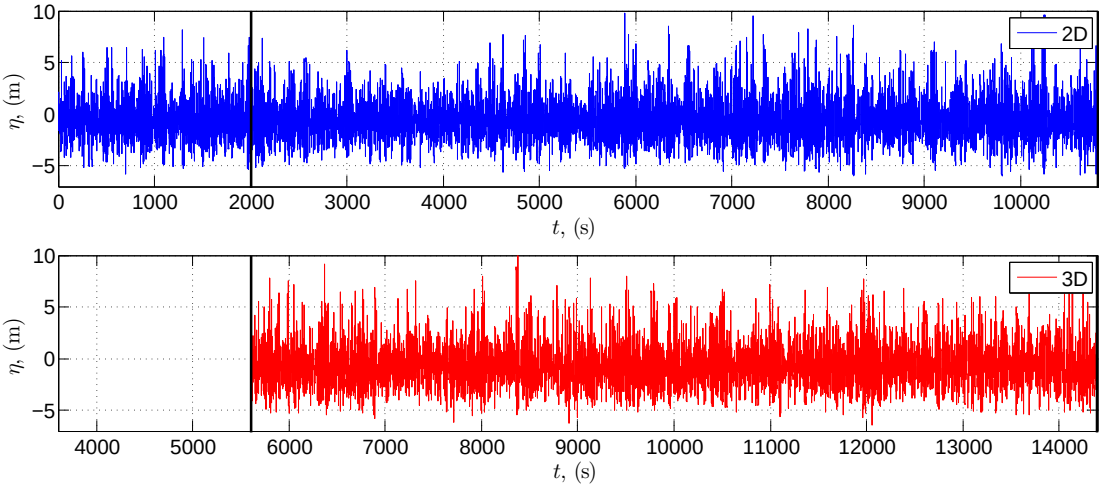

Figure 9.4: *The time series of the unidirectional and multi-directional wave realizations. The black lines indicate the part of the time series which are compared.*

In figure 9.5a the probability density function (PDF) of the wave height are compared. The bin size is 2 m. The wave heights are calculated as the difference in the maximum and minimum value of the surface elevation between two zero-down-crossings. The PDFs are also fitted to the Rayleigh probability distribution (red and blue curve in the figure). There is good agreement between the PDFs and the Rayleigh probability distributions. The distributions of the wave heights in unidirectional and multi-directional wave field are similar. However, the multi-directional wave

	Uni	Multi	Uni/Multi
H_s (m)	8.04	8.02	0.998
Sk (-)	0.64	0.58	0.89

Table 9.2: *The significant wave height and skewness of the unidirectional and multi-directional wave realization.*

realization contains more waves with wave height $H < 5\,\text{m}$, while the opposite is seen for the larger wave height, $6\,\text{m} < H > 10\,\text{m}$. The multi-directional wave realization has also more waves with wave heights larger than 10 m.
In figure 9.5b the amplitude spectrum of the two wave realizations are compared. To calculate the wave spectrum the time series of the surface elevation has been divided in 11 intervals of 800 s. The raw spectrum for each 800 s episode was first smoothed by computing the running mean value along a 7 point moving stencil. The spectrum in the figure is then the average of the 11 smoothed spectra. This was done to get more a smooth spectrum. Otherwise the scattering would be very large, and it would be difficult to compare the two wave spectra. There is good agreement between the two wave spectra. In both spectra it is possible to identify the second-order higher harmonics at $\hat{f} \sim 0.16\,\text{Hz}$. It is also seen that the unidirectional surface elevation has more energy at some low-frequencies waves.
This can again be explained by the nonlinearity of the unidirectional wave realization, where the long waves have longer time to develop while in the multi-directional wave realization the long waves occur in shorter time.

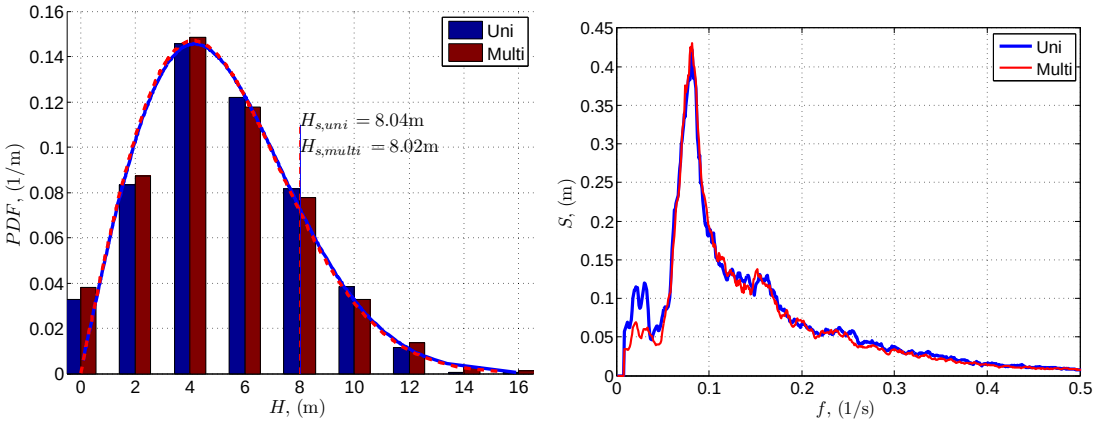

(a) The probability density function of the wave heights. The PDFs are also fitted to the Rayleigh probability distribution (red and blue curve).

(b) Amplitude wave spectrum.

Figure 9.5: *Statistical properties of the wave height and surface elevation of the two-dimensional and multu-dimensional wave realizations*

In figure 9.6 the probability of exceedance of the largest peaks between each zero-down-crossing of the free surface elevations are compared. The probability of exceedance of the surface elevation is fitted with the Rayleigh distribution and the extreme data (data which has a probability of exceedance smaller than 0.02) are fitted with a Gumbel distribution. The same was done in chapter 4. The Rayleigh distribution does not represents the peaks of the surface elevation well for any intervals of the probabilities of exceedance while the extreme data are represented well by the Gumbel distribution. For probabilities of exceedance larger than 0.04 the peaks are largest for the unidirectional waves. This result deviates a little from the probability density functions of the wave heights in figure 9.5a, where there was more agreement between the probability functions of the two wave realizations. The larger peaks of the unidirectional waves must be due to the skewness which is largest for the unidirectional surface elevation.

For probabilities of exceedance smaller than 0.01 it is the multi-directional surface elevation that has the largest peaks. This is in accordance with the wave heights, which also are largest for the multi-directional waves. While the larger skewness and larger content of subharmonic second-order energy indicate a generally larger level of nonlinearity for the unidirectional waves, the single waves associated with the extreme multi-directional surface elevations may well be more nonlinear than for the unidirectional wave field. The occurrence of the large surface elevations in multi-directional wave field appear to be due to directional focusing. Weather nonlinearity plays a role for the probability of this occurrence is an open question.

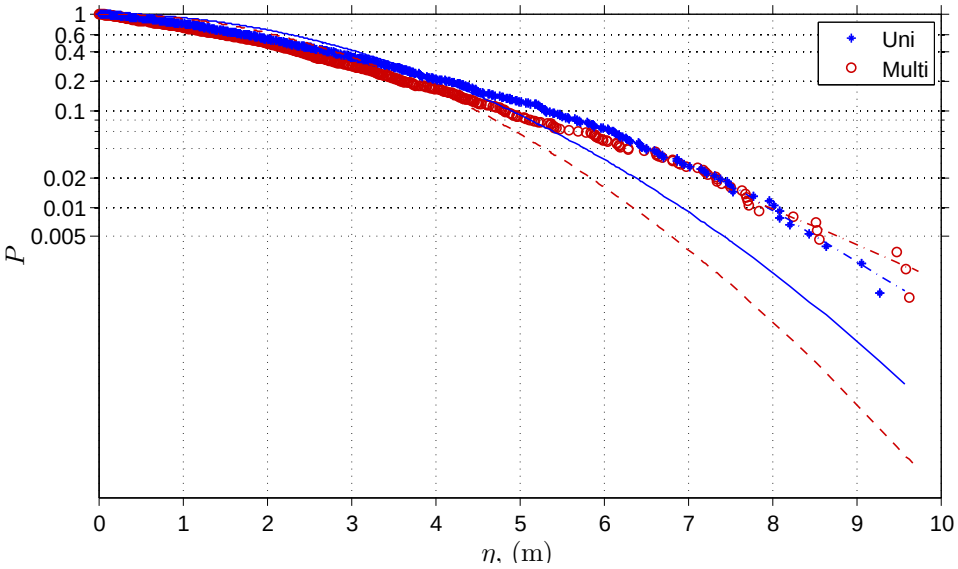

Figure 9.6: *The probability of exceedance of the positive peaks of the surface elevation. The full and dashed line indicate the Rayleigh-distribution and the dashed-dotted lines the Gumbel-distribution.*

In figure 9.7 the probability of exceedance of the largest peaks between each zero-down-crossing of the inline force in the direction of the unidirectional waves are compared.
The force transducer, which measure the hydrodynamic forces, are excited when a large wave hits the structure. This response is omitted in the analysis, by only consider zero-down-crossing-periods larger than 3 s. The forces due to the waves in the main part of the wave spectrum are in this way still included in the analysis.
The probability of exceedance is fitted with the Weibull distribution and the extreme data are again fitted with the Gumbel distribution. The Weibull-distribution represents the data well for probabilities of exceedance larger than 0.2, while the extremes again are described well by the Gumbel distribution, except for the largest peak of the multi-directional wave realization, which stands out and is much larger than all other peaks. No particular significance is attached to this peak. It is therefore not concluded that the multi-directional waves result in the largest forces from this single point, and it is ignored in the following.
The probability of exceedance is similar for values larger than 0.6, while for probability of exceedance smaller than 0.6 the unidirectional wave realization results in the largest forces, which is in accordance with expectations. For the smallest probability of exceedance the difference in the forces is up to 20 %. The larger forces can be due to the skewness which is largest for unidirectional wave realization. Since the forces are inertia-dominated they depends most on the acceleration of the waves, and the acceleration is larger the more steep the waves in the wave realization are. It is, however, surprising that the difference between the forces do not exists for all the forces as the spreading of 0.875 exists for both the small and large waves in the multi-directional waves. Since the waves are inertia dominated the spreading of 0.875 should also be seen for both large and small forces. It is not believed that it is due to the response of the force transducer, since this excitation is omitted by only consider force periods larger than 3 s.
The three largest peaks of the unidirectional forces lie below the Gumbel distribution. This can perhaps be due to wave breaking, the forces can simply not be larger than this, because the waves

than will break.

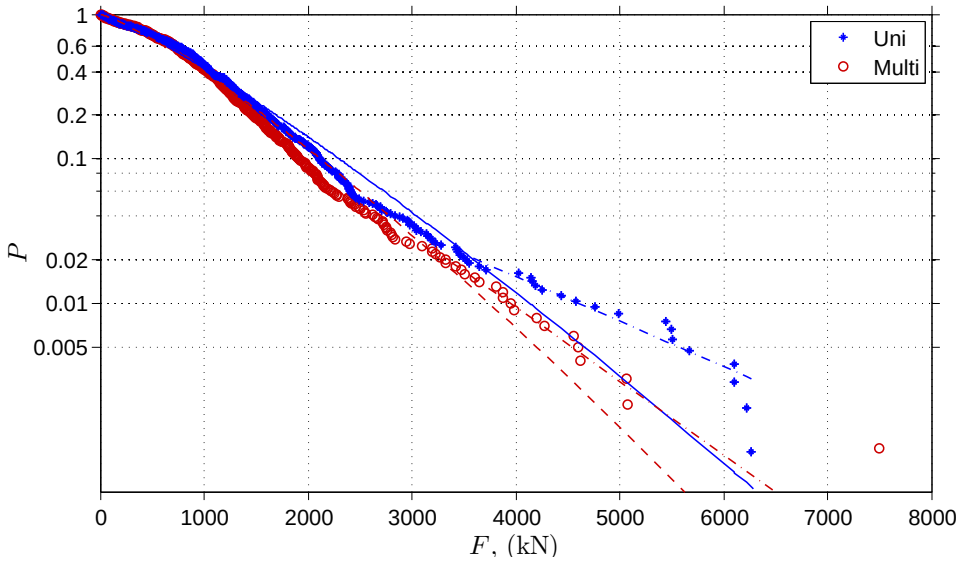

Figure 9.7: *The probability of exceedance of the positive peaks of the inline force. The full and dashed line indicate the Weibull-distribution and the dashed-dotted lines the Gumbel-distribution.*

9.3 Numerical Calculations

In this section the effects of the wave directionality are analysed in dynamic calculations. The numerical analysis is based on short times series of only 360 s, due to limited time to make the calculations. The analyses therefore only give an indication of the consequence of considering a multi-directional wave realization in the aeroelastic calculations. In the analysis Flex5 is modified so that the wave kinematics are included in both the fore-aft and side-to-side direction.

In the numerical analysis it is only the multi-directional experimental wave realization which is reproduced in OceanWave3D. If both the unidirectional and multi-directional wave realization were reproduced it would be difficult to ensure the same statistical properties of the wave realizations due to the short length of the time series. Instead the unidirectional wave realization is generated by a JONSWAP-spectrum at the generation zone which is adjusted iteratively until the significant wave height at the location of the cylinder is the same in two calculations.

To reproduce the multi-directional model test (which is provided by Bo Terp Paulsen), the wave maker signal from the experiment was converted to a flux-condition at the boundary of the potential flow solver. This technique enables a direct representation of the wave maker motion at the expense of excluding absorption of reflected, backward propagating waves. The presence of such waves, however, is expected to be negligible in the numerical model due to the down-wave absorption zone. The profile of the sea bed in the multi-directional calculation is shown in figure 9.8 with a red curve. The profile is similar to the model set-up shown in figure 9.3, but the end of the domain in the shallow part is 1 m longer to make the absorption zone longer in the calculations. The inner boundary of the absorption zone is shown with a dashed line. In the figure the profile is moved 8 m to the right to compare the profile with the profile from the unidirectional calculations, which is shown with a blue curve in the figure. This profile is equal to the profile considered in the CFD-calculations in chapter 8. The inner boundaries of the relaxation zones of this calculation are indicated with blue dashed lines.

In figure 9.8 the water depth where the wave realizations are considered, $h = 0.524\,\mathrm{m}$ in model scale, is also indicated. The water depth is a little smaller than in the model tests, where the depth was 0.55 m. This is due to the smoothing of the corners of the profiles in the calculations, which is necessary to avoid reflections. The slope of the sea bed is therefore not constant 1:25 along the sloping part of the sea bed. It was decided to consider the waves at the same distance from the

wave makers as in the model test (7.75 m), instead of at the same depth. Since the analysis do not consist in comparing the model tests and the calculations, it is not found to be important for the further analysis.

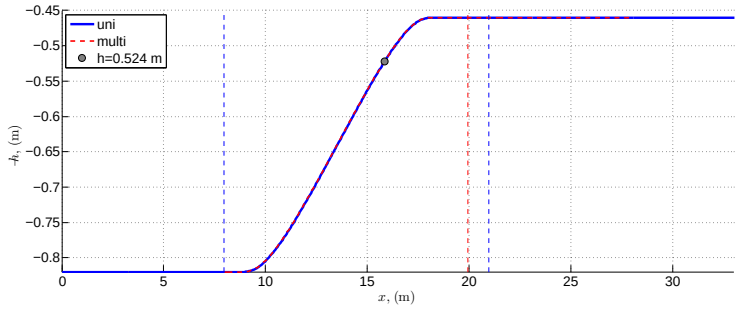

Figure 9.8: *The profile of the sea bed in the two calculations. The circle indicates where the wave realizations are considered. Also the inner boundaries of the relaxation zones in the calculations are indicated with vertical dashed lines.*

The grid spacing in the profile of the 3D-calculations in model scale in the main wave direction is 0.067 m and 0.37 m perpendicular to this direction. A wave that moves in the main direction with a frequency of 2.13 Hz (0.35 Hz in full scale) is therefore only resolved with 5 points. Since the spreading is 0.875 there is no waves which move perpendicular to the main direction, but for waves with an angle to the main direction the resolution is still smaller than in the main direction. This is not ideal, but chosen due to the computational time which is demanding in 3D-calculations. In the vertical direction 11 grid points are used which should be sufficient to describe the waves in the wave spectra. However, due to the lack of grid points in the horizontal directions, it is not certain that all waves in the wave spectra are fully converged. The lack of convergence can result in less broad band forcing. The profile of the 2D-calculations has the same grid spacing as in chapter 8 in the horizontal direction. Waves with frequencies smaller than 0.32 Hz should therefore be converged in this calculation. In the vertical direction 11 grid points are used.
Both the multi-directional and unidirectional calculation of the wave realizations are in model scale and afterwards the surface elevation and wave kinematics are scaled to full scale to allow aeroelastic computations at full scale. As mentioned in chapter 8 the potential flow solver is inviscid and therefore perfect to Froude-scaling.
In the aeroelastic calculations the diameter of the monopile is $D = 6\,\text{m}$ and the thickness is $\mathtt{t} = 60\,\text{mm}$. The water depth is $h = 19.2\text{m}$. The significant wave height, $H_s = 8.3\,\text{m}$, is equal to the calculations in chapter 8, and following the analysis there, the wind speed corresponding to the considered sea state of $V = 30$ m/s, is therefore applied in the present analysis. The wind turbine is therefore parked and the blades pitched to 87° in the calculations. Since the response in both the fore-aft and side-to-side direction is considered, the turbulence of the wind is included in the present aeroelastic calculations, to include the effects from the wind in both directions. The turbulent intensity is $I_t = 0.13$. From the analysis in chapter 5 it shall be remembered that in a storm condition with a parked wind turbine, the aerodynamic forcing and damping are strongest in the side-to-side direction.
As in section 4.4.1, a logarithmic damping of 8 % is applied to represent the damping contributions of soil damping, hydrodynamic damping, structural damping in the tower and monopile and tower dampers.

The force coefficients in Morison's equation, (3.40) and (3.41), at full scale are $C_m = 1$ and $C_D = 1$ to be consistent with the main part of analyses in the thesis.
The wave particle acceleration in Morison's equation (3.40) in a single point is now calculated as

$$a(z,t) = \frac{\partial u}{\partial t} + \frac{\partial u}{\partial z}w(z,t) + \frac{\partial u}{\partial x}u(z,t) + \frac{\partial u}{\partial y}v(z,t) \tag{9.14}$$

$$a_v(z,t) = \frac{\partial v}{\partial t} + \frac{\partial v}{\partial z}w(z,t) + \frac{\partial v}{\partial x}u(z,t) + \frac{\partial v}{\partial y}v(z,t), \tag{9.15}$$

where u and a are the particle velocity and acceleration in the x-direction and v and a_v are the particle velocity and acceleration in the y-direction. In the analyses here the x-direction corresponds to the fore-aft direction. The point force, equation (3.41), changes also in directional waves. Following Rainey (1989) the point force in three dimensions is given as

$$\underline{F_s} = \frac{1}{2}\tan(\tilde{\theta})\underline{\mathsf{n}}_1\rho\mathscr{A}C_m(\underline{u} - \underline{\mathsf{u}})^2, \tag{9.16}$$

where $\underline{\mathsf{n}}_1 = [1\,1\,0]^\mathsf{T}$ is the horizontal vector pointing out from the surface elevation, as indicated in figure 9.9. The angle $\tilde{\theta}$ is the angle between a unit vector pointing upwards, $\underline{\mathsf{n}}_2 = [0\,0\,1]^\mathsf{T}$, and the normal vector of the surface elevation, $\underline{\mathsf{n}}_3$, also indicated in figure 9.9. The normal vector is given as $\underline{\mathsf{n}}_3 = [-\eta_x\ -\eta_y\ 1]^\mathsf{T}$, where η_x and η_y are the derivatives of the surface elevations with respect to the x and y directions. The angle $\tilde{\theta}$ can be found from

$$\tan(\tilde{\theta}) = \frac{\sqrt{|\underline{\mathsf{n}}_3|^2 - |\underline{\mathsf{n}}_2|^2}}{|\underline{\mathsf{n}}_2|} = \sqrt{\eta_x^2 + \eta_y^2}. \tag{9.17}$$

Combining equation (9.16) and (9.17) and further dividing the point force into the fore-aft and side-to-side direction gives

$$F_{s,x} = -\frac{1}{2}\sqrt{\eta_x^2 + \eta_y^2}\rho\mathscr{A}C_m(u - \mathsf{u})^2, \tag{9.18}$$

$$F_{s,y} = -\frac{1}{2}\sqrt{\eta_x^2 + \eta_y^2}\rho\mathscr{A}C_m(v - \mathsf{v})^2. \tag{9.19}$$

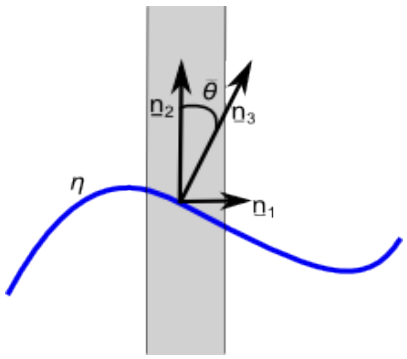

Figure 9.9: *The vectors used to calculate the point force as the surface elevation passes the monopile.*

9.3.1 The free surface elevation

In the following the free surface elevation of the calculated unidirectional and multi-directional wave realizations are compared. The significant wave height and the skewness of the two wave realizations are stated in table 9.3. The difference in H_s and Sk is 0.3 % and 3 %, respectively. Statistically there is therefore good agreement between the two wave realizations. The skewness of the unidirectional wave realization is largest, which is in agreement with the findings from the model tests, where the difference, though, was significant larger.
In figure 9.10 time series of the free surface elevation of the unidirectional and multi-directional wave realizations are compared. It is clear to see that these are two different wave signals. However, in both signals a large wave with approximately same peak value occur after $t = 115\,\mathrm{s}$ and $t = 300\,\mathrm{s}$
In figure 9.10 the amplitude spectra of the surface elevations are shown. The raw spectrum is smoothed by computing the running mean value along a 7 point moving stencil. The two spectra compare generally well, however the unidirectional spectrum contains more energy at the second

	Uni	Multi	Uni/Multi
H_s (m)	8.31	8.33	1.003
Sk (-)	0.63	0.61	0.97

Table 9.3: *The significant wave height and skewness of the unidirectional and multi-directional wave realization.*

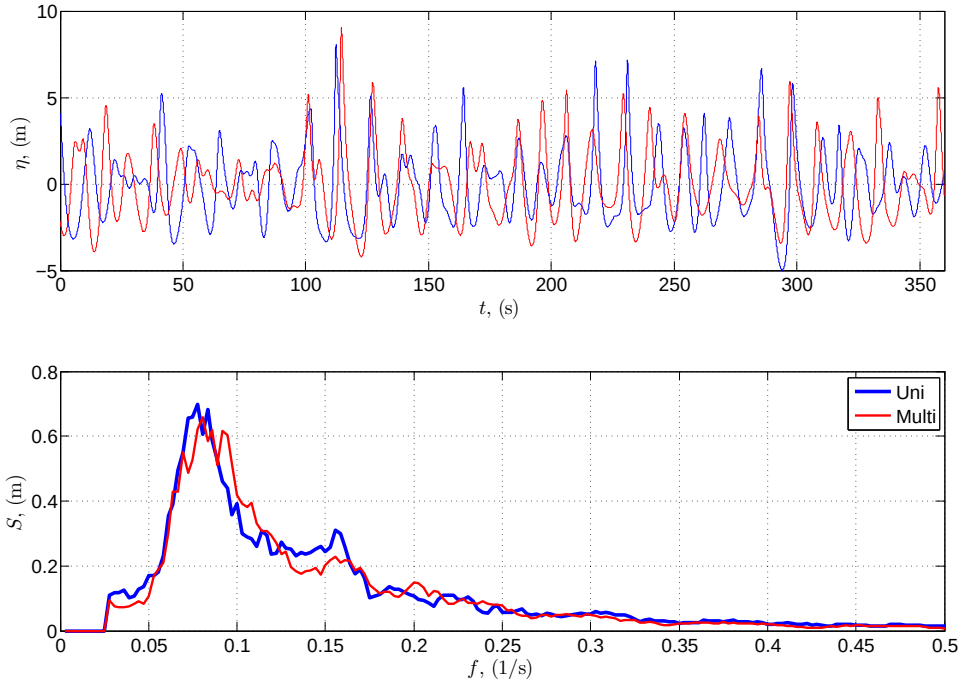

Figure 9.10: *The surface elevation of the unidirectional and multi-directional wave realization and the corresponding spectra.*

harmonic of $f = 0.16\,\text{Hz}$. This is in accordance with the previous findings that the nonlinearity is developed most for the unidirectional wave realizations.
The probability of exceedance of the largest peaks between each zero-down-crossing of the free surface elevations are compared in figure 9.11 and fitted to the Rayleigh distribution. Due to the short length of the signal, the extremes are not considered separately. The Rayleigh distribution represent the data well excepts for the smallest probabilities of exceedance where there is some deviation. The two largest peaks in the signals have a probability of exceedance of zero. They are therefore not shown in the figure because the y-axis is in logarithmic scale. However, in figure 9.10 it is seen that the largest surface elevations in both signals occur at $t = 300\,\text{s}$ and that they are of approximately same size. This explains why the Rayleigh distributions are similar in spite of the large deviation of the peaks with low probability of exceedance.
For probability of exceedance larger than 0.2 the multi-directional wave realization has the largest peaks, while the peaks are largest for the unidirectional wave for probabilities of exceedance smaller than 0.2. This is opposite to what was seen in the model tests, where the multi-directional wave realization has the largest peaks for low probability of exceedance. The directional focusing which was seen for the experiments of the multidirectional large waves are therefore not seen in the numerical analysis, probably due to the short length of the time series.

9.3.2 Dynamic analysis

In the following the aeroelastic calculations with the two wave realizations are compared. In the analysis the sectional moments in the bottom of the tower and in the bottom of the monopile both in the fore-aft and side-to-side direction are considered, to investigate the differences in the

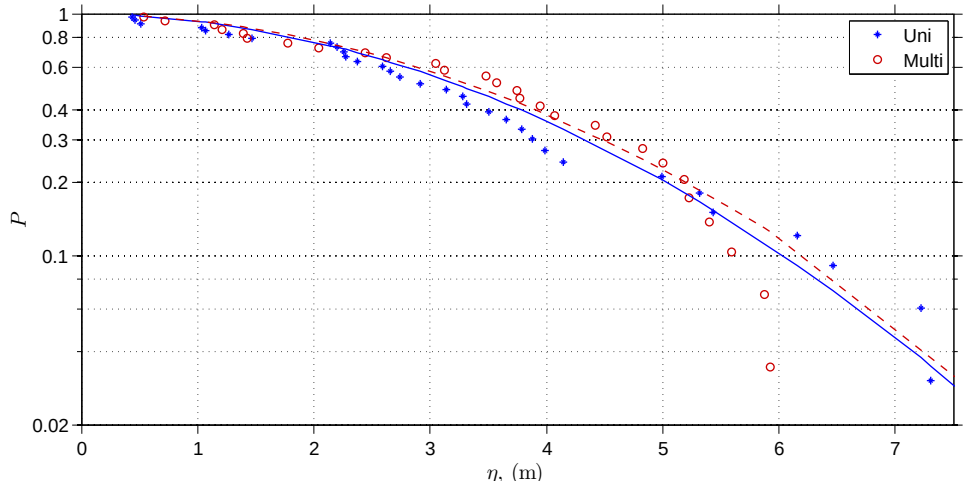

Figure 9.11: *The probability of exceedance of the positive peaks of the surface elevation. The full and dashed line indicate the Rayleigh-distribution*

structural response, when the waves are unidirectional and multi-directional.
In figure 9.12 and 9.12 the probability of exceedance of the positive peaks of the sectional moments in the bottom of the tower and monopile is shown. Due to the wind forcing the forces and moments are shifted to larger values above zero. The positive peaks are therefore defined as peaks larger than the mean of the signals. The data are fitted with the Weibull distribution which represents the data well in the tower, but less well in the monopile.
It is seen that the unidirectional wave realization results in the largest peaks for all probability of exceedance. For the largest peaks the differences are approximately 30 % in the tower and 20 % in the monopile. The difference becomes smaller as the probability of exceedance increases, but it is significant for probabilities of exceedance smaller than 0.8. The result is interesting because the crest value of the unidirectional surface elevation are not largest for all probabilities of exceedance. The reason that the forces are largest can be due to the skewness which was a little larger for the unidirectional wave realization and because the nonlinearity have longer time to develop in the unidirectional waves. The results are in accordance with the model tests, where it was also found that the forces are largest for the unidirectional waves in spite of the largest peaks in the surface elevation is largest for the multi-directional waves.
As an example the sectional moments in the fore-aft direction in the bottom of the tower are shown as function of time in the intervals $t = 105 - 130\,\mathrm{s}$ and $t = 290 - 320\,\mathrm{s}$, in figure 9.14. In these intervals two large waves of approximately same time occur in the two wave realizations. The response due to the unidirectional waves is larger than the response due to the multi-directional waves. It is of course two different waves, which are compared, but the result still indicates that the response is larger due to unidirectional waves.
In figure 9.15 and 9.16 the probability of exceedance of peaks of the sectional moments in the bottom of the tower and monopile in the side-to-side direction are shown. In the side-to-side direction the aerodynamic forcing is dominating, because the blades are pitched 87°, which also are seen in the probability curves. The multi-directional and unidirectional wave realizations result in almost the same moments, despite the absence of wave forcing from the unidirectional wave realizations in this direction. In the monopile there is some deviation in the curves. Surprisingly, the unidirectional wave realization results in the largest peaks for the smallest probabilities of exceedance. This must be because the multi-directional waves dampen the response sometimes, when the wave forcing is in opposite direction of the structural motion.

9.3.3 Equivalent loads

The equivalent loads in the bottom of the tower and monopile in the fore-aft and side-to-side direction are compared in the following. The analyses are based on the sectional moments and are only calculated for $\mathsf{m} = 5$. The time series are short, so the analysis only gives an indication of

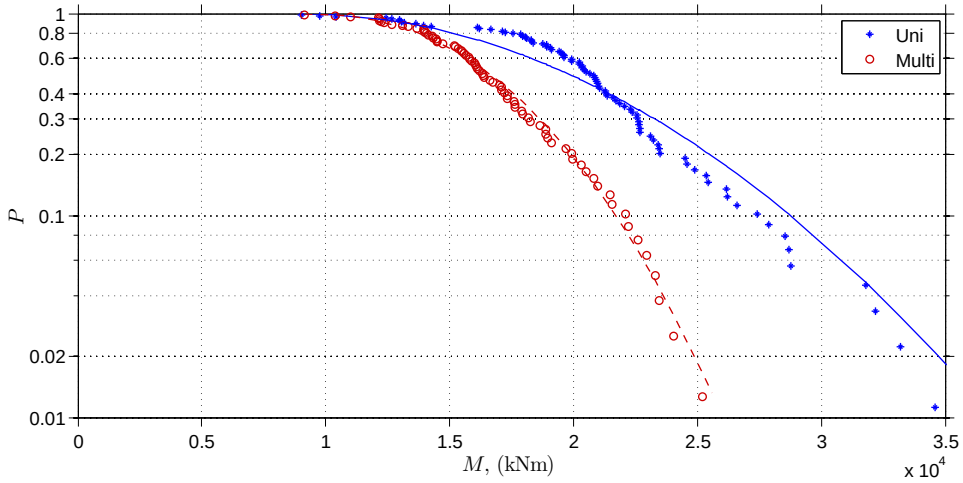

Figure 9.12: *The probability of exceedance of the positive peaks of the sectional moment in the bottom of the tower in the for-aft direction.*

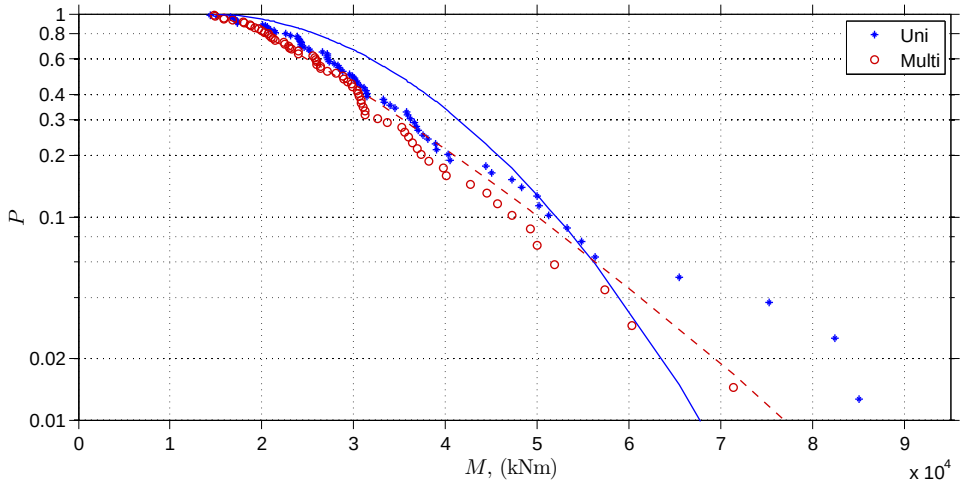

Figure 9.13: *The probability of exceedance of the positive peaks of the sectional moment in the bottom of the monopile in the fore-aft direction.*

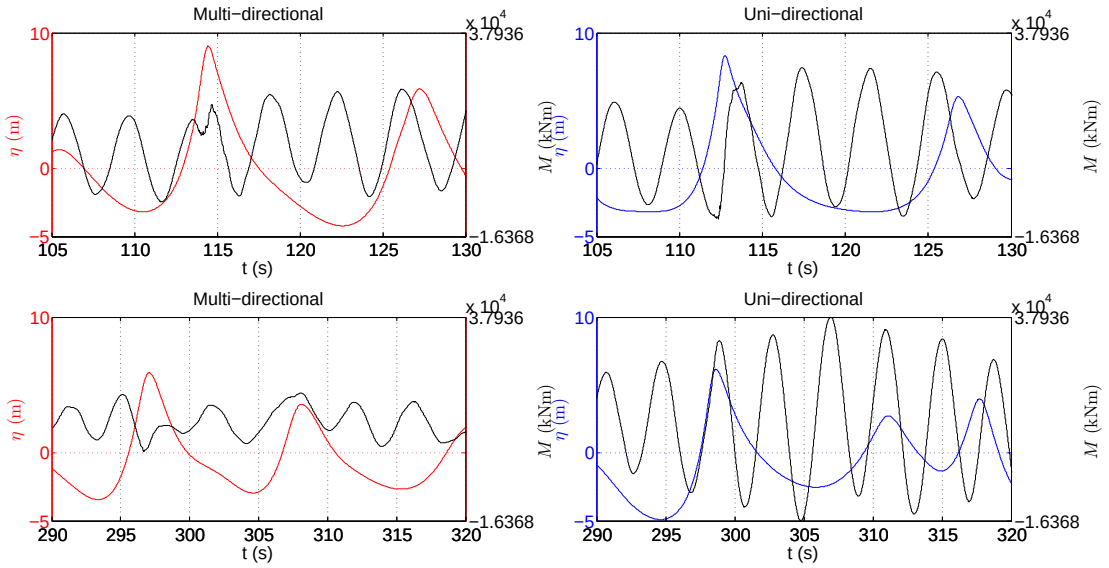

Figure 9.14: *The sectional moments in the fore-aft direction in the tower in two intervals.*

how the fatigue damage will change when the waves are multi-directional compared to when they are unidirectional. It should further be noted that the sea state is an extreme sea state.
In the tower it is seen that the equivalent loads of the unidirectional wave realization are similar in the fore-aft and side-to-side direction. This is due to the dominance of the aerodynamic forcing in the side-to-side direction, which also explains why there is no significant difference between the equivalent loads of the unidirectional and multi-directional wave realizations in the side-to-side direction. In the for-aft direction the equivalent load of the multi-directional wave realization is smaller than the equivalent load of the unidirectional wave realization. This is due to the smaller forces of the multi-directional wave realization, and because the unidirectional wave realization further causes larger dynamic excitation.
In the monopile the equivalent loads are largest in the fore-aft direction for both wave realizations, due to direct exposure to waves in this direction. In the fore-aft direction the equivalent load of the unidirectional wave realization is largest. This is again because the wave forces are largest for the unidirectional waves due to the larger wave skewness and nonlinearity of these waves. In the side-to-side direction the equivalent loads of the two wave realizations are almost identical. This must be due to the aerodynamic dominance.
In figure 9.18 the difference between the equivalent loads due to the multi-directional and unidirectional waves is shown. In the fore-aft direction, both in the tower and in the monopile, the differences are significant. The equivalent loads due to the unidirectional wave realization are 34 % larger in the tower and 10 % larger in the monopile. The difference is largest in the tower, due to the dynamic excitation which is largest in the tower. The result indicates, in spite of the short length of the time series, that the unidirectional waves result in the largest equivalent loads.
In the side-to-side direction the difference between the equivalent loads is 0.1 % in the tower and in the monopile the equivalent load due to the unidirectional wave is 1 % larger. This result again emphasises that the wind is dominant in the side-to-side direction during storm when the wind turbine is parked. The reason that it is the unidirectional wave which results in the largest equivalent load in the monopile must be a coincidence, since the unidirectional wave forcing is zero in this direction and a difference of 1 % is not significant.
In a situation where the wind turbine operates it is believed that the equivalent loads due to the multi-directional wave realization would be larger than the equivalent loads due to the unidirectional wave realization in the side-to-side direction. This is due to the smaller effects from the wind which would exist in the side-to-side direction in such a situation. A further investigation of this effect is left for future studies.

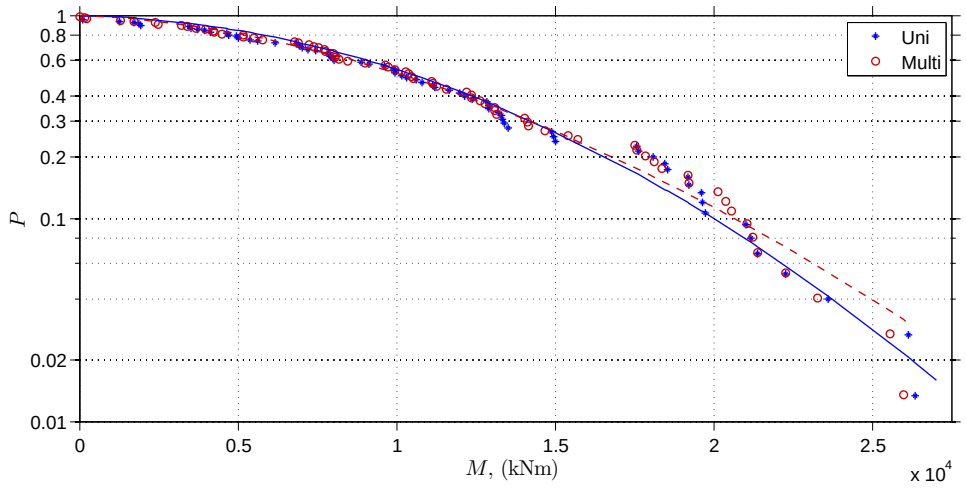

Figure 9.15: *The probability of exceedance of the positive peaks of the sectional moment in the bottom of the tower in the side-to-side direction.*

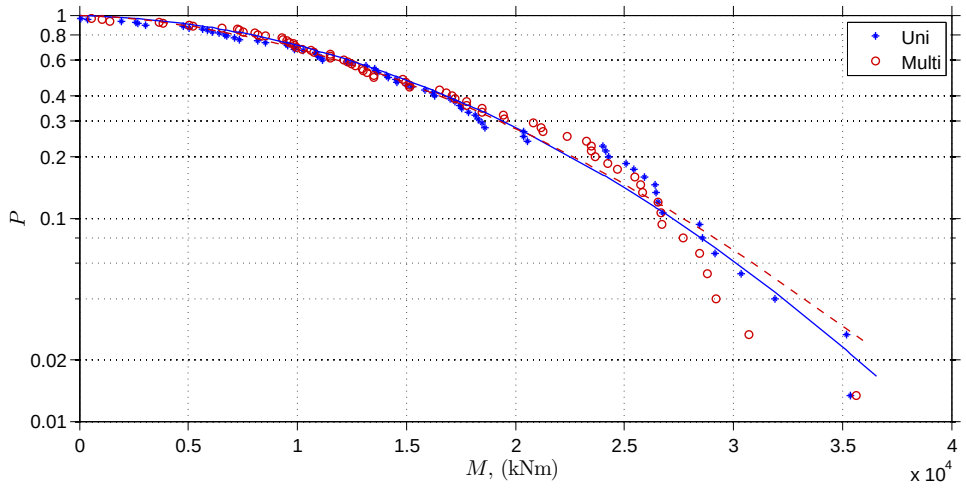

Figure 9.16: *The probability of exceedance of the positive peaks of the sectional moment in the bottom of the monopile in the side-to-side direction.*

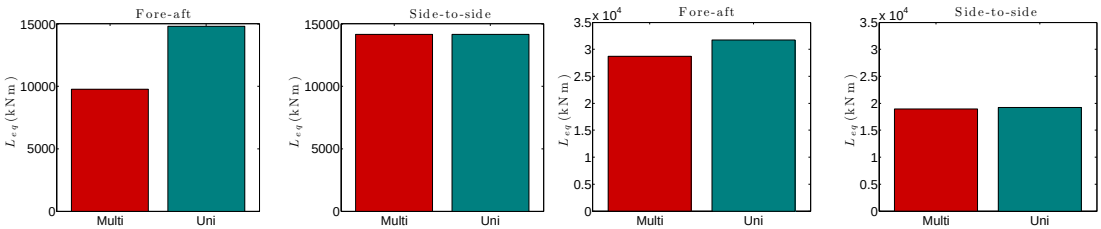

(a) Tower. **(b)** Monopile.

Figure 9.17: *Equivalent loads due to the unidirectional and multi-directional wave realization.*

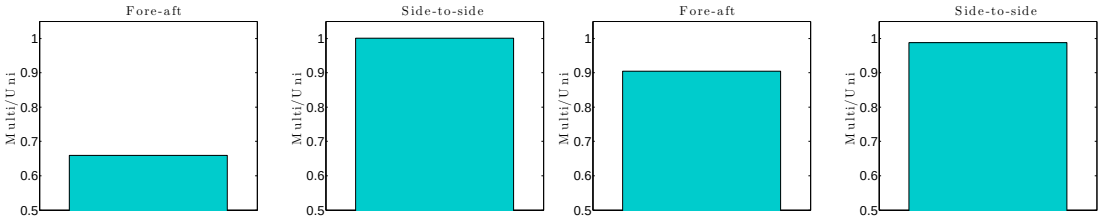

(a) Tower. **(b)** Monopile.

Figure 9.18: *Ratio between equivalent loads due to the multi-directional and unidirectional wave realization.*

9.4 Summary

In the present chapter a small study on the effects of the wave directionality has been carried out. In the first part of the analysis two model tests were considered. A unidirectional and multi-directional wave realization based on the same JONSWAP spectrum were compared. The significant wave height and wave height distribution were found to compare well. The skewness of the unidirectional wave realization was found to be largest. Physically it seems plausible, because the nonlinearity of the waves have longer time to develop in the unidirectional waves. The positive peaks in the surface elevation is largest for the unidirectional waves for probabilities of exceedance larger than 0.4 which is in accordance with the skewness of the waves. For the smallest probabilities of exceedance the multi-directional wave realization has the largest peaks. However, when the peaks of the measured inline force in the main wave direction in the model tests were compared, it was seen that the unidirectional wave realization induces the largest forces, which is up to 20 % larger for the largest peaks. The larger skewness can be the reason for this. It was however, surprisingly that the difference for the smallest forces was very small. Since the waves are inertia dominated it was expected that the spreading of the waves would result in a reduction of the forces also for the smallest waves.

In the dynamic analysis the multi-directional wave realization from the model test was reproduced in OceanWave3D and compared to a calculated unidirectional wave realization based on a JONSWAP-spectrum. In spite of the short length of the time series the analysis indicates that the structural response in the wind turbine tower and monopile can be different if the wave directionality is included in the analysis. The dynamic excitation which occur for the present waves, is reduced significantly with the multi-directional wave realization. The difference between the response was largest in the tower which also was seen in the equivalent loads. This is due to the structural excitation which is largest in the tower. In the side-to-side direction no significant difference between the two wave realizations was observed, which is due to the aerodynamic dominance in this direction.

A limitation of the analysis is the problem with convergence in the numerical calculations. The waves in the high frequency part of the wave spectra are not resolved with enough grid points in the horizontal directions. The problem is most significant for the multi-directional waves, because the distance between the grid points across the main wave direction were significantly larger than in the main wave direction. The lack of convergence can result in smaller broad band forcing.

Chapter 10

Conclusion

In the present thesis an offshore wind turbine on a monopile has been considered. The response in the tower and monopile has been investigated when exposed to linear and fully nonlinear irregular waves. The primary focus of the investigations has been the consequence of incorporation of full nonlinearity in the wave kinematics. However, also other effects such as damping from the waves and the soil and the influence of directional spreading of the waves have been considered. The main findings and conclusions from the chapters are summarized in the following.

Six wind and sea states were considered in the main part of the thesis. The wind and sea states are representative for the North Sea and cover the conditions from below cut-in wind speed to above cut-out wind speed. The comparison of the linear and nonlinear wave realizations showed that the wave transformation was different. The significant wave height of the linear and nonlinear wave realizations were not the same at the four water depths. The free surface elevation and wave kinematics of the linear wave realization were therefore scaled by multiplying the ratio between the nonlinear and linear significant wave heights to ensure that the linear and nonlinear wave loads were based on the same significant wave height. Further, the skewness of the nonlinear wave realizations increased and the spectra of the surface elevations changed as energy was moved to larger and smaller frequencies in the nonlinear wave spectra. Surprisingly, the energy was not taken from the peak of the wave spectra but from the high frequency part of the spectra, which implied that the linear wave spectra contained most energy around the structural first eigenfrequency, relatively to the nonlinear spectra.

The static analysis of the wave forces showed that the nonlinear wave realizations resulted in larger inline forces and overturning moments and that the difference between the linear and nonlinear forces and moments increased with increasing significant wave height.

The nonlinear effect where the steepness of the nonlinear waves increases as the water depth decreases, which causes larger wave forces, was not pronounced in the comparison of the linear and nonlinear inline forces and overturning moments for the first four sea states with significant wave height up to 4.4 m. Only for the largest sea state a clear trend showed that the difference between the linear and nonlinear wave forces increased with decreasing water depth.

In the static analysis it was further found, that since irregular nonlinear waves can be more steep and narrow crested than regular stream function waves, the nonlinear irregular waves can result in significant larger inline force and overturning moment.

The dynamic response in both the tower and monopile was investigated for co-directional wind and waves. When the wind turbine was operating, the aerodynamic forces were dominating and much stronger than the forces from the waves, and it was difficult to see a difference between the response due to the linear and nonlinear wave forcing in the tower. In situations where both the aerodynamic forces and damping were insignificant, excitation of the structural first eigenfrequency due to high frequency wave loads was seen. The monopile reacted quasi-statically to the wave loads and induced excitation of the structural first eigenfrequency with a significant oscillation of the tower.

The comparison of the linear and nonlinear wave realizations in the dynamic analyses did not show a strong effect from the wave nonlinearity. The linear and nonlinear accumulated equivalent load did not vary more than 9 % and the linear accumulated equivalent load was actually largest

for $h = 30\,\text{m}$. This is explained by the broad band forcing which was largest for the linear wave realizations. The linear accumulated equivalent load increased relative to the nonlinear accumulated equivalent load when the water depth changed from $h = 40\,\text{m}$ to $h = 30\,\text{m}$ both in the tower and monopile. This is also explained with the broad band forcing, which is smaller for the nonlinear wave realizations because energy is moved to higher and lower frequencies and this effect becomes stronger when the depth is decreased.
As the water depth was decreased from $h = 30\,\text{m}$ to $h = 25\,\text{m}$, the nonlinear accumulated equivalent load increased relative to the linear accumulated equivalent load. This may be explained by the increase of steepness of the nonlinear waves which results in larger wave forcing and also more dynamic excitation, which is a nonlinear effect. Of nonlinear effects such as springing, ringing and dynamic excitation, the dynamic excitation was dominating and observed in the response of the tower and monopile caused by the largest nonlinear wave realization. The results further showed that the largest wind and sea states in spite of their low probability of occurrence can be important for the fatigue damage both when the linear and nonlinear waves are considered.
The effects of wave nonlinearity was also investigated in a misaligned wind and wave climate for the same six wind and sea states. The effect of the broad band forcing increased in the side-to-side direction due to lack of aerodynamic damping which amplified the effects from the waves. The linear accumulated equivalent load in the tower was larger than the nonlinear accumulated equivalent load for the three largest water depths in the side-to-side direction. This result shows that the energy distribution in the wave spectrum can be very important in the fatigue damage and that it in some situations can be more important than the actually size of the wave forcing, which was largest for the nonlinear wave realizations.
An analysis with five other sea states with larger significant wave heights showed that in a misaligned wind and wave climate the nonlinearity of the waves can increase the accumulated equivalent load significantly in the tower in the side-to-side direction. For the considered five sea states the nonlinear accumulated equivalent load was 35 % larger than the linear accumulated accumulated equivalent load.
An example of other findings is that for the parked wind turbine in storm conditions the effect of the wave forcing was reduced in the side-to-side direction. This was both because the misalignment between the wind and waves only was 60° but also because the aerodynamic damping and forcing are strong in the side-to-side direction due to the pitched blades.
The analyses contribute to the interpretation that the nonlinearity of the waves are important in ultimate load analyses, and that the nonlinearity can be important in the fatigue analyses. In order to investigate the importance of the nonlinearity and the dynamic response due to the nonlinearity it is further important to understand and know the amount of damping which exists in an offshore wind turbine and its foundation.

The hydrodynamic damping was calculated in WAMIT and was found to be between 0.2 % and 0.5 % in logarithmic decrement. This damping is therefore small compared to other damping effects, however not small enough to be neglected. The damping increases with increasing water depth and is largest at the structural first eigenfrequency.
A cyclic soil model was implemented in Flex5 to investigate how the soil affects the response of the monopile and tower. The cyclic soil model was compared to an elastic soil model with standard p-y curves and a constant damping factor. The comparison showed that the overall damping from the soil can be represented by a constant damping term. However, in order to get the correct damping, the damping factor has to be adjusted according to the wind and sea states which are considered, as the damping ratio of the cyclic model depends on the amplitude of the pile displacement. Further, the cyclic soil model resulted in a larger excitation of high frequency oscillation of 1.3 Hz. The frequency corresponds to a global eigenfrequency whit 80 % of the model energy distributed in the tower and monopile. This high frequency excitation is assumed to be due to the creation of the gap behind the pile in the cyclic model. This larger excitation caused larger equivalent loads, particular in the monopile, which indicates that even if the constant damping in the elastic model represents the soil damping well, it can be non-conservative to use the elastic model as the detailed and sometimes rapidly varying soil force is not included in that model.
The wave loads based on the potential flow solver and Morison's equation were compared to forces calculated in the CFD-solver OpenFOAM. The analysis showed that it is difficult to describe the

hydrodynamic forces in an irregular time series with Morison's equation if both the largest and smallest forces are based on the same force coefficients. Even if there is good agreement between the peaks of hydrodynamic forces based on Morison's equation and those from the CFD-solver, it was found that the difference in the peaks of the sectional forces in the tower can be significant in the dynamic analysis. This was due to differences in steepness of the waves from the potential flow solver and the CFD-solver which resulted in very different structural responses because a larger steepness causes larger dynamic excitation. In the present analysis, the excitation was largest due to the Morison forces.
In the last analysis in this thesis the effect of wave directionality was investigated. The analyses were both based on experiments and numerical calculations. The analyses indicate that the directionality of the waves can lead to a significant decrease in the wave forcing. This is both because the skewness of the waves decreases in multi-directional waves, and because the nonlinearity of the large unidirectional waves has longer time to develop relative to the multi-directional waves. In the dynamic analysis it was found that the reduction of the sectional forces due to the wave directionality is largest in the tower. This is due to the structural excitation, which is much smaller with the multidirectional waves.

The main limitation of the studies in the present thesis is that the waves are not fully converged. The waves in the wave realizations with frequencies between 0.25-0.35 Hz had relative errors of 3-8 %, respectively. In the static analysis this is not believed to be important, since the waves in the part of the wave spectra with most energy are converged. However, in the dynamic analysis it can be important for the results, since it was found that the broad band forcing contributed significantly to the fatigue damage. It is therefore expected that the fully converged wave realizations will have a larger contribution to the fatigue damage caused by the broad band forcing.
Another limitation in the study is the lack of a breaking wave load model, and the approach of damping of the unrealistic large waves in the two largest nonlinear wave realizations. The approach was very non-physical, but gave more realistic results than a case where the unrealistic large waves were not damped.
However, the limitations do not change the interpretation that the nonlinearity of the waves can be important in the design of offshore wind turbines.

Suggestions for further work

The results of this thesis lead to many new and follow up questions which should be investigated in further work. The most prevailing questions are mentioned below.

- First of all the five wave realizations should be recalculated to ensure that the lack of convergence in the wave realizations does not have significant influence on the main findings.
- An improvement of the wave-breaking description in the wave model would clear up the uncertainties in the analyses, when the largest waves are considered.
- An incorporation of MacCamy-Fuchs theory to include a diffraction correction of the added mass coefficient would also improve the analysis. It was not included in the present analysis because it was not possible to distinguish between the free and bound waves in the nonlinear wave realizations. However, it is expected that the effects from the broad band forcing will decrease if the theory is included because it leads to smaller inertia coefficients for the waves in the high frequency part of the wave spectra.
- A more thorough fatigue study should be conducted where more load cases are considered in the analysis to investigate the effects of the nonlinearity more deeply. In this analysis time should be spend on analysing for which waves nonlinear effects such as springing, ringing and impulsive excitation occur and further how often they occur.
- It would also be interesting to improve the soil model, such that the description of the full extent of the monopile is included in the calculations. Further, the model of Klinkvort (2012) should be implemented. This model includes the back filling of the soil in the gap, which most likely will cause more dynamic responses due to soil.

- The thesis touched on the topics of direct application of CFD wave loads and inclusion of wave directionality, both with a main focus on quantifying the load effects relatively to the unidirectional wave loads based on the undisturbed wave kinematics. It could be interesting to make more dynamic analysis with the forces from the CFD-solver to quantify the apparent load reduction associated with the more detailed CFD-description of the waves. A larger analysis of the importance of the multi-directional seas, both linear and nonlinear, should also be conducted, where more sea states are considered. Both these analyses can supplement the present study and contribute to the understanding of the importance of including the wave nonlinearity in the design of offshore wind turbines.

Bibliography

Agarwal, Puneet & Manuel, Lance 2011 Incorporating irregular nonlinear waves in coupled simulation and reliability studies of offshore wind turbines. *Applied Ocean Research* **33** (3), 215–227.

API 2010 *Recommended Practice for Planning, Designing and Constructing Fixed Offshore Platforms—Working Stress Design (API RP 2A-WSD)*. American petroleum institute.

Babanin, A.V. 2009 Breaking of ocean surface waves. *Acta Physica Slovaca* **59** (4), 305–535.

Bredmose, H., Schløer, S. & Paulsen, B.T. 2012 Higher-harmonic response of a slender cantilever beam to fully nonlinear regular wave forcing. In *Proceedings of the ASME 2012 31th International Conference on Ocean, Offshore and Arctic Engineering*.

Bredmose, H., Slabiak, P., Sahlberg-Nielsen, L. & Schlütter, F. 2013 Dynamic excitation of monopiles by steep and breaking waves. Experimental and numerical study. In *Proceedings of the ASME 2013 32st International Conference on Ocean, Offshore and Arctic Engineering*.

Camp, T.R., Morris, M.J., van Rooij, R., van der Tempel, J., Zaaijer, M., Henderson, A., Arguriadis, K., Schwartz, S., Just, H., Grainger, W. & Pearce, D. 2003 Design methods for offshore wind turbines at exposed sites. *Tech. Rep.*. Garrad Hassan and Partners Ltd., EU Joule III JOR3-CT95-0284.

Chaplin, J. R., Rainey, R.C. T. & Yemm, R.W. 1997 Ringing of a vertical cylinder in waves. *Journal of Fluid Mechanics* **350**, 119–147.

Cook, M.F. & Vandiver, J.K. 1982 Measured and predicted dynamic response of a single pile platform to random wave. In *OTC 4285 (Offshore Technology Conference report)*.

DNV-OS-J101 2010 *Design of Offshore Wind Turbines*. Det Norske Veritas.

Downing, S. D. & Socie, D.F. 1982 Simple rainflow counting algorithms. *International Journal of Fatigue* **4** (1), 31–40.

Engsig-Karup, A.P., Bingham, H.B & Lindberg, O. 2009 An efficient flexible-order model for 3D nonlinear water waves. *Journal of Computational Physics* **228** (6), 2100–2118.

Faltinsen, O. 1993 *Sea Loads on Ships and Offshore Structures*. Campridge University Press.

Faltinsen, O.M., Newman, J.N. & Vinje, T. 1995 Nonlinear-wave Loads On a Slender Vertical Cylinder. *Journal Of Fluid Mechanics* **289**, 179–198.

Fenton, J.D. 1988 The numerical solution of steady water wave problems. *Computers & Geosciences* **14** (3), 357–368.

Fenton, J.D. 1990 Nonlinear wave theory. In B. LeMéhauté and B. M. Hanes (Eds.). *The Sea - Ocean Engineering Science* **9**, 3–25.

Fischer, T., Rainey, P., Bossanyi, E. & Kühn, M. 2011 Study on control concepts suitable for mitigation of loads from misaligned wind and waves on offshore wind turbines supported on monopiles. *Wind Engineering* **35** (5), 561–574.

Fischer, T., de Vries, W. & Schmidt, B. 2010 Upwind Design Basis. WP4: Offshore Foundations and Support Structures. *Tech. Rep.*. Project UpWind, Allmandring 5B, 70550 Stuttgart, Germany.

Forristall, G.Z. & Ewans, K.C. 1997 Worldwide measurements of directional wave spreading. *Journal of Atmospheric and Oceanic Technology* **15** (2), 440–469.

Frandsen, S., Tarp-Johansen, N.J., Hansen, E.A., Høgedal, M., Ibsen, L.B. & Jensen, L. 2006 Offshore wind turbine design: addressing uncertainty drivers. In *Proceedings of European Wind Energy Conference & Exhibition: EWEC 2006*.

Gravesen, H., Larsen, L.S., Bingham, H.B., Tarp-Johansen, N.J., Pedersen, J. & Vølund, P. 2003 Consequences of steep waves and large wave forces to offshore wind turbine design. In *European wind energy conference and exhibition*. Madrid, Spain.

Grue, J. & Huseby, M. 2002 Higher-harmonic wave forces and ringing of vertical cylinders. *Applied Ocean Research* **24** (4), 203–214.

Gujer, P. 2005 Overall damping for piled offshore support structures, guideline for the certification of offshore wind turbines. *Tech. Rep.*. Germanischer Lloyd, Wind Energy.

Hald, T. & Høgedal, M. 2005 Implementation of a finite element foundation module in flex5 using craig–bampton substructuring. In *Proceedings of Copenhagen offshore wind*.

Hansen, M.H, Hansen, A., Larsen, T.J, Øye, S., Sørensen, P. & Fuglsang, P. 2005 Control design for a pitch-regulated, variable speed wind turbine. *Tech. Rep.*. Risø National Laboratory, Roskilde, Denmark.

Hededal, O. & Klinkvort, R.T 2010 A new elasto-plastic spring element for cyclic loading of piles using the p-y-curve concept. *Numerical Methods in Geotechnical Engineering - Benz & Nordal (eds)* **2**.

Henderson, A.R., Zaaijer, M.B. & Camp, T.R. 2003 Hydrodynamic loading on offshore wind turbines. In *Offshore Wind Energy in the Mediterranean and Other European Seas Conference (OWEMES)*.

Hirt, C.W. & Nichols, B.D. 1981 Volume of fluid (VOF) method for the dynamics of free boundaries. *Journal of computational physics* **39** (1), 201–225.

IEA 1990 *Expert Group Study on Recommended practices for Wind Turbine Testing and Evaluation. Part 3. Fatigue loads.*, 2nd edn. International Energy Agency Programme for Research and Development on Wind Energy Conversion Systems.

IEC61400-1 2006 *International Standard. Wind turbines – Part 1: Design requirements*, 3rd edn.

IEC61400-3 2009 *International Standard. Wind turbines – Part 3: Design requirements for offshore wind turbines*, 1st edn.

Jacobsen, V. & Rugbjerg, M. 2005 Offshore Wind Farms–the Need for Metocean Data. In *Proceedings of Copenhagen offshore wind*.

Johannessen, K., Meling, T.S. & Haver, S. 2002 Joint distribution for wind and waves in the northern north sea. *International Journal of Offshore and Polar Engineering* **12** (1), 1–8.

Jonkman, J.M., Butterfield, S., Musial, W. & Scott, G. 2009 Definition of a 5-MW reference wind turbine for offshore system development. *Tech. Rep.*. National Renewable Energy Laboratory.

Jonkman, J.M. & Musial, W. 2010 Offshore code comparison collaboration (OC3) for IEA task 23 offshore wind technology and deployment. *Tech. Rep.*. National Renewable Energy Laboratory.

Kühn, M. 2001 Dynamics and Design Optimation of Offshore Wind Energy Conversion Systems. PhD thesis, Delft University of Technology.

Kim, T. & Natarajan, A. 2013 Effect of coupled non linear wave kinematics and soil flexibility on the design loads of offshore wind turbines. In *51st AIAA Aerospace Sciences Meeting*.

Klinkvort, R.T. 2012 Centrifuge modelling of drained lateral pile - soil response. PhD thesis, The Technical University of Denmark, DTU Civil Engineering.

Klinting, P. & Sand, S.E. 1987 Analysis of prototype freak waves. *Tech. Rep.*. Dansk Hydraulisk Inst., Hørsholm (Denmark).

Krokstad, J.R., Stansberg, C.T., Nestegard, A. & Marthinsen, T. 1998 A new non-slender ringing load approach verified against experiments. *Journal of Offshore Mechanics and Arctic Engineering* **120** (1), 20–29.

Larsen, T.J., Madsen, H.A., Hansen, A.M. & Thomsen, K. 2005 Investigations of stability effects of an offshore wind turbine using the new aeroelastic code HAWC2. In *Proceedings of Copenhagen Offshore Wind*, pp. 25–28.

Longuet-Higgins, M.S. 1985 Accelerations in steep gravity waves. *J. Phys. Oceanogr.* **15**, 1570—-1579.

MacCamy, R.C. & Fuchs, R.A. 1954 Wave forces on piles: A diffraction theory. *Tech. Rep.*. U.S. Army Corps of Engineering, Beach Erosion Board, Tech. Memo. No. 69.

Malenica, $\check{S}$. & Molin, B. 1995 Third-harmonic wave diffraction by a vertical cylinder. *Journal of Fluid Mechanics* **302**.

Mann, J. 1998 Wind field simulation. *Probabilistic Engineering Mechanics* **13** (4), 269–282.

Manners, W. & Rainey, R.C.T. 1992 Hydrodynamic forces on fixed submerged cylinders. *Proceedings of the Royal Society of London. Series A: Mathematical and Physical Sciences* **436** (1896), 13–32.

Marino, E., Borri, C. & Peil, U. 2011 A fully nonlinear wave model to account for breaking wave impact loads on offshore wind turbines. *Journal of Wind Engineering and Industrial Aerodynamics* **99** (4), 483–490.

Massel, S.R. 2001 Wavelet analysis for processing of ocean surface wave records. *Ocean Engineering* **28** (8), 957–987.

van der Meulen, M.B., Ashuri, T., van Bussel, G.J.W. & Molenaar, D.P. 2012 Influence of nonlinear irregular waves on the fatigue loads of an offshore wind turbine. In *To be published in Torque 2012 conference proceedings*.

Mitche, R. 1944 Mouvement ondulatoires de la mer en profondeur constante ou decroissante. *Annales des Ponts et Chaussées* **44**, 42–78.

Mitsuyasu, H., Tasai, F., Suhara, T., Mizuno, S., Ohkusu, M., Honda, T. & Rikiishi, K. 1975 Observations of the directional spectrum of ocean waves using a cloverleaf buoy. *Journal of Physical Oceanography* **5** (4), 750–760.

Molenaar, D.-P. 2003 Cost-effective design and operation of variable speed wind turbines. PhD thesis, Delft University of Technology.

Newman, J. N. 1994 Wave effects on deformable bodies. *Applied Ocean Research* **16** (1), 47–59.

Nielsen, A.W., Schlütter, F., Sørensen, J.V.T. & Bredmose, H. 2012 Wave loads in a monopile in 3d waves. In *Proceedings of the ASME 2012 31st International Conference on Ocean, Offshore and Arctic Engineering*.

Norton, E.J. 2003 Recommendations for design of offshore wind turbines. *Tech. Rep.*. Garrad Hassan and Partners Ltd., (RECOFF-project).

Økland, O.D. 2010 Fatigue assessment for kvitebjørn jacket. *Tech. Rep.*. Marintek, Marine Technology Centre, Otto Nielsens veg 10, 7450 Trondheim, Norway.

Øye, S. 1996 Flex4 simulation of wind turbine dynamics. In *28th IEA Meeting of Experts Concerning State of the Art of Aeroelastic Codes for Wind Turbine Calculationsn (available through International Energy Agency)*.

Passon, P. & Kühn, M. 2005 State-of-the-art and development needs of simulation codes for offshore wind turbines. In *Copenhagen Offshore Wind 2005 Conference and Expedition Proceedings*.

Paulsen, B.T., Bredmose, H. & Bingham, H.B. 2012 Accurate computation of wave loads on a bottom fixed circular cylinder. In *International Workshop on Water Waves and Floating Bodies*.

Paulsen, B.T., Bredmose, H., Bingham, H.B. & Schløer, S. 2013*a* Steep wave loads from irregular waves in an offshore wind turbine foundation: computation and experiment. In *Proceedings of the ASME 2013 32st International Conference on Ocean, Offshore and Arctic Engineering*.

Paulsen, B. T., Bredmose, H. & Bingham, H. B. 2013*b* An efficient domain decomposition strategy for wave loads on surface piercing circular cylinders. Manuscript submitted for publication.

Paulsen, B. T., Bredmose, H., Bingham, H. B. & Jacobsen, N.G. 2013*c* Forcing of a bottom mounted circular cylinder by steep regular water waves at finite depth. Manuscript submitted for publication.

Quarton, David *et al.* 2005 An international design standard for offshore wind turbines: IEC 61400-3. Garrad Hassan, Garrad Hassan and Partners Ltd, St Vincent's Works, Silverthorne Lane, Bristol BS2 0QD, UK.

Rainey, R.C.T. 1989 A new equation for calculating wave loads on offshore structures. *Journal of Fluid Mechanics* **204**, 295–324.

Rainey, R.C.T. 1995 Slender-body expressions for the wave load on offshore structures. *Proceedings of the Royal Society of London. Series A: Mathematical and Physical Sciences* **450** (1939), 391–416.

de Ridder, E.J., Aalberts, P., van den Berg, J., Buchner, B. & Peeringa, J. 2011 The dynamic response of an offshore wind turbine with realistic flexibility to breaking wave impact. In *Proceedings of the 30th International Conference on Ocean, Offshore and Arctic Engineering*.

Rychlik, I. 1987 A new definition of the rainflow cycle counting method. *International Journal of Fatigue* **9** (2), 119–121.

Sand, S.E. & Mynett, A.E. 1987 Directional wave generation and analysis. In *Proc. IAHR Seminar on Wave Analysis and Generation in Laboratory Basins, 22nd IAHR Congress, Lausanne, Switzerland*.

Schaumann, P. & Böker, C. 2007 Influence of Wave spreading in Short-term Sea States on the Fatigue of Offshore Support Structures at the Example of the FINO1-Research Platform. DEWI-Magazin Nr. 30, Deutsches Windenergie Institut, `http://www.dewi.de/dewi/index.php?id=46&L=3dchjtrwcmnqhhu`.

Schløer, S., Bredmose, H. & Bingham, H.B. 2011 Irregular wave forces on monopile foundations. Effect of full nonlinearity and bed slope. In *Proceedings of the ASME 2011 30th International Conference on Ocean, Offshore and Arctic Engineering*.

Schløer, S., Bredmose, H., Bingham, H.B. & Larsen, T.J 2012 Effects from fully nonlinear irregular wave forcing on the fatigue life of an offshore wind turbine and its monopile foundation. In *Proceedings of the ASME 2012 31th International Conference on Ocean, Offshore and Arctic Engineering*.

Sharma, J.N. & Dean, R.G. 1981 Second-order directional seas and associated wave forces. *Society of Petroleum Engineers Journal* **21** (1).

Sumer, M.B. & Fredsøe, J. 2002 *The Mechanics of Scour in the Marine Environment*. World Scientific Publishing Co. Pte. Ltd.

Sumer, M.B. & Fredsøe, J. 2006 *Hydrodynamics around cylindrical structures*. World Scientific Publishing Co. Pte. Ltd.

Tarp-Johansen, N. J., Andersen, L., Christensen, E.D., Mørch, C., Kallesøe, B. & Frandsen, S. 2009 Comparing sources of damping of cross-wind motion. In *European Offshore Wind Conference (EOW). Stockholm, Sweden: European Wind Energy Association*.

Thomassen, P.E., Bruheim, P.I., Suja, L. & Frøyd, L. 2012 A novel tool for fem analysis of offshorewind turbineswith innovative visualization techniques. In *International Offshore and Polar Engineering Conference*.

Toffoli, A., Onorato, M. & Monbaliu, J. 2006 Wave statistics in unimodal and bimodal seas from a second-order model. *European Journal of Mechanics-B/Fluids* **25** (5), 649–661.

Twidell, J. & Gaudiosi, G., ed. 2009 *Offshore Wind Power*. Multi-Science Publishing Co. Ltd.

Van Der Tempel, J. 2006 Design of support structures for offshore wind turbines. PhD thesis, Delft University of Technology.

Vogt, Y. 2013 Windmills at sea can break like matches. `http://www.apollon.uio.no/english/articles/2013/windmills.html`, accessed: 2013-06-27.

WAFO-Tutorial 2011 *WAFO -a Matlab Toolbox for Analysis of Random Waves and Loads*. Lund University.

Waisman, F., Gurley, K., Grigoriu, M. & Kareem, A. 2002 Non-Gaussian model for ringing phenomena in offshore structures. *Journal Of Engineering Mechanics-ASCE* **128** (7), 730–741.

Walter, M. H. 1999 Sea spectra revisited. *Marine Technology* **36** (4), 221–227.

Wienke, J. & Oumeraci, H. 2005 Breaking wave impact force on a vertical and inclined slender piles -theoretical and large-scale model investigations. *Coastal Engineering* **52** (5), 435–462.

Wilkes, J. & Moccia, J. 2013 Wind in power: 2012 European statistics. *Tech. Rep.*. European Wind Energy Association.

Williams, J.M. 1981 Limiting gravity waves in water of finite depth. *Philosophical Transactions of the Royal Society of London. Series A, Mathematical and Physical Sciences* **302**, 139–188.

DTU Wind Energy is a department of the Technical University of Denmark with a unique integration of research, education, innovation and public/private sector consulting in the field of wind energy. Our activities develop new opportunities and technology for the global and Danish exploitation of wind energy. Research focuses on key technical-scientific fields, which are central for the development, innovation and use of wind energy and provides the basis for advanced education at the education.

We have more than 230 staff members of which approximately 60 are PhD students. Research is conducted within 9 research programmes organized into three main topics: Wind energy systems, Wind turbine technology and Basics for wind energy.

Technical University of Denmark
DTU Vindenergi
Frederiksborgvej 399
Building 118
4000 Roskilde
Denmark
Telefon 46 77 50 85
info@vindenergi.dtu.dk
www.vindenergi.dtu.dk